529-1380

MARTIN MARIETTA ENERGY SYSTEMS LIBRARIES

3 4456 0383928 3

ORNL-3836
UC-20 – Controlled Thermonuclear Processes
TID-4500 (43rd ed.)

THERMONUCLEAR DIVISION
SEMIANNUAL PROGRESS REPORT
FOR PERIOD ENDING APRIL 30, 1965

OAK RIDGE NATIONAL LABORATORY
CENTRAL RESEARCH LIBRARY
CIRCULATION SECTION
4500N ROOM 175
LIBRARY LOAN COPY
DO NOT TRANSFER TO ANOTHER PERSON.
If you wish someone else to see this report, send in name with report and the library will arrange a loan.
ORNL-118 (6-97)
(3 5-60)

OAK RIDGE NATIONAL LABORATORY
operated by
UNION CARBIDE CORPORATION
for the
U.S. ATOMIC ENERGY COMMISSION

Printed in USA. Price $5.00. Available from the Clearinghouse for Federal Scientific and Technical Information, National Bureau of Standards, U.S. Department of Commerce, Springfield, Virginia

LEGAL NOTICE

This report was prepared as an account of Government sponsored work. Neither the United States, nor the Commission, nor any person acting on behalf of the Commission:

A. Makes any warranty or representation, expressed or implied, with respect to the accuracy, completeness, or usefulness of the information contained in this report, or that the use of any information, apparatus, method, or process disclosed in this report may not infringe privately owned rights; or

B. Assumes any liabilities with respect to the use of, or for damages resulting from the use of any information, apparatus, method, or process disclosed in this report.

As used in the above, "person acting on behalf of the Commission" includes any employee or contractor of the Commission, or employee of such contractor, to the extent that such employee or contractor of the Commission, or employee of such contractor prepares, disseminates, or provides access to, any information pursuant to his employment or contract with the Commission, or his employment with such contractor.

ORNL-3836

Contract No. W-7405-eng-26

THERMONUCLEAR DIVISION
SEMIANNUAL PROGRESS REPORT
For Period Ending April 30, 1965

SEPTEMBER 1965

OAK RIDGE NATIONAL LABORATORY
Oak Ridge, Tennessee
operated by
UNION CARBIDE CORPORATION
for the
U. S. ATOMIC ENERGY COMMISSION

MARTIN MARIETTA ENERGY SYSTEMS LIBRARIES
3 4456 0383928 3

Contents

INTRODUCTION vii

ABSTRACTS ix

1. INJECTION AND ACCUMULATION: SINGLE-PASS EXPERIMENTS (DCX-1) 1
   - 1.1 Introduction 1
   - 1.2 Microinstability Losses 1
   - 1.3 Microinstability Mode Assignments 6
   - 1.4 Stabilization Experiments 7
   - 1.5 Lorentz Dissociation of H_3^+ 11
   - 1.6 Lorentz Dissociation of Directly Extracted H_2^+ 12
   - 1.7 Injector Modifications 13
   - 1.8 Acknowledgments 13

2. INJECTION AND ACCUMULATION: MULTIPLE-PASS EXPERIMENTS (DCX-2) 15
   - 2.1 Introduction 15
   - 2.2 Lithium-Arc Experiments 15
     - 2.2.1 The Study of the Origin of the Central Peak 15
     - 2.2.2 Pressure and Beam-Current Variations 16
     - 2.2.3 Arc-Current Variation 18
     - 2.2.4 Background Plasma 19
     - 2.2.5 Radial Diffusion of Lithium Ions 20
   - 2.3 Hydrogen-Arc Experiments 20
   - 2.4 Gas Dissociation 21
   - 2.5 Radio-Frequency Measurements 22
   - 2.6 Central-Peak and Side-Lobe Plasmas 27
   - 2.7 Molecular-Ion-Beam Structure 30
   - 2.8 Vacuum Conditions 31

3. ELECTRON-CYCLOTRON HEATING 33
   - 3.1 Electron-Cyclotron Heating Experiments in the EPA Facility 33
     - 3.1.1 Introduction 33
     - 3.1.2 Neutral-Beam Injection Studies 33
     - 3.1.3 Future Modifications 34

3.2 Electron-Cyclotron Heating Experiments in the Redesigned ELMO Facility 34
3.2.1 Preliminary Experiments 34
3.3 Electron-Cyclotron Heating Experiments in the Physics Test Facility (PTF) 35
3.3.1 Instability Studies 35

4. PLASMA PHYSICS 36
4.1 Beam-Plasma Interaction Experiments 36
4.1.1 Evidence for Burnout; Plasma Power Measurements 36
4.1.2 Microwave-Cutoff Experiments in Burnout V 38
4.1.3 Attempts to Measure Plasma Density in Burnout IV with a Gold-Vapor Probe 39
4.1.4 Development of a Hot-Electron-Plasma Blanket 40
4.1.5 Measuring Hot-Electron Density with Molybdenum Dust 45
4.2 Further Time-of-Flight Studies of Ionic Sound Waves 45
4.2.1 Introduction 45
4.2.2 Interference Experiments 46
4.2.3 Rectilinear Propagation 49
4.2.4 Ion-Wave Focusing 49
4.2.5 Reflection Experiments 50
4.2.6 Magnetic Field Effects 50
4.2.7 Anticoincidence Observing 51
4.2.8 Cutoff and Dispersion Experiments 51
4.3 Use of a Grid-Dip Meter to Measure Electron Density 53
4.4 Plasma-Impedance-Measuring Technique 54
4.5 Beam Stabilization in the Calutron 55
4.6 Studies of Minimum-*B* Field Shapes for Gas-Arc Flute Suppression 58
4.7 The Hydrogen Arc in the Long Solenoid 61
4.7.1 Introduction 61
4.7.2 Geometry 61
4.7.3 Baffle Saturation Currents 62
4.7.4 Anode Measurements 63
4.7.5 Power Distribution 64
4.8 Excitation Heating of Ions by Electrons 64
4.8.1 Introduction 64
4.8.2 Cooling Rate for Ions 64
4.8.3 Estimate of Cross Section for Heating Step 65
4.8.4 Estimate of the Excitation Cross Section 66
4.8.5 Conclusions 66

5. ATOMIC AND MOLECULAR CROSS SECTIONS 67
5.1 Highly Excited States of H_2 67
5.2 Low-Energy Proton and Hydrogen Atom Detectors 68
5.3 Thermal Detectors 71
5.4 Energy Loss in Foils 72
5.5 Atomic and Molecular Processes Information Center 73

6. HIGH-CURRENT ION-BEAM PRODUCTION AND INJECTION 74

7. PLASMA THEORY AND COMPUTATION 81
7.1 Prospects for Mirror Confinement 81
7.2 Anomalous Plasma Diffusion in Magnetic Wells 82
7.3 Flute Instabilities at Ion Gyrofrequency 82
7.4 Unstable Electrostatic Plasma Waves Propagating Perpendicular to a Magnetic Field 84
7.5 Relativistic Corrections to the $k_{\parallel} = 0$ Maser Instabilities 86
7.6 Electron Streams and Arcs in Finite Plasmas 87

8. MAGNETICS AND SUPERCONDUCTIVITY 90
8.1 Report on a Seminar Concerning the Relations Between Gas and Solid-State Plasmas (Oak Ridge, March 29–30, 1965) 90
8.1.1 Introduction 90
8.1.2 Presentations and Discussions 91
8.1.3 Conclusion 94
8.2 A Note on the *G-v* Optimum Relations for Magnet Coils 94
8.2.1 Introduction 94
8.2.2 The Optimization Equation 94
8.2.3 Numerical Values 95
8.2.4 Conclusion 97
8.3 Investigations on the Possibility of Using Indium Arsenide Films for Cryogenic Micro Hall Probes 97
8.3.1 Introduction 97
8.3.2 Preparation of InAs Films 97
8.3.3 Experimental Results 99
8.3.4 Conclusions 102
8.4 A Simple System for Introducing 200 amp into Liquid-Helium Environments 102
8.5 Investigations of Flux Jumps in Niobium-Zirconium 103
8.5.1 Introduction 103
8.5.2 Experiments with Hollow and Solid Cold-Worked Nb–25% Zr Cylinders 104
8.5.3 Discussion of the Experimental Results by Means of Simple Models of Hard Superconductors 105
8.5.4 Velocity of the Longitudinal Propagation of Flux Jumps in Nb–25% Zr Cylinders 106
8.5.5 Flux Jumps in an Nb–25% Zr Test Coil 107
8.6 Experimental Simulation of Large High-Field Superconducting Magnet Operation 109

9. CHEMISTRY OF TRITIUM IN CONTROLLED FUSION DEVICES 111
9.1 Source Processing 112
9.2 Vacuum System Processing 113
9.3 Blanket Assembly Processing 114
9.4 Coolant Processing 115
9.5 Tritium Inventory 115
9.6 Startup Processing 116

10. FUSION CHAIN REACTIONS 117
10.1 Introduction 117
10.2 Revised Nuclear Cross Sections 117
10.3 Theoretical Multiplication Constant 118
10.4 Thermally Induced Chain-Center Generation 118
10.5 Chain-Breaking Reactions 118
10.6 The Grad-Burkhardt Effect 119
10.7 Self-Stabilizing Reaction Modes 119

11. DESIGN AND ENGINEERING: NOTES 120
11.1 Encapsulation of Electromagnets 120
11.2 Epoxy Encapsulation for Electrical Coils 120
11.3 Encapsulating Technique 122
11.4 Epoxy Outgassing 123
11.5 Coils for Nonvacuum Service 125
11.6 Aluminum Corona Shield Fabrication 125
11.7 High-Temperature Electrostatic Probes 127
11.8 Brazing Connectors to Electromagnet Coils 128
11.9 Braze Welding Copper-Nickel Tubing 129

12. DESIGN AND ENGINEERING: SERVICE REPORT 130

PUBLICATIONS, PAPERS, AND TRAVELING LECTURE PROGRAM 131

Introduction

A. H. Snell

In this report we reach a crisis in our injection-accumulation program. On the one hand, we have the DCX-1 microinstability studies telling us rather plainly that, although we can adjust and manipulate things so as to gain a factor of 2 in density here, or a factor of 3 there, nevertheless, the prospect of a factor of 1000 is dim indeed without a major reconstruction.

On the other hand, we have the theoreticians telling us in Sect. 7.1 what we need to do, and, indeed, telling us more plainly than ever before that plasmas in open-ended magnetic traps can be made stable. The trouble is that when one thinks in terms of a reactor, the numbers adduced by the theoreticians are forbidding. The chain of reasoning goes like this: (1) to recover the injection energy by conversion of nuclear power, it has previously been recognized that the optimum injection energy is high: at least 100 kev; (2) for microstability, the plasma needs to be 100 Larmor diameters across; (3) consequently, the volume becomes very large, and the injected beams require forbidding currents. Add to this the fact that for macrostability a magnetic well is needed, and a second block of power of equally arresting magnitude enters the picture.

Nevertheless, the theoretical situation has acquired new directness and new strength. The arguments concerning both macro- and microstability rest on energy principles; only in the case of high-frequency longitudinal disturbances ($\omega > \omega_{ci}$) is there an exception, and here other arguments can be used to say that these disturbances probably need not be feared. The generality of the energy-principle reasoning is appealing; no longer need one think of this kind of instability or of that kind, always with a suspicion that there may be some that one has not thought of. Experimentalists now have a set of ideas around which they can crystallize their long-range thought; they can see in sharper focus the magnitude of the job that faces them and visualize both the difficulties and the promise of success on the scale of a large reactor.

But in the face of the immediate state of affairs, the experimentalists must ask the questions: Need the apparatus really be as large as suggested by these theoretical requirements for stability? Are there not some tricks that can be used or some clear-cut questions that can be answered in an experiment of approachable size? How much can one reduce the injection energy before scattering becomes too severe or the injection currents become too hard to realize? What are the chances of getting away with a smaller plasma diameter? These questions take time to answer, but we must now face them in order to see whether we can propose a DCX-3 experiment that would have a good chance of giving a decisive answer in the matter of plasma confinement in the open-ended systems. An apparatus capable of answering the questions would have to surmount our present limitation set by microinstability, which it could probably do if we make a thorough attempt at randomization. The apparatus should take us further: it should permit a study of the sensitivity to scaling, through variability in the number of contained Larmor diameters and in the parameter ω_{pi}/ω_{ci}. This should give the clue indicating the final size required for stability. At a trapping energy of 50 kev, it is easy to see that such an experiment would be a major undertaking, rivaling DCX-2; at low energies (several kev) the job might be much more approachable without sacrifice in the essential information to be gained. At the moment of writing, we continue to study both approaches.

Turning from the large and fundamental issues to say a little about other items of local trailblazing, we have the installation of the hydrogen arc in DCX-2 described in Sect. 2, with some observations of DCX-2's performance under these conditions. We have in Sect. 3.2 a very preliminary report on the properties of the 8-mm microwave-heated electron-cyclotron plasma in ELMO at the 1-kw power level; it is stable like the previous plasmas in PTF and EPA, and it emits many more neutrons than did the 3-cm microwave plasmas, probably because of a combination of higher density and higher electron temperature. In the beam-plasma interaction business, old-time readers of these reports may remember that, as a result of the interplay between scattering and charge-exchange losses in a mirror configuration, the low-energy ions reside mostly in an energy "pocket" at about 70 ev (here we do not talk about the group in the 20-kev region, which is also present). Now, as the result of burnout of the neutrals by a factor of 2000 or so, we would expect the pocket to move to about 1 kev when the burnout condition comes into effect. This energy shift is observed (Sect. 4.1.1), and when coupled with a density of over 10^{12} cm^{-3}, we see that we have here quite a respectable hot-ion, steady-state plasma, although the mean containment times of individual ions is not yet known. In another variant of the beam-plasma interaction work (Sect. 4.1.4), it has been demonstrated that an annular, hot-electron "blanket" can be generated by running a "mode II" discharge off-axis, in a magnetic mirror pair. One curious feature of the performance is that after stopping the discharge, the fast electrons sometimes decay slowly for a while (as judged by x-ray measurements) but then suddenly disappear.

The technology of intense ion beam generation and control shows a marked step forward in Sect. 6. A representative set of figures now is a steady 0.45 amp of H^+ at 60 kev through an aperture 1¼ in. in diameter and 2 ft from the source. Some gain has been achieved by throwing away two of the classical features of the duoplasmatron, namely, the ion-source coil and the ferromagnetic intermediate electrode, and replacing them, respectively, with a coil around the anode cup and with an intermediate electrode made of copper. A diagram of the new source is given in Fig. 6.8.

In superconductivity, flux jumps have been a prime subject of investigation. Their velocity of propagation in a cylinder of Nb-Zr has been measured (hundreds of meters per sec, see Fig. 8.19), and their occurrence is found to be associated with certain regions of magnetic-field strength (Fig. 8.20). The region below 5 kilogauss is especially dangerous, and tests of a superconducting coil in an applied external magnetic field show a correlation of the strength of the "degradation effect" with the presence in the superconducting windings of field regions of this magnitude (Sect. 8.6).

Under the influence of H-ion bombardment, metals can absorb as much as 1 atm cm^3 of H_2 per cm^3 of metal. In Sect. 9 an estimate is given of the implications of this in the matter of the tritium economy of a D-T reactor. Again we see a set of imposing numbers, this time referring to the tritium inventory that might be tied up in the ion sources, the main vessel wall, the blanket, and the coolant systems of a 1000-Mw reactor. All of this tritium will decay at the rate of about 1%/month. Although the numbers of Table 9.3 make one pause, and imply a disagreeable reprocessing and tritium-recovery cycle for substantial parts of the reactor, nevertheless, at this moment we are not greatly alarmed. The basic assumptions of the calculation must be examined carefully, and checked experimentally. If they stand, various chemical palliative schemes and choices of material must be considered. But if the necessity of reprocessing remains, then a new and perhaps costly item will have to be added to the economics of fusion-power production.

We close with an item in basic physics. In Sect. 5.1, experiments are described in which fast H_2 molecules, formed by passage of H_2^+ ions through gas, are seen to be ionized by an electric field. This is analogous to the ionization of H atoms in highly excited states, which in controlled fusion forms the basis for trapping by Lorentz ionization. The implication of the effect in H_2 molecules is that H_2 may have excited electronic levels in which one electron is excited into distant orbits about an H_2^+ core. The hydrogen molecule may accordingly have a system of principal quantum states that for high n approximate those of the classical hydrogen atom.

Abstracts

1. INJECTION AND ACCUMULATION: SINGLE-PASS EXPERIMENTS (DCX-1)

Microinstability-driven losses from the DCX-1 plasma continue to be the principal subject of investigation. A review is given of past studies, mostly involving plasmas established by Lorentz dissociation of H_2^+ generated from H_3^+ in a water-vapor cell. New observations include the following: (1) the gyrofrequency mode of instability is, on a time-averaged basis, more effective than the diminished-frequency mode in driving radial losses; (2) axial losses driven by the diminished-frequency mode are present, but are of little consequence in comparison with radial losses; and (3) plasmas established by Lorentz dissociation of H_3^+ and of H_2^+ extracted directly from duoplasmatron sources are also subject to instability losses.

The applicable theoretical literature is cited in an effort to make mode assignments for the observed microinstabilities. Unique assignments cannot be made. The theoretically recognized instabilities which cannot be dismissed from consideration in connection with this experiment are the negative mass, drift-cyclotron, maser, and Harris instabilities.

Two techniques aimed at stabilization by disordering proton orbits have been applied. The first consisted in driving proton axial oscillations with externally applied electric fields and was not successful. The second technique involved shifting the H_2^+ beam away from the standard injection trajectory so as to avoid introducing protons on near-equilibrium orbits. The proton-density threshold for appearance of microinstability signals at ω_{ci} increases rapidly with displacement of the molecular ion trajectory, in an extreme case, from 3×10^5 cm^{-3} to 1×10^8 cm^{-3}. However, the limiting fast-proton density increases by only modest factors, 2 to 3.

Details of Lorentz trapping of H_3^+ and of H_2^+ beams extracted directly from duoplasmatron sources are given, and some improvements in the injector system are described.

2. INJECTION AND ACCUMULATION: MULTIPLE-PASS EXPERIMENTS (DCX-2)

During this report period the DCX-2 plasma was studied under a wide variety of conditions. Both hydrogen and lithium arcs as well as the background gas and cold plasma were used to dissociate the molecular hydrogen ion beam. The lithium arc was operated on axis, and 1 and 3 in. off axis on the side opposite the injector. With the arc 3 in. off axis the arc-dissociated protons symmetrically encircled the machine axis with no precession. This arrangement should have emphasized any form of streaming interaction occurring, and in fact the critical current for the appearance of the central peak was below 0.2 ma where previously no central peak had been seen with 0.4 ma injected. The plasma density, however, differed only slightly from that obtained with the lithium arc on axis and 1 in. off axis. The position and tilt angle of the injection duct were varied along with the molecular ion orbit diameter, but these changes in the injection geometry had little effect on the properties of the trapped plasma. An experiment to measure the radial distribution of lithium in DCX-2 indicates an enhanced radial transport of lithium from the main arc column, with deposits of lithium observed to a radius of 6 in. The lithium arc voltage was varied over a wide range with no significant effect on the density of the trapped plasma, but a broad optimum in arc current was found near the normal operating current of 20 amp.

The important question of the presence and magnitude of plasma losses other than from charge exchange has not been answered conclusively. Results of a systematic variation of the pressure in the plasma region with lithium arc dissociation and the beam current are not well understood because of interaction between the various parameters. Cooling the end liner regions with liquid nitrogen to improve the vacuum conditions and randomly modulating the injected ion energy had little effect on the trapped-plasma properties.

The maximum energetic plasma density achieved during this report period was 4×10^9 ions/cm^3 with lithium arc dissociation. There is evidence that the plasma density does not increase proportionately for beam currents above 25 ma. Insufficient data concerning the nature of the arc and the change in composition of the background plasma at the higher beam currents make it uncertain, however, that a density limit determined by microinstabilities has been reached.

A hydrogen arc has also been run in DCX-2, and preliminary results have been obtained. Fluting of the arc column has prevented a reduction of the pressure in the plasma region below 3×10^{-6} mm Hg. The lower maximum hot-ion density achieved was 1 to 2×10^9 ions/cm^3.

Nitrogen gas dissociation yielded plasma densities less than 1×10^8 ions/cm^3. However, with hydrogen gas dissociation, a large energy spread and a maximum plasma density of 5×10^8 ions/cm^3 were obtained with no central peak occurring when the pressure was raised sufficiently.

The ion cyclotron harmonics always prominent in high-energy injection experiments have been observed recently up to the 100th harmonic with relatively high intensity. A new spectrometer has permitted observation of the rf to above 2 Gc. Despite considerable difficulty in obtaining uniform response of the probes in the frequency range above several hundred Mc, a probe has been developed which is flat to more than 2 Gc.

The composition, total density, and radial density distribution of the cold plasma with which most of the energetic ions charge exchange still cannot be determined accurately, although more is now known of the residual gas composition through routine monitoring of the vacuum conditions in DCX-2 with a residual gas analyzer.

An interesting structure to the molecular ion beam has been discovered. Scans with the collimated energy-sensitive detectors show narrow peaks at specific pitch angles, even when the beam is stopped after a few turns. Two possibilities for the mechanism which produces the group of particles with low axial energy have been investigated, but the imprecision of measurement of plasma properties makes it difficult to choose between these two or other possible models. Improved diagnostic equipment is being developed for this purpose.

3. ELECTRON-CYCLOTRON HEATING

A 20-kev neutral hydrogen beam is being injected into an electron-cyclotron plasma in the EPA facility. However, because of difficulties resulting from the magnetic-field gradient, the magnetic-field coils are being replaced. The new coils will produce a less-steep radial gradient and a smaller mirror ratio.

An electron-cyclotron plasma has been successfully formed in the redesigned ELMO facility. The power source used to generate the hot-electron plasma consists of two 8-mm, 1-kw, continuous-wave traveling-wave-tube oscillators. No consistent measurements of temperature and density are available yet.

4. PLASMA PHYSICS

Studies using the beam-plasma interaction to "burn out," or highly ionize, a dense cloud of gas contained in a magnetic-mirror machine are continuing. Here we report on spectroscopic evidence that the helium neutral density in one mirror machine has been reduced by a factor of about 1000 by applying sufficient power to the plasma. Evidence supporting this factor of 1000 in neutral density reduction is obtained by studying the energy spectrum of hot ions contained in the device. Counter experiments suggest that the region between the mirrors is a neutron source with a source strength of 6×10^5 neutrons/sec.

Microwave cutoff measurements were attempted to try to determine the plasma density in the large Burnout V mirror machine. In mode I (quiescent plasma), 3-cm microwaves were attenuated and 1.2-cm microwaves penetrated freely, which implies that the mode I plasma density lies between 1×10^{12} and 8×10^{12} electrons/cm^3. In mode II, anomalous

results were obtained. The signal with plasma present was consistently higher than with plasma absent.

Attempts to use a neutral beam of gold vapor to measure plasma density were only partly successful. The gold beam was severely attenuated, but was not cut off completely. The neutral-beam transmission sets a value for the plasma density that is too low when compared with other measuring techniques. However, intermittent breakdown of the mode II discharge was observed. Therefore, gold could be passing through the system when plasma was absent.

The mode II reflex discharge has been shown to be an effective means of producing a hot-electron plasma. An experiment has been carried out using the mode II reflex discharge in a geometry in which the arc electrodes are mounted off axis. In this method of operation, a blanket or annulus of hot electrons is produced by the azimuthal drift of electrons in the magnetic-field gradient. The density of the plasma annulus has been inferred both from the x-ray intensity and spectrum and from the temperature of molybdenum dust dropped into the plasma.

Properties of collisionless ionic sound waves produced in a quiescent discharge tube have been observed. The waves have been shown to exhibit interference effects, to propagate rectilinearly, to be capable of being focused, to apparently not be reflected from solid surfaces, to be sensitive in propagation velocity to weak magnetic fields, and to cease to propagate when the wave frequency is increased toward the ion plasma frequency.

The density of plasma in a quiescent discharge tube has been inferred by using an ordinary radio grid-dip meter to couple to and determine the electron plasma frequency.

A technique has been derived for measuring the rf impedance between grids immersed in a plasma, even though the grids are several wavelengths away from the measuring apparatus. The technique promises to be useful in determining the plasma frequency in the lower plasma density range where microwaves cannot be used.

Some of the rf frequencies observed in the calutron beam are known to shift with pressure. It is shown that this frequency shift is due to electrons which are oscillating along the magnetic-field line through the positive potential well of the beam (Philips ion gage type of oscillation).

Calculations of $\int (\nabla B/B^2)\, dl$ have been carried out for the Gas Arc Facility mirror-coil system and compared with the observed suppression of the flutes in the deuterium arc as a function of anode position. The fields available with the Gas Arc Facility using booster coils are also shown. The use of a compensated quadrupole is discussed in which the flux lines are caused to return to their initial radial position by reversing the current in the quadrupole conductors at a specified axial position.

The hydrogen arc, as operated in the long solenoid, has three distinct regions. There is a pink central core $\frac{1}{4}$ in. in diameter, corresponding to the diameter of the tip of the cathode. This core carries the major part of the current of the arc. This central core is surrounded by an intermediate region having an outside diameter of approximately 1 in. This intermediate region carries ions toward the cathode. The intermediate region is characterized by a paler pink color than the core. The visible part of the third region is approximately 4 in. in diameter and is a pale blue color. This outer region carries ions and gas in both directions toward the ends of the tank. Under certain conditions a net flow in either direction can be obtained.

Measurements indicate that the core has a high negative potential with respect to ground and carries a large portion of the arc current. Operation of the arc in a mirror field indicates that baffle saturation currents are dependent on magnetic field and position of the baffles. Arc power distribution to the electrodes is included.

Multiple inelastic collisions in energetic carbon-arc plasmas appear to provide a mechanism for strong heating of ions by electrons. A downward revision of the usual energy transfer rate for cooling sluggish carbon ions by collisions with cold electrons accentuates the nonthermodynamic nature ($T_+ \sim 100 \times T_-$) of such plasmas.

5. ATOMIC AND MOLECULAR CROSS SECTIONS

The population and existence of highly excited states of H_2 formed from electron capture of H_2^+ in hydrogen gas have been determined. For a 50-kev H_2 particle, the fraction in high quantum states increases monotonically from 3.5×10^{-4} at an electric field of 6.8×10^3 v/cm to 6.0×10^{-4} at

4×10^4 v/cm. These excited states have been described as a single, high-quantum-orbital electron plus an H_2^+ core with the orbital electron existing in states similar to the high quantum states of hydrogen atoms.

Direct-current measuring techniques have been used to determine the response of silicon semiconductor detectors from low-energy protons or neutral hydrogen atoms. A small voltage was applied across the barrier to bias out leakage currents, and the dc flow arising from particle impact was determined. The gain increased with increasing particle energy, and the average expended energy per electron collected was 4.1 and 3.8 ev/electron for H^+ and H_3^+ respectively.

Detection of low-energy protons with silicon-barrier detectors using conventional pulse-height analysis has been extended to the 7-kev range. Vacuum-tube preamps arranged from minimum input capacitance resulted in a full width at half maximum amplitude of 6.5 kev with 15-kev protons. Replacing the preamp with a field-effect transistor preamp mounted in the vacuum system and cooled with liquid nitrogen decreased the resolution to 3.35 kev for 7.2-kev protons.

Barium titanate crystals have been used as a pyroelectric detector for low-energy protons. Minimum detectable power was 10^{-4} w/cm^2, corresponding to polarization currents of 10^{-12} amp.

Integral energy loss of protons passing through 600-A aluminum foils has been determined by measuring the dc gain of a silicon semiconductor detector with and without the foil placed in front of the detector. Results obtained for 10- to 30-kev protons are a factor of 203 greater than those obtained by more conventional techniques.

6. HIGH-CURRENT ION-BEAM PRODUCTION AND INJECTION

Studies have continued on the 100-kv test stand for the production of intense hydrogen-ion beams in the energy range 20 to 100 kev. Total hydrogen-ion beams of 900 ma can be produced at energies of 70 kev. Well-collimated H^+ beams up to 450 ma can be produced at energies of 60 kev. Attempts to produce intense H_2^+ beams have been limited to only 150 ma from a total hydrogen beam of 300 ma.

7. PLASMA THEORY AND COMPUTATION

Prospects for stable plasma confinement by magnetic mirrors look encouraging. Requirements according to the present stability picture are outlined in Sect. 7.1.

Two new stability results particularly concerned with mirror confinement are obtained. In Sect. 7.2, it is argued that a magnetic well suppresses all universal modes if $\Delta B/B > T_e/T_i$, where B is the central field, ΔB is the well depth $\perp\vec{B}$, and T_e/T_i is the ratio of electron and ion temperatures. In Sect. 7.3 it is shown that flute modes of the mirror-loss cone instability are suppressed if $\omega_{pi}/\omega_{ci} < (R/\rho_i)^{3/4}$, where ω_{pi} and ω_{ci} are the ion-plasma and cyclotron frequencies, ρ_i is the ion gyroradius, and R is the plasma radius.

Ion-ion instabilities near the ion gyrofrequency are found in which the perturbed electric field is strictly perpendicular to the external magnetic field if the ion distribution in perpendicular energy is not monotonic. Such distributions occur in mirror containment devices. The instabilities are not damped by providing hot electrons, but achievable spread in the ion perpendicular energy does provide stabilization. A special flutelike case with purely imaginary frequency is hardest to control (see Sect. 7.4). Relativistic corrections are given in Sect. 7.5.

A finite one-dimensional plasma consisting of a cold-ion background and a cold-electron stream has been shown to be absolutely unstable when the perturbations are allowed to feed back through a passive, unspecified circuit external to the plasma. These results follow from the solution of the dispersion relation obtained by applying the appropriate boundary condition on the charge-density perturbation of the plasma. This charge-density perturbation is obtained as a solution of a homogeneous, linear, second-order differential equation derived from the zeroth- and first-moment equations describing the ions and electrons. Ramifications of the results are discussed (see Sect. 7.6).

8. MAGNETICS AND SUPERCONDUCTIVITY

Recently, much work has been done on the B_{min} geometry applied to the magnetohydrodynamic stability of gas plasmas. Experiments of this

kind are often difficult to interpret, time consuming, and expensive. One is tempted to make small-scale experiments with corresponding magnetic-field geometries performed with solid-state plasmas. This makes sense, of course, only if the following question can be satisfactorily answered: To what extent can the electron-hole, solid-state plasma be considered as analogous to a gaseous plasma?

At the Thermonuclear Division an informal seminar was arranged in order to learn in detail about the relevant work of experts in this field. After stimulating presentations and discussions, the following conclusions were achieved: Any laboratory doing thermonuclear research should be informed about progress in the understanding of the properties of plasmas in solids. Attempts to study containment geometries using solid-state plasmas show the advantages possible. On the other hand, a clean interpretation of solid-state experiments requires much more understanding of surface effects and other differences between solid-state plasmas and gas plasmas. At this time the value of solid-plasma experiments for gas-plasma research seems to be restricted to producing occasionally interesting clues for making analogous experiments with gas plasmas.

For the design of conventional and superconducting magnet coils, it is important to find the coil parameters which yield the highest field efficiency (expressed by the Fabray factor G) if the coil volume factor v is known. Fabray published a table of optimized coil parameters and D. B. Montgomery presented an equation for finding, in a simple way, approximate values of these parameters. In both cases, however, the authors did not show any derivation of their "G-v optimization." A reevaluation of this problem seemed to be desirable. This was achieved by means of a new calculation method, with the result that Fabray's values appreciably deviate, in part, from the exact figures. Montgomery's formula yields, in general, better results. Besides a comparative table of parameter values, this paper presents new types of graphs which are useful for magnet-coil design work.

The development of micro Hall probes consisting of thin bismuth films has been described in a previous report. Since there are certain inherent disadvantages with bismuth, the III-V semiconducting compounds indium antimonide and indium arsenide, which exhibit a large Hall effect, were considered for further developmental work. Because of the temperature dependence of the relevant properties of the first-mentioned semiconductor, the final choice was to investigate carefully the possibility of using indium arsenide films for the mentioned purpose.

These preliminary investigations indicate that it is possible to obtain indium arsenide films, by means of vacuum deposition, which exhibit behavior similar to the bulk material. These films may be used satisfactorily as Hall generators at 4.2°K and below. Their sensitivity is sufficiently high that they may be employed to measure magnetic fields of <1 gauss intensity, and their response is approximately linear from 0 to 50 kilogauss. Their temperature dependence is very slight between 300 and 4.2°K, and their change in sensitivity upon thermal cycling is relatively small. Micro probe geometries were developed with active surfaces of 0.1×0.1 mm and smaller.

As reported previously, for introducing currents of several hundred amperes into liquid-helium environments, a special design was developed in this laboratory. It used liquid-nitrogen cooling of the high-temperature ends of the leads and employed stranded wires to take advantage of the heat capacity of the evaporating helium. Extended developmental work showed that a very efficient design can be achieved without liquid-nitrogen cooling by forcing the evaporating helium through copper tubing of appropriate length. It was necessary to consider the viscous drag of helium in the hollow leads in order to avoid dangerous overpressure in the Dewar vessels.

Investigations of superconducting niobium-zirconium magnet coils show the close relationship between the so-called degradation effect and the flux jump phenomenon. The latter can be studied most easily by using hollow or solid cylinders in longitudinal external fields. By other authors, a simplified theory for the one-dimensional case has been developed which showed the dependence of the critical external field upon the rate of field rise under nearly adiabatic conditions. Similar work has been done here; however, in addition, the influence of the sample radii and of the external-field "history" has been considered. It was also possible to measure the velocity of the longitudinal propagation of the flux jump and its dependence on the external field. Finally, flux jumps were observed in a test coil wound with 10-mil unplated Nb–25% Zr wire. As to be expected, the flux jump energies are large when the

coil self-field and the external field are in opposite directions. With various, constant transport-current densities, critical external-field strengths were measured with increasing and with decreasing external fields. An analysis of the magnitude of the resulting fields inside the coil-winding volume shows that flux jumps at field strengths smaller than 5 kilogauss are dangerous. This agrees with magnetization measurements in external fields with varying transport currents.

Finally, tests were made with superconducting sample coils of large diameter but with small cross-sectional areas using external fields up to 75 kilogauss. These fields were produced by a conventional 7-Mw water-cooled magnet with a $6\frac{1}{2}$-in. working diameter. Well reproducible results have been achieved, and it is assumed that eventually this kind of data will be of value for the design of large superconducting magnet coils.

9. CHEMISTRY OF TRITIUM IN CONTROLLED FUSION DEVICES

Consideration of fuel-cycle chemistry in tritium-burning controlled-fusion devices must include recognition of possible, intolerably large inventory levels. Steady-state inventory levels in the presence of tritium ion or atom fluxes will be flux dependent but will in any event require appropriate design considerations. Processing for tritium recovery and for isotope separation from protium and deuterium will probably be an essential part of a tritium-burning device. Basic chemical considerations and some experimental corroboration have led to the conclusion that inventory control by processes appropriate to the various regions of a controlled-fusion reactor is chemically possible.

10. FUSION CHAIN REACTIONS

The concepts of a negative temperature coefficient and the Grad-Burkhardt effect (for reducing magnetic bremsstrahlung) are discussed briefly in relation to thermonuclear fusion and fusion chain reactions.

11. DESIGN AND ENGINEERING: NOTES

A brief discussion is given of the progress of a program to develop encapsulated electromagnets, including the ability to operate these magnets directly in a vacuum system at 10^{-7} torr base pressure. Another aspect of electromagnet technology described is a method for brazing consistently good connectors which serve as both electrical and cooling-water terminals without damaging nearby electrical insulation. A description is included of the fabrication procedure for making a particularly difficult aluminum corona shield, which is an example of the kinds of metal fabrication problems we encounter. Progress in the development of small-diameter, high-temperature electrostatic probes is reported. Differential vacuum-system liners capable of high-temperature bakeout and subsequent cryogenic-temperature cooling have been the source of leaks in ultrahigh vacuum systems due to corrosion problems. An approach to alleviating this problem is described.

12. DESIGN AND ENGINEERING: SERVICE REPORT

The design and engineering activities are generally reported incidentally with the research efforts of other groups of the Thermonuclear Division. These activities include execution or coordination of engineering design, shop fabrication, building operations, and maintenance. During this interval, members of the Engineering Services Group have engaged in a modest amount of technology development.

1. Injection and Accumulation: Single-Pass Experiments (DCX-1)

J. L. Dunlap
R. S. Edwards
G. R. Haste
L. A. Massengill
C. E. Nielsen[1]
H. Postma
L. H. Reber[2]
R. G. Reinhardt
W. J. Schill
E. R. Wells

1.1 INTRODUCTION

Microinstability-driven losses from the DCX-1 plasma continue to be the principal subject of investigation. Section 1.2 reviews past studies, mostly involving plasmas established by Lorentz dissociation of H_2^+ generated from H_3^+ in a water-vapor cell. New observations include: (1) that the gyrofrequency mode of instability is, on a time-averaged basis, more effective than the diminished-frequency mode in driving radial losses; (2) that axial losses are present, driven by the diminished-frequency mode, but are of little consequence in comparison with radial losses; and (3) that plasmas established by Lorentz dissociation of H_3^+ and of H_2^+ extracted directly from duoplasmatron sources are also subject to instability losses. Section 1.3 considers the question of mode assignments for the observed microinstabilities.

In Sect. 1.4, the emphasis shifts to descriptions of the results achieved by applying two different techniques aimed at stabilization by disordering proton orbits. The first consisted of driving proton axial oscillations with externally applied electric fields and was not successful. The second technique involved shifting the H_2^+ beam away from the standard trajectory to avoid introducing protons on near-equilibrium orbits. The proton-density threshold for appearance of microinstability signals at ω_{ci} increases rapidly with displacement of the molecular-ion trajectory, in an extreme case, from 3×10^5 to 1×10^8 cm^{-3}. However, the limiting fast-proton density increases by only modest factors, 2 to 3.

Details of Lorentz trapping of H_3^+ and of H_2^+ beams extracted directly from duoplasmatron ion sources are reported in Sects. 1.5 and 1.6. Some improvements in the injector system are described in Sect. 1.7.

1.2 MICROINSTABILITY LOSSES[3]

We remind the reader that this plasma is afflicted by at least two microinstabilities. One, which we have termed the azimuthal instability and will shortly subdivide into two distinct modes, produces rf signals in the neighborhood of the proton-cyclotron

[1]Consultant from Ohio State University.

[2]Deceased.

[3]We have submitted for publication two papers on this subject: "Energetic Plasma Losses Due to Microinstabilities," by J. L. Dunlap, G. R. Haste, H. Postma, and L. H. Reber, submitted to *Physical Review Letters;* and "Microinstability Limitations of the DCX-1 Energetic Plasma," by J. L. Dunlap, G. R. Haste, C. E. Nielsen, H. Postma, and L. H. Reber, submitted to *Physics of Fluids*.

harmonics and dominates the fluctuations of B_z (the θ rf magnetic probe signals) and of electrostatic potential (considering only the high-frequency fluctuations of ϕ). It is this instability that drives proton losses. The other microinstability, which we have termed the axial instability, dominates fluctuations of B_θ (the Z rf magnetic probe signals), causes rapid ejections of electrons and corresponding fluctuations of the plasma dc potential, and has a more complex frequency spectrum (though ω still $\gtrsim \omega_{ci}$).

There are two modes of azimuthal instability. One, which for convenience we term the gyrofrequency mode, has been long recognized. It has the lower density threshold (as low as 3×10^5 energetic protons per cm^3; see Sect. 1.4). It probably involves mostly protons on near-equilibrium orbits, since the lowest rf signals generated are about 14.6 Mc/sec, the gyrofrequency on equilibrium orbit. The second mode, which we term the diminished-frequency mode, was first described in the preceding report.[4] The rf signals are 1–2 Mc/sec below the gyrofrequency-mode signals. Reducing the radius of the plasma has no effect on the lower frequency limit of the gyrofrequency-mode signals, but increases the limit for the diminished-frequency mode. Protons involved in this mode are therefore sampling the magnetic field at the periphery of the plasma.

Most observations of the diminished-frequency mode have been made with Lorentz dissociation of H_2^{+*} (H_2^+ generated from H_3^+ in a water-vapor cell). The threshold is associated with a critical central proton density of $5–10 \times 10^7$ cm^{-3}, a value which by variation of H_2^{+*} current has occurred for τ_{DK} in the range $2 \leqq \tau_{DK} \leqq 30$ sec. Some plasma properties associated with long τ_{DK} values seem to be required for this mode, for, with gas dissociation at higher pressures, densities as high as $1–2 \times 10^8$ cm^{-3} are achieved and the mode is not present.

Studies of the direct loss of trapped protons were described in the three previous progress reports. In the first,[5] we reported experiments using Lorentz dissociation of H_2^{+*} in which charge-exchange measurements indicated direct losses and a limiting central density in the neighborhood of 1×10^8 cm^{-3}. In the second,[6] several similar experiments showed limits of $1–2 \times 10^{12}$ for the total number of trapped protons and of $1–2 \times 10^8$ cm^{-3} for central density; flutes were excluded; and the axial instability was shown not to be responsible for proton losses. In the third,[7] a number of ancillary experiments excluded several explanations not connected with instability (e.g., attenuation of charge-exchange currents because of the low-energy cutoff of the foil-covered neutral-particle detectors and axial scattering of the plasma beyond the range of the charge-exchange detectors), and correlation of the radial loss of energetic protons with radio-frequency signals from the diminished-frequency microinstability mode was reported.

Studies of the microinstability losses continued during the present report period. We report the results of these studies in the remainder of this section.

We now recognize that the gyrofrequency mode is, on a time-averaged basis, more effective than the diminished-frequency mode in driving radial losses. The losses driven by the gyrofrequency mode occur at the same density threshold as those driven with the diminished-frequency mode, $5–10 \times 10^7$ cm^{-3}. With the standard molecular-beam trajectory (that whose closest approach to the magnetic axis is tangent to the proton equilibrium orbit) the rf signals from the gyrofrequency mode are nearly always present, and the associated radial loss current is nearly constant. As a consequence, it is difficult to establish the zero level of these losses. Slight shifts of the beam trajectory had been found to provide momentary interruptions of the gyrofrequency mode, and this technique was utilized to define the required zero level. Results obtained with H_2^{+*} injection are shown in Fig. 1.1. The radial losses are those to the end foil detector previously described.[8] In normal operation, the amplitude of these radial losses is much smaller than those driven by the diminished-frequency mode, but the time-averaged loss current seems to be greater by about an order of magnitude.

---

[4] *Thermonuclear Div. Semiann. Progr. Rept. Oct. 31, 1964*, ORNL-3760, p. 7.

[5] *Thermonuclear Div. Semiann. Progr. Rept. Oct. 31, 1963*, ORNL-3564, pp. 10–12.

[6] *Thermonuclear Div. Semiann. Progr. Rept. Apr. 30, 1964*, ORNL-3652, pp. 1–7 and 14–22.

[7] *Thermonuclear Div. Semiann. Progr. Rept. Oct. 31, 1964*, ORNL-3760, pp. 5–9.

[8] *Thermonuclear Div. Semiann. Progr. Rept. Oct. 31, 1964*, ORNL-3760, Fig. 1.9 and p. 7.

PHOTO 68439

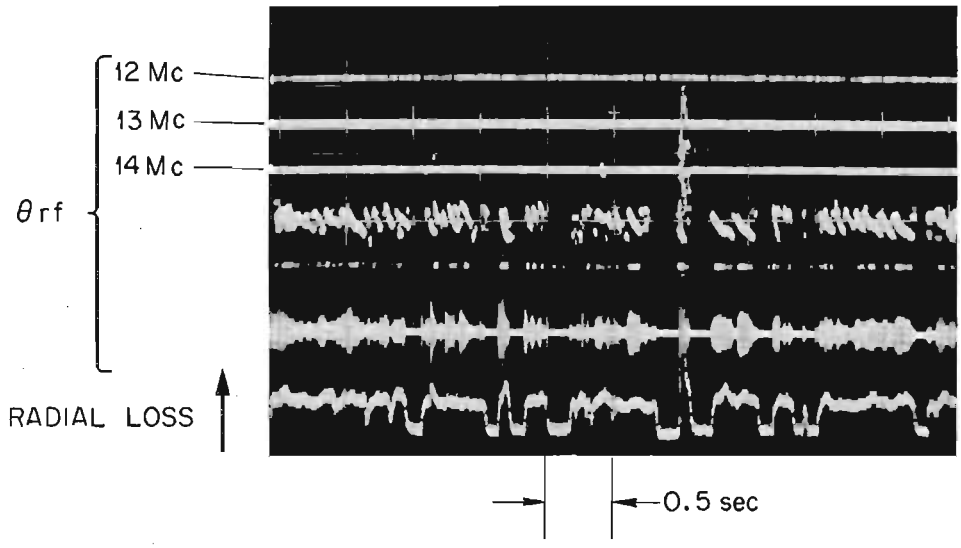

Fig. 1.1. Simultaneous Recordings of θ RF and Radial Loss of Protons to the End Foil Detector (460 μa H_2^{+*}, $\tau = 6\frac{1}{2}$ sec). The upper 4 cm of the oscillogram is the time-resolved frequency spectrum of the rf signal in the neighborhood of ω_{ci} with marker frequencies at 12, 13, and 14 Mc/sec. The intermediate trace is the oscilloscope display of the rf signal. The bottom trace is the radial loss signal. The diminished-frequency mode occurs only once (at 6 cm), and there the amplitude of the radial loss signal is greater than 3 cm. There is an almost continuous radial loss associated with the gyrofrequency mode.

Axial losses correlated with rf signals from the microinstabilities also have been observed. So far, these measurements have been confined to plasmas established by Lorentz dissociation of H_2^{+*}. The detector was a foil-covered Faraday cup mounted near the magnetic axis just outside one mirror and inclined at an angle of about 15° with respect to the median plane. A 25-μin. nickel foil was used to ensure that the cover was free of pinholes and thus that the current measurements were not influenced by collection of slow plasma. This type of foil has an energy cutoff of 150 kev for incident protons or hydrogen atoms. The question of the relative contributions of energetic ions and of energetic neutrals to the loss signal is somewhat academic, since a charge-exchange neutral to this detector represents a proton that would shortly have escaped the mirror. Typical results of measurements with the standard molecular-beam trajectory are shown in Fig. 1.2. That the large axial losses are correlated with diminished-frequency-mode signals was confirmed by simultaneous measurements of the frequency distribution of the θ rf signals. Very small fluctuations of loss current are sometimes observed in coincidence with fluctuations of gyrofrequency-mode signal amplitude. However, in contrast with the radial losses, there is no steady nonzero level of axial loss current. As a result, it is obvious that the diminished-frequency mode completely dominates the axial losses. Present data indicate that the axial losses are minor in comparison with the radial losses.

The magnitude of the instability losses has been evaluated from the direct observations of these losses as well as from failure of charge-exchange accountability. Though the results are not in substantial disagreement, the evaluation from direct observation is less accurate because of difficulties involved in estimating required geometric factors. Therefore we still rely primarily on measurements of the charge-exchange currents and on the several ancillary experiments, previously reported,[7] which have given a high level of confidence in these measurements.

PHOTO 68440

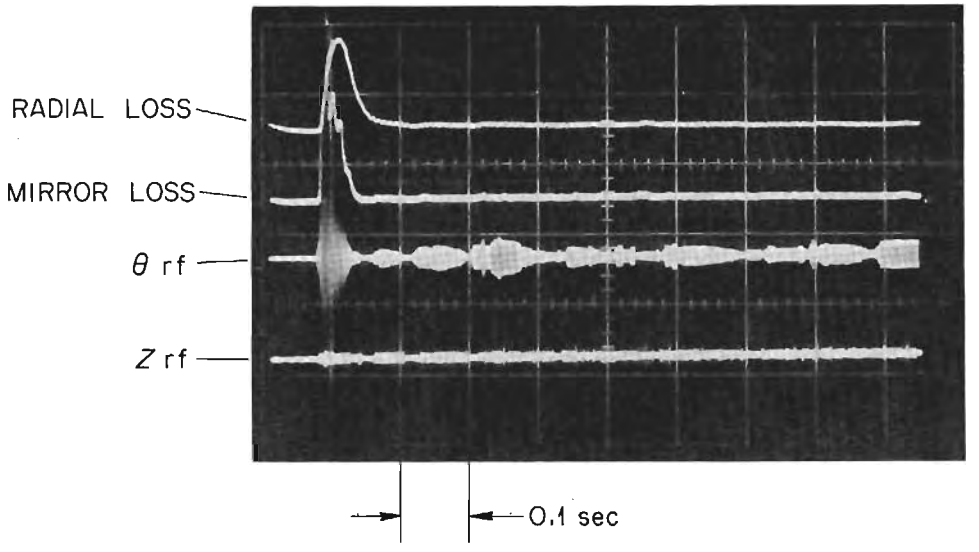

Fig. 1.2. Simultaneous Recordings of Radial and Mirror Losses of Protons, and of θ and Z RF (440 μa H_2^{+*}, 4×10^{-9} Torr, 10-msec Filter in Radial Loss Circuit). From frequency analysis, the θ rf signal is due to the diminished-frequency mode at 1 cm and to the gyrofrequency mode elsewhere.

Results of the charge-exchange measurements for a typical run with Lorentz dissociation of H_2^{+*} are given in Figs. 1.3–1.6. Figure 1.3 clearly shows the failure of change-exchange accountability; at base pressure, only 25% of the proton input current registers as charge-exchange loss current. In some runs this value has been as low as 10%. The total number of stored protons has a definite limit of $1–2 \times 10^{12}$ (see Fig. 1.4). A combination of the instability losses and instability-induced axial scattering (Fig. 1.5) causes the central density to saturate at $1–2 \times 10^8$ cm^{-3} (Fig. 1.6), an order of magnitude less than expected in the absence of these effects. In the absence of instabilities, the extrapolations of total number stored (Fig. 1.4) and of central density (Fig. 1.6) would be a factor of 2–3 higher at base pressure, for the instabilities cause proton-energy dispersion and degradation that result in charge-exchange lifetimes that are $\frac{1}{2}$ to $\frac{1}{3}$ those expected for 300-kev protons.

We have recently extended our observations of instability losses to plasmas established by the Lorentz dissociation of H_2^+ extracted directly from the ion source (Sect. 1.6). Radial losses correlated with the gyrofrequency mode are observed at a central-density threshold of about 5×10^7 cm^{-3} whenever $\tau_{DK} > 1$ sec. (Investigations of axial losses have not been made.) At shorter lifetimes this threshold can be exceeded (to the maximum available densities of $1–2 \times 10^8$ cm^{-3}) without instability losses. With 10 ma injected H_2^+ current, a Lorentz trapping fraction of $1–2 \times 10^{-5}$, and $\tau_{DK} = 4$ sec, only 20% of the proton input current is lost by charge exchange, and the plasma is limited in total number of protons stored (to about 1×10^{12}) and in central fast-proton density (to about 1×10^8 cm^{-3}). With this trapping technique, the diminished-frequency mode is less common than with H_2^{+*} injection.

Instability losses have also recently been observed from plasmas established by Lorentz dissociation of H_3^+ (Sect. 1.5). The potentially accessible densities were lower, and the indications of limiting total number and central density were less dramatic, though these appear to be about 1×10^{12} and 1×10^8 cm^{-3}.

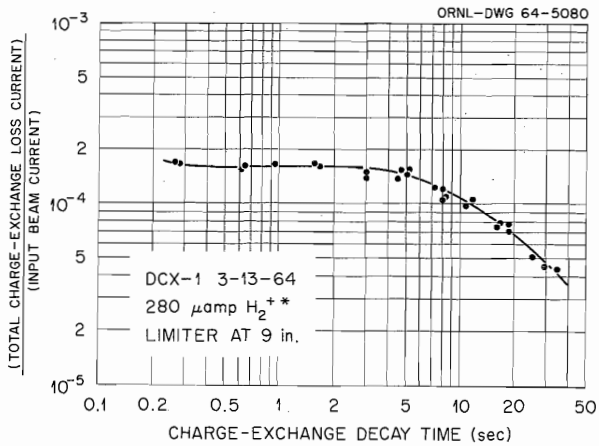

Fig. 1.3. Total Charge-Exchange Loss Current (Normalized) as a Function of Charge-Exchange Decay Time, Showing that at the Longer Decay Times Charge Exchange Fails to Account for the Proton Input Current.

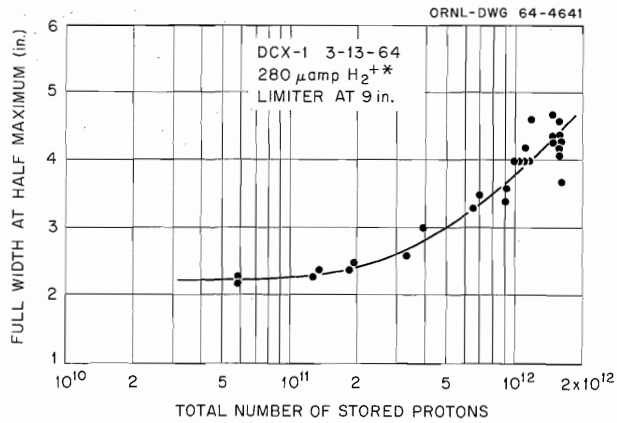

Fig. 1.5. Full Width at Half Maximum of the Axial Density Profile as a Function of the Total Number of Stored Protons, Showing Axial Expansion Driven by Instabilities. The axial density profile is the axial distribution of the $I\tau$ products from the individual charge-exchange detectors.

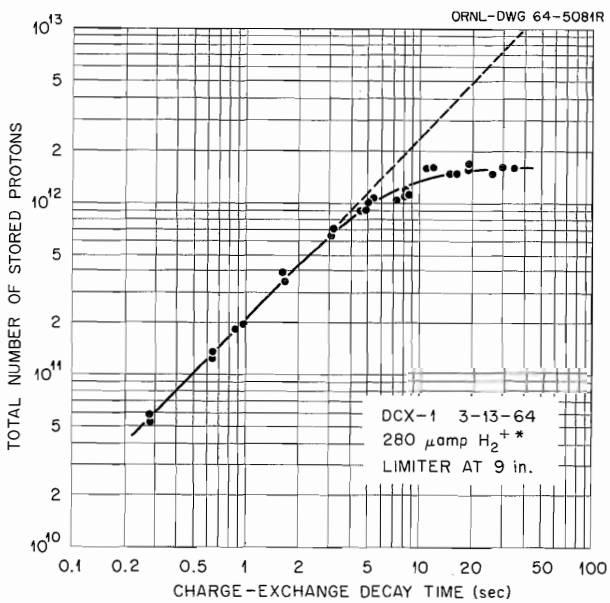

Fig. 1.4. Total Number of Stored Protons as a Function of Charge-Exchange Decay Time. The departure from proportionality indicates a loss other than charge exchange.

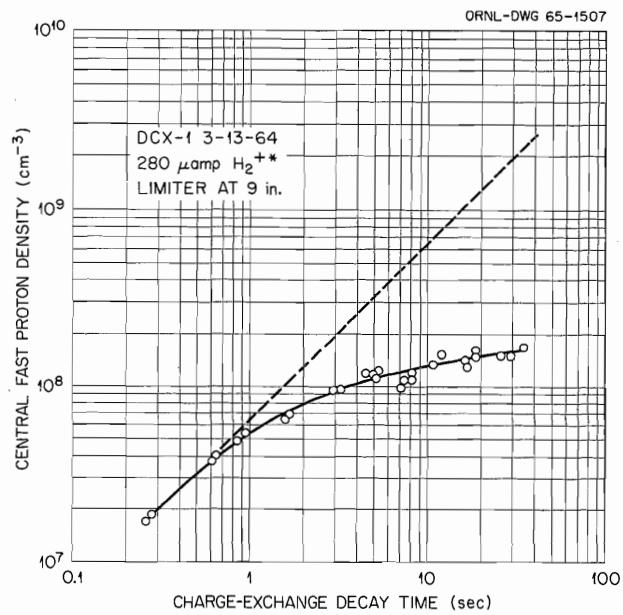

Fig. 1.6. Central Fast-Proton Density as a Function of Charge-Exchange Decay Time. The density is calculated from the central charge-exchange detector signal. The dashed line represents the density potentially accessible (on the basis of uniform input rate, no instability losses, and no expansion of plasma volume).

1.3 MICROINSTABILITY MODE ASSIGNMENTS

Theoretical work on models representative of the plasma established in these experiments has revealed a number of microinstabilities. Two general categories of these can be immediately dismissed from further consideration in connection with this experiment. Because $\beta \lesssim 10^{-5}$, the plasma is stable against magnetic velocity-space instabilities driven by the pinch mechanism.[9] Because $\omega_{pi} \ll \omega_{ci}$, the plasma is also stable against the $k_{\parallel} = 0$ limits of the maser[10] and drift-cyclotron[11] instabilities. The instabilities that remain can be classified as those driven by the ion diamagnetic current and those driven by the non-Maxwellian ion distribution. In the theoretical literature, there are, in the first class, the drift-cyclotron instability with $k_{\parallel} \neq 0$ (see refs. 11 and 12) (an ion-electron interaction) and the negative-mass instability[13] (an ion–magnetic-gradient interaction). In the second class there are the maser[14] and Harris[15] instabilities with $k_{\parallel} \neq 0$, both of which are ion-electron interactions. According to theory, sufficient criteria for individually eliminating these instabilities are:

$$k_{\parallel} v_{\parallel i} > \omega_{pi} \qquad \text{(drift cyclotron, } k_{\parallel} \neq 0,\ \rho_i \approx R) \quad (1)$$

$$k_{\parallel}/k_{\perp} > (RB^{-1}\, dB/dr) \qquad \text{(negative mass)} \quad (2)$$

$$k_{\parallel} v_{\parallel e} > \omega_{ci} \qquad \text{(maser and Harris, } k_{\parallel} \neq 0) \quad (3)$$

Theoretical models from which these results were derived mostly neglect axial restoring forces, spatial boundary conditions, magnetic gradients, and other possible salient features of the experiment. Efforts to incorporate some of these features into theory are under way.

Criteria (1) and (3) above result from essentially Landau damping by ions and electrons respectively. Condition (2) is the criterion that ion-electron plasma interaction dominates rather than negative mass because of the large field $E_{\parallel}$ in the direction of free-electron motion.[16] The proper minimum value of $k_{\parallel}$ ($k_{\parallel \min}$) to employ is an unsolved finite-plasma problem. Among the estimates for $k_{\parallel \min}$, the largest, being the reciprocal of the plasma width before instability, rules out all the above instabilities. On the other hand, if $k_{\parallel \min}$ can be an order of magnitude smaller, still corresponding to wavelengths which easily fit within the chamber, the drift-cyclotron, negative-mass, maser, and Harris instabilities are all allowed. Therefore, we conclude that, unless we exclude all the above theoretical instabilities, we cannot a priori exclude from consideration any aside from the ion-ion and magnetic velocity-space instabilities.

There are, however, density thresholds for instability. For the negative mass, the threshold is thought to be low but has been calculated only for beams. For the other possible instabilities, the ion-electron interactions, the lowest threshold for any ratio $T_{\perp i}/T_{\parallel i}$, etc., is typically the resonance condition,[17,18,19]

$$\omega_{pe} = \omega_{ci}\,. \qquad (4)$$

However, for very cold electrons the growth constant for the drift-cyclotron instability does not vanish when $\omega_{pe} < \omega_{ci}$ but only decreases rapidly.

The resonance condition for ion-electron interaction [Eq. (4)] requires $n_e = 2\text{–}3 \times 10^6\ \text{cm}^{-3}$. The electron densities with normal steady-state operation are much greater than this value, so $\omega_{pe} > \omega_{ci}$ and the ion-electron interactions are allowed. However, as indicated in Sect. 1.4, the lowest threshold for observation of microinstability signals is 3×10^5 fast protons/cm^3. Under these threshold conditions, the electron density should be equal to the hot-ion density. At threshold, the resonance condition is not satisfied, even allowing

---

[9] H. P. Furth, *Phys. Fluids* **6**, 48 (1963).

[10] R. A. Dory, G. E. Guest, and E. G. Harris, *Phys. Rev. Letters* **5**, 131 (1965).

[11] A. B. Mikhailovskii and A. V. Timofeev, *Soviet Phys. JETP (English Transl.)* **17**, 626 (1963).

[12] P. Burt and E. G. Harris, *Phys. Fluids* **4**, 1412 (1961); E. G. Harris, *The Effect of Finite Ion and Electron Temperatures on the Ion Cyclotron Resonance Instability*, CLM-R32 (1963).

[13] A. A. Kolomenskii and A. N. Lebedev, *At. Energ. (U.S.S.R.)* **7**, 549 (1959); C. E. Nielsen, A. M. Sessler, and K. R. Symon, *Intern. Conf. High-Energy Accelerators Instrumentation, CERN, Geneva, 1959, Proc.*, p. 239.

[14] M. N. Rosenbluth and R. F. Post, *Phys. Fluids* **8**, 547 (1965).

[15] E. G. Harris, *J. Nucl. Energy: Pt. C* **2**, 138 (1961).

[16] T. K. Fowler and E. G. Harris, private communication.

[17] G. E. Guest and R. A. Dory, *Thermonuclear Div. Semiann. Progr. Rept. Oct. 31, 1964*, ORNL-3760, p. 70.

[18] L. S. Hall, W. Heckrotte, and T. Kammash, UCRL-7677 (to be published).

[19] G. K. Soper and E. G. Harris (to be published in *Physics of Fluids*).

a factor of 2 error in the hot-ion density measurement. We are therefore inclined to attribute the threshold to the negative-mass or, since the electron temperature is low, possibly drift-cyclotron instabilities, but not to the maser or Harris instabilities.

1.4 STABILIZATION EXPERIMENTS

Here we describe the results of applying two different techniques aimed at achieving some degree of stabilization by disordering proton orbits. The first consisted of driving proton axial oscillations by applying rf fields to plates at the ends of the plasma and was not successful. The second technique, at least partially successful, involved shifting the H_2^+ beam away from the standard trajectory to avoid introducing protons on near-equilibrium orbits.

Our initial calculations had indicated that 300-kev protons near the equilibrium orbit have an axial-oscillation frequency of 4.5 Mc/sec for small displacements, and that 300-kev protons with the permitted range of guiding center locations in the median plane have frequencies of 3.5–6 Mc/sec for displacements of 6 in. The output of a noise source was filtered to reject components outside a 4–5 Mc/sec range and was then amplified by a circuit capable of producing 100 v (peak to peak). Metallic end walls were positioned at $Z = \pm 5\frac{1}{2}$ in. One of these was grounded, and the other was connected to the amplifier output. Operation was under conditions that produced significant instability losses. It was expected that an rf voltage could be found that would rapidly disorder the near-equilibrium orbits and change but little those orbits already having significant amplitudes of axial oscillation. Some suppression of the azimuthal instability and some relaxation of instability losses might then ensue. This was not the case; the application of an rf voltage only enhanced the discrepancy between the charge-exchange loss current and the proton trapping rate, and indeed could produce such a discrepancy under conditions where it was not initially present. Similar results were obtained when using a continuous-wave drive at 4–5 Mc/sec.

We now understand the reason for this result. The initial calculations were in error. They were based on computer studies of protons in axial oscillation with different amplitudes but with the same total energy, 300 kev. This situation does not correspond to the action of the rf driving voltage, for it produces different amplitudes of oscillation by changing the total energy while leaving constant the energy associated with r and θ motions. Properly formulated computer studies showed that the axial-oscillation frequency for protons initially on the equilibrium orbit was essentially unchanged for oscillation amplitudes out to $Z = 5\frac{1}{2}$ in., the location of the driving plates. Since the oscillation energy gained per cycle from the rf voltage increases with displacement amplitude, the trapped protons were simply driven into the end plates.

A number of experiments that involve variation of the molecular-ion trajectory have been performed. In each case, the trajectory was confined to the median plane, as in normal operation. The range of trajectories available is restricted to those which allow the beam to pass through the liner and terminate on the rotating-drum target. With fixed containment field and injection energy the range is limited, but a wider range can be obtained by varying either of these parameters. We chose to operate with full 600-kev injection energy and to vary the magnetic field, since only lower injection energies were available and these would result in lower charge-exchange lifetimes and lower potentially accessible densities. The capacity of the available dc generators and the current ratings of the outer field coils required removing these coils from the circuit and energizing the inboard coils with separate generators. The outer coils are 5 ft from the median plane, and the magnetic field shape in the plasma region is changed very little by the removal of the outer coils. We have not detected any changes in plasma behavior due to the slight difference in field shapes.

Two of the experiments involved studies of the threshold density for the gyrofrequency mode as a function of the molecular-beam trajectory. Gas dissociation was employed. The threshold was determined by evaluating the central density at which rf signals at ω_{ci} first appeared during the plasma buildup interval following injection of the H_2^+ beam, and by evaluating the steady-state central density barely sufficient to give these signals. The thresholds from these two methods were essentially equal.

In the first experiment, the containment field was fixed at the usual value (B_0 = 10 kilogauss,

which gives the 3.25-in. equilibrium radius for 300-kev H^+), and the beam trajectory was varied by the steering magnet, which controls the beam entrance angle. The lowest threshold, 4×10^5 cm^{-3}, was obtained with the standard H_2^+ trajectory (beam turnaround tangent to the 300-kev-proton equilibrium orbit). This trajectory introduces protons with the most ordered initial distribution. With this trajectory, the threshold was found to be reproducible over a wide range of operating pressure and H_2^+ current.

In the second experiment, the range of trajectories was extended by also varying the strength of the containment field. Again, the minimum threshold was obtained with the standard trajectory, and progressive variation from this trajectory resulted in progressively higher thresholds. The results of one run are shown in Fig. 1.7. The threshold increased a factor of 40 with beam turnaround at the magnetic axis. Other runs, presumably with a molecular beam of poorer focus, resulted in a minimum threshold of 3×10^5 cm^{-3} and a threshold of 1×10^8 cm^{-3} with beam turnaround at the magnetic axis.

Increase of instability threshold with orbit disorder is a qualitative feature of the theories. The distributions, in canonical angular momentum, of initially trapped protons are being calculated for several trajectories employed in the work which led to the results of Fig. 1.7. These distributions will be supplied to the Theoretical Group in hopes that theory can be made more quantitative in this respect.

The technique of trajectory variation has been used, with moderate success, to suppress instability-driven losses from plasmas established by injection of H_2^{+*} and from those established by injection of H_2^+ extracted directly from the ion source. The degree of suppression gradually increased with displacement of the trajectory from the standard one. The data we show are for the two extreme cases: beam turnaround at the equilibrium orbit radius and at the magnetic axis. The observations employing Lorentz trapping of H_2^{+*} are the more straightforward and will be described first.

Figure 1.8 shows the steady-state charge-exchange loss current from the plasma as a function of charge-exchange decay time for two injection orbits. The upper curve was obtained with the H_2^{+*} turnaround at the 300-kev-proton equilibrium radius (3.25 in.). The lower curve was obtained with an increased field value that shifted the turnaround to the magnetic axis and the equilibrium radius to 2.6 in. Gas dissociation dominates for $\tau < 0.1$ sec and Lorentz dissociation dominates for $\tau > 0.1$ sec. There is charge-exchange accountability (no instability losses of protons) at $\tau < 1$ sec, and instability losses are present at longer τ values. Injection through the axis results in a shorter molecular-beam path length for trapping by gas dissociation and therefore the displacement in the region dominated by gas dissociation. The situation is more complicated in the region dominated by Lorentz dissociation. Not only is the path length shorter, but also the range of equivalent electric field that can produce Lorentz trapping is shifted, and thereby the range of molecular states that can be dissociated and trapped. The result is that the normal trajectory produces a Lorentz trapping fraction that is higher by a factor of about 2 (ref. 20). At the longest τ value available for comparison (8 sec), the charge-exchange currents for the two trajectories are equal. At this point the ratio of instability loss current to proton input current is 0.8 for the standard trajectory and 0.6 for the displaced trajectory. Both curves are approaching limiting 45° slopes (constant number of stored protons) at each end of the τ range. Because of the lower proton input rate, the displaced trajectory would have the lower number of stored protons at high pressure. At low pressure, however, the curves are crossing, and the displaced trajectory will have the higher number (see Figs. 1.10 and 1.12).

The experiments that employed injection of H_2^+ obtained directly from the ion source made use of the later of the two sources described in Sect. 1.6. Proton trapping at low pressures was dominated by Lorentz dissociation.

Figure 1.9 shows the effects of trajectory variation upon a plasma established by injection of a low H_2^+ current, 1.3 ma. The trajectories are the same two as those used to secure the data of Fig. 1.8, and through-axis injection was again achieved by an increase in magnetic field. As explained in connection with Fig. 1.8, through-axis injection results in a somewhat lower proton trapping rate,

[20] This experimental result is contrary to the conclusion of many earlier calculations which predicted that the displaced trajectory would result in a higher Lorentz trapping fraction. The calculation is being reviewed.

so the curve for this trajectory is displaced to lower ordinate values. With this low injected current, instability losses are not severe even with the standard molecular trajectory. There is, however, a degree of improvement gained by use of the displaced trajectory, as indicated by the slight convergence of the two curves at longer decay times.

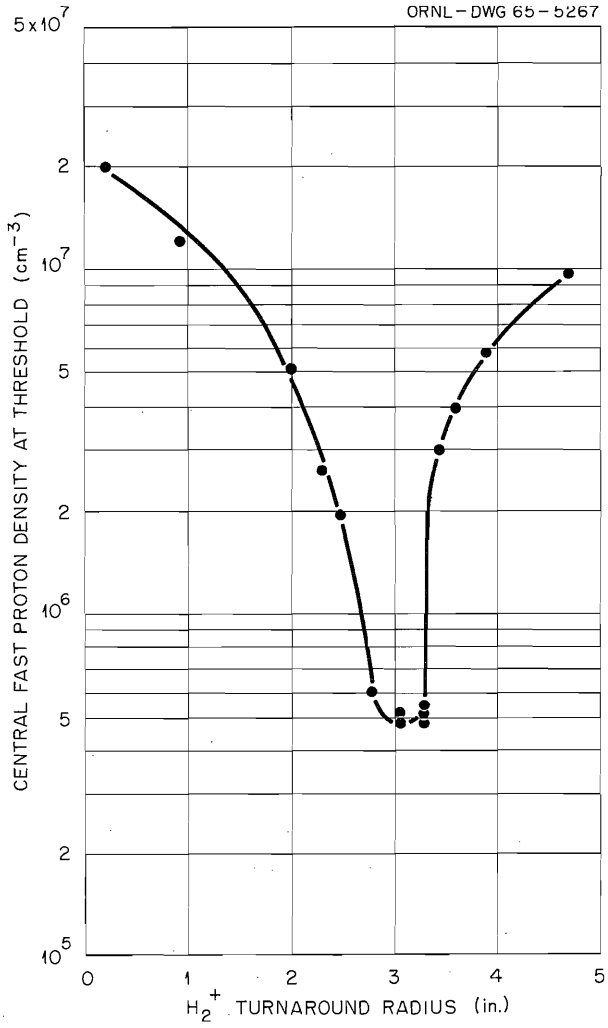

Fig. 1.7. Proton Density at Threshold for Appearance of RF Signals at ω_{ci} as a Function of Molecular-Beam Trajectory (5×10^{-7} Torr, Magnetic Field Increased for Points at $r \leq 2.5$ in.).

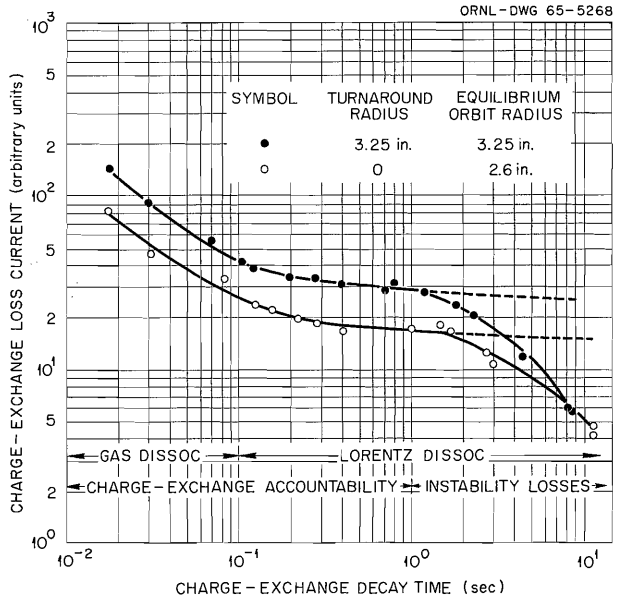

Fig. 1.8. Charge-Exchange Loss Current as a Function of Decay Time for the Standard and a Displaced Molecular-Ion Trajectory (500 μa H_2^{+*}, Helium Gas Leak).

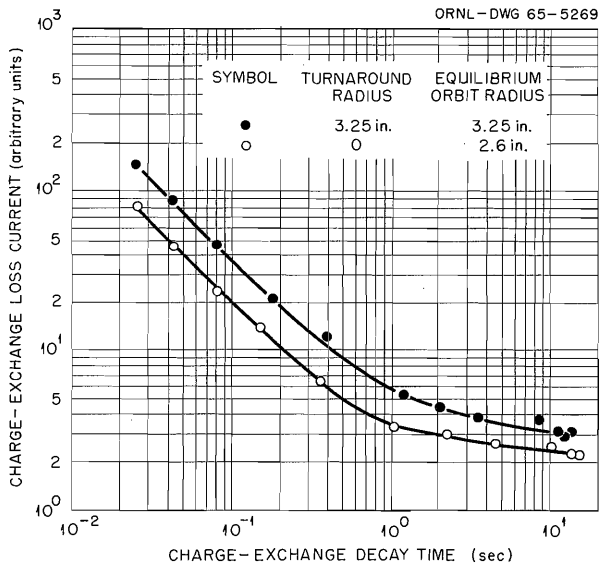

Fig. 1.9. Charge-Exchange Loss Current as a Function of Decay Time for the Standard and a Displaced Molecular-Ion Trajectory (1.3 ma H_2^+, Helium Gas Leak).

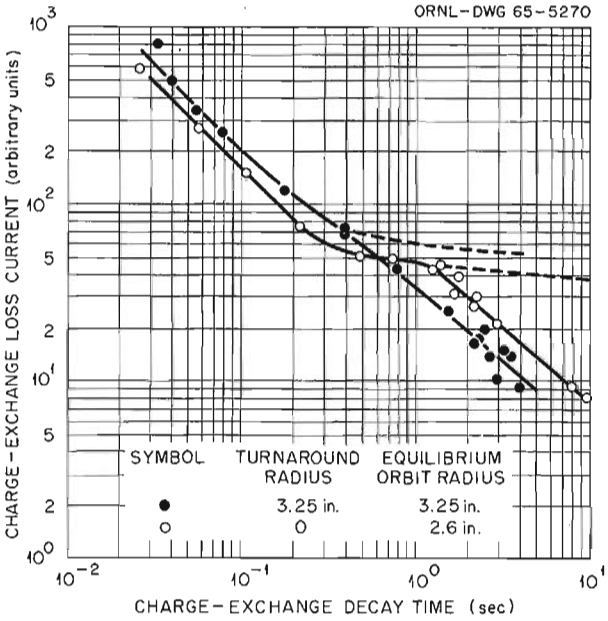

Fig. 1.10. Charge-Exchange Loss Current as a Function of Decay Time for the Standard and a Displaced Molecular-Ion Trajectory (10 ma H_2^+, Helium Gas Leak).

Figure 1.10 also presents results of trajectory variation, but this time the injected H_2^+ beam was 10 ma, and instability losses dominated at long decay times. The trajectories are the same as those used for the data of Figs. 1.8 and 1.9. The displacement of the curves at short decay times is somewhat less than that of the two preceding figures, presumably because of changes in beam focus. The dotted-line extrapolations represent the behavior expected in the absence of instability losses. The source conditions for 10 ma injected current are more favorable for excited-state production than the conditions for 1.3-ma injection. The Lorentz trapping fraction is therefore somewhat higher, and with 10 ma, Lorentz trapping begins to dominate at $\tau \approx 0.6$ sec. In the region dominated by instability losses, the shift to through-axis injection results in improvement from two points of view. First, the ratio of instability loss current to proton input current is decreased. At $\tau \approx 4$ sec, this ratio is 0.8 for the standard trajectory and 0.55 for the displaced trajectory. Secondly, there is less energy dispersion (Fig. 1.11), and as a result, the decay time is longer at a given pressure. This last effect is most pronounced at base pressure, when the standard trajectory gave $\tau = 4$ sec and the displaced trajectory gave $\tau = 10$ sec. At base pressure, the central fast-proton density obtained with the displaced trajectory was 2×10^8 cm^{-3}, a factor of 2.5 greater than that obtained with the standard trajectory.

Figure 1.12 is a plot of the number of stored protons (from Z, θ, t integrals of the decaying charge-exchange currents) as a function of decay time for the data of Fig. 1.10. A somewhat higher limiting number is obtained with the displaced trajectory, but the results for both trajectories are clearly instability limited.

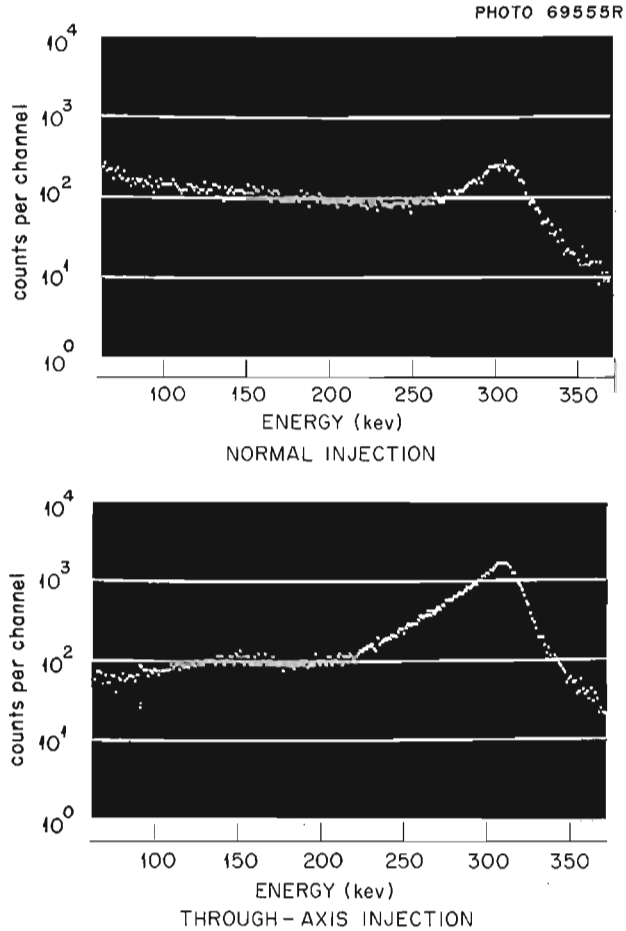

Fig. 1.11. Comparison of Energy Spectra of Charge-Exchange Neutrals for the Standard and a Displaced Trajectory (10 ma H_2^+, 5×10^{-9} Torr, Detector at Median Plane).

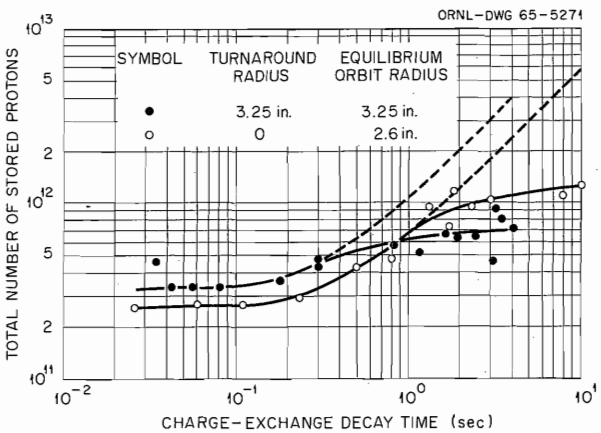

Fig. 1.12. Total Number of Stored Protons as a Function of Decay Time for the Standard and a Displaced Molecular-Ion Trajectory (10 ma H_2^+, Helium Gas Leak). The dotted lines represent the potentially accessible densities.

In summary, retaining the molecular-ion trajectory in the median plane but shifting the turnaround radius away from the equilibrium orbit radius of 300-kev protons has a marked effect on the density threshold for onset of the instability mode responsible for most of the instability losses. With the standard trajectory, the threshold (in central fast-proton density) is $3–5 \times 10^5$ cm^{-3}. With through-axis injection, the threshold increases to $2–10 \times 10^7$ cm^{-3}. Under conditions dominated by instability losses, shifting to through-axis injection improves the performance by a combination of two effects: the instability loss current is decreased, and the energy dispersion of the trapped protons is reduced, so the charge-exchange lifetime is longer. The total stabilizing effect is, however, modest. The limiting density is increased by a factor of only 2–3, and the plasma losses are still instability dominated.

1.5 LORENTZ DISSOCIATION OF H_3^+ [21]

We have previously reported,[22] and now regularly employ, proton trapping resulting from the Lorentz dissociation of H_2^{+*} formed from H_3^+ in a water-vapor cell. We have recently observed proton trapping resulting from the Lorentz dissociation of H_3^+ extracted directly from the duoplasmatron ion source. Here we describe results of three experiments involving H_3^+ injection. All employed the two-coil magnetic field.

Two experiments used the H_3^+ output from an ion source optimized for H_2^+ production (Sect. 1.7). In one, the central field value was the usual 10 kilogauss, and H_3^+ was injected at 400 kev in order to obtain the same beam trajectory as is normally used with 600-kev H_2^+ injection (beam turnaround at 3.25 in.). With constant injected beam, the charge-exchange loss rate was measured as a function of charge-exchange decay time, the latter being controlled with a helium-gas leak (Fig. 1.13). The evidence for Lorentz dissociation is that usually quoted – the trapping rate is proportional to pressure (varies as $1/\tau$) at high pressures but then becomes essentially constant at low pressures. In this experiment the Lorentz trapping fraction was $1–2 \times 10^{-5}$, an order of magnitude less than that which we obtain when injecting H_2^{+*} from the water-vapor cell. The gradual decrease in ordinate values near base pressures does not represent a true reduction of trapping rate, but rather the failure of charge-exchange accountability due to microinstability-driven losses (Sect. 1.2) which entered at the usual threshold density of $5–10 \times 10^7$ cm^{-3}.

In the second of the experiments with this source, a central field value of 12.3 kilogauss was used to allow injection of 600-kev H_3^+ on a trajectory with beam turnaround close to the equilibrium orbit radius of 200-kev protons. The data again indicated a Lorentz trapping fraction of $1–2 \times 10^{-5}$.

A similar 600-kev-injection experiment was performed using the H_3^+ output from a different source, one optimized for H_3^+ production (Sect. 1.7). This source was not favorable for the production of excited vibrational states, for the Lorentz trapping fraction was not greater than $1–2 \times 10^{-6}$.

In these experiments, the H_3^+ ions should dissociate into $H_2 + H^+$ and not $H_2^+ + H$, since the latter process would require an additional

[21] Part of this material will appear as "Lorentz Dissociation of H_3^+ in DCX-1," G. R. Haste, J. L. Dunlap, H. Postma, and L. H. Reber, *Nucl. Fusion* **5**, 2 (1965).

[22] H. Postma, G. R. Haste, and J. L. Dunlap, *Nucl. Fusion* **3**, 128 (1963).

1.8 ev. We have experimentally verified, by measurements of the energy distributions of escaping charge-exchange neutrals and considerations of the cross sections involved, that the trapped energetic ions are predominantly protons of about the energy expected ($E_0/3$). Only about 1% of the trapped energetic ions are H_2^+ (at approximately $2E_0/3$).

The injection of 600-kev H_2^{+*} from the water-vapor cell still results in higher accessible densities than does H_3^+ injection. The conversion from H_3^+ to H_2^{+*} in the cell is only 10% efficient, so it is true that the available H_3^+ current is greater by an order of magnitude. The highest accessible densities with H_3^+ injection result from the use of 600-kev molecular ions and of the source which gives a trapping fraction of $1\text{–}2 \times 10^{-5}$. Then the proton input current is equal to that available with H_2^{+*} injection, since the higher trapping fraction for H_2^{+*} ($1\text{–}2 \times 10^{-4}$) just balances the H_3^+ current advantage. However, H_2^{+*} is favored since it produces 300-kev protons that have a much longer change-exchange lifetime than the 200-kev protons produced by 600-kev-H_3^+ injection.

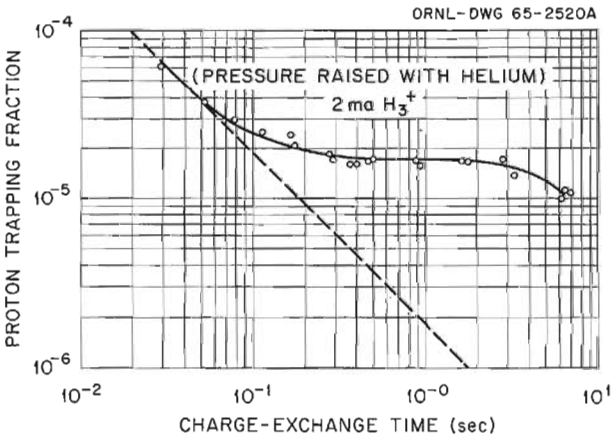

Fig. 1.13. Proton Trapping Fraction (the Total Charge-Exchange Loss Current Normalized to the Injected Molecular-Ion Current) as a Function of Decay Time (2 ma H_3^+, Helium Gas Leak). The departure from proportionality indicates Lorentz trapping.

1.6 LORENTZ DISSOCIATION OF DIRECTLY EXTRACTED H_2^+

Our earlier measurements of the Lorentz trapping fraction for 600-kev H_2^+ extracted directly from the duoplasmatron ion source fixed the upper limit of this fraction at 1×10^{-7}, quite negligible in comparison with the $1\text{–}2 \times 10^{-4}$ obtained with H_2^{+*} injection.[22] The source was recently changed to one permitting larger H_2^+ currents (Sect. 1.7), and much higher Lorentz trapping fractions, as great as 1×10^{-5}, are now obtained.

The usual evidence for Lorentz trapping is shown in Fig. 1.14. The injected H_2^+ current for these data was 1 ma. The extrapolated 45° slope is the response expected for gas dissociation and charge-exchange loss of monoenergetic protons in a gas

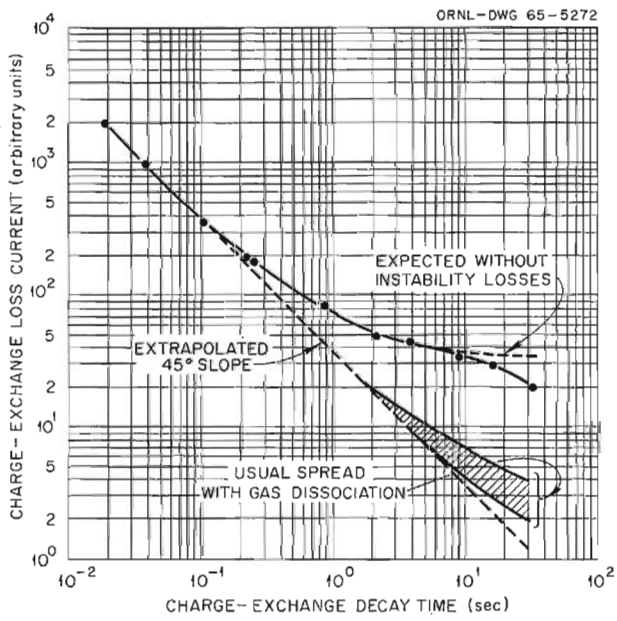

Fig. 1.14. Charge-Exchange Loss Current as a Function of Decay Time (1 ma H_2^+, Helium Gas Leak). The extrapolated 45° slope represents the response expected for gas dissociation and charge-exchange loss in a background gas of constant composition. The crosshatched area indicates the departure from this extrapolation that is normally observed with gas dissociation. The extrapolation of experimental data at long τ represents the response expected without instability losses.

background changing in density but not in composition. The cross-hatched area represents the departure from this slope encountered in earlier gas-dissociation runs. The departures were presumed to be the result of changes in gas composition as base pressure was approached, but may have also involved some negligible Lorentz trapping. The data points are obviously well outside this range and indicate that Lorentz trapping dominates for $\tau > 1$ sec, with a trapping fraction of about 7×10^{-6}. Instability losses are present at $\tau > 10$ sec.

The trapping fraction depends somewhat on the conditions of source operation. Happily, those for higher extracted H_2^+ current (essentially higher arc and source-magnet currents) result in larger Lorentz trapping fractions. For example, the data for 10 ma injected H_2^+ current (Fig. 1.10) show a trapping fraction of 1×10^{-5}.

The 10 ma is the maximum H_2^+ current which we at present can comfortably inject into DCX-1. With a Lorentz trapping fraction of 1×10^{-5}, the proton input current at low pressures is nearly that available with Lorentz dissociation of H_2^{+*} (800 μa of H_2^{+*} and a trapping fraction of $1\text{–}2 \times 10^{-4}$).

1.7 INJECTOR MODIFICATIONS

The operation of the injector system has been improved by three modifications during the present report period.

We now have two new ion sources, one optimized for H_3^+ production and one optimized for H_2^+ production. Both were constructed according to the latest prescriptions of the Ion Source and Accelerator Group. The H_3^+ source operates comfortably at 8 ma and provides 800 μa of H_2^{+*} for Lorentz trapping. This current is somewhat more than a factor of 2 greater than that previously available and results in potentially accessible densities near 1×10^{10} cm^{-3}. The potential of the new H_2^+ source has not been thoroughly explored on DCX-1. However, it does supply well-behaved injected currents of 10 ma, a figure that in the past has been often quoted but only rarely obtained.

The details of source geometry and of operating currents and potentials have been cataloged in an effort to isolate those features which caused the changes in Lorentz trapping fractions discussed in Sects. 1.5 and 1.6. Unfortunately, the catalog is lengthy and most items vary from source to source, so it does not answer this question.

Space-charge spreading of the beam has been markedly reduced by incorporating an accel-decel beam neutralizer. This technique was described earlier.[23] In DCX-1, the neutralizer was set up by applying a 4-kv negative potential to an element that surrounds the beam just below the einzel lens (Fig. 1.15).

The substitution of a solenoid lens for focus control in place of the magnetic quadrupole in the 600-kev beam section has improved beam focus. The performance of the quadrupole was too sensitive to shifts of the beam from the lens axis.

1.8 ACKNOWLEDGMENTS

We are indebted to O. B. Morgan for assistance in problems relating to the injector system, to Mozelle Rankin and D. A. Griffin for several computer studies, and to T. K. Fowler for numerous helpful discussions.

[23] *Thermonuclear Div. Semiann. Progr. Rept. Oct. 31, 1964*, ORNL-3760, p. 66.

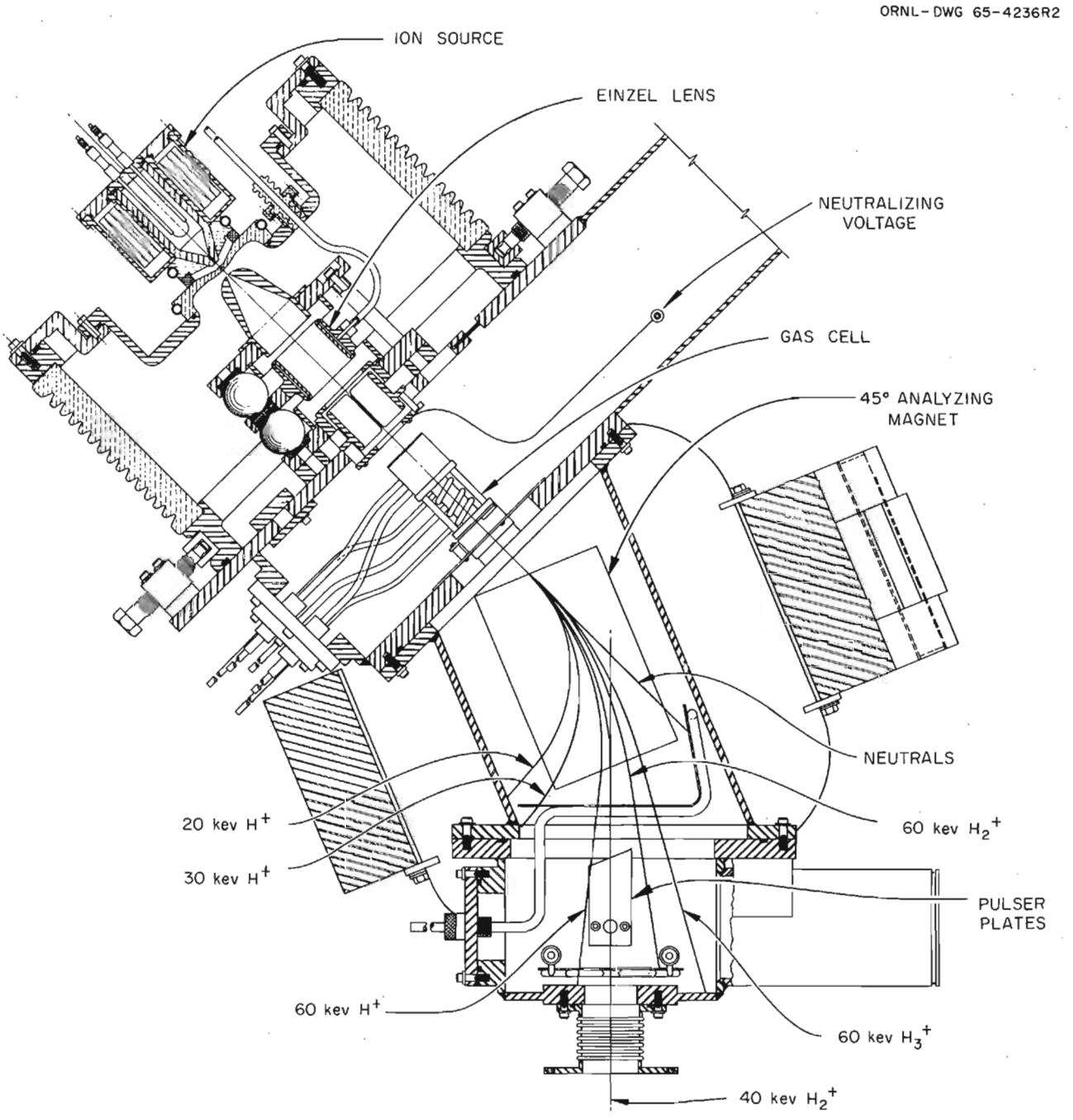

Fig. 1.15. Diagram of the DCX-1 Source Arrangement Used for H_2^{+*} Injection. For H_2^+ injection the gas cell is removed and the pulser plates are shifted to the position previously occupied by the gas cell.

2. Injection and Accumulation: Multiple-Pass Experiments (DCX-2)

P. R. Bell
J. S. Culver
R. C. Davis
S. M. DeCamp
J. C. Ezell
R. A. Gibbons[1]
G. G. Kelley
N. H. Lazar
J. F. Lyon
O. B. Morgan
T. F. Rayburn
R. F. Stratton
C. W. Wright
A. J. Wyrick

2.1 INTRODUCTION

Further information concerning the nature of the plasma contained in DCX-2 has been obtained under a wide variety of conditions. Hydrogen and lithium arcs as well as hydrogen and nitrogen gas backgrounds have been used to dissociate the molecular-hydrogen-ion beam. The maximum hot-ion density (4×10^9 ions/cm^3) was obtained using the lithium arc. The maximum densities with hydrogen-arc, hydrogen-gas, and nitrogen-gas breakup were 1 to 2×10^9, 5×10^8, and 1×10^8 ions/cm^3 respectively. The lithium-arc parameters (position, current, and voltage) and the injection geometry (molecular-ion-orbit diameter and injection-duct position and tilt angle) were varied and their effect on the trapped plasma studied. The energy of the injected molecular ions was noise modulated ±25 kev to study the effect on plasma energy spreading. No effect on energy spreading or plasma density was observed. The improved hydrogen arc developed in the Long Solenoid was installed in DCX-2, and preliminary results have been obtained. Experiments were performed to study the origin of the large group of particles with small axial energy (central-peak plasma) and the nature of the cold plasma in which the energetic protons charge exchange.

Several new diagnostic tools have given us a better look at the DCX-2 plasma than ever before. Our new rf spectrometer can sweep a range of 2 Gc from 0 to 42 Gc, and new rf probes have been developed to reduce the problem of probe resonances. Collimated foil neutral detectors that look only at certain pitch angle ranges, and energy-sensitive detectors that can make parallel slit scans while looking only at certain pitch angles (such as the central peak only or the side lobes) have also been used.

2.2 LITHIUM-ARC EXPERIMENTS

2.2.1 The Study of the Origin of the Central Peak

The most striking phenomenon in the DCX-2 plasma is the existence of two distinct components in the energetic plasma.[2] One component (the central peak) has high total energy with very low axial energy, the other (the side lobes) has lower total energy and an axial energy approximately equal to that at injection. Two possible models for the formation of the low-axial-energy group have been suggested. A form of streaming interaction may exist between the counterstreaming particles that make up the side lobes. The

[1]Deceased.

[2]P. R. Bell *et al.*, *Thermonuclear Div. Semiann. Progr. Rept. Oct. 31, 1964*, ORNL-3760, p. 12.

other possibility is that cold hydrogen ions are resonantly heated to high energy by essentially perpendicular fields at a rate fast enough to avoid their being lost by charge exchange during heating.

If the counterstreaming action is taking place, it will be enhanced by an increase in the current density of the counterstreaming particles. This density was increased in DCX-2 by modifying the injection geometry. The usual position of the arc, 1 in. from the machine axis diametrically opposite the point of injection, results in trapped protons which precess during multiple reflections to fill a cylinder 8 in. in diameter. The injected proton Larmor diameter is 5 in., and the guiding centers remain at 1.5 in. from the axis. If the protons were injected with their guiding centers on the machine axis, however, there would be no precession, and a greatly increased current density of counterstreaming particles would be expected. This condition was brought about in DCX-2 by moving the arc 3 in. from the axis, with the injector left in its normal position 9 in. from the axis. The field was decreased enough to cause the molecular ions to pass through the arc. The trapped protons then had a 6-in.-diam orbit centered on the machine axis.

The modification had no appreciable effect on the trapped-plasma density or on the average amount of charge-exchange current from the central distribution relative to the current from the side lobes in the normal range of injected currents. At very low current ($\sim$0.2 ma), however, a relatively large central peak was seen, although no peak was visible in a similar experiment at 0.4 ma when the arc was 1 in. off axis.

Some evidence exists for the model of heating of cold ions. The lithium ions of the arc are heated when the beam is on, since the lithium cyclotron harmonics are seen when the beam is on and are not seen when the beam is off. If nonresonant lithium ions are heated this much, it is possible that cold hydrogen ions may be heated to a much greater extent. Also, the plasma is not as effective at pumping hydrogen as was expected. Apparently the cold hydrogen ions are being heated by collective interaction with the fast ions more quickly in the perpendicular direction than they can scatter axially and are prevented from flowing out of the plasma region along flux lines through the mirrors. An experiment to see if deuterons might also be heated in a similar way by the plasma gave negative results. A large deuterium gas feed did not result in an observable increase in the neutron yield from volume and wall reactions. If the cold deuterium had been heated to a temperature of 10 to 12 kev, it would have been detected.

If the hydrogen ions are being heated from low energies, more high-energy ions might be found than were trapped from the 600-kev H_2^+ beam. An accurate study of particle accountability, however, is quite difficult due to the imprecision with which plasma properties can be measured. Although the dissociation rate probably can be determined to within a factor of 2, the total rate of loss of the energetic particles from the machine cannot be measured. The flow of particles to the injector is unknown, and even the magnitude of the charge-exchange current is uncertain because of a possibly large contribution from low-energy particles where the spectrum cannot be measured at present. The time variation of the energy spectrum following turn-on of the H_2^+ beam has been studied to observe the course of the heating of the cold ions, but the results are not reliable, and the measurement must be improved. A study of the low end of the trapped-proton energy spectrum would be helpful (50 kev is the lower limit at present), and improved energy-sensitive detectors with only a few kev resolution are being developed for this purpose.

2.2.2 Pressure and Beam-Current Variations

A series of experiments has been performed to determine the properties of the energetic plasma with respect to variation of pressure and beam current. It might be expected that a systematic variation of single parameters could delineate such important properties as the nature and magnitude of the non-charge-exchange losses. As will be seen, however, all the machine variables are so strongly interrelated that no simple interpretations are possible.

In one experiment the machine pressure was raised by introducing a small flow of H_2 into the plasma region. Data were obtained for a pressure variation of a factor of 10 (1.7×10^{-7} to 1.5×10^{-6} mm Hg) with the lithium arc 1 in. off axis and the normal orbit diameter such that the beam passed through the arc. The pressure in the plasma region also was varied by adding nitrogen

gas and by the use of liquid-nitrogen cooling of the end walls to reduce the base pressure. The results are shown in Table 2.1. The estimate of the total density in the plasma is based on the total number of charge-exchange particles striking the walls after the beam is turned off. It is believed to be a reliable determination of the particles per unit volume which die by charge exchange during decay. If other losses exist, the density is an underestimate. The plasma radius is assumed to be 6 in. independent of pressure. The results cannot be interpreted in any simple way because of the variation of mean energy of the plasma and because the pressure-dependent composition and density of the background plasma are not known and cannot be measured with any degree of certainty. The variation in density of only a factor of 3 despite the gage variation of a factor of 10 in pressure (the actual variation in neutral-gas density is even greater since the gage efficiency for hydrogen is only approximately one-third that for nitrogen) would suggest that losses other than charge exchange are taking place. This interpretation cannot be made, however, because of the variation of average energy and average lifetime of the trapped particles. In fact, if the gas composition is assumed constant so that the charge-exchange cross section does not change, the values of $\overline{\tau}_{cx}$ are seen to follow the plasma density much better than the pressure does. This effect suggests that charge exchange dominates the loss rate, but this interpretation too is doubtful because of the unknown background density in the region of the hot plasma.

A series of measurements was made on the plasma with reduced beam currents. The use of a small aperture in the ion-source anode made possible the injection of currents as small as ~0.2 ma. The density, determined from the integral of the charge-exchange flux after beam turn-off, was measured as a function of current. The injected beam was determined from the current to a movable collimated foil detector positioned to look at the peak in the spatial distribution of the dissociation current. The density as seen in different port positions as a function of the injected current inferred from the foil-detector signal is plotted in Fig. 2.1. The average energy of the trapped plasma also increases as the beam current is increased, but the most significant change is in the observed pitch-angle distribution. At the lowest currents, a narrow central peak is seen. At higher currents, the central peak is still the dominant feature, but the side lobes are quite prominent. These data are all for the arc 3 in. south of center and the field reduced to produce a 12.4-in.-diam molecular-ion orbit.

Table 2.1. Plasma Properties at Different Pressures

Pressure (mm Hg)	$n_+ = \dfrac{\int_{\text{beam off}}^{\infty} I\,dt}{V}$	$\overline{\tau}_{cx}$ [a] (msec)	$\overline{E}$ (kev)
	$\times 10^9$		
$5\text{–}7 \times 10^{-8}$ [b]	3.1	100	550
1.7×10^{-7}	3.0	63.2	660
4.7×10^{-7} [c]	2.1	18.2	583
1.2×10^{-6} [c]	0.97	6.3	487
8×10^{-7} [d]	1.4–1.7	6.5	554

[a]Based on the density calculated from the ion gage pressure.

[b]Liquid-nitrogen-cooled walls.

[c]H_2 gas feed into plasma region.

[d]N_2 gas feed into plasma region.

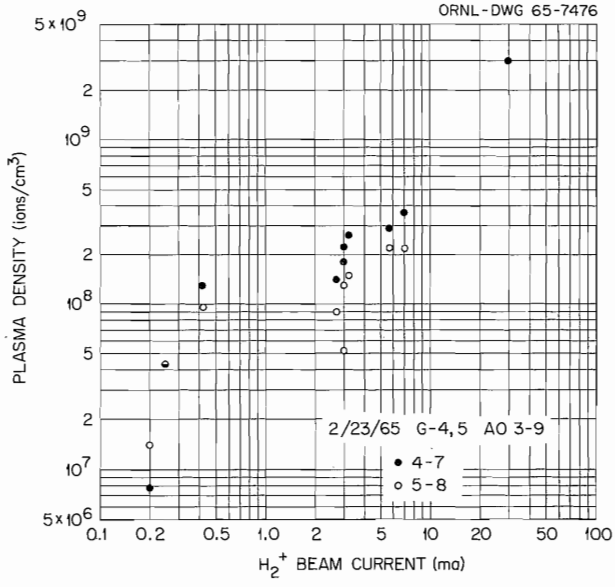

Fig. 2.1. Energetic-Plasma Density as a Function of the Injected Current.

2.2.3 Arc-Current Variation

Besides changing the actual location of the lithium arc in DCX-2, we varied the arc current and voltage (usually 18 amp and around 200 v) from 5 amp up to 40 amp and from 100 v up to 280 v in our study of the effect of the arc parameters on the trapped plasma. The arc current was varied by adjustment of the current-regulated supply. The voltage was varied by adjusting the heat input to the anode boiler, which varied the pressure of lithium vapor in the anode. Changes in the arc voltage have no appreciable effect, but the plasma properties do change significantly as the arc current (and hence density) is varied. Figure 2.2 shows the mean energy of the trapped protons vs arc current, assuming a nitrogen charge-exchange cross section. The lower average energy at higher arc current may be due to an increased energy loss to arc electrons and arc-generated cold plasma. This is also seen in Fig. 2.2 in the behavior of the mean charge-exchange lifetime with arc current.

Two measures of the variation of trapped-particle density with arc current are shown in Fig. 2.3, the density based on the integral of the total neutral current to the foil neutral detectors ($\int I_{cx}\, dt$) and the $I_{cx}\bar{\tau}_{cx}$ value calculated from the energy spectrum of neutrals incident on the energy-sensitive detectors. The density ($n_+ = I_{cx}\bar{\tau}_{cx}/V$) exhibits a fast rise at low current ($\bar{\tau}_{cx}$ approximately constant, but I increasing due to increasing arc dissociation of the H_2^+ beam) and a slower fall at high current (I approximately constant since the beam dissociation fraction has leveled off at a high level while $\bar{\tau}_{cx}$ has decreased), with a broad maximum in the range 15 to 25 amp arc current. These several indications show that optimum performance is obtained in the current range where we normally operate. At much lower arc current, the arc is not very effective in dissociating the H_2^+ beam, and at much higher current, the trapped energetic plasma may be losing too much energy to the arc and the associated cold plasma.

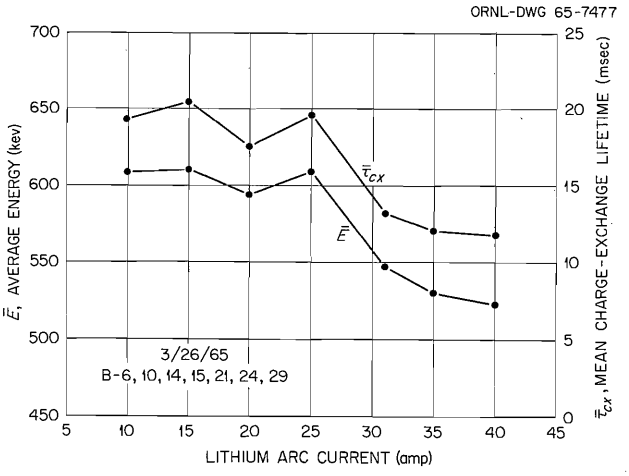

Fig. 2.2. Average Energy and Mean Charge-Exchange Lifetime for the Trapped Distribution as Seen in Port Position 4-4 vs Lithium-Arc Current. A nitrogen charge-exchange center density of 5×10^{10} atoms/cm^3 has been assumed.

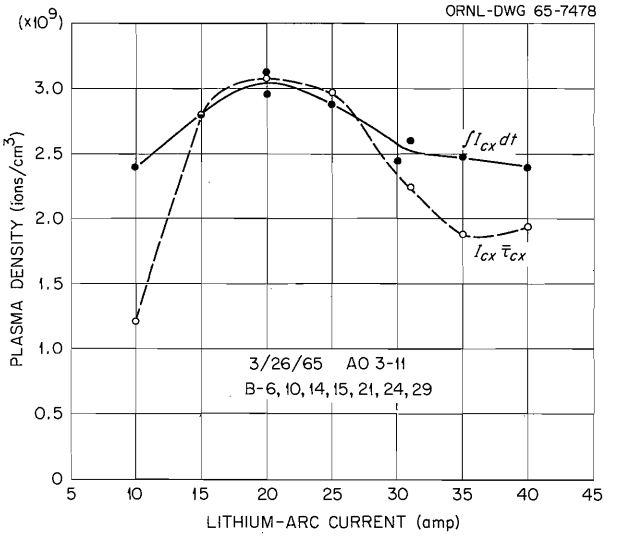

Fig. 2.3. Plasma Density vs Lithium-Arc Current. The densities based on the integral of the neutral current were observed in port position 4-7, and the densities based on the calculated $I_{cx}\bar{\tau}_{cx}$ were observed in port position 4-4. The $I_{cx}\bar{\tau}_{cx}$ values have been normalized to the integral-based density at 15 amp arc current.

2.2.4 Background Plasma

The background plasma cannot be measured in the region occupied by the hot ions, but it has been observed along flux lines through the hot plasma both inside and beyond the mirrors. In one particular experiment with lithium-arc dissociation, a multigridded probe was scanned in an arc centered at the wall of the central chamber and passing 2 in. from the axis. It was located 46 in. from the midplane just beyond the point of reflection of the injected ions, axially at the opposite end of the machine from the injector, and on the same side of the axis as the injector. The probe has a circular aperture 1 in. in diameter with three planar grids of 100-mesh, 0.001-in.-diam tungsten. The aperture was oriented in a plane perpendicular to the machine axis. During the experiment the two outer grids were at wall potential. A suitable voltage was applied to the third grid to suppress either ions or electrons. The collector was swept ±500 v. At all positions, the electron current was cut off by a potential of −130 v on the third grid. Analysis of the resulting oscilloscope traces was done in the manner described previously.[3] The results are shown in Fig. 2.4. The maximum plasma potential is seen to be about 60 v, falling rapidly at 4 to 5 in. from the axis. The axial component of the ion energy and the current density change less abruptly but become quite small at about ±7.3 in. An anomalous rise of almost a factor of 2 is seen in the current along flux lines through the injector.

The cause of the abrupt fall in plasma potential at intermediate radii is not known. It is quite low at all radii, however, in comparison to results with gas breakup. The axial component of the ion energy is considerably higher than had been observed earlier with gas breakup, but recent gas-breakup experiments in hydrogen may have shown higher energies.

[3]P. R. Bell *et al.*, *Thermonuclear Div. Semiann. Progr. Rept. Apr. 30, 1963*, ORNL-3472, p. 19.

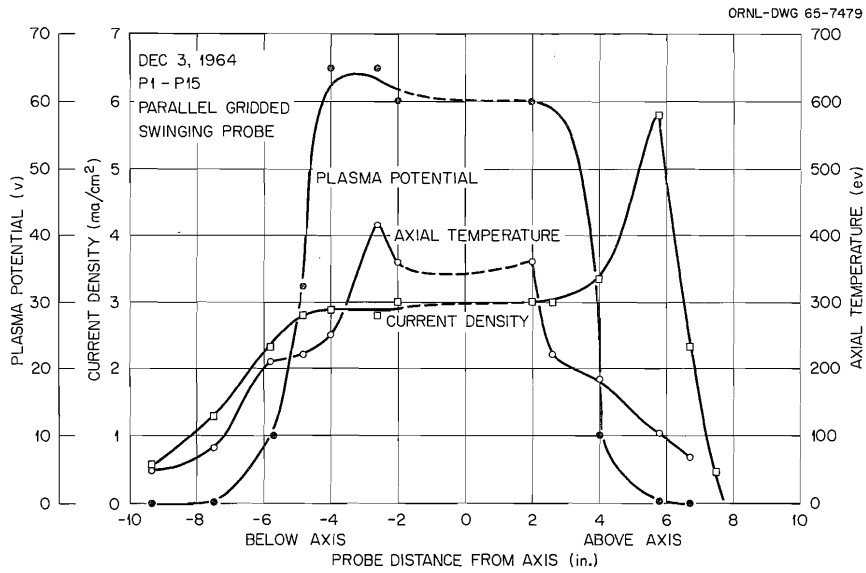

Fig. 2.4. Cold-Plasma Characteristics as a Function of Radius Obtained from a Gridded Probe. The probe was moved on an arc that passed the axis at a distance of 2 in.; therefore, the points at ±2 in. are identical.

2.2.5 Radial Diffusion of Lithium Ions

The current of lithium ions from the arc as a function of radius was measured by allowing the lithium to condense on a water-cooled copper strip. The strip was positioned on a radius of the machine at 90° to the position of the arc and extended to within 2 in. of the axis. Lithium was collected on the side facing the anode for approximately an hour with no energetic-ion injection, after which it was removed and the deposit scraped off in sections and analyzed. A second run was made with injection at 50% duty cycle, correcting for the amount deposited during the off time by assuming it to be the same as during the beam-off run. The radial current was found to fall approximately exponentially with an e-folding length of 2.8 cm and 1.6 cm for the beam-on and beam-off experiments respectively. The total current of lithium beyond a radius of 2 in. was 2.7 amp and 0.45 amp, respectively, assuming a distribution symmetric about the axis and undisturbed by the presence of the strip.

2.3 HYDROGEN-ARC EXPERIMENTS

Although the lithium arc is an efficient dissociation center for the molecular-ion beam, it also contributes to charge-exchange loss of the energetic trapped protons. Parallel-slit scans with the energy-sensitive detectors looking at the plasma produced by lithium-arc dissociation show that the arc contribution to the charge-exchange loss is at least as much as that from the background gas and cold plasma. To eliminate this loss, a hydrogen arc has been run in DCX-2, and preliminary results have been obtained.

The experience of Francis and Bell[4] in the Long Solenoid Facility led to the belief that an arc with low gas feed could be operated in DCX-2 at a pressure of 1 to 5×10^{-7} mm Hg if titanium evaporation were used outside the mirrors. Arc flutes such as are seen in the Gas Arc Facility[5] are present in the DCX-2 arc, however, and have prevented the attainment of pressures below about 2.5×10^{-6} mm Hg. The flutes carry plasma out radially, where the ions flow to the end walls of the central region and recombine.

Several difficulties have had to be overcome to permit the arc operation in DCX-2. The greatest problem was the design of the cathode. Even with cathodes reduced in size so that the current density was approximately the same as the earlier high-current arcs (110 to 180 amp), the arc would not run without a shield around the cathode to keep the pressure in this region sufficiently high when the gas flow was reduced. The cathode shield developed in the Long Solenoid Facility, however, has permitted reduction of the gas feed to ~ 0.3 cm^3/sec into the anode with approximately an equal amount of ions being added to the arc along the length of the column by the influx of neutral hydrogen. The loss rate of ions out of the arc by fluting is not well established, but estimates of the pumping speed would suggest ~ 0.3 cm^3/sec loss to the walls. Approximately an equal amount flows to the end regions through the mirrors. The arc runs generally at a current of 75 to 80 amp at 200 to 250 v. If 100% efficiency of ionization in the anode is assumed, 0.3 cm^3/sec produces ~ 4 amp of ions – a considerably lower ratio of ion current to electron current than is found in condensable-vapor arcs but not in disagreement with other gas arcs run in the Gas Arc Facility. The anode which has produced the lowest pressure in DCX-2 is of the same conical design as used for the earlier gas-arc experiments in DCX-2, where a gas flow of ~ 10 cm^3/sec was required. A 1.5-in.-ID cylindrical anode with a 3-in.-diam cylindrical sleeve, however, required the lowest gas flow at only slightly higher pressure.

The presence of the arc flutes has been demonstrated by the use of gridded probes. Two probes biased to collect saturation ion current in ports 2-7 and 7-7 show good correlation of the pulses when the probes are placed on the same flux line but rather poor correlation when they are displaced radially. From the time delay between the pulses the radial velocity is estimated to be 6×10^6 cm/sec.

The impurity light radiated from the arc has been observed with a Jarrell-Ash spectrometer having ~ 0.2 A resolution. The ~ 0.7-A width of the 4647-A C^{2+} line yields a temperature of ~ 50 ev for carbon ions, assuming the width is due

[4] J. E. Francis and P. R. Bell, this report, sect. 4.

[5] R. A. Gibbons and N. H. Lazar, *Phys. Rev. Letters* **13**, 703–5 (1964).

only to thermal Doppler broadening. Nitrogen and oxygen impurity lines show similar widths. Some of the observed width may result from a rotation of the arc, but these observations of equal temperatures of the impurities are not inconsistent with similar measurements in the Gas Arc Facility, although the temperatures are a factor of 3 higher. The arc density has not been measured and is probably critically dependent upon the alignment of the anode and the cathode on the same flux line. Variations in pressure and operating voltage of 50% occur when the anode and cathode are moved only a few millimeters.

The radial distribution of the arc plasma has been measured from currents observed on a probe. The results (Fig. 2.5) indicate an e-folding distance of 1.3 cm inside a radius of 19 cm, but a considerably slower variation outside this distance. The density at the highest current reading is $\sim 10^9$ ions/cm^3 at 3 in. from the arc center if an axial velocity of 10^7 cm/sec is assumed. Extrapolation to the arc surface yields a density of $\sim 10^{14}$ ions/cm^3, which probably is an overestimate.

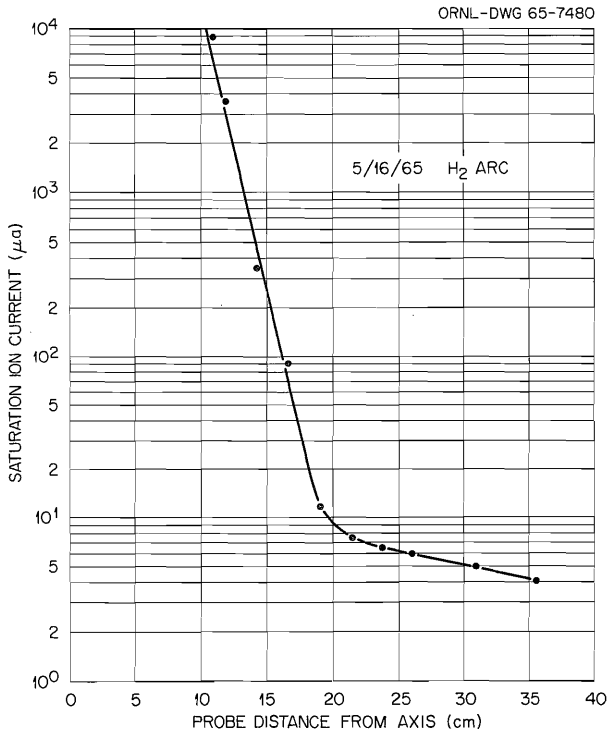

Fig. 2.5. The Radial Distribution of the Arc Plasma as Measured by the Saturation Ion Current to a Gridded Probe.

Pumping-speed measurements of the arc were made by bleeding hydrogen into the plasma region at a known rate. If the increased pressure in the end regions is neglected (a small correction), the arc pumping speed is about 2.2×10^4 liters/sec at a pressure of ~ 5 to 8×10^{-6} mm Hg. If the arc length and radius are assumed to be 400 cm and 0.5 cm, respectively, the arc appears to be 42% black – a behavior not inconsistent with that of other gas arcs.

An evaluation of the usefulness of the arc as a dissociation medium is complicated by the possible influence of several effects. The percentage dissociation of the molecular-hydrogen-ion beam and the observed trapped-plasma density increase with increased gas feed to the arc. It is not clear, however, that the increase in observed density is due only to increased dissociation, since the partial pressure of hydrogen in the plasma region is also increased. As will be explained below, an increase in hydrogen pressure in the same pressure range with gas breakup also increases the density of the trapped plasma. Integrals of the charge-exchange flux give densities of 1 to 2×10^9 ions/cm^3 at a gage pressure of 5×10^{-6} mm Hg.

Perpendicular-slit scans of the plasma produced by hydrogen arc breakup show the same narrow central peak and symmetrically positioned side lobes in the pitch-angle distribution seen with lithium-arc dissociation and in some gas-breakup runs. As expected, parallel-slit scans show no peak in the direction of the arc, indicating that the arc does not contribute appreciably to the charge-exchange loss.

2.4 GAS DISSOCIATION

Experiments with gas dissociation performed during this report period have led to some new results. Gas dissociation at base pressure ($\sim 2 \times 10^{-7}$ mm Hg) gives significantly lower density ($\sim 1 \times 10^8$ ions/cm^3) than is obtained with the arcs. When nitrogen gas is introduced into DCX-2, the charge-exchange current increases, and the plasma density remains approximately constant as the pressure is increased, as expected. The decreased lifetime is offset by an increased trapping rate, although an exact balance is not expected due to variations in energy mixing.

However, when hydrogen gas is added, the plasma density increases, reaching a maximum value of 5×10^8 ions/cm^3 at a gage pressure of 1.8×10^{-5} mm Hg. The energy of the trapped plasma spreads, and the mean energy rises. Figure 2.6 shows the variation of density and the mean energy of this plasma as a function of gage pressure. Perpendicular-slit scans did not show a central peak during this experiment, although a central peak has always been associated with a large energy spread in the past.

Previous experiments with hydrogen-gas dissociation had not revealed this behavior, and the reason may have been due to a high impurity level in the gas that was introduced into the plasma region. The charge-exchange cross section for protons in hydrogen is typically an order of magnitude less than that for protons in other gases around 200 kev and two orders of magnitude less around 800 to 1000 kev. Since the charge-exchange loss rate depends on $n_{cx}\sigma_{cx}$, a very high purity of hydrogen is needed if the plasma behavior is to be dominated by the hydrogen background. Even during this experiment, the mass analyzer scans indicated that only 85% of the gas was hydrogen.

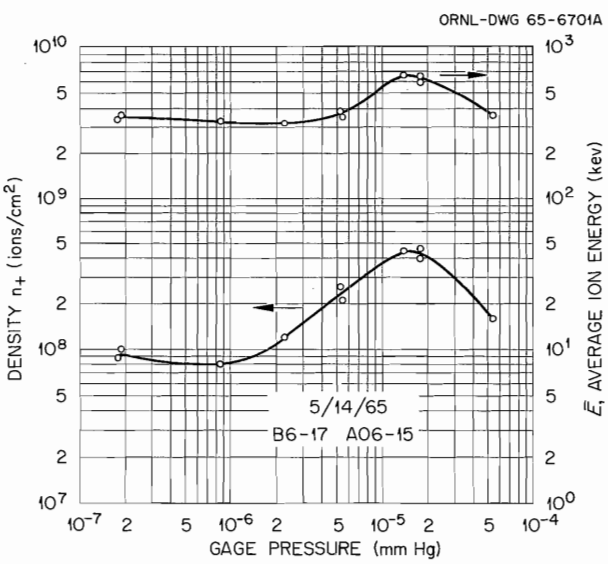

Fig. 2.6. Density and Mean Energy of the Trapped Plasma Produced by Gas Dissociation as a Function of Pressure. The pressure was raised by adding hydrogen.

2.5 RADIO-FREQUENCY MEASUREMENTS

Previous measurements had shown that the ion-cyclotron harmonics from the plasma at highest density still retained considerable intensity at 100 Mc, the limit of our spectrometer. A new spectrometer was therefore obtained to extend the measurements.

The proton-cyclotron harmonics were found under some conditions to extend well beyond 2 Gc (Fig. 2.7*a*) with either H_2- or Li-arc dissociation. The intensity of these harmonics was quite considerable with only about 30 db difference in intensity between the 100th harmonic and the strongest line (2d).

An expansion of the lower-frequency region in Fig. 2.7*b* shows that most of the spectrum is formed from the proton-cyclotron lines, as had been observed previously. The new spectrometer sweeps the spectrum rather slowly (30 cps), but display of the frequency-vs-time plot (Fig. 2.7c) still provides useful information. The fundamental is seen to continue irregularly for $\frac{1}{2}$ sec, and even the fourth harmonic continues noticeably after injection of the beam cases.

During this report period, quite high plasma densities were obtained with gas dissociation at high hydrogen pressure. This high density was accompanied by a large energy spread and a broad rf spectrum; Fig. 2.8*a* shows the wide spectrum. Notice the ill-resolved group of lines over the central third of the spectrum. This region is quite intense, even though a good rf probe was used, and there is considerable rf to 2 Gc. The lower-frequency region is shown in Fig. 2.8*b* and consists of the even harmonics only of the proton-cyclotron frequency and all the harmonics of the molecular-ion frequency. Compare this with Fig. 2.8c and *d* of the same frequency regions with a hydrogen arc operating.

A relatively strong white noise from the arc was found to extend with almost undiminished strength to more than 2 Gc. A curious, complex, very broad peak was found in the arc spectrum, as shown in Fig. 2.7e and *f*. This peak was not seen in most of our spectra, was easily accounted for, and was suspected of being some form of instrumental effect. The rf electric probes being used had rather good properties to ~100 Mc but were untrustworthy much above this frequency,

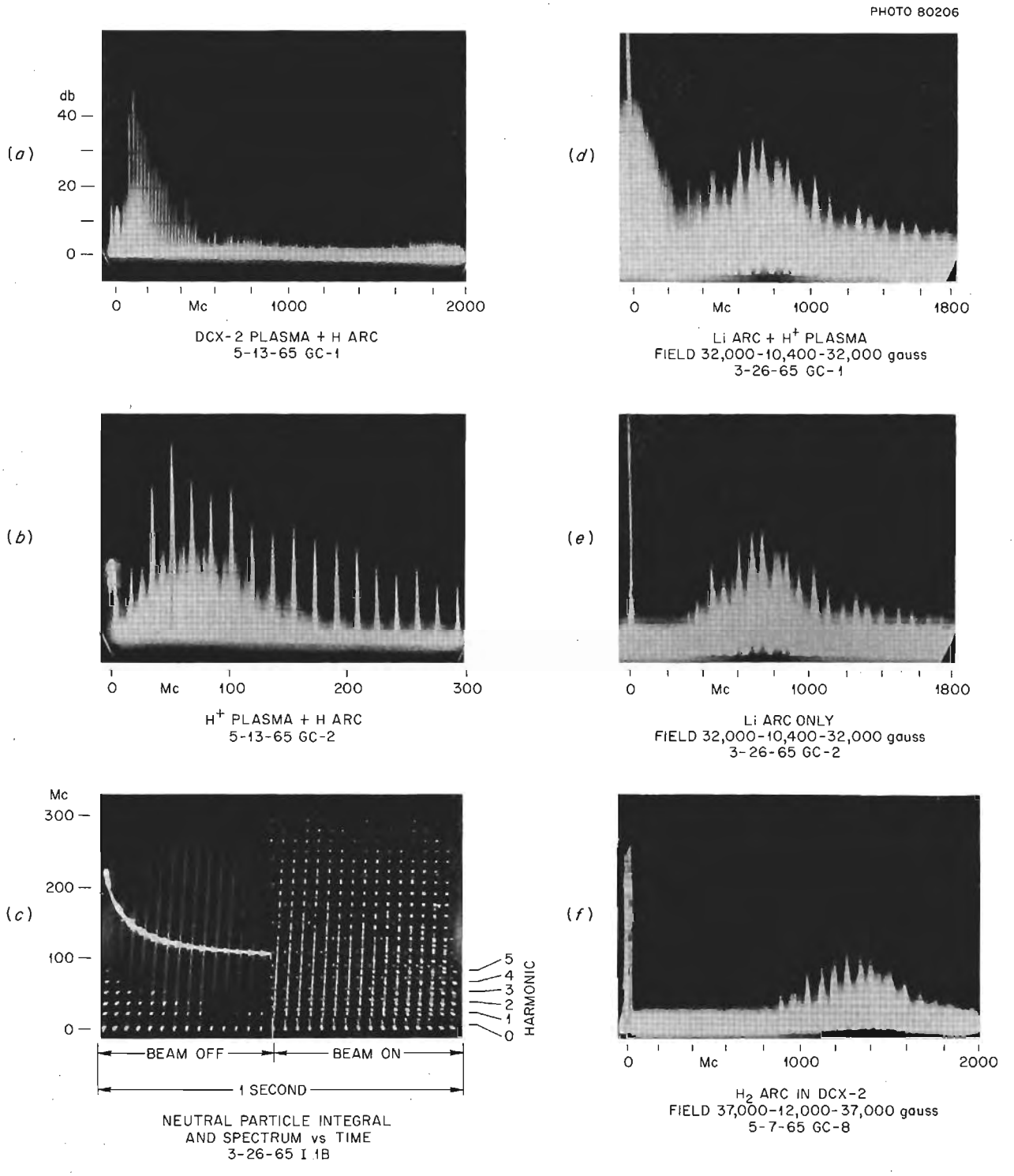

Fig. 2.7. RF Spectra From DCX-2 Plasma. The amplitude scale is logarithmic with 1 decade per division. The spectrum (c) is a frequency-time plot with an integral of the charge-exchange neutral current superimposed. The integral increases downward. The spectrum was made by deflecting the oscilloscope beam vertically while intensely modulating the beam with the spectrometer output.

since the outer shield extended inward some distance beyond its last attachment to the DCX-2 liner, and the RF 71 B/U cable from the machine to the control room was 125 ft long. A fixed rf probe with better properties, connected by 125 ft of Andrews HJ4-50 cable, is shown in Fig. 2.9. The spectrum in Fig. 2.8c was obtained with this probe and should be compared with Fig. 2.7*f*.

A movable probe was prepared (Fig. 2.10) and provided with a graphite grounding plug in hopes of preventing the resonance of the whole probe as a grounded antenna. In order to test the response of the probe, an oscillator was attached to a short transmitting antenna placed alongside the probe in a section of metal sheet to serve as a ground plane. The oscillator was swept through its range at approximately constant output, and the results are shown in Fig. 2.11*a*. The trace should have produced a linear increase since both antennas are short and the response of the spectrometer is logarithmic. The strong peak and dip above 600 Mc are due to the resonance of the cavity in the reentrant port plug. A much shorter reentrant plug, whose bottom was at the position of the dotted line in Fig. 2.10, was substituted, and the cavity region was filled with bronze wool. The resonance was much improved, as shown in Fig. 2.11*b*. Unfortunately, this probe was quite unsuccessful, as is shown in the spectrum series (Fig. 2.12). Prominent resonances were obtained as the probe was extended into the liner. A plot is shown in Fig. 2.13. The peaks are at odd quarter wavelengths of probe length, showing that the signal into the cable corresponds, as it should, to the current near the end of the extended part of the whole probe shaft. The distance from the zero position (with the tip of the probe antenna at the liner wall) to the intersection of the extension of lines fitted to the points is about 4 cm, while the actual minimum length of the probe from the graphite plug to the antenna tip was 3.7 cm. This check shows that the whole probe is involved in the resonance.

Effects of this sort are a serious limitation on measurement of plasma rf spectra at high frequencies. A new probe with a $5\frac{1}{2}$-in.-diam outer shell, coupled closely to the liner wall where it enters, is being prepared in an attempt to reduce the probe resonance while permitting a movable probe.

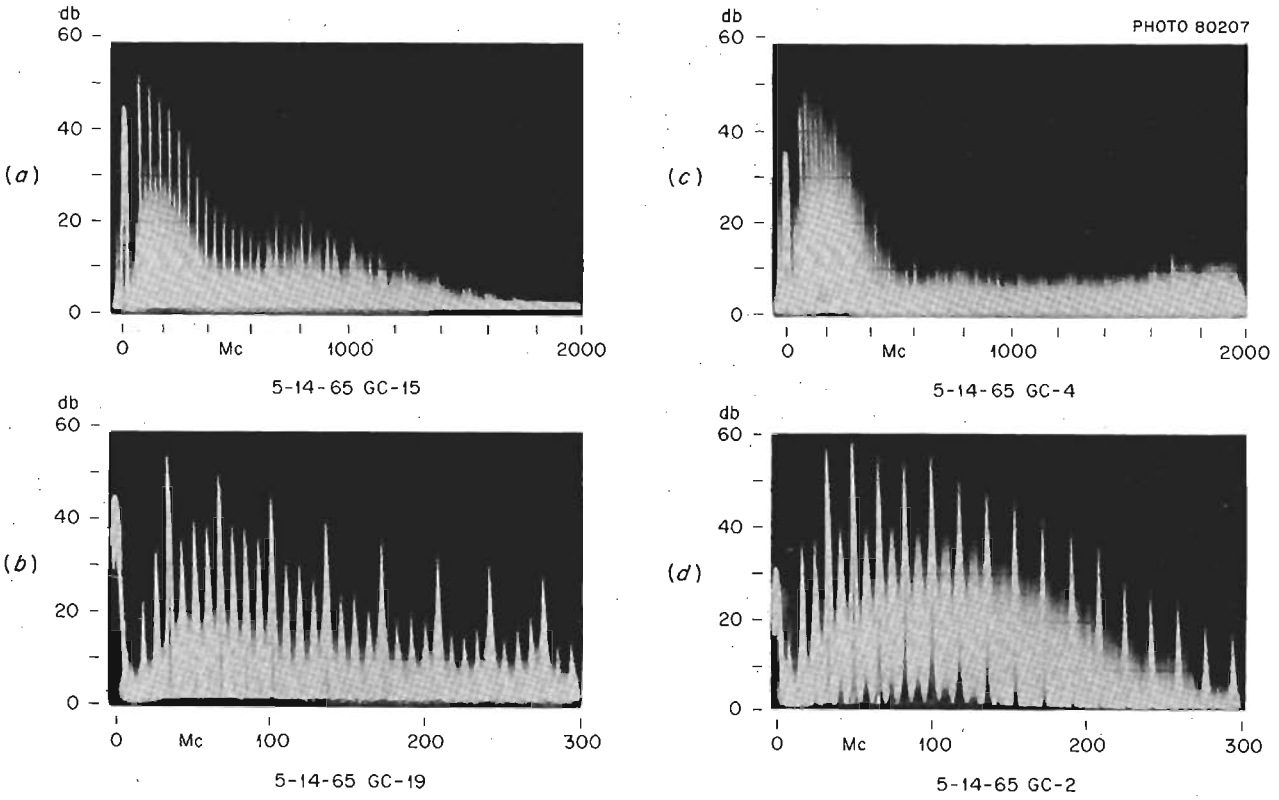

Fig. 2.8. Comparison of RF Spectra with Gas Dissociation and H_2 Arc Dissociation. (*a*) and (*b*) are dissociation by hydrogen gas; (*c*) and (*d*) are dissociation in the hydrogen arc.

ORNL-DWG 65-7481A

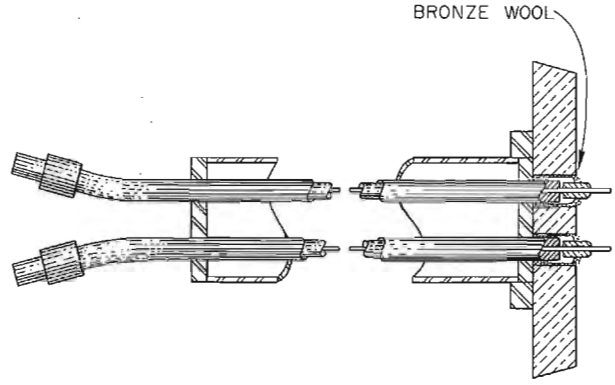

Fig. 2.9. Broadband Radial Electric RF Probe, 0–3 Gc.

ORNL-DWG 65-7482A

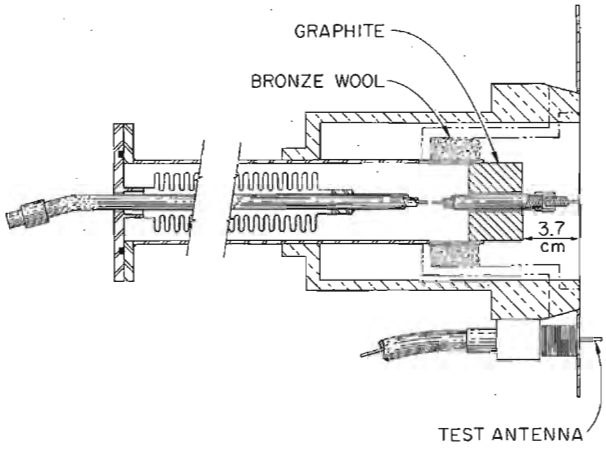

Fig. 2.10. Unsuccessful Movable RF Electric Probe. This probe shows strong external resonances.

PHOTO 80208

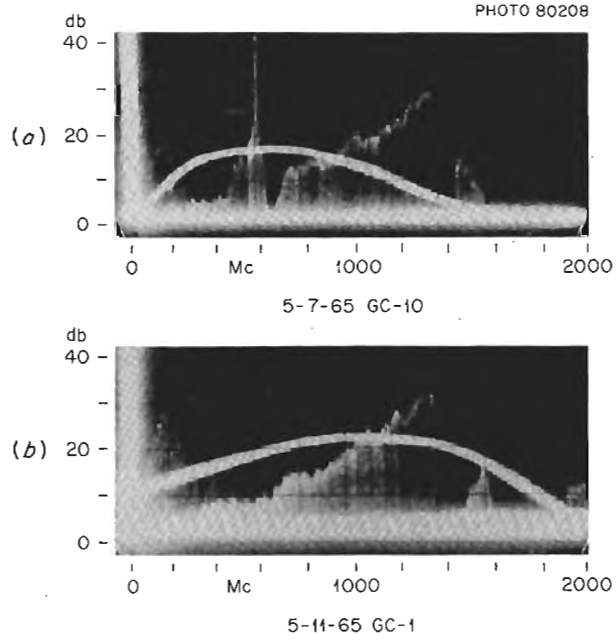

Fig. 2.11. Test of RF Probe of Fig. 2.10 at Minimum Extension. Transmission from an adjacent, fixed short probe. (*a*) Deep reentrant port plug; (*b*) short reentrant port plug filled with bronze wool.

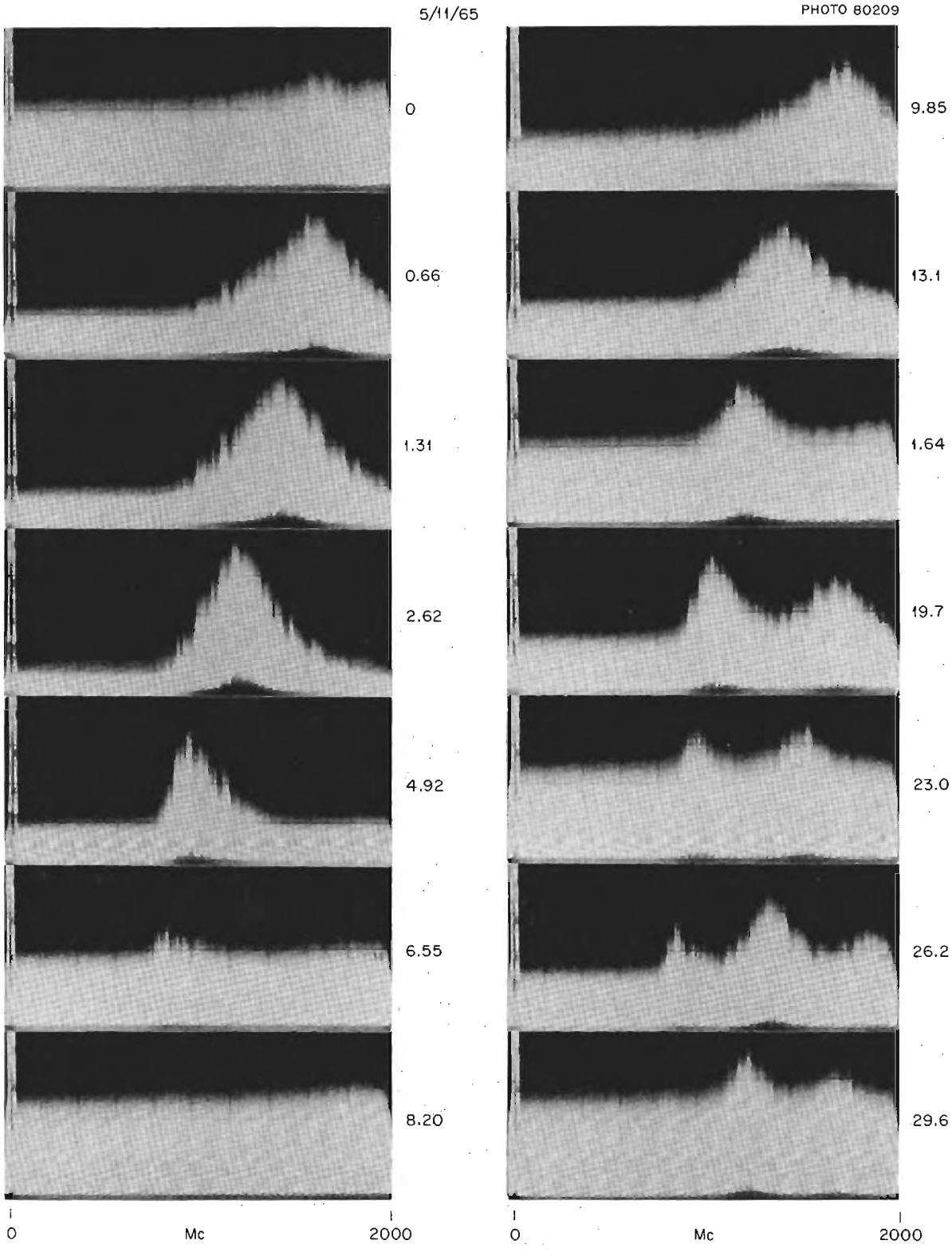

Fig. 2.12. Response of the Probe of Fig. 2.10 to the White Noise from a Hydrogen Arc. The numbers beside the traces indicate the length of extension beyond minimum extension in centimeters.

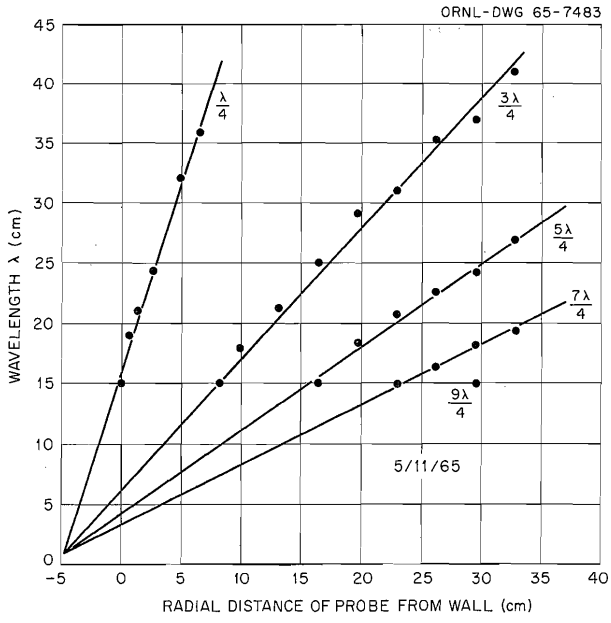

Fig. 2.13. Plot of Wavelengths Corresponding to the Peaks in Fig. 2.11 vs Probe Extension Beyond Minimum.

2.6 CENTRAL-PEAK AND SIDE-LOBE PLASMAS

The energy analyzers described previously[2] were used again to determine the energy spectrum, the radial distribution, and the distribution of pitch angles of the energetic proton plasma by sorting the charge-exchange neutrals in energy and angle of incidence upon the detector. The terms "parallel slit" and "perpendicular slit" in describing the energy analyzer scans designate the direction of the slit relative to the direction of the magnetic field.

To study the two separate energetic-ion groups in the DCX-2 plasma, energy-resolved parallel-slit scans were made with a bar across the collimating slit such that only protons with a pitch angle greater than ±3° were counted. Figures 2.14 and 2.15 show parallel-slit scans made with and without the obstructing bar respectively.

The neutral current to the detectors has three components: the 300-kev dissociation neutrals from the beam (broad peak between 30 and 24°), charge exchange in the lithium arc (peak at −6°), and charge exchange in the background gas and cold plasma. The beam dissociation neutrals are seen in both figures (in the energy scans that include 300 kev), since the beam pitch angle is greater than 3° (typically 6 to 7°, but depends on the exact field shape).

Several differences are readily apparent in the two sets of scans and are directly attributable to the differences in the pitch-angle distributions. The plasma seen with the central peak included (Fig. 2.15) has a rather broad peak and extends quite far out in radius (12 in.), while that seen with the central peak blocked (Fig. 2.14) has a sharper peak and is limited to a smaller radius (6 in.). If the charge-exchange background plasma had been uniform, these peaks would be symmetric about an angle corresponding to one Larmor radius from the machine axis. A large peak due to charge exchange in the arc is seen in all of the scans with the central peak included, but is seen only at low energies with the central peak blocked. The mean energy of the trapped particles in the total plasma is much larger than that of the side-lobe plasma alone (747 vs 295 kev), and this is reflected in the slower falloff of count rate with energy seen in Fig. 2.15 as compared with Fig. 2.14. The sharp fall in count rate seen at 30° is due to an acceptance angle cutoff of the detector and not to a boundary of the plasma.

Fluctuations in the current to the foil neutral detectors have been mentioned previously. These fluctuations were studied further using blinders designed to restrict the angular acceptance either to the central peak or to the side lobes. Three detectors spaced axially but at the same azimuthal position were used. A detector in port position 4-8 (ref. 6) accepted particles with pitch angles between 2 and 6°. One in 5-8 accepted 0 to 2°, and one in 6-8 was uncollimated. The results are shown in Fig. 2.16*a* and *b*. The detector looking at the side lobes and the uncollimated detector show essentially identical signals, but there is little correlation with the response from the central-peak plasma. Also, the fluctuations of the signal from the peak are much smaller.

[6]Figure 2.1 in ORNL-3472 is a key to port locations; position 4-8 means ring 4 position 8, etc.

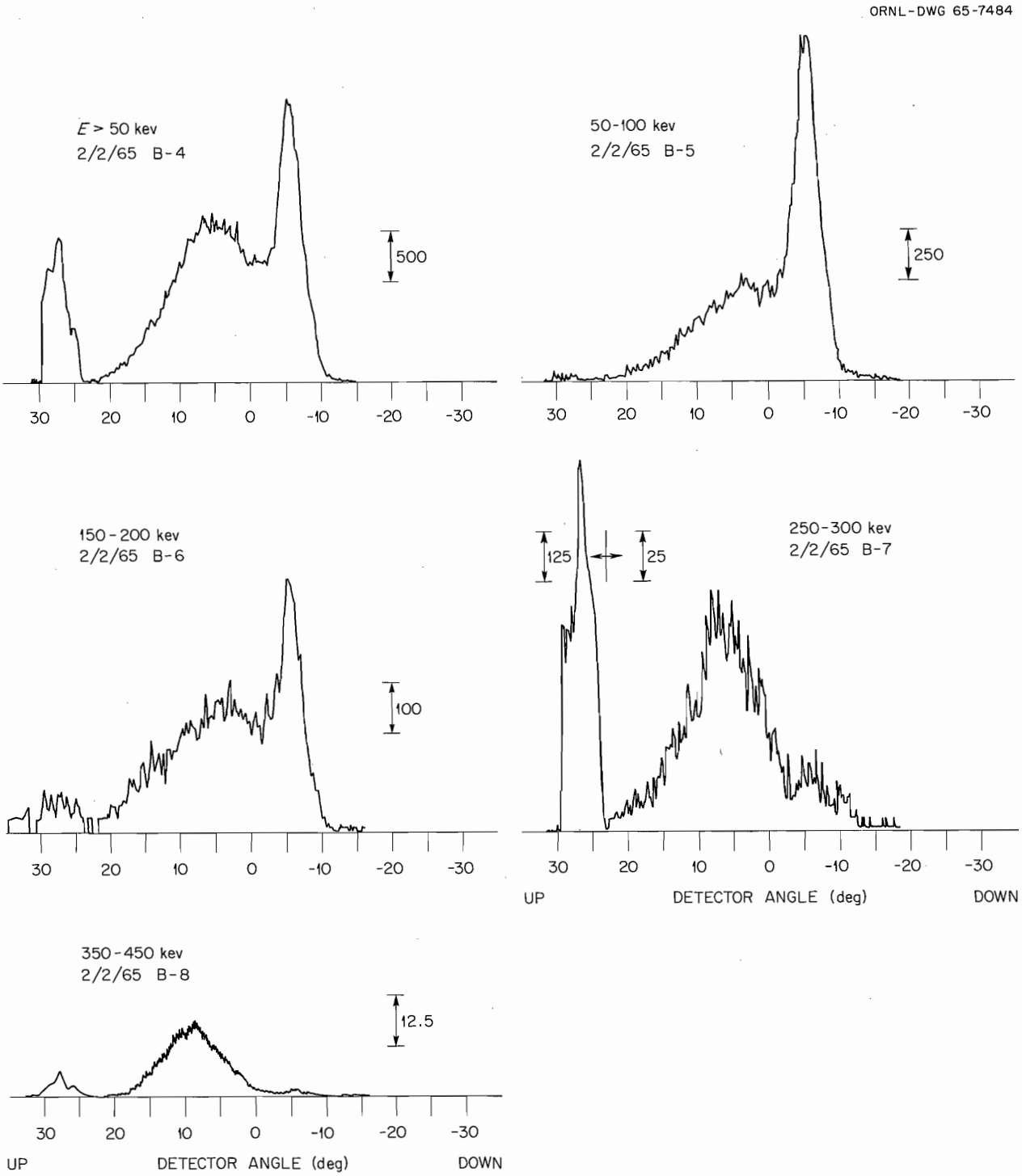

Fig. 2.14. Radial Distribution of Charge-Exchange Current as Seen from Port Position 4-4 with the Central Peak Blocked. These are parallel-slit scans of the side-lobe plasma only. The average energy of this plasma is 295 kev. The relative vertical scales are shown on the individual pictures in counts/sec.

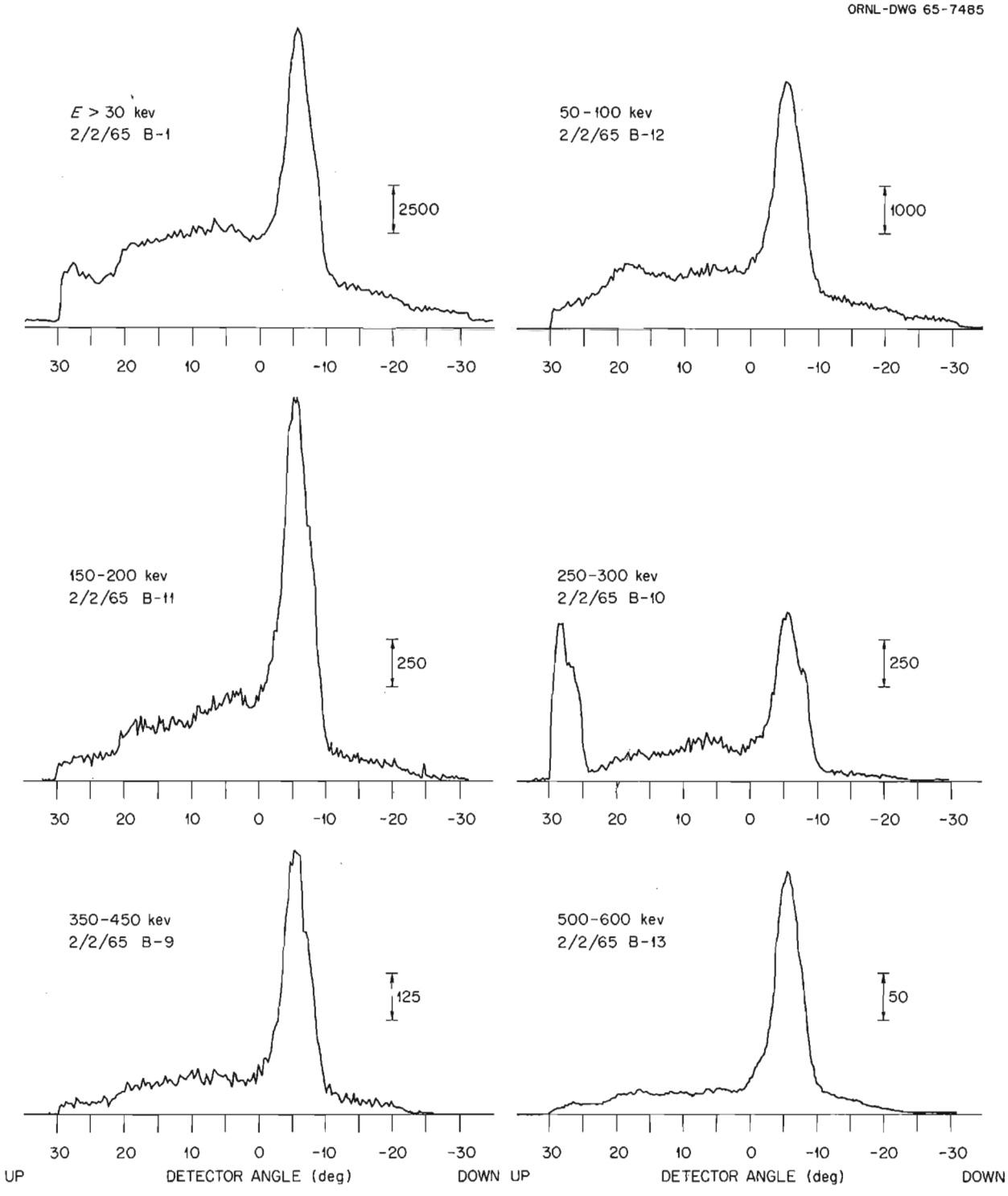

Fig. 2.15. Radial Distribution of Charge-Exchange Current as Seen from Port Position 4-4. These parallel slit scans include both the central peak and side lobe plasmas. The average energy of the trapped plasma is 747 kev. The relative vertical scales are shown on the individual pictures in counts/sec.

PHOTO 80210

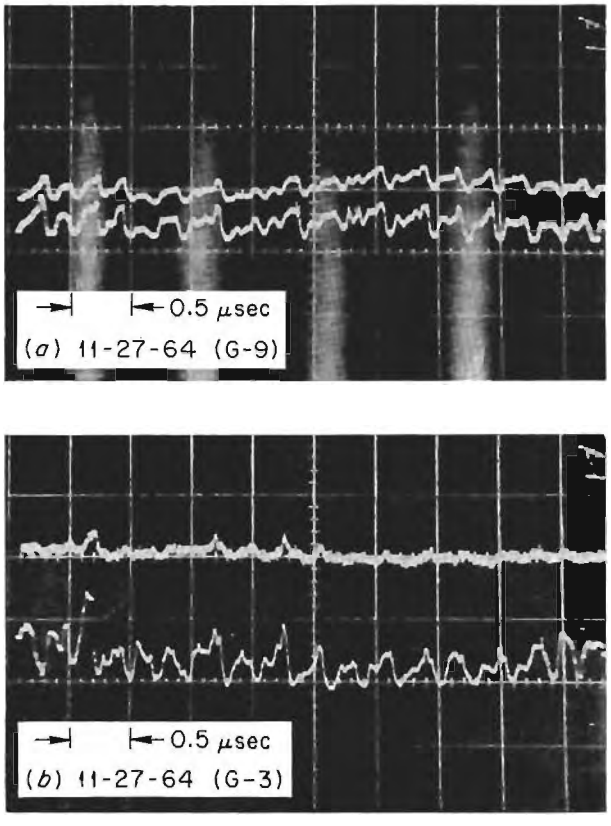

Fig. 2.16. Fluctuations in the Charge-Exchange Current to Neutral Foil Detectors. In (*a*) the upper trace is the response from an uncollimated detector, and the lower trace is the response of a detector collimated to look at the side-lobe plasma. In (*b*) the upper trace is the response from a detector collimated to look at the central-peak plasma, and the lower trace is the same as in (*a*).

2.7 MOLECULAR-ION-BEAM STRUCTURE

Perpendicular-slit scans taken in port positions 2-7 and 3-7 (15 and 29 in. from the injection snout respectively) have disclosed an unsuspected structure to the 600-kev H_2^+ beam. Some typical scans taken in these ports are shown in Fig. 2.17. The beam-pitch-angle structure is most prominent in port positions 2-7 and 3-7 although it is also present in 4-7 and 4-4 and can even be detected in 5-7. Note the sharp beam peaks at certain well-defined pitch angles. The outermost

ORNL-DWG 65-7486

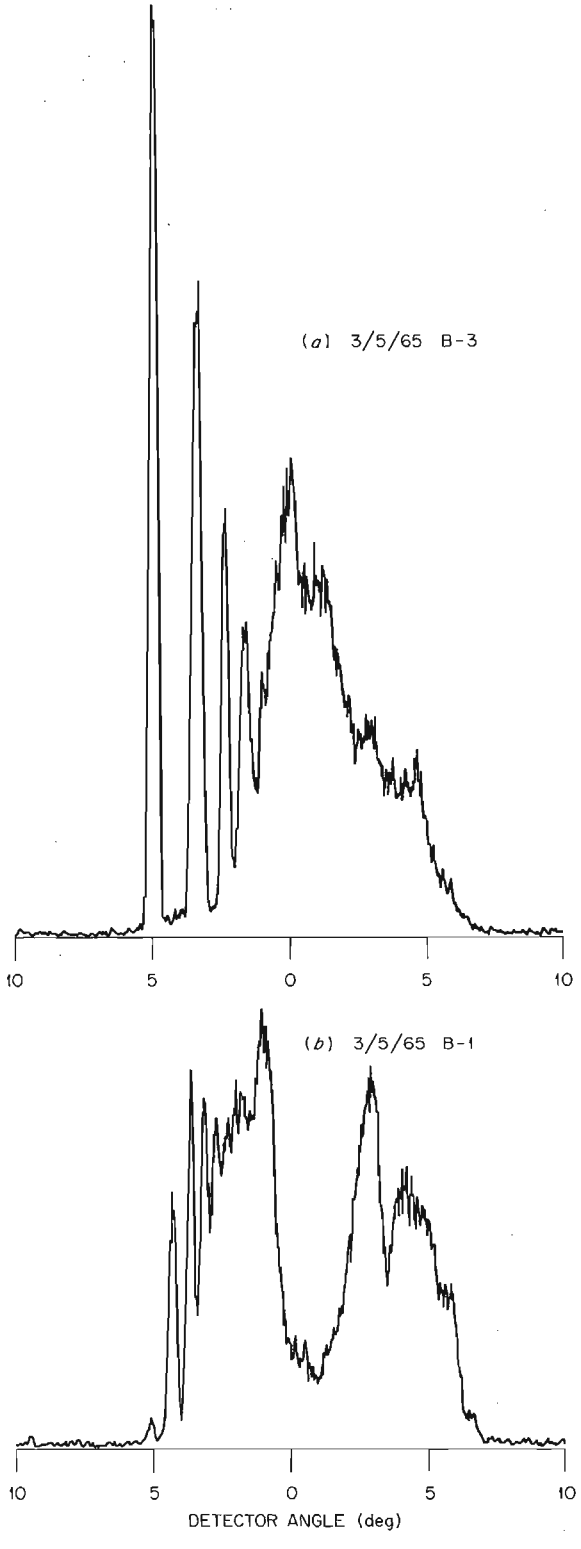

Fig. 2.17. Pitch-Angle Distributions as Seen from Port Positions 2-7 and 3-7. The sharp peaks are caused by the H_2^+ beam.

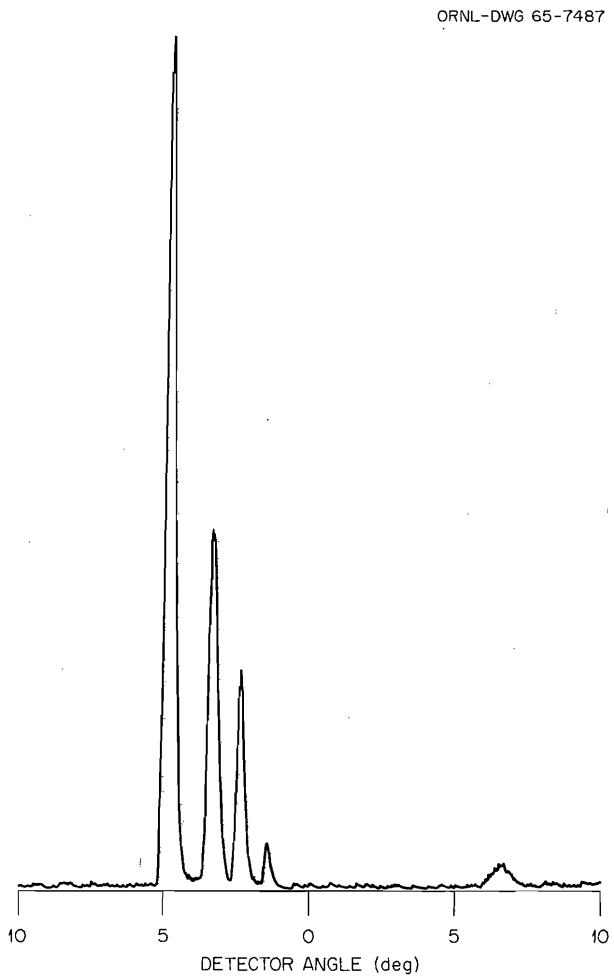

Fig. 2.18. Pitch-Angle Distribution as Seen from Port Position 2-7 with the Downgoing Beam and Plasma Stopped by a Water-Cooled Paddle in Port Position 2-3.

peak in these scans has approximately the same pitch angle (5°), and the spacing between it and the other peaks diminishes as the distance from the snout increases. The pitch angles at which these peaks occur in any one port are approximately fixed, the same values being obtained with gas breakup at beam currents of 3 and 45 ma and with lithium-arc breakup at 45 ma. Pressure variation from 2×10^{-7} to 4×10^{-5} mm Hg does not change these angles, and they are relatively insensitive to changes in the trapped plasma. The beam peaks remain at the same pitch angles even if the beam is stopped after a few turns and the trapped plasma is suppressed (see Fig. 2.18) by the insertion of a large water-cooled paddle into the plasma region. Large changes in the magnetic dip and in the beam lens current have little effect either, although the flat field condition does not seem to affect these angles. Apparently this behavior is not caused by any peculiarity of the energy-sensitive detectors, but rather is a property of the beam. Although this beam structure may have no great effect on the trapping and heating of particles, it is an additional indication that the plasma trapped in DCX-2 is far from simple.

2.8 VACUUM CONDITIONS

In an effort to improve the quality of the vacuum in DCX-2, liquid-nitrogen cooling of the end portions of the inner liner was tried. The base pressure fell from 1.8×10^{-7} to 5×10^{-8} mm Hg, but no significant increase was noted in the trapped-plasma density with lithium-arc dissociation. The pressure change was accounted for principally by a decrease in the partial pressure of water vapor and in hydrogen, which is formed by reaction of the water vapor with the titanium evaporators.

A Veeco Residual-Gas Analyzer is routinely used to monitor the vacuum conditions in DCX-2. Typical mass analyses for both lithium- and hydrogen-arc operation are given in Table 2.2. Lithium-arc operation generally was accompanied by a decrease of pressure in the liner region. Hydrogen-arc operation gave methane increases of 0.5 to 1.5×10^{-7} mm Hg along with the higher organics and water. Although these results are typical for the composition of the background gas measured at the liner walls during this report period, the composition of the cold plasma which provides most of the charge-exchange background may be quite different.

Beam injection appears to be associated with an increase of mass 26 relative to mass 27, which indicates acetylene synthesis ($\Delta p \cong 2$ to 4×10^{-8} mm Hg), and increases of masses 15 and 16, in-

dicating methane generation ($\Delta p \cong 1 \times 10^{-7}$ mm Hg). These increases were also accompanied by generation of CO and CO_2 ($\Delta p \cong 1 \times 10^{-7}$ mm Hg) and other organic compounds ($\Delta p \cong 2 \times 10^{-7}$ mm Hg). Operation of the titanium evaporators has been found to be associated with an increase of hydrogen pressure (especially marked with background water pressures near 10^{-6} mm Hg), a water pressure decrease, marked decrease of air and other inorganic gases (CO_2, CO, N_2, and O_2), and a general decrease in the average molecular weight of organic compounds, with methane occasionally increasing substantially.

Table 2.2. Typical Gas Analyses in DCX-2

Partial pressures in units of 10^{-7} mm Hg uncorrected for ionization efficiency

Type of Species	Li Arc	H_2 Arc
Organic gases	0.4	2.1
Air and other inorganic gases	0.1	3.1
Water vapor	0.8	3.6
Hydrogen	0.2	32.0
Total	2.5	40.8

3. Electron-Cyclotron Heating

3.1 ELECTRON-CYCLOTRON HEATING EXPERIMENTS IN THE EPA FACILITY

W. B. Ard
M. C. Becker[1]
R. A. Dandl[1]
H. O. Eason
A. C. England
G. M. Haas
H. C. Hoy
R. L. Knight
N. H. Lazar
R. L. Livesey
O. D. Matlock
M. W. McGuffin

3.1.1 Introduction

Measurements of the trapped-proton density and lifetime have been made with an energetic neutral beam injected into the electron-cyclotron plasma (ECP). The EPA machine is now undergoing extensive modification involving new coils to improve the field shape and to increase trapping volume.

3.1.2 Neutral-Beam Injection Studies

The 20-kev energetic neutral beam, described in the last two semiannual reports,[2,3] has been used for proton-trapping studies in the ECP in the EPA facility. Presently, up to 40 ma of energetic neutral atoms have been injected into the EPA facility through a 2-in.-diam aperture.

A major change accomplished during the period of this report was to move the neutral-beam center line farther from the magnetic axis of the EPA. The beam center line was shifted to 4 in. from the axis from its old position of 2 in. from the axis. This change allowed protons to be trapped with their guiding centers on the magnetic axis, a condition not possible before. This change was made in hopes that both the proton density and lifetime would increase.

Prior to the moving of the beam, decay times between 100 and 200 μsec were obtained with the beam injected into the ECP. With the beam injected into the machine with no ECP but with the same gas pressure as with the ECP ($\sim 1 \times 10^{-5}$ torr) at the surface of the cavity, a decay time of ~ 10 μsec was observed. This latter decay time is in approximate agreement with the calculated charge-exchange decay time for H^+ in H_2 gas at a gage pressure of 1×10^{-5} torr. Hence, the lifetime appeared to increase by approximately a factor of 10 to 20 with the ECP. As stated previously, this was the expected increase in lifetime if the predominant neutral species in the plasma were fast "Franck-Condon" hydrogen atoms[3] resulting from ionization and dissociation of H_2 by electrons.

With the new beam position, the experiment was repeated with poorer results. A typical decay is shown in Fig. 3.1. The decay time in this figure is ~ 50 μsec, and no decay times longer than this have been seen. Due to the possible presence of stray charged particles entering the detector from the beam tube, as well as to the detector sensitivity, an accurate measurement of the trapped-proton density cannot be given. However, calculations give a lower limit of 10^5 ions/cm^3 for particles whose guiding centers are near the machine axis. The actual density may exceed this by more than an order of magnitude.

---

[1] Instrumentation and Controls Division.

[2] *Thermonuclear Div. Semiann. Progr. Rept. Apr. 30, 1964*, ORNL-3652, sect. 3.1.

[3] *Thermonuclear Div. Semiann. Progr. Rept. Oct. 31, 1964*, ORNL-3760, sect. 3.1.

PHOTO 80172

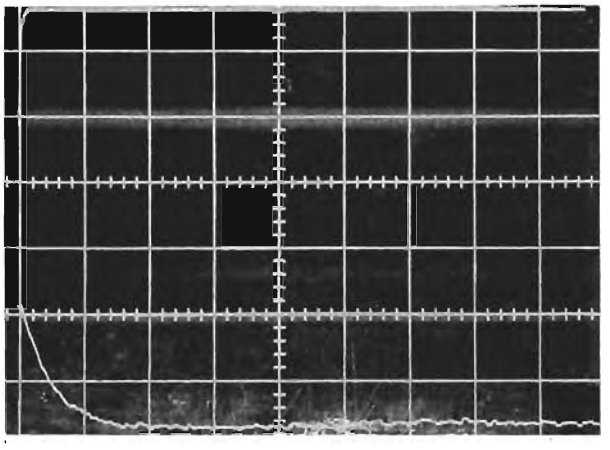

Fig. 3.1. Typical Decay Following Beam Turnoff. The top trace is the beam, and the lower trace is the detector signal. The sweep speed is 100 μsec/cm. The detector views the plasma at a minimum radius of ~7 in. from the axis.

Although, as mentioned above, an absolute value of the density cannot be given at this time, a comparison of the trapped-ion densities with and without the ECP can be made. There is an increase of at least a factor of 10 in the density with the ECP as compared tc the density without the ECP.

3.1.3 Future Modifications

At the present time, the EPA facility is undergoing extensive modifications. The present coils are being replaced with a pair of coils identical to the DCX-1 outboard coils, separated to provide a 2:1 magnetic-mirror field. As a result, there will be less-pronounced radial gradient. With the old coils, calculations showed that 20-kev protons ionized 7 in. or more from the axis were not contained in the machine due to the sharp radial gradient. The new coils will allow particles to be trapped and contained when ionized at least as far out as 12 in.; hence, the trapping volume should increase.

In addition, a beam pulser is being added to allow a periodic beam turnoff. The microwave-cavity ends are being modified to fit the larger magnetic field coils and also to allow the use of an arc.

3.2 ELECTRON-CYCLOTRON HEATING EXPERIMENTS IN THE REDESIGNED ELMO FACILITY

W. B. Ard
M. C. Becker[1]
R. A. Dandl[1]
H. O. Eason
A. C. England
G. M. Haas
R. L. Livesey
M. W. McGuffin

3.2.1 Preliminary Experiments

The ELMO facility was put into operation as a millimeter-wavelength, mirror-contained, electron-cyclotron-plasma generator in late April 1965. The power source consists of two 8-mm, 1-kw continuous-wave (each) traveling-wave-tube oscillators. Presently, the waveguide circuit of these oscillators is padded to permit 1370 w into the plasma cavity under ideal conditions. This arrangement will probably be changed by midsummer. In any event, preliminary experiments have yielded the following observations:

1. The plasma has been formed in the mirror field with up to 1100 w of microwave power.
2. The plasma is formed when using deuterium gas as a feed with the central gage pressure between 0.5 and 2×10^{-5} torr.
3. Hard x rays are emitted by the plasma. The rate of neutron emission from Coulomb dissociation of deuterium is at least two orders of magnitude above that from an equivalent plasma formed with the same amount of power at a 3-cm wavelength.
4. The general operating conditions and ability to match power into the cavity are not significantly different from those observed in the Physics Test Facility (PTF) and the EPA facility.

To date, our diagnostics and those features of the basic devices bearing on them are being debugged, so that insufficient experimental time has been available to permit determination of the temperature, density, and volume of this plasma. Figure 3.2 shows a photograph of the facility as of late 1964.

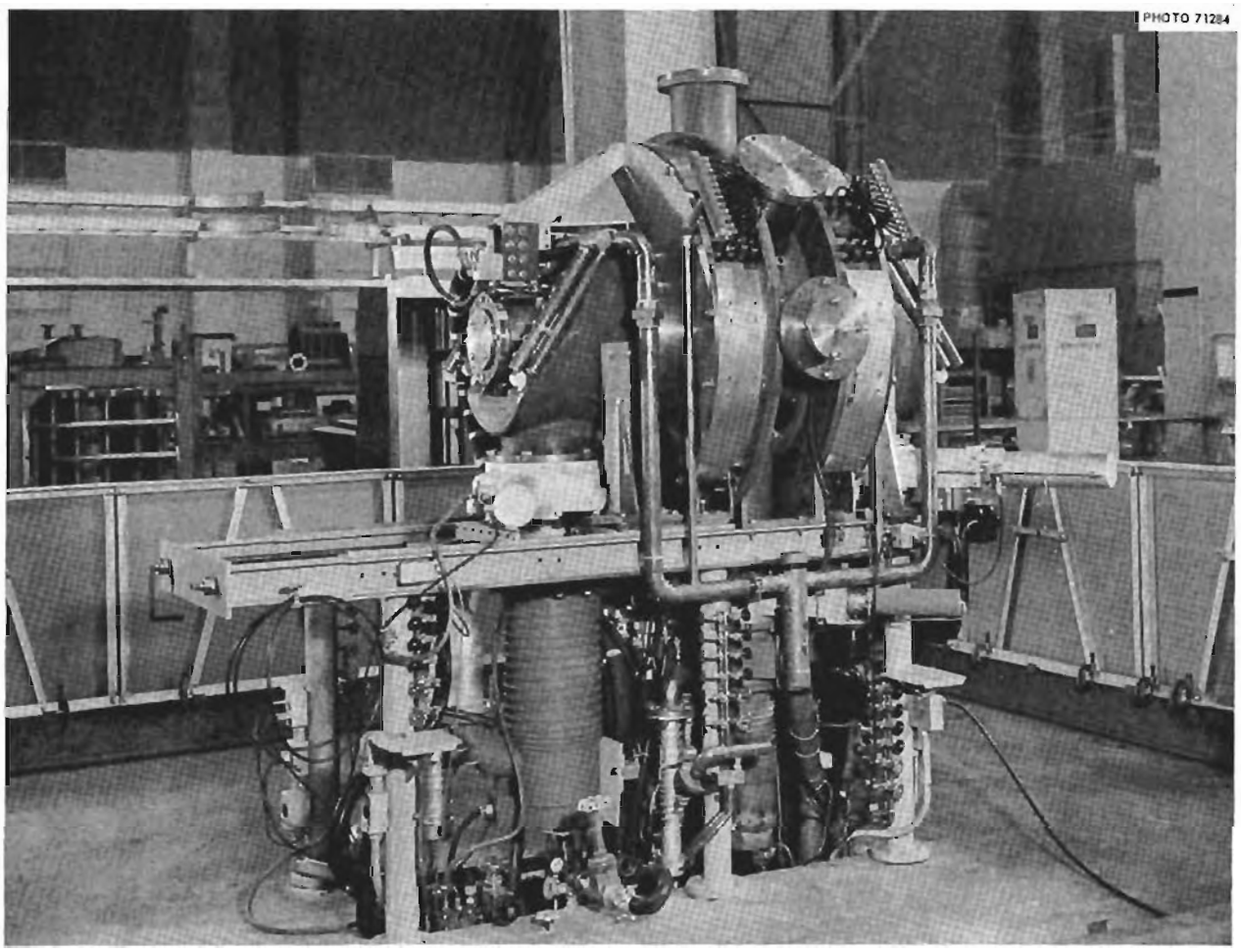

Fig. 3.2. Photograph of the Redesigned ELMO Facility.

3.3 ELECTRON-CYCLOTRON HEATING EXPERIMENTS IN THE PHYSICS TEST FACILITY (PTF)

W. B. Ard
M. C. Becker[1]
R. A. Dandl[1]
H. O. Eason
A. C. England
G. M. Haas
R. L. Livesey
M. W. McGuffin

3.3.1 Instability Studies

The Physics Test Facility (PTF) is currently being used for the investigation of unstable regimes of electron-cyclotron plasmas. It has been known for a long time that, under certain conditions, hot-electron plasmas are subject to instabilities which result in the rapid loss of a considerable fraction of the stored plasma energy. At least two types of instabilities have been observed. One type results in a rapid loss of energetic electrons through the magnetic mirrors. The other results in a loss of energetic electrons across the magnetic field lines. Both types of instability are of rather short duration, less than 50 μsec. Present experiments are directed toward determining the nature of the instabilities and finding what particular properties of the plasma suppress them.

4. Plasma Physics

4.1 BEAM-PLASMA INTERACTION EXPERIMENTS

4.1.1 Evidence for Burnout; Plasma Power Measurements

Igor Alexeff R. V. Neidigh
W. D. Jones W. F. Peed

In the last semiannual report[1] we described beam-plasma interaction experiments in the Burnout series of devices and cited some evidence for a highly ionized and somewhat warmed-up plasma. The report continues and now includes additional evidence for near-total ionization and heating in Burnout IV and some preliminary Burnout V data.

The intensity of the neutral-helium spectral line (5876 A) from the Burnout IV plasma is plotted as a function of radius at the midplane in Fig. 4.1. This is an Abel inversion of the raw data and contrasts the light distribution for the relatively cold plasma of the mode I type of discharge and the active mode II plasma. Note that in mode II the intensity on the axis is lower by more than 1000, that is, more than 99.9% ionized.

This spectral line of ionic helium was observed by using a band-pass filter in the optical system. We did not have the proper filter combination to observe a single ion line without some adjacent neutral spectra, so both ion and some neutral spectra are plotted similarly in Fig. 4.2. It is significant that the mode I intensity is less than mode II at radii greater than 1 in. If the neutral spectra could be subtracted out, the contrast would be even greater, and the cross-over would move closer to the axis. Absolute intensities are not significant in mode II, since much of the helium must be completely stripped of electrons. Some stripping is indicated by analysis of the background ions using the velocity-selector analyzer.[2] Peaks are observed at He^+ and He^{2+} with about equal amplitudes.

Burnout and subsequent heating at larger-than-beam radii by further increase in beam power appears possible in the mode II plasma. When deuterium gas is used, the analyzer has shown that a 65–75 ev "pocket" of long-lived background deuterons appears at the onset of mode II.[1] The energy of this pocket is determined by the combined effect of multiple-scattering and charge-exchange losses. Ions are more effective scatterers ($2\sqrt{2}$) than neutrals, so the loss by scattering is slightly increased, but the charge-exchange loss is considerably decreased by the depletion of the neutrals. Both effects cause the pocket of long-lived ions to shift to higher energy. Reference to Fig. 4.3 will show how this is possible. The figure also shows that a neutral-density depletion factor of 2000 is required to move the energy pocket up to the 1-kev value observed in Burnout IV. Again, this is a 99.9% increase in ionization over that obtained at the perimeter of the plasma at the onset of mode II. The conclusion is that once the mode II is obtained, additional beam power does indeed cause the near-complete ionization in the beam volume to spread, filling the entire anode cavity and, in addition, raising the ion temperature.

Duration of the decay of the Burnout IV plasma is largely dependent on the influx of neutral gas after power turnoff. We are presently experimenting with a valve on the gas feed to control this neutral influx. The maximum duration of the plasma rf signals that we have seen thus far has been 0.010 sec.

---

[1] *Thermonuclear Div. Semiann. Progr. Rept. Oct. 31, 1964*, ORNL-3760, sect. 4.1, p. 30.

[2] *Thermonuclear Proj. Semiann. Rept. Jan. 31, 1960*, ORNL-2926, sect. 2.2, p. 30.

In Burnout V we have used deuterium gas feed and monitored neutrons. Upon letting the apparatus down to air, a neutron source was placed at the end-plate positions on the magnetic axis to calibrate the counters and establish the possibility of neutrons arising from the midplane of the apparatus. A BF_3 counter, with cadmium around its moderator and limonite-paraffin blocks to moderate all but the neutrons from directly above, measured the flux. A schematic diagram of the arrangement and a presentation of the data are shown in Fig. 4.4. Note that the count rate at *C* obtained from the experiment and normalized at *AK* is greater than that from the sources at 1 and 3. The difference represents a source strength of about 6×10^5 neutrons/sec.

More than 90% of the beam power in Burnout V has now been accounted for by observing the temperature rise in the water used to cool the different parts of the apparatus. An example of the Burnout V power distribution compared with that of Burnout IV is shown in Table 4.1. Note that at least 45% of the Burnout V beam power is lost in the end plates, compared to less than 10% in Burnout IV. This may account for the failure of Burnout V to achieve the 100-kw beam power anticipated. Sixty kilowatts (20 kv, 3 amp) has been attained on a few occasions. The limitations appear to be partly due to insufficient axial space outside the mirrors and heavy-ion impurities. Power distribution in Table 4.1 also indicates less-than-desirable reflection of the electron beam.

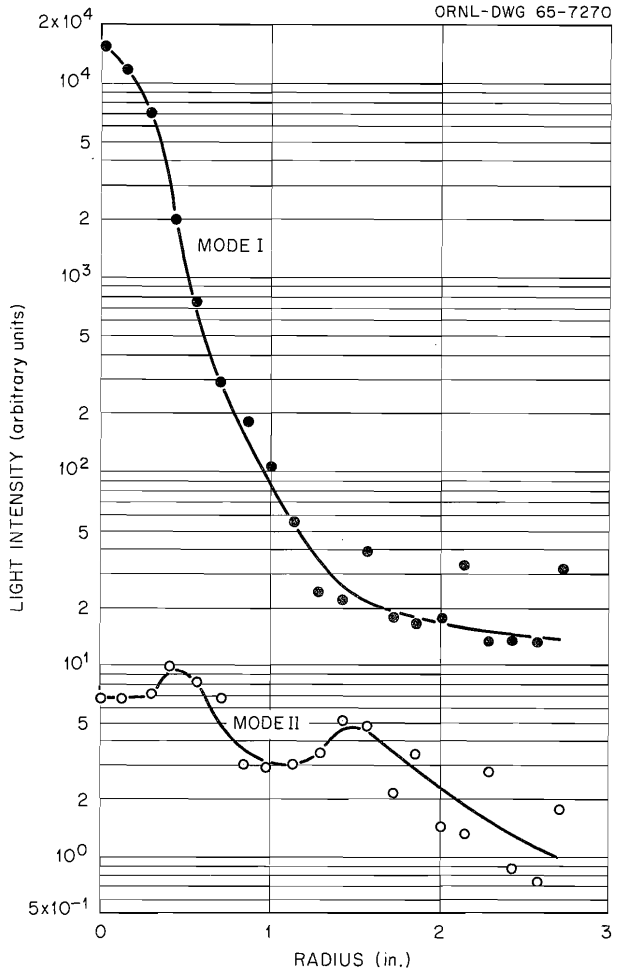

Fig. 4.1. Burnout IV, Helium Discharge, Neutral Light. The intensity of the 5876-A spectral line of helium is plotted as a function of radius. Zero is on the axis. All radii are in the midplane.

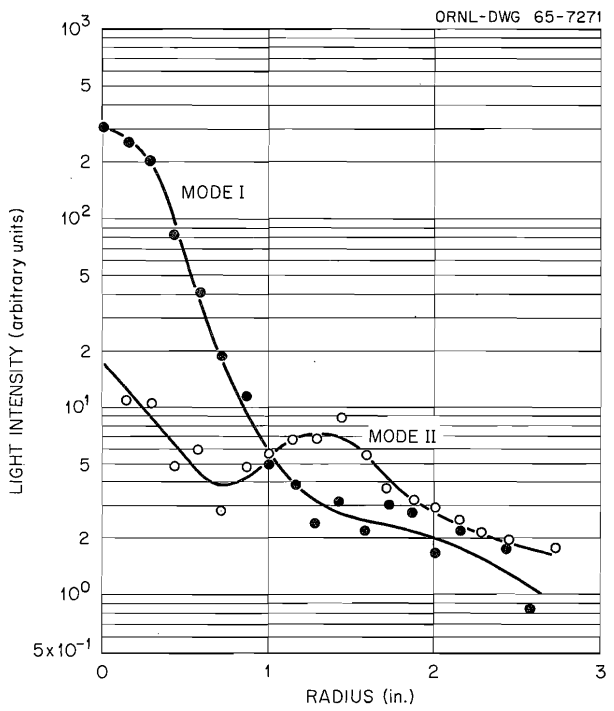

Fig. 4.2. Burnout IV, Helium Discharge, Ion plus Neutral Light. Zero is on the axis. All radii are in the midplane.

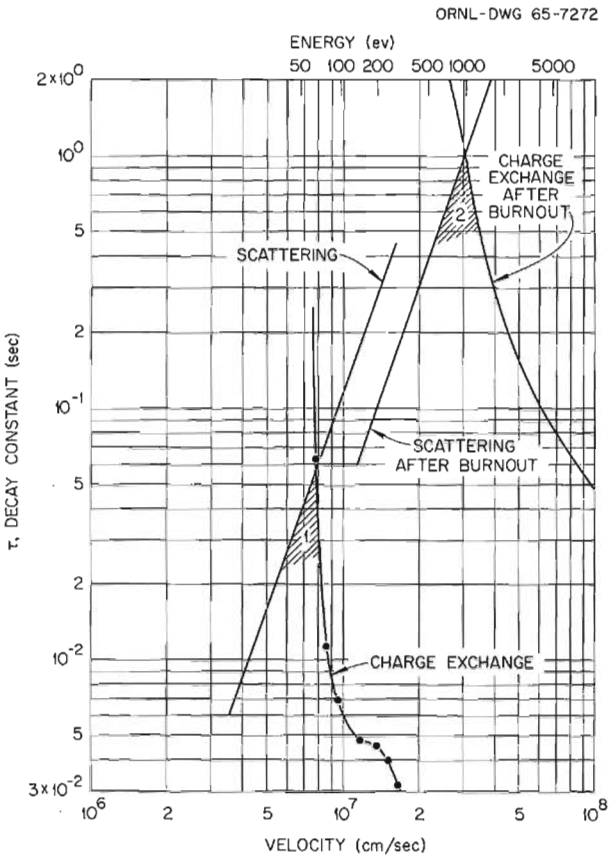

Fig. 4.3. Burnout IV. The calculated plasma decay constant τ for charge-exchange and multiple-scattering loss processes. The "pocket" at 1 is calculated for a neutral pressure of 10^{-5} torr. At 2 ion-ion scattering is assumed, and charge-exchange losses are reduced until the pocket is at 1000 ev as observed experimentally.

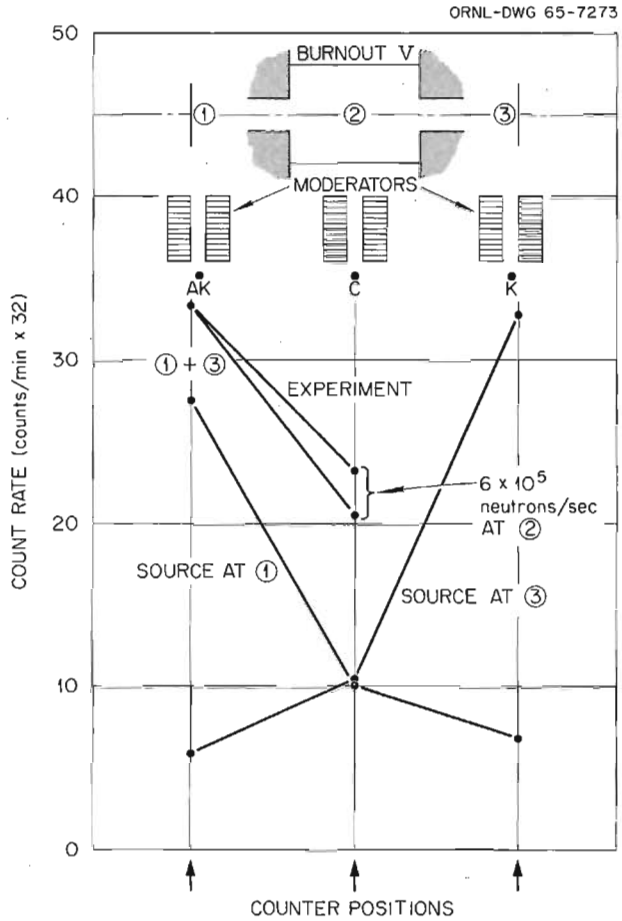

Fig. 4.4. Burnout V Schematic and Neutron-Source Intensities. The moderator was limonite-paraffin blocks. The BF_3 counters were at *AK*, *C*, and *K* positions. The paraffin moderator of the counter was covered with cadmium.

Table 4.1. Comparison of Power Distribution in Burnout V with That of Burnout IV

Position	Distribution (%)	
	Burnout IV	Burnout V
Cathode end plate	4	18
Cathode end of liner	40	13.5
Midplane liner	13	8.7
Anticathode end of liner	40	24.5
Anticathode end plate	3	27.5

4.1.2 Microwave-Cutoff Experiments in Burnout V

Igor Alexeff R. V. Neidigh
W. D. Jones W. F. Peed

Cold-plasma theory predicts that if electromagnetic radiation in the so-called QT-O mode is incident upon a plasma, cutoff will occur in the transmission path when the local electron-plasma frequency becomes higher than the frequency of the incident electromagnetic radiation.[3] For

[3] T. H. Stix, *The Theory of Plasma Waves*, p. 40, McGraw-Hill, New York, 1962.

standard (3-cm wavelength) X-band radiation, the cutoff density is $\approx 1.2 \times 10^{12}$ cm^{-3}. The object of the present experiment was to try to observe a cutoff of the radiation and thus to obtain a lower limit on the density.

The results were far from being clear cut. For mode I operation we saw what can probably be interpreted as a cutoff: the amount of microwave signal reaching the detector was much less (a factor of 3 or 4) when the plasma was present than when it was absent. The results for mode II operation were completely ambiguous as far as a cutoff interpretation was concerned: instead of the received signal being decreased when the plasma was present, the signal was observed to be increased, sometimes by as much as a factor of 10.

When the 3-cm-wavelength source was replaced by a 12-mm-wavelength source, no cutoff was observed for mode I. This suggests that the mode I density is $<8 \times 10^{12}$ cm^{-3}. For mode II operation, amplification was again observed. All components for this experiment, however, were X-band, except the source, and it is doubtful whether a proper cutoff interpretation of the results could be made since the radiation was quite probably not all in the QT-O mode.

The results of the mode II measurements may possibly be interpreted by assuming that the plasma is acting like an amplifier. In view of current theory for beam-plasma systems, however, this does not seem too unreasonable. Perhaps, therefore, microwave-cutoff experiments are valid only when made on relatively cold, passive systems.

Figure 4.5 shows a block diagram of the experimental setup. The klystron was modulated by the internal oscillator of the lock-in amplifier, so that there was no possibility of frequency drift between the modulated klystron and the lock-in amplifier. Radiation from the plasma itself was so copious that it was necessary to have an attenuator between the plasma and the detector to protect the detector.

An undesirable, but not easily avoidable, feature of this experiment was scattering of the microwave radiation to the detector. The smallness of the ports in the plasma liner which are available for the microwave diagnostics necessitated the use of microwave horns having a small ratio of horn size to wavelength. This led to poor focusing of the microwave beam. In experiments with a mockup of the inner plasma liner, it was found that 90 to 95% of the signal reaching the detector was due to scattering off the liner wall.

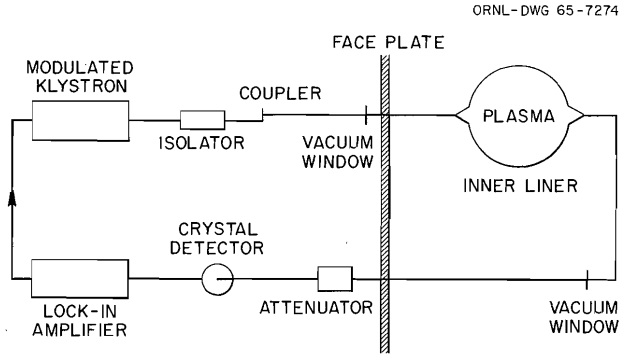

Fig. 4.5. Block Diagram of Apparatus Used to Look for a Microwave-Transmission Cutoff.

4.1.3 Attempts to Measure Plasma Density in Burnout IV with a Gold-Vapor Probe

Igor Alexeff

One possible method of measuring the plasma density in the Burnout machines is by using a jet of gold vapor. Such a technique was used earlier with the hot-electron plasma.[4] However, in this burnout work, the plasma is enclosed in a metal cavity that is being severely sputtered by an intense discharge. Therefore, we modified the evaporation geometry to reduce sputtering and consequent destruction of the gold collector. Another objective was to prevent much gold from entering the plasma cavity, where the gold possibly would be sputtered all around, and eventually appear in the gold detector.

The apparatus used is shown in Fig. 4.6. The gold beam is partly collimated, passes through the plasma, enters a second collimator, and is

[4] *Thermonuclear Div. Semiann. Progr. Rept. Apr. 30, 1963*, ORNL-3472, sect. 3.2.

collected on a microscope cover glass. The procedure was to first condense onto one cover glass with no plasma present, move a second cover glass into position and condense with plasma present, and finally put in a third cover glass and condense with no plasma present. All three condensations were made for the same length of time. By comparing the density of the gold film obtained from the second cover glass with the average obtained from the first and third, the amount of gold-beam attenuation produced by the plasma could be computed.

Severe attenuation of the gold beam was observed in our one successful run, which indicates that some strong plasma phenomenon is taking place in Burnout IV. The attenuation observed was a factor of 7, corresponding to a plasma density of from 3×10^{10} to 10^{11} electrons/cm^3. This density is smaller than that obtained by other techniques. However, the high voltage was off at least 3% of the time due to sparking during the long evaporation runs. We do not know how much time is required for the plasma to build up after the voltage is restored, so perhaps the gold passed through when no plasma was present. Careful estimates were made of the effects due to "hardening" of the gold beam, or, in other words, shifting of the velocity spectrum of the gold beam toward higher velocities by attenuation of the slower atoms. This hardening effect was computed to be small.

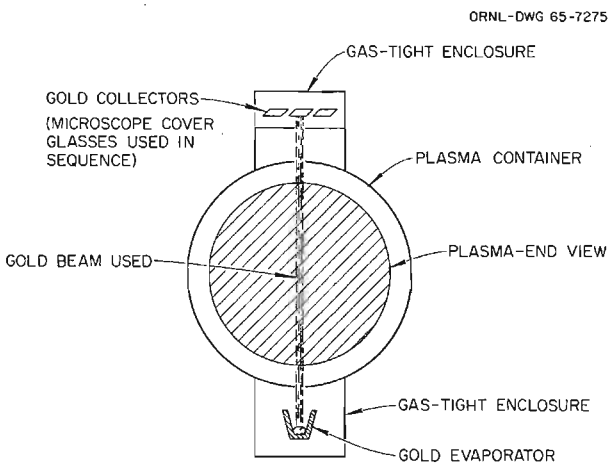

Fig. 4.6. Schematic of Molecular-Gold-Beam Apparatus.

A possible way of securing more reliable results would be to use a lighter element than gold in the molecular beam which would not be as severely attenuated and thus produce results not as susceptible to small effects such as short periods of off time during the run.

4.1.4 Development of a Hot-Electron-Plasma Blanket

V. J. Meece R. V. Neidigh
W. L. Stirling

The mode II reflex discharge has been shown to be an effective means of producing a hot-electron plasma.[5] Electron density in the range of 10^{11} to 10^{12} cm^{-3} at an electron temperature of about 100 kev has been achieved when operating the discharge electrodes on the magnetic axis in a 3:1 mirror system. The present experiment utilizes the mode II reflex discharge in a geometry in which the arc electrodes are mounted off axis. In this method of operation, a blanket or annulus of hot electrons is produced by the azimuthal drift of electrons in the magnetic field gradient.

Figure 4.7 shows a cross-sectional view of the Beam Plasma Facility in which the experiment is run. The axial separation of the magnetic mirrors, 2:1 ratio on axis, is 67 in. The radial displacement of the arc electrodes from the axis is 6 in.; at midplane, the discharge is centered 8.75 in. off axis. The arc operates in a magnetic field region having a 2.3:1 mirror ratio. In all experiments thus far, the anode is 6 in. long and is separated from the cathode by $\frac{5}{8}$ in. Two different anodes have been used, one with a $\frac{1}{2}$-in. inner diameter and the other with a $\frac{3}{8}$-in. inner diameter. There is a grounded $\frac{1}{8}$-in.-thick plate with a hole in it for passage of the discharge column. This plate is 2 in. in front of the anticathode.

Figure 4.8 shows a pinhole-camera picture of the visible light when the discharge is operating in an electron-heating mode. The camera is looking along the axis and is mounted 10 in. off

[5] Igor Alexeff and R. V. Neidigh, *Thermonuclear Div. Semiann. Progr. Rept. Oct. 31, 1963*, ORNL-3564, pp. 51–54.

ORNL-DWG 65-5528

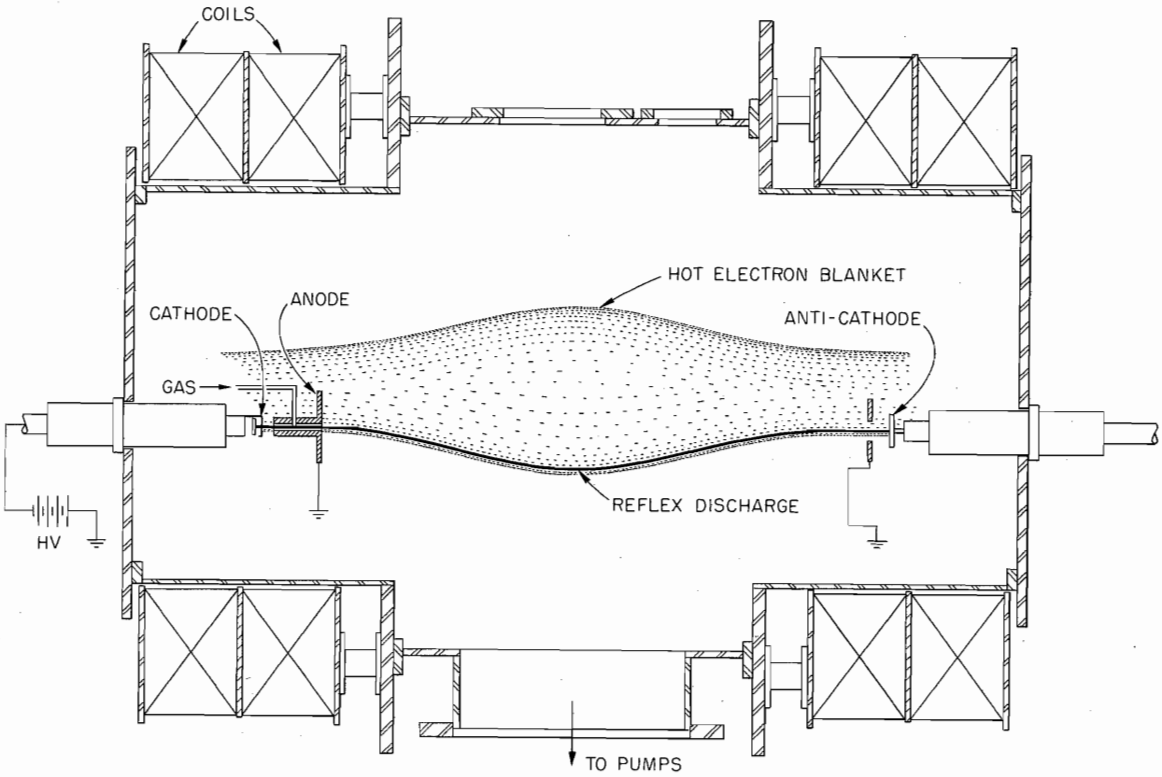

Fig. 4.7. Beam Plasma Facility Axial Cross Section.

axis. Observation tangential to the annulus produces the sharp definition on the right side of the picture. The main discharge column is at the bottom center. In Fig. 4.9, the camera is still 10 in. off axis but is now located directly above the discharge column. Here, a thin tantalum paddle was located on the midplane and was so positioned as to intercept completely that part of the annulus. Since the magnetic field is in the direction of observation, the annulus is produced by the azimuthal drift of electrons in the magnetic field gradient. By observing the intensity of x rays produced for different axial positions of the paddle, it can be shown that the hot electrons originate predominantly in the midplane region.

Four different experiments have been utilized to gain information about the plasma properties. In all experiments, a hydrogen gas arc was used, and the x rays detected by an NaI scintillation spectrometer have been taken as evidence for electron heating.

The paddle experiment, previously mentioned, yielded qualitative information about the buildup of the electron blanket. In addition, the paddle has shown that the maximum x-ray intensity is achieved when the paddle is about 1 in. above the visible plasma glow, which is 2 to 4 cm thick. The x-ray production is stopped when the paddle interrupts even a part of the glowing region (on midplane). Similar behavior is observed when probing radially outward from within the blanket. X-ray intensity is maximum just inside the glow, and production is again stopped upon intercepting the glow.

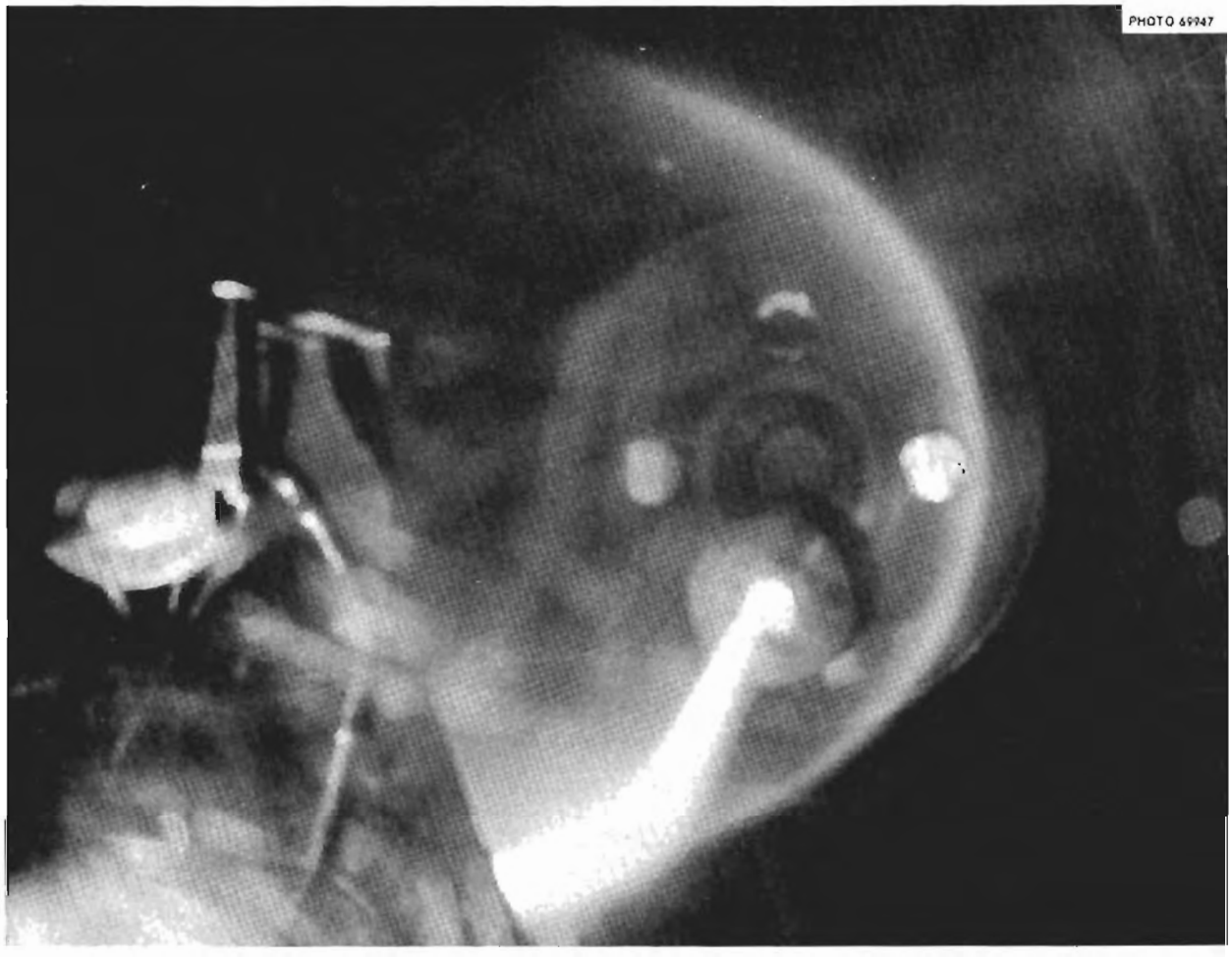

Fig. 4.8. Mode II Reflex Arc and Plasma Annulus.

The second experiment made use of a very fine molybdenum powder which could be dropped through the plasma. Axial movement of the molybdenum shaker showed that the hot electrons existed in a blanket from the midplane origin to the mirror. In Sect. 4.1.5, a calculation based on an assumed equilibrium temperature of the molybdenum particles is presented in which the electron density is determined to be about 2×10^5 to 3×10^5 cm^{-3}. That calculation makes use of an independent measurement of the electron temperature. This temperature was determined in a third set of experiments in which the x-ray detector was collimated to observe only those x rays produced in the midplane region.

Figure 4.10 shows a semilogarithmic plot of the x-ray distribution from the midplane section observed with a multichannel analyzer. A ^{137}Cs spectrum is also shown for energy calibration. Using the slope of the semilogarithmic plot, an electron temperature of 80 kev is determined. More accurately, the ordinate should be multiplied by the channel energy before taking the logarithm. The simpler method used here yields a conservative estimate of the temperature. Knowing the electron temperature, the electron density may be estimated by calculating the total photon energy emitted from the blanket per cubic centimeter per second. Such calculations show that, with the $\frac{1}{2}$-in.-ID anode, the density can be made to vary from 8×10^4 to 5×10^5 cm^{-3}.

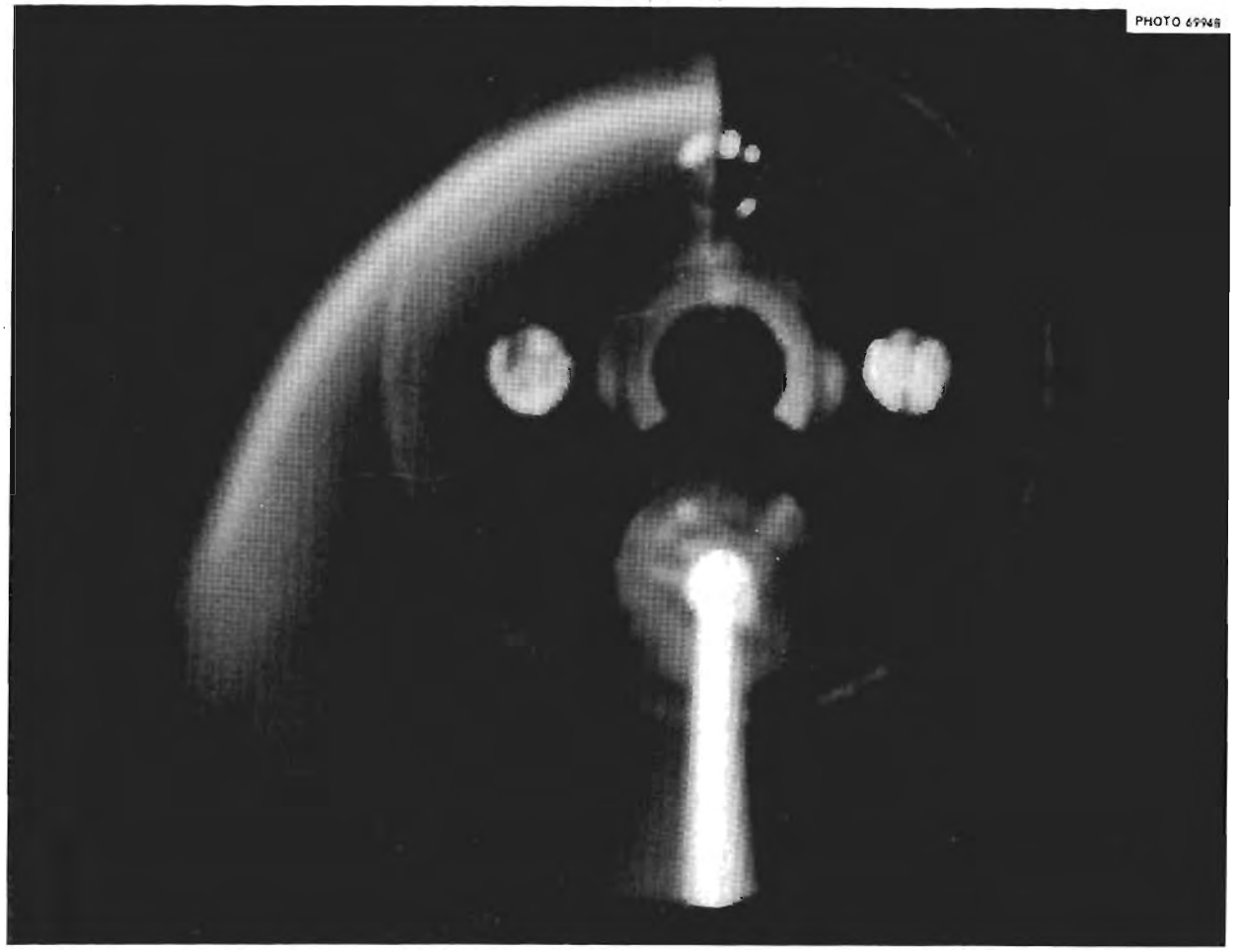

Fig. 4.9. Mode II Reflex Arc and Plasma Annulus with Vertical Paddle.

The fourth experiment was a measurement of the decrease of the x-ray intensity with time after turnoff of the discharge. For such a measurement, the analyzer was operated in the time mode. The discharge was shorted in a time on the order of 1 μsec; simultaneously, the analyzer was gated on for a preset scaling time. Figure 4.11 shows the accumulation of 40 such decay traces. The intensity decreases with a lifetime of about 1.5 sec for some 400 msec, and then drops sharply to background. The general behavior of the decay is the same regardless of the position of the x-ray detector. In some instances, the long-lived portion lasts only 250 msec and the falloff to background is not so rapid. The falloff phenomenon is not understood.

For comparison, the relaxation time for scattering electrons out the mirrors by multiple small-angle collisions was calculated. An electron temperature of 80 kev was used, and the assumption was made that the scattering was due to the neutral background gas. The value obtained is 445 msec, about one-third of the measured lifetime. The agreement is not bad considering the uncertainty in the neutral density and the possibility of error in the electron temperature, which enters the calculation as $(T_e)^{3/2}$. No consideration was made in the calculation for mirror effects such as the fact that the particles undergo scattering through all regions of the mirror and not just at the midplane.

Results from operating the discharge with the $\frac{3}{8}$-in.-ID anode are preliminary. The measured x-ray distribution yields an electron temperature of about 150 kev and a density of about 10^7 cm^{-3}. Efforts are under way to increase further the electron density and to get the discharge to operate in a higher magnetic field than the nominal 2-kilogauss axial midplane value.

ORNL-DWG 65-6630

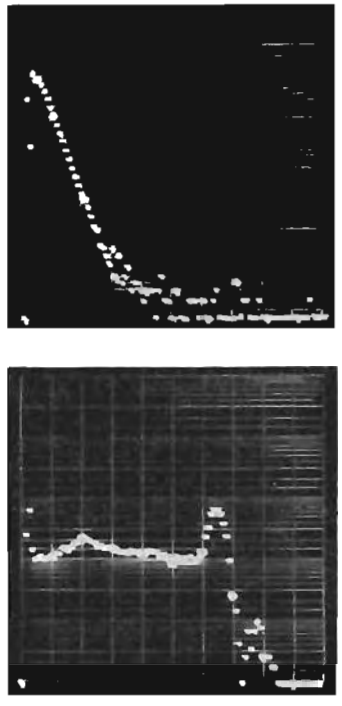

Fig. 4.10. Semilogarithmic Plot of X-Ray Distribution.

ORNL-DWG 65-6631

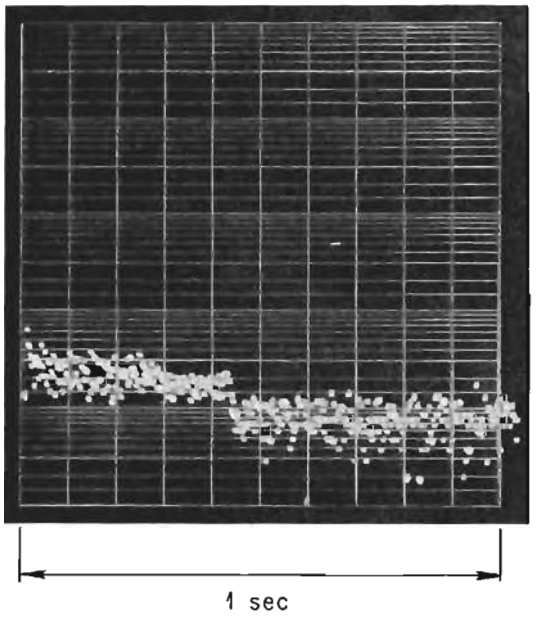

Fig. 4.11. Vertical Paddle Adjusted for Maximum X-Ray Intensity – Detector on East End Aligned with Axis.

4.1.5 Measuring Hot-Electron Density with Molybdenum Dust

Igor Alexeff

In some experiments of Stirling (Sect. 4.1.4), molybdenum dust became incandescent when dropped into the hot-electron plasma produced by a mode II arc. In this calculation, we attempt to use the molybdenum dust as a quantitative tool to measure plasma density.

We first note that the color temperature of the dust does not change appreciably if one or if several dust particles are used. Therefore, we infer that a few particles do not perturb the plasma appreciably. Next, we note that we can estimate the temperature of a particle rather accurately from the color of the emitted light. We can then compute the power radiated per unit area from the particle. Equating this radiated power with the power brought in by bombarding electrons, we obtain a value for a function of electron temperature and density. The numerical relationship used is shown below:

$$W = \alpha\beta T^4 = n_e v_e (m_e v_e^2/2)/4 \ .$$

Here W is the power radiated per unit area, α is the Stefan-Boltzmann radiation constant, β is a correction factor for the emissivity of a molybdenum surface, T is the temperature of the molybdenum particle as estimated from its color, n_e is the electron density, v_e is the average electron velocity, and m_e is the electron mass.

For the above equation, a value for v_e is estimated in two ways: first, from the shape of the x-ray spectrum emitted by the apparatus, and second, by a measurement of the lifetime of the hot electrons, which are lost by gas scattering into the mirror loss cones. The temperature found in the runs concerned (which were early runs) was 50 kev. The density obtained was 2.7×10^5 electrons/cm^3. This number compares reasonably well with the value of 8×10^4 found from the x-ray-photon intensity.

Two factors, either of which could have invalidated the measurement, were: (1) that the electrons were not losing all of their energy in a single collision with a molybdenum dust particle; (2) that the molybdenum dust did not spend enough time in the hot-electron layer to come to thermal equilibrium. A check of the average diameter of the dust particles by use of a microscope gave a value of about 50 μ. Since 50-kev particles can penetrate only about 4 μ of molybdenum, the electrons probably did lose most of their energy in a single collision. A simple calculation shows that the dust particles have ample time to reach thermal equilibrium in their transit through the hot electron layer.

4.2 FURTHER TIME-OF-FLIGHT STUDIES OF IONIC SOUND WAVES

Igor Alexeff W. D. Jones

4.2.1 Introduction

We have continued our investigation of the properties of ionic sound waves propagating in diffusion-type, rare-gas plasmas using the time-of-flight technique.[6] We have been able to show that: (1) the waves can be made to exhibit classical wave-interference effects; (2) the waves propagate in a rectilinear manner; (3) the waves can be focused; (4) the waves do not appear to be reflected from solid surfaces; (5) the waves seem to be very sensitive to the presence of magnetic fields; and (6) the waves experience a cutoff in propagation near the calculated ion-plasma frequency, apparently with no dispersion. In addition to studying these properties of the waves, we have found that much of the background noise in our plasmas is correlated in phase with the 60-cycle filament heating current and thus can be "tuned out" by simple anticoincidence observing.

Figure 4.12 shows the apparatus typically used in our experiments.[6] The measurements are made in a spherical, glass discharge tube about 20 cm in diameter, with background gas pressures ranging from a few tenths of a micron to a few microns. The plasmas in which the waves are propagated are rare-gas plasmas, being formed from the main discharge produced by the anode-cathode assembly seen on the right side of the tube. In these plasmas, the mean free paths of the particles are comparable to the dimensions of the plasma, and $T_e >> T_i$.

[6]Igor Alexeff and W. D. Jones, *Thermonuclear Div. Semiann. Progr. Rept. Oct. 31, 1964*, ORNL-3760, p. 41.

The ionic sound waves are propagated between negatively biased probes. The waves are generated at one of the probes either by voltage pulses or by sinusoidal voltages which produce a time variation of the potential of the probe. The arrival of an ion wave at the second probe is evidenced by a perturbation of the ion current to this probe. Previous measurements[6] have shown that these waves are collisionless, that is, the adiabatic compression coefficient γ of the electron gas is equal to 1.

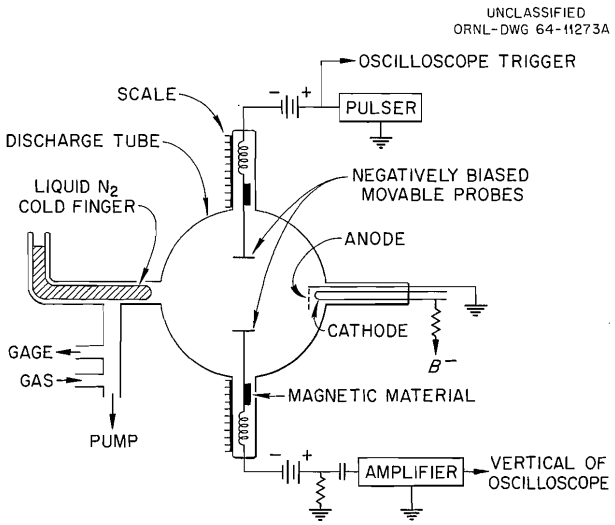

Fig. 4.12. Apparatus Used in Time-of-Flight Studies of Ionic-Sound-Wave Propagation.

4.2.2 Interference Experiments

The interference experiments have been of two kinds. First, we have been able, using two ion-wave sources, to see both constructive and destructive interference of two ion waves at a detector. Second, we have been able to see, under certain conditions, what appears to be an interference phenomenon in the sheath surrounding a single ion-wave source.

As was noted above, our ion-wave sources are simple disc probes which are biased negatively so that they are surrounded by an ion sheath. We have found[6] that if we put a positive voltage step on such a biased probe, an ion wave will be produced whose leading edge is a compression. Similarly, a negative voltage step produces an ion wave whose leading edge is a rarefaction.

In the first experiment, which showed destructive interference, we used two ion-wave sources and one ion-wave detector, or, in other words, an "ion-wave interferometer." By placing a positive voltage step on one of the emitters and a negative voltage step on the other emitter, we could cause a compression wave and a rarefraction wave to arrive at the detector at the same time, thus leading to destructive interference. By varying the relative times of pulsing of the two probes, the interference could be made to take place gradually. This is shown in Fig. 4.13. In this figure, the positive voltage step was always imposed on one of the probes at the same time relative to the triggering of the oscilloscope, giving rise to the positive, stationary pulse seen on the upper trace. The time of negative pulsing of the other probe was varied relative to this time, giving rise to the negative, moving pulse seen on the upper traces. It is noted that maximum interference occurs, not when the two probes are pulsed simultaneously, but rather when the "lower" probe was pulsed somewhat before the "upper" probe. This is because, in this particular experiment, the lower probe was located farther from the detector than was the upper probe, and thus had to be pulsed earlier in order for its wave to arrive at the detector at the same time as the other wave.

As might be expected, if, instead of putting steps of opposite polarity on the two emitters, one puts voltage steps of the same polarity on both emitter probes, then we see constructive interference at the detector rather than destructive interference.

The interference which we think we see in the sheath surrounding a single emitter probe will be discussed now. When we superimpose a voltage step on the probe, we believe that an ion wave is generated instantaneously throughout the sheath. Since the ion-wave velocity is only around 10^5 cm/sec in xenon, for example, it takes around 10 μsec for the wave to propagate completely out of the sheath, which can be a centimeter or more in thickness.[6] Therefore, if a second voltage step of the opposite polarity is placed on the emitter in a time shorter than 10 μsec after the initial pulse, a wave of the opposite kind should be generated throughout the sheath and should partially neutralize or interfere with that part of the first wave still in the sheath. Figure 4.14 seems to verify that this is indeed what happens.

PHOTO P-69117

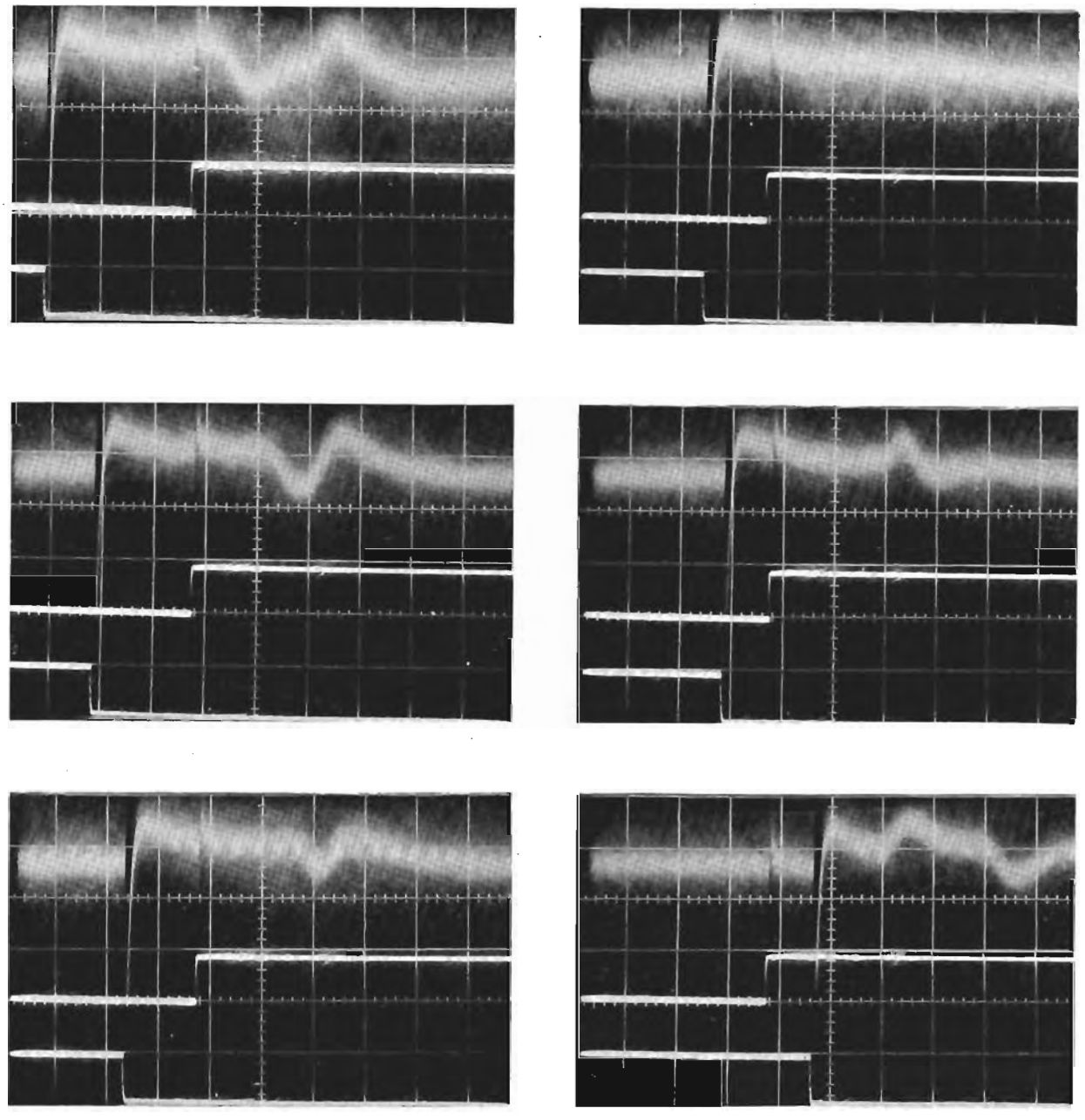

Fig. 4.13. Destructive Interference of Two Ion Waves at the Detector. The upper trace is the signal at the detector probe. The central trace shows a positive step voltage applied to one transmitter probe at a point constant in time. The lower trace shows the negative step voltage applied to the other transmitter at a variable point in time. The upper right-hand picture shows essentially complete destructive interference. The plasma is formed of xenon. The time scale is 20 μsec per large division.

PHOTO P-69115

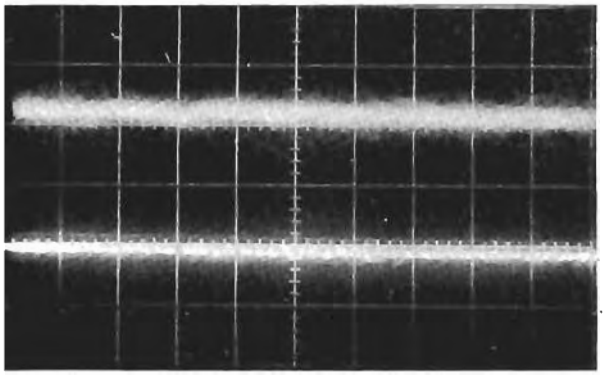

0.1 μsec PULSE

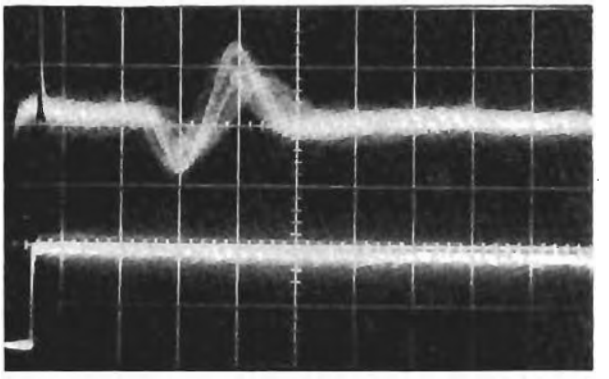

10 μsec

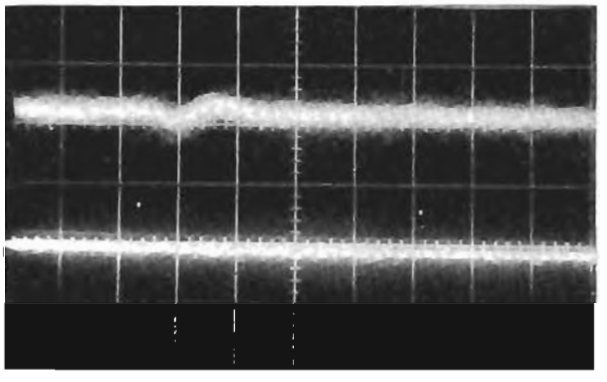

0.25 μsec

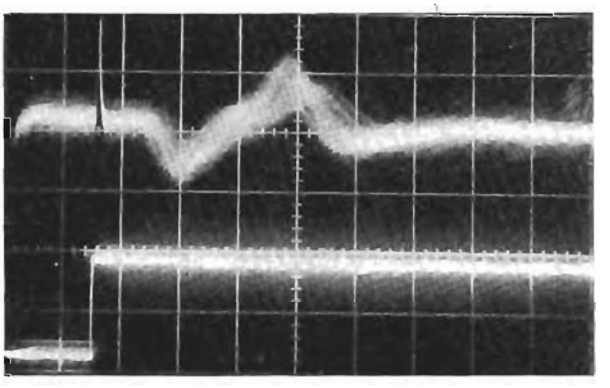

30 μsec

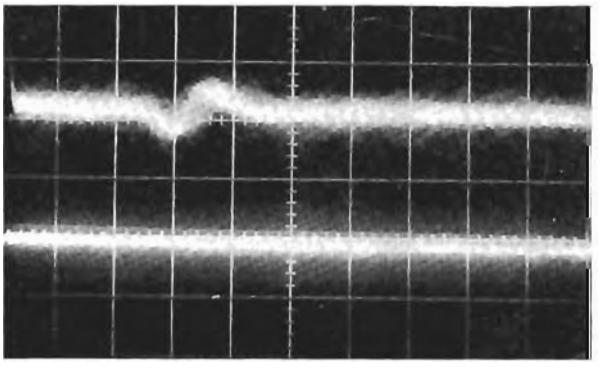

1.0 μsec

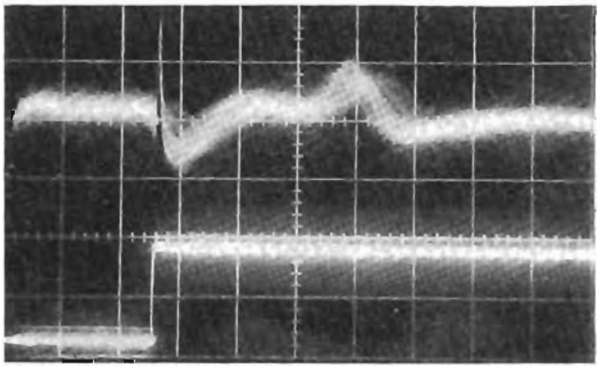

50 μsec

Fig. 4.14. Ion-Wave Interference in the Emitter Sheath. The bottom trace shows the voltage applied to the transmitter probe. The upper trace shows the signal on the receiver probe. Both the negative and the positive voltage transitions of the driving square-wave pulse produce ion waves. When the two transitions are too close together (short pulse), the two resultant ion waves appear to produce destructive interference. The plasma is formed of xenon. The time scale is 20 μsec per large division.

Putting a square wave pulse on the probe is equivalent to superimposing two step voltages of opposite polarity on the probe, separated in time by the length of the pulse. Figure 4.14 shows what happens when a square wave pulse of shorter and shorter duration is placed on the emitter probe. For pulses of long duration, the wave formed in the sheath by the first step of the pulse has plenty of time to get out before the second wave is formed, so that (see lower right photo) the two waves do not interfere. As we make the pulse shorter and shorter, the two waves get closer and closer together. Once the pulse gets shorter than about 10 μsec – the time required for a wave to propagate completely out of the sheath – the two waves begin to interfere. For 0.1-μsec pulses, the interference seems to be complete.

4.2.3 Rectilinear Propagation

That the ion waves propagate in a direct line-of-sight manner was demonstrated by the following experiment. A metal plate, just slightly larger in diameter than the detector probe, was arranged so that it could be rotated into the line of sight between emitter and detector, thus "shadowing" the detector. Figure 4.15 shows the amplitude of the detected signal both with (upper trace) and without (lower trace) the metal plate in the obstructing position. The results seem to be clear cut – the ion waves propagate in a rectilinear manner. The results also demonstrate, incidentally, that we are indeed observing a propagating phenomenon rather than a relaxation phenomenon of some kind in the plasma.

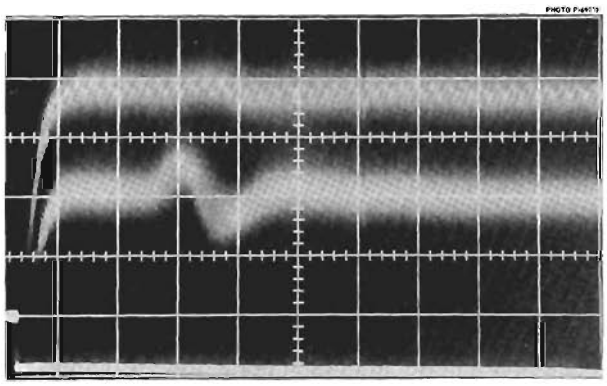

Fig. 4.15. Amplitude of Ion-Wave Signal With (Upper Trace) and Without (Lower Trace) a Metal Plate Obstructing the Rectilinear Flow to the Detector. The plasma is formed of xenon. The time scale is 20 μsec per large division.

4.2.4 Ion-Wave Focusing

Another property of ion waves which we have observed is their ability to be focused. To demonstrate this property, we used a large concave emitter probe and moved a detector probe radially in and out of the optical focus of the concave emitter. Figure 4.16 shows how the amplitude of the ion-wave signal to the detector varied with the radial position of the detector. The data show quite clearly that the waves are focused by the concave emitter.

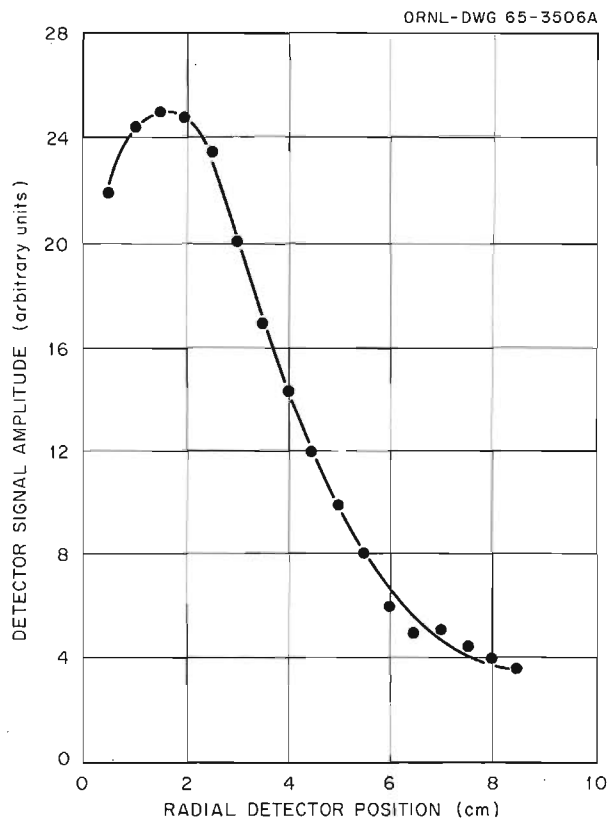

Fig. 4.16. Focusing of Ion Waves.

4.2.5 Reflection Experiments

We have made many unsuccessful efforts to see reflections of ion waves. We have looked for reflections from walls of glass tubes of various shapes as well as from biased and unbiased metal walls. Figure 4.17 shows a typical arrangement used with a spherical tube to look for the reflections. The emitter and detector probes are located roughly at conjugate foci of the reflecting surface. Since this arrangement should virtually eliminate any $1/r^2$ decrease in the ion-wave signals, we conclude that, if the waves are reflected from solid surfaces, it is only very weakly. Taking $1/r^2$ losses into account, we estimate that we should be able to see easily a reflected wave having an amplitude only 1/1000 as large as the ion-wave signals normally detected in ordinary propagation experiments.

ORNL-DWG 65-4602A

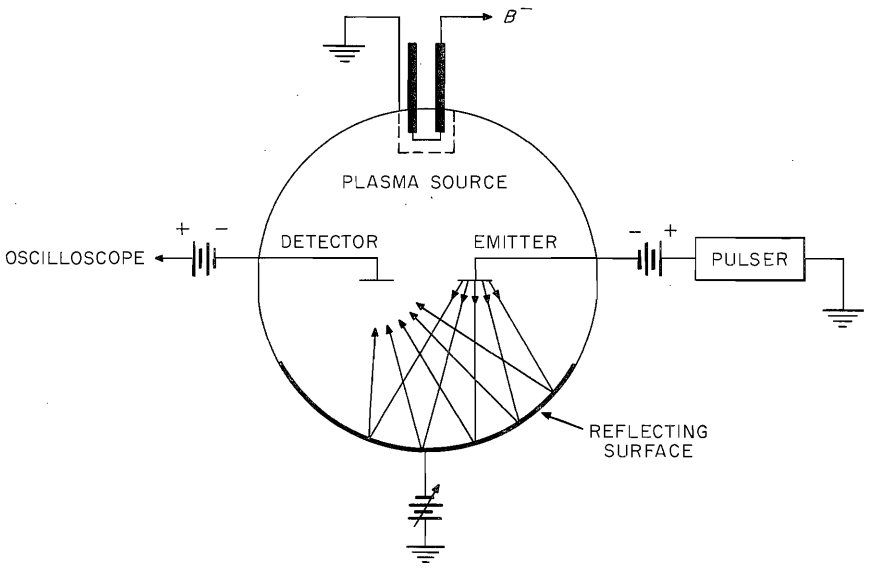

Fig. 4.17. Apparatus Used to Look for Reflection of Ion Waves.

4.2.6 Magnetic Field Effects

For some time we have been puzzled because we could see occasionally what appeared to be two sets of ion waves propagating at the same time – having both different amplitudes and different velocities. We have now found that these effects are due apparently to the magnetic field of the hot-filament cathode. Having learned the explanation of the phenomena, we can now produce equivalent behavior by use of an external bar magnet.

To demonstrate the effects, we arranged the diagnostics so that the oscilloscope and the pulsing equipment could be coherently triggered at any point on the positive or negative half-cycles of the 60-cycle filament heating current. With the anode-cathode assembly rotated so that the filament (a 1-cm-long straight wire) was approximately perpendicular to the path of propagation,

it was found that if we triggered on one half of the cycle we observed an ion-wave signal having a certain amplitude and velocity; if we triggered on the opposite half-cycle we observed an ion-wave signal having a different amplitude and propagation velocity. If we triggered randomly, we saw both signals simultaneously. If the filament were then rotated 90°, so as to be approximately parallel to the propagation path, the two signals became approximately the same, having approximately equal amplitudes and velocities that were intermediate between the values observed when the two signals were unequal.

Thus, in view of the similar effects which can be produced with a bar magnet, it appears that the effects are correlated with the 60-cycle variation of the magnetic field about the filament and occur only for certain orientations of this field relative to the direction of propagation. Since both the filament and the external bar magnet were several centimeters from the propagation path, it would appear that ion waves are extremely sensitive to the presence of magnetic fields.

4.2.7 Anticoincidence Observing

It was discovered that much of our plasma background noise is correlated in phase with the 60-cycle filament heating current. The obvious thing to do, then, is to look at ion-wave propagation only during the quiet parts of the cycle. This is done, in the manner described in the preceding section, by coherently triggering the oscilloscope and pulsing apparatus with the 60-cycle voltage on the filament. By utilizing this technique, we have virtually eliminated any need for coherent-detection techniques[7] in ordinary ionic-sound-wave measurements.

4.2.8 Cutoff and Dispersion Experiments

Theoretically, for plasmas whose $T_e \gg T_i$, the ionic-sound-wave velocity is expected to depend on frequency in the manner shown in Fig. 4.18.[8] Vertically is plotted wave velocity divided by the classical Tonks-Langmuir ionic-sound-wave velocity v_0; horizontally is plotted wave frequency divided by ion-plasma frequency. For frequencies low compared to the ion-plasma frequency, the wave velocity is constant. As the frequency increases toward the ion-plasma frequency, the waves slow down, then cease to propagate. The purpose of these experiments was to try to observe the predicted dispersion and cutoff.

The results have not been completely unambiguous. We have indeed observed a frequency cutoff near the ion-plasma frequency, using both pulse and sinusoidal exciting voltages. The disagreement between experiment and theory varies from a factor of less than 2 to a factor of more than 10, usually being from 3 to 5. We have not, however, observed any dispersion.

Typical pulse results are shown in Fig. 4.19. If a step function is applied to the transmitting probe, we find later in time an ion-wave signal appearing on the receiving probe. A step function of opposite sign produces an ion wave of opposite sign. The point to note is that the rise time of the ion-wave signal is much longer than the rise time of the transmitting step function. We can use the rise time of the received signal to infer the cutoff frequency of the plasma.

A quantitative check of rise time vs plasma density shows that the rise time is a monotonically decreasing function of plasma density, as is expected. However, the cutoff frequency, as inferred from the pulse data, is lower than the ion-plasma frequency by about an average factor of 4, ranging from a factor of 1.5 to a factor of 10.

One possibility why the cutoff frequency observed by pulse techniques is too low is that the high-frequency components can be lost by dispersion, as well as by attenuation. Therefore, we repeated the experiment with sine waves. This technique should yield a cutoff not sensitive to dispersion. Figure 4.20 shows a typical response of the system to a sinusoidal driving signal. The lower trace shows coherent bursts of sine waves superimposed on the transmitting probe, while the upper trace shows the signal at the receiving probe. The received signal has two components – a rapidly propagating component due to electrostatic coupling, and the slowly propagating ion-wave component. Obviously, the ion-wave component must be separated from the direct-coupled signal by a time-of-flight technique. Thus, coherent sine-wave bursts were used rather than continuous sine-wave transmission.

[7] Igor Alexeff and W. D. Jones, *Themonuclear Div. Semiann. Progr. Rept. Oct. 31, 1964*, ORNL-3760, p. 39.

[8] Lyman Spitzer, Jr., *Physics of Fully Ionized Gases*, 2d ed., p. 60, Eq. (3-23), Interscience, New York, 1962.

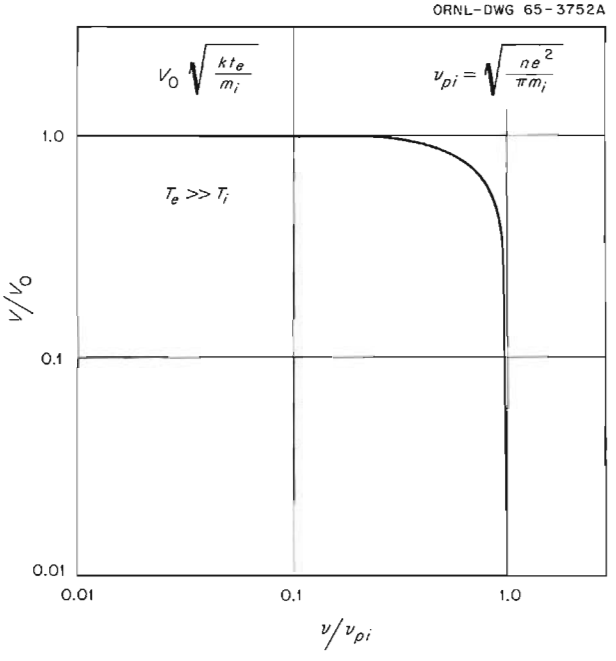

Fig. 4.18. Theoretical Slowdown of Ion Waves near the Ion-Plasma Frequency (See Ref. 8).

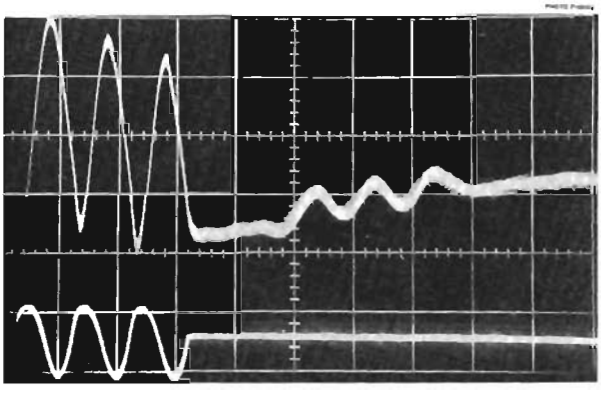

Fig. 4.20. Typical Plasma Response to a Sinusoidal Driving Voltage on the Emitter. The lower trace shows the driving voltage. The upper trace shows the received signal. The first burst of received sine waves corresponds to electrostatic pickup. The second burst is due to the slowly propagating ion waves. The plasma is formed of xenon. The time scale is 20 μsec per large division.

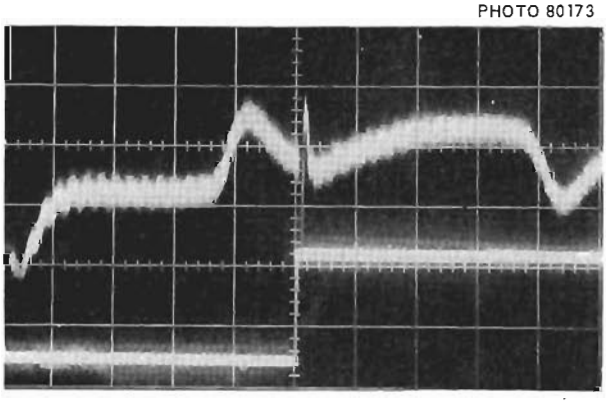

Fig. 4.19. Typical Pulse Results Showing Rise Time of Driving Step Function and of Received Ion-Wave Signal. The lower trace represents the voltage applied to the transmitting probe. The upper trace shows the ion-wave signal at the receiving probe. The ion-wave signal appears on the receiver about 80 μsec later than the transmitting pulse. The plasma is formed of xenon, and the time scale is 20 μsec per large division.

Figure 4.21 shows a typical cutoff observation using the coherent-sine-wave-burst technique. Each successively higher trace corresponds to a higher transmitter frequency. The transmitter voltage was kept constant. Note how the received sine-wave signal gradually dies away. For these particular data the cutoff frequency is only about a factor of 4 below the calculated ion-plasma frequency. In general, however, this technique does not yield cutoffs which agree any more closely with the expected cutoff than do the cutoffs obtained by the pulse technique.

As noted at the beginning of this section, one expects to see dispersion if we are observing the cutoff of ion waves at the ion-plasma frequency. So far, we have not seen any evidence for dispersion. The above results – that sine-wave and pulse techniques both yield essentially the same results – is some evidence against dispersion being present. From Fig. 4.20, one can see no evidence for slowdown with increasing frequency. Finally, in pulse work we generally do not see any increase in the width of the received signal with increase in propagation path length, which also suggests that dispersion is not present.

One possible explanation of the failure to observe dispersion is that the cutoff is not occurring in the bulk of the plasma but in sheaths covering

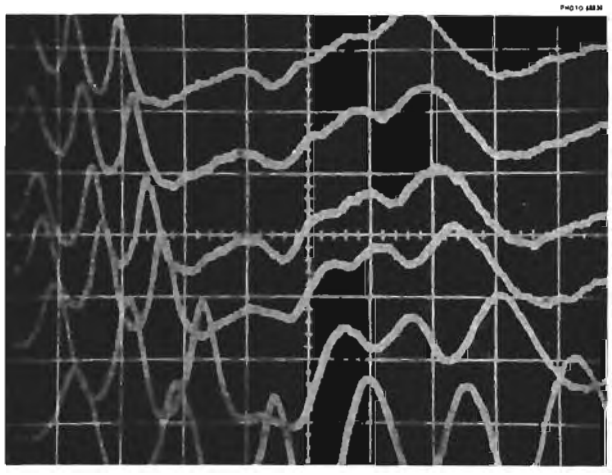

Fig. 4.21. Typical Cutoff Data Using Coherent-Sine-Wave-Burst Technique. These traces represent received signals only. The first three sine waves are due to electrostatic pickup, and the second three are due to ionic sound waves. Each successively higher trace corresponds to a successively higher frequency. Note that as the frequency is increased, the ion-wave signal dies away. The frequencies shown are 60, 80, 100, 110, 120, and 130 kc. The ion-plasma frequency calculated from Langmuir-probe data was 430 kc. The plasma is formed from xenon, and the time scale is 10 μsec per large division.

the ion-wave probes. Experimentally, we observe sheaths about 10 Debye lengths thick on these probes. These sheaths are comparable in thickness to the observed cutoff wavelength (wave velocity ÷ cutoff frequency) and may produce an interference effect. However, even if the cutoff occurs in the sheath and not in the bulk of the plasma, the basic cause of the cutoff is probably the same – the ion-wave propagation breaks down when electrostatic fields can penetrate the plasma for distances comparable to a wavelength.

4.3 USE OF A GRID-DIP METER TO MEASURE ELECTRON DENSITY

Igor Alexeff W. D. Jones

We have found that an ordinary grid-dip meter can be used quite easily to determine electron density in our gas discharge tubes. A grid-dip meter is basically a tuned oscillator with a current meter in the grid circuit. When the oscillator is brought near a resonant structure, power is coupled out of the oscillator, and the self-rectified grid current exhibits a dip. We have found in our discharge-tube measurements that the meter dips at the electron-plasma frequency, from which measurement the electron density can be calculated.

Figure 4.22 shows how the grid-dip meter is used to make density measurements of our discharge-tube plasmas. The instrument is simply brought near the discharge tube and adjusted until a dip occurs on the meter. The electron-plasma frequency is then read directly from the meter dial, which is calibrated in terms of frequency.

Figure 4.23 shows a comparison of electron-plasma frequencies measured directly by the grid-dip meter and those calculated from density measurements made by a Langmuir probe. Over a density range of about 200 to 1, the maximum disagreement is about a factor of 3. The Langmuir probe and dip meter were positioned approximately as shown in Fig. 4.22 when the measurements shown in Fig. 4.23 were being taken. The fact that the dip meter was located outside the discharge tube and thus had to look at lower-density plasma near the tube wall may explain why the dip meter values are consistently lower than the values obtained from the Langmuir probe measurements. Another possibility for the disagreement is that the dip meter may be exciting plasma oscillations of the sphere as a whole. This oscillation should occur at a frequency $1/\sqrt{3}$ times the plasma frequency.

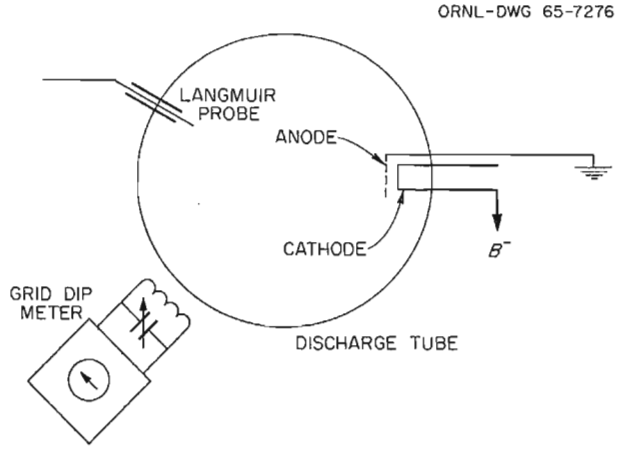

Fig. 4.22. Use of a Grid-Dip Meter to Measure Plasma Density.

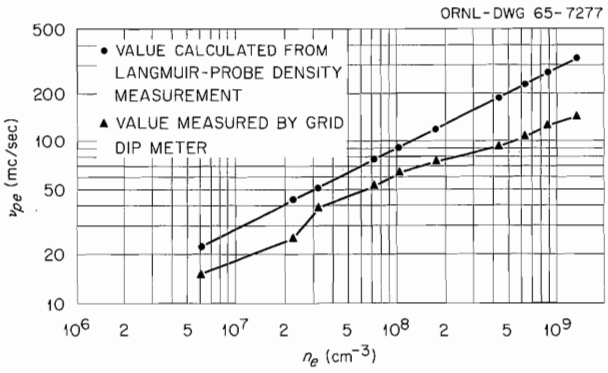

Fig. 4.23. Comparison of Electron-Plasma Frequencies.

4.4 PLASMA-IMPEDANCE-MEASURING TECHNIQUE

E. H. Christy, Jr.

Measurements of the vhf electrical impedance of a pair of plane parallel grids immersed in a plasma have been undertaken recently, the aim being a comparison of experiment with theories of the plasma capacitor impedance as described by Hall,[9] Shure,[10] and more recently Guest.[11] The latter work describes the capacitor impedance in the presence of beam-plasma interaction.

Impedance measurements in the 40 to 300 Mc range are generally awkward because of the detectors required for rf bridges and the multitude of adjustments to be made. A method which is quicker than, though not necessarily as accurate as, the bridge has been used for our measurements with quite good results. It has been proven to be reliable and reproducible and requires relatively few components.

As can be seen in Fig. 4.24, the two main components are a Tektronix sampling oscilloscope equipped with high-impedance cathode-follower probes and a General Radio constant-impedance adjustable coaxial transmission line. The dual-channel 3S76 preamplifier allows *x-y* as well as two-trace displays. All circuits are put together with General Radio 50-ohm coaxial components. The equivalent electrical circuit is shown in Fig. 4.25. Voltage V_2 is applied to the vertical axis of the scope, and V_1 to the horizontal axis, the scope pattern being an ellipse, in general. If Z_x were purely resistive, then

$$\frac{V_2}{V_1} = \frac{Z_x}{Z_x + 100},$$

and Z_x could be easily determined from the slope of the resultant straight-line scope pattern. Further, from basic transmission-line theory, placing Z_x exactly one-half wavelength away from the point of measurement of V_2 does not alter the characteristics of the circuit.

To measure a general Z_x having both resistance and reactance, the transmission line is first adjusted to $\lambda/2$ with Z removed, that is, an open-circuited condition. Adjustment to exact length is represented by a straight scope trace at exactly 45°. With Z_x in place and the scope generally displaying an ellipse (indicating some reactance), the adjustable line is shortened or lengthened to close the ellipse. If Z_x is capacitive, the line must be shortened; if inductive, the line must be lengthened. From the slope of the now straight-line scope trace and the above equation, one finds a value of pure resistance which is entered onto the resistance axis of a 50-ohm Smith chart (transmission-line calculator).[12] The fraction of a wavelength at the operating frequency that the line was adjusted, determined from a calibrated scale on the line mount, is also entered as the second coordinate on the chart. Intersection of these coordinates on the constant VSWR (voltage standing-wave ratio) circle of the chart gives the value of $Z_x = R_x \pm jX_x$, which is read directly.

No attempt has been made to refine the method to a high degree of accuracy. Two obvious limitations are in the integrity of the 100-ohm resistor and the uncertain effects of scope probe loading. The latter is significant above 300 Mc but could be taken into account by calibration with a good standard termination. For the 100-ohm unit, three 33-ohm carbon resistors are used in series in a 50-ohm coaxial housing and appear adequate for the work at present. Over 100 measurements have

[9] R. B. Hall, *Am. J. Phys.* **31**, 696 (1963).

[10] F. C. Shure, *J. Nucl. Energy, Pt. C* **6**, 1 (1964).

[11] G. Guest, *Thermonuclear Div. Semiann. Progr. Rept. Apr. 30, 1964*, ORNL-3652, p. 100.

[12] Engineering Staff of Hewlett-Packard Co., *Microwave Theory and Measurements*, p. 93, Prentice-Hall, New York, 1962.

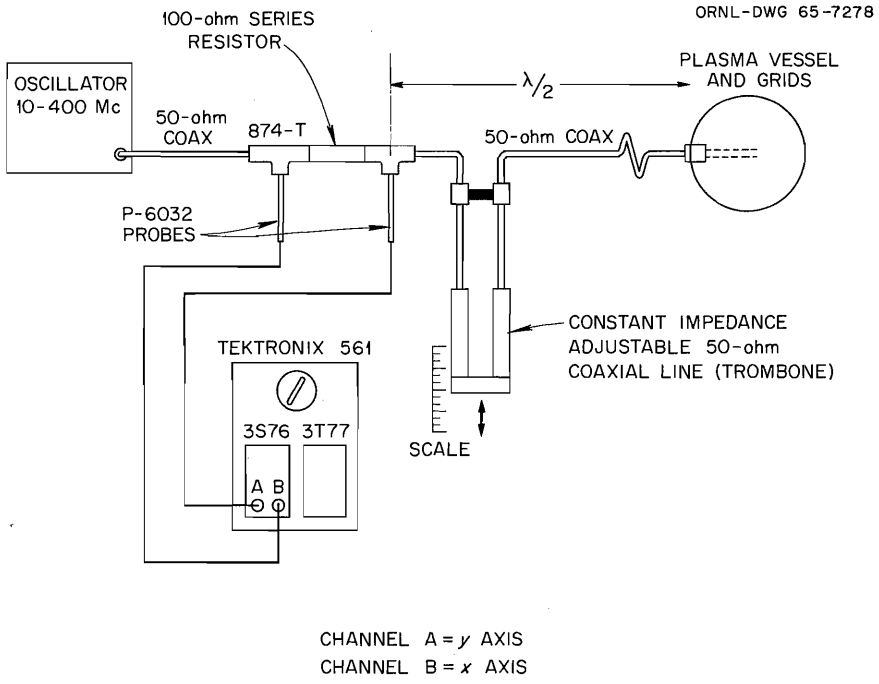

Fig. 4.24. Grid Impedance-Measuring Scheme.

been made with this technique between 40 and 300 Mc. Measurements of impedance standards over this range yield accuracies of ±5% or better. The plasma capacitor impedance has been measured as a function of density in some preliminary experiments, and the resultant curves bear close resemblance to those predicted in ref. 9. A more careful study, including the beam plasma interaction effect, is commencing.

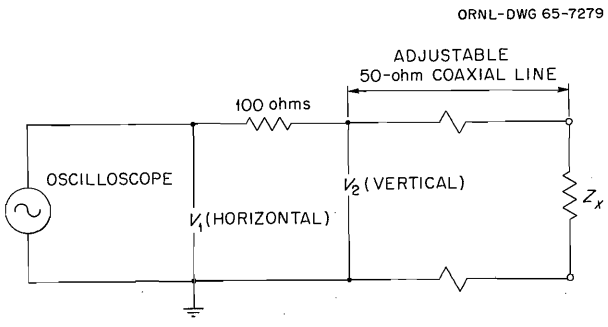

Fig. 4.25. Equivalent Electrical Circuit of Impedance-Measuring Apparatus.

4.5 BEAM STABILIZATION IN THE CALUTRON

O. C. Yonts E. D. Shipley

The experimental arrangement for studying the calutron beam is shown in Figs. 4.26 and 4.27. The Faraday cup and the movable walls are perpendicular to the magnetic field. The Faraday cup collects slow ions and/or electrons falling out of the beam region along the magnetic field lines. The movable walls cover the beam region from source to receiver. The argon beam used in these experiments is from a line source $4 \times {}^{3}/_{16}$ in. The beam widens to approximately $5 \times {}^{1}/_{2}$ in. at the collector (no magnetic focusing as in a standard calutron) and is approximately $4{}^{1}/_{2} \times 5$ in. at the 90° point, where the Faraday cup is located. Beam current at the collector for the experiments described here was 85 ma.

It has been known for some time that, as the background pressure in the calutron is raised, the rf signals, which occur in bands of frequencies and which can be observed in various ways, are shifted toward higher frequency values. We had always assumed that these rf signals were due to electrons oscillating across the ion beam. The results below show that this is one possible explanation for this type of frequency shift.

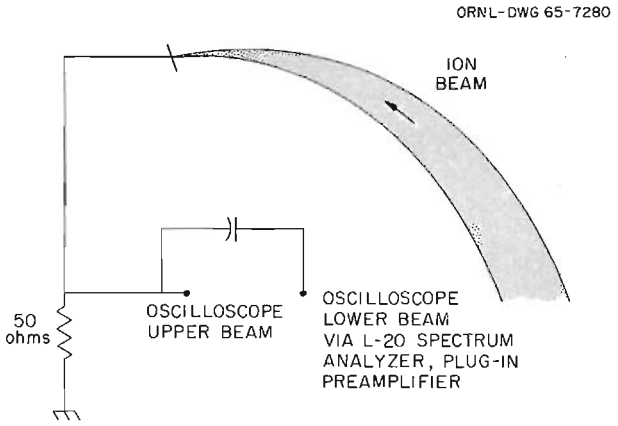

Fig. 4.26. Collector and Monitoring Arrangement.

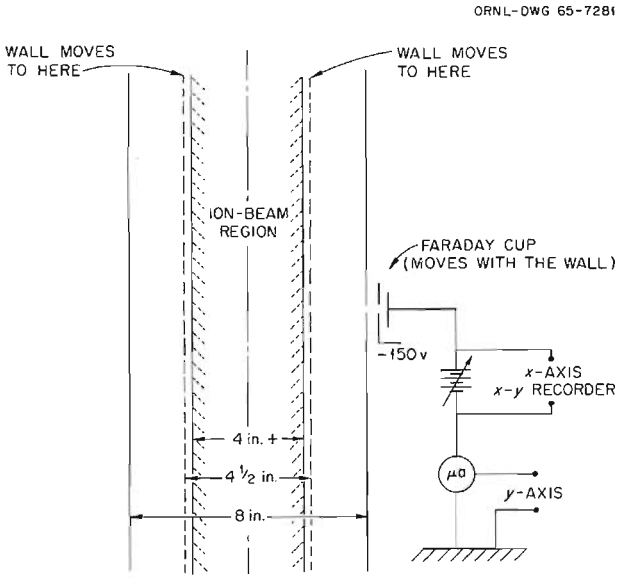

Fig. 4.27. Moving-Wall Experimental Arrangement.

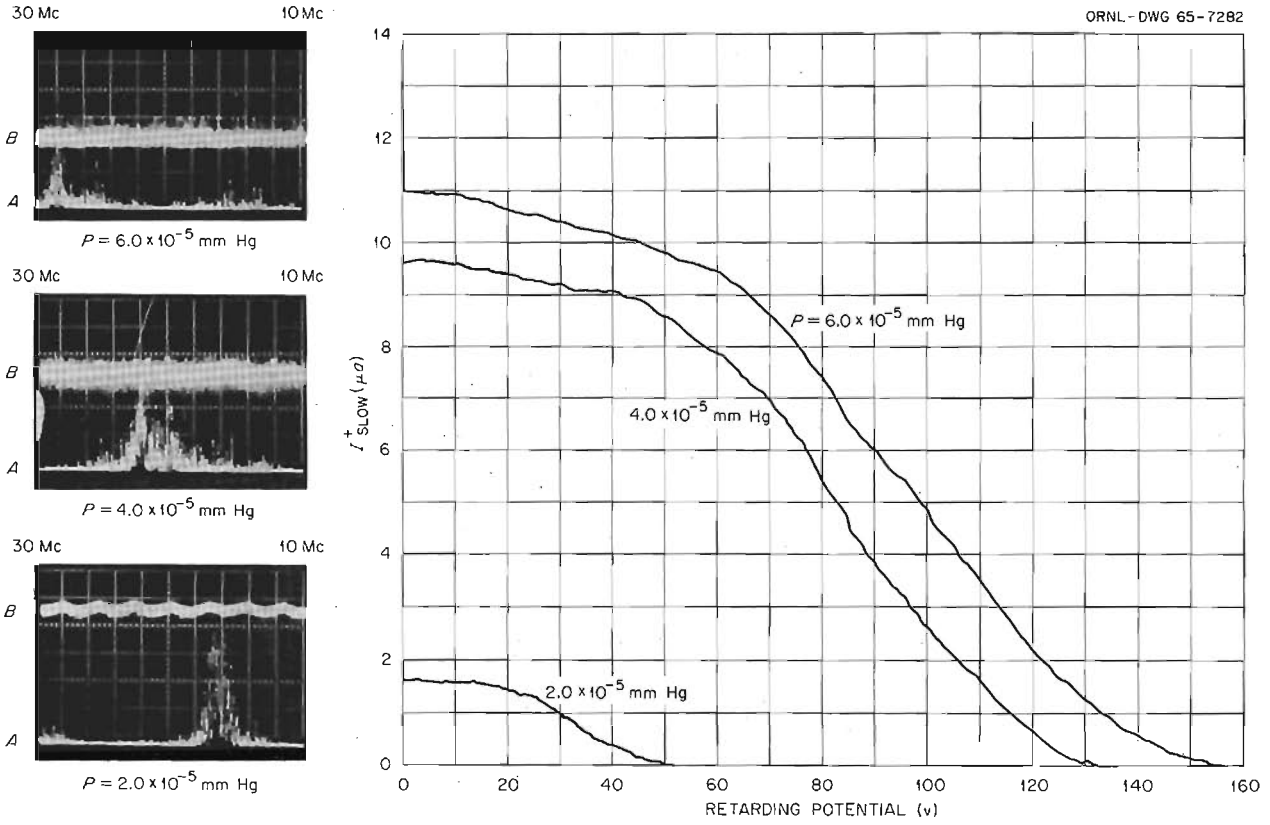

Fig. 4.28. Eight-Inch Wall Spacing. Frequency shift and retarding potential change with pressure.

The slow-ion retarding-potential curve can be used as a measure of the positive potential-well depth of the beam region. Three typical curves of the type used are shown in Fig. 4.28. Taking the midpoint of the down slope as an average value of ion energy, this should also be an average value of the energy of the oscillating portion of the trapped electrons. Using the value as the midpoint of a band of frequencies, curve 1 in Fig. 4.29 was calculated assuming that electrons oscillated to some region near the wall. (This assumption was made since, at pressure above 3×10^{-5}, a glow fills the tank from wall to wall.) Curve 2 in Fig. 4.29 shows the experimental points taken from a series of photographs such as those in Fig. 4.28. Since the curves are approximately the same shape, only displaced, the most obvious conclusion is that the distance assumed is wrong. If the energy and frequency are taken as correct, then the oscillating distance can be calculated. This is shown in Fig. 4.30. It seems, then, that at least this group of electrons is confined to the beam region.

Moving the walls in to the edge of the beam results in the retarding-potential curves and frequencies shown in Fig. 4.31. The almost linear falloff in energy at high pressure leads one to say that all electron energies are possible, so that, as pressure is raised, the band observed at low pressure should simply spread, and this seems to happen, as is shown by the photographs.

We wish to thank J. P. Wood and H. L. Huff for their many creative contributions throughout the course of these experiments.

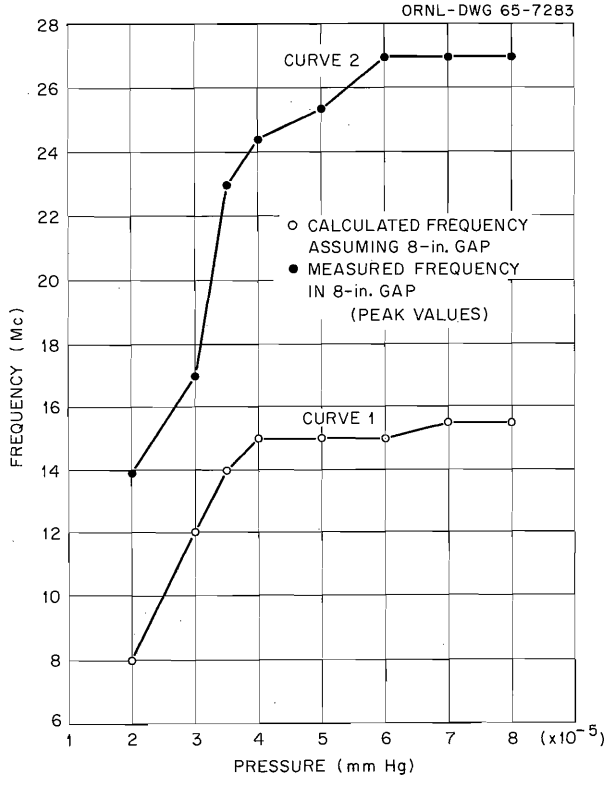

Fig. 4.29. Frequency vs Pressure.

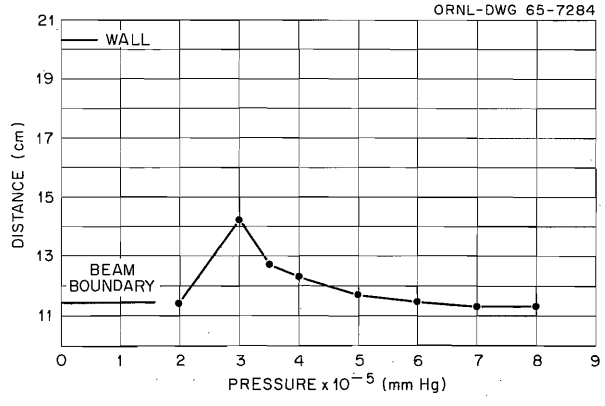

Fig. 4.30. Electron Pigging Distance vs Pressure (Peak Value).

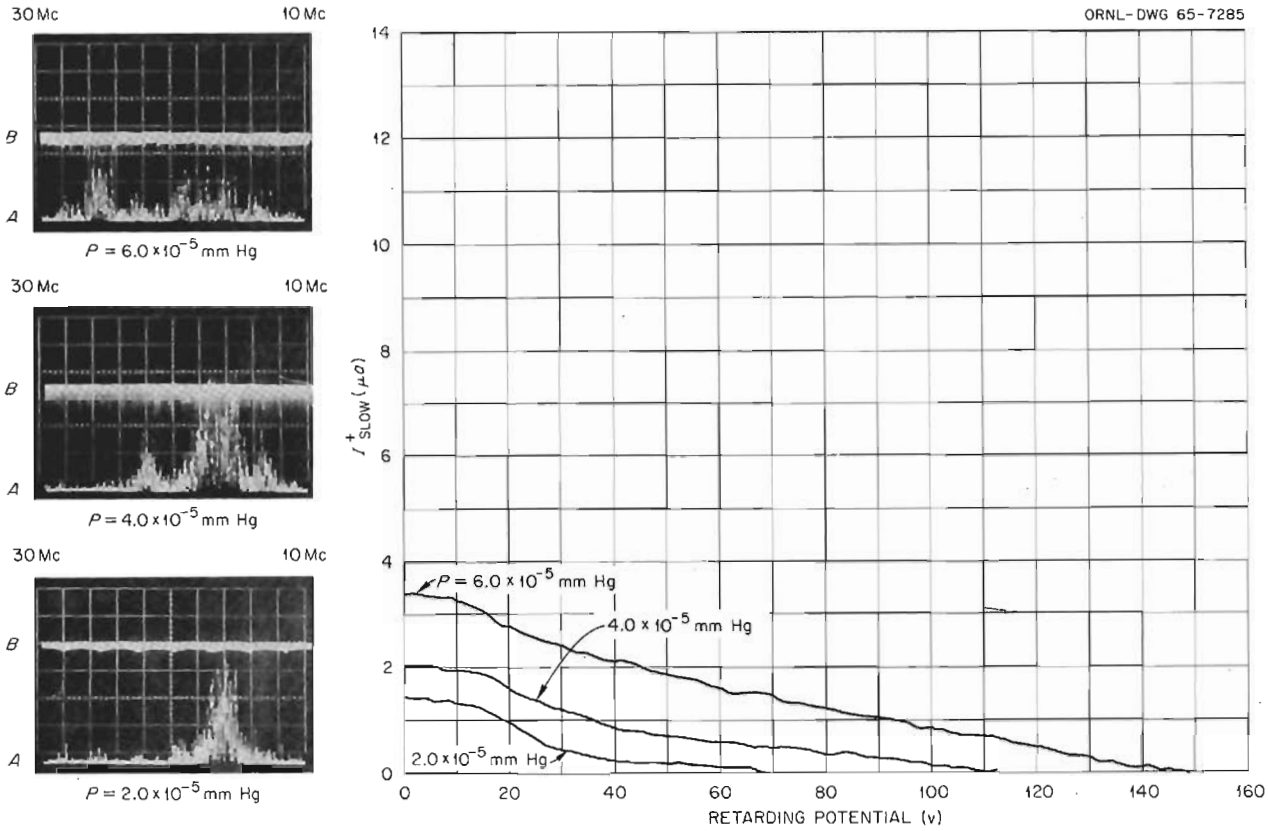

Fig. 4.31. 4.5-in. Wall Spacing. Frequency shift and retarding potential change with pressure.

4.6 STUDIES OF MINIMUM-*B* FIELD SHAPES FOR GAS-ARC FLUTE SUPPRESSION

N. H. Lazar Mozelle Rankin
R. A. Gibbons[13]

We have reported previously[14] that plasma flutes which are formed during the operation of a deuterium arc in a 2:1 mirror geometry may be suppressed when the arc anode is moved toward the cathode. The flute suppression appears to be related to the field shape, since experiments with the same-length arc but with the electrodes symmetric about the midplane show that fluting occurs. A deuterium arc was also operated in the ELMO geometry between electrodes ~1 m apart. With a Helmholtz field, plasma flutes were seen. Upon energizing the ELMO mirror coils, which strengthens the central field, the flutes were again suppressed.

In order to obtain a proper theory for the plasma behavior, some averaging of the plasma over the length of the arc is necessary.[15] As a first step in this direction, calculations of the integral

$$\mathcal{J} = \int \frac{\nabla B}{B^2}\, dl$$

were made for the Gas-Arc Facility mirror geometry. The procedure was to calculate the fields for a selected interval in z along a given flux line. The direction of the normal and binormal were then found at the end of the interval, and the field components at a point a selected distance

[13]Deceased.

[14]R. A. Gibbons and N. H. Lazar, *Thermonuclear Div. Semiann. Progr. Rept. Oct. 31, 1964*, ORNL-3760.

[15]H. P. Furth, *Phys. Rev. Letters* 11, 308 (1963).

along the normal were then calculated. The normal gradient was thereby obtained. This procedure is repeated to evaluate the integral.

The results of such a calculation for an integration from the cathode location to the anode position are shown in Fig. 4.32. Also plotted on a logarithmic scale is the ion current to the probe as shown in the previous progress report. Although the most rapid fall in ion current to the probe is in the region where $\mathcal{J}$ is attaining its largest positive values, a significant decrease in transport is seen as $\mathcal{J}$ decreases in the region where the face of the anode varies from +35 to +15 cm.

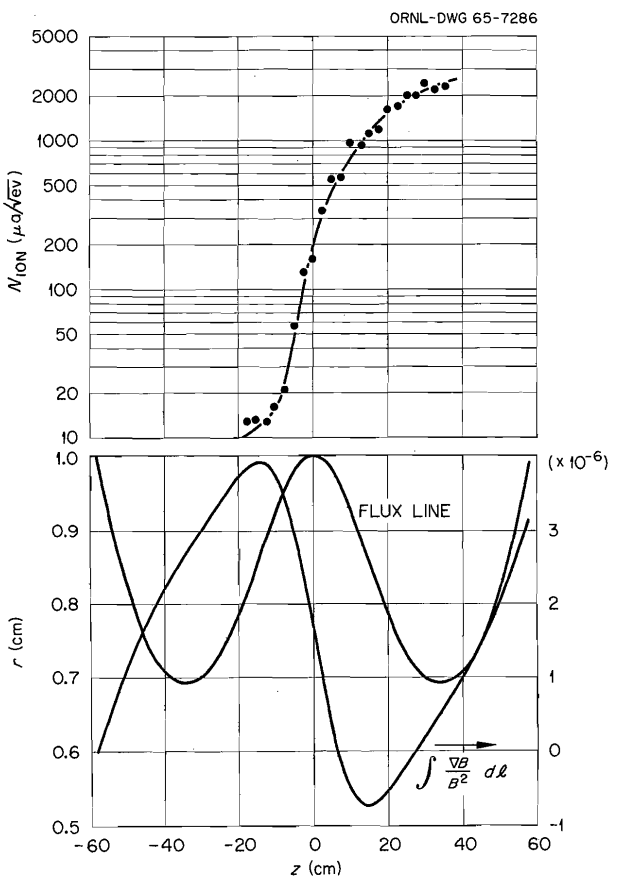

Fig. 4.32. Flux Line and $\int (\nabla B/B^2)\, dl$ Calculated for Gas Arc Facility Mirror-Coil Geometry. The upper curve shows the observed ion density at 2 cm from the arc as a function of the anode position.

The Gas-Arc Facility is presently being modified so that experiments with variable radial gradients may be carried out. A second pair of coils have been constructed, and the fields obtainable are shown in Fig. 4.33. The calculations of $\mathcal{J}$ for these fields are currently in progress.

A series of calculations have also been initiated on a modified quadrupole system in which, it is hoped, an arc should operate successfully and in which a minimum-B geometry should be obtained over any desired arc length. The problem of using a simple quadrupole (Ioffe) system with an arc is that the flux line through the cathode will not pass through the anode. This property of the flux line may be compensated for by taking advantage of the symmetry of a quadrupole system. If, after the flux line has moved radially a given distance, the direction of current in all the conductors is reversed, the symmetry of the system should ensure that the flux line returns along a symmetric path toward the original values. This symmetry property has been verified by flux-line calculations for a specific case. Of course, since for a quadrupole the field far from the ends of the system is perpendicular to a solenoidal field, a combination of these two systems may be made to produce any desired field gradient.

To estimate the magnitude of the field gradient, it may be noted that the field in the plane at 45° between conductors has been expressed analytically as a function of radius by Gauster:[16]

$$B_r = \frac{0.8I}{a} \frac{\zeta}{1+\zeta^4} ,$$

where I is the current in amperes, a the radial distance to the conductors, and $\zeta = r/a$. Assuming the axial field B_z is purely solenoidal, the equation for the flux line is

$$z_2 - z_1 = \frac{a^2 B_z}{0.8I} \left(\ln \frac{\zeta_2}{\zeta_1} + \frac{\zeta_2^4 - \zeta_1^4}{4} \right) .$$

Also, the normal gradient in the field is seen to be

$$\frac{B_r}{B_z^2} \left(\frac{dB_r}{dr} \right) \simeq \left(\frac{0.8I}{B_z a} \right) \frac{\zeta}{a} (1 - 5\zeta^4) .$$

[16] W. F. Gauster, private communication.

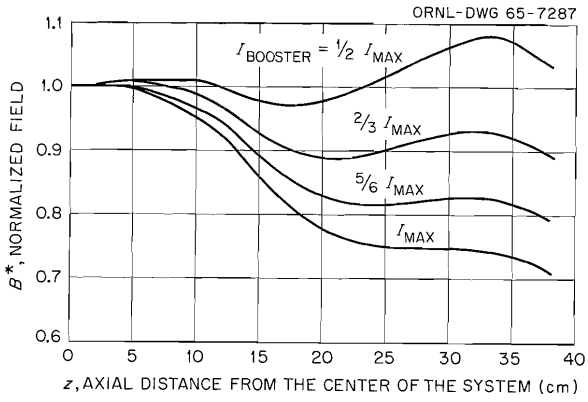

Fig. 4.33. Typical Field Shapes Available in the Gas Arc Facility with the Booster Coils. The fields are normalized to unity at the midplane.

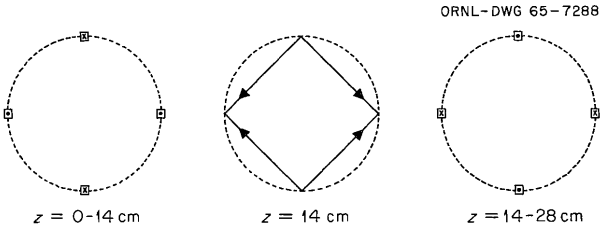

Fig. 4.34. Sections Through Proposed "Compensated" Quadrupole at Various Axial Distances.

The results of the flux-line calculations are shown in Figs. 4.35 and 4.36 for the "compensated" quadrupole geometry indicated in Fig. 4.34. The direction of current in the connections between the "rotated" sections is such as to minimize their contribution in the volume between the conductors. The radial and azimuthal positions of the flux line at each z position are shown in Figs. 4.35 and 4.36, respectively, for flux lines starting at various radii and angles at $z = 0$ cm. The axial field was chosen as 3000 gauss and $I = 3000$ amp. The conductor radial position was taken as 4 cm. The values of I and a were chosen to produce a radial gradient of 5×10^{-3} gauss/cm in the 45° plane. It is apparent that the flux line returns almost exactly to its initial value of $\mathcal{A}$ at will. In the case of the use of such a geometry with an arc, it is possible to use this field *outside* the mirrors and, hopefully, to effect a significant suppression of the flutes along the entire arc length. An experiment to test this hypothesis will be carried out in the EPA field.

The authors would like to thank W. F. Gauster for the calculation of the directions of the normal and binormal to the flux lines.

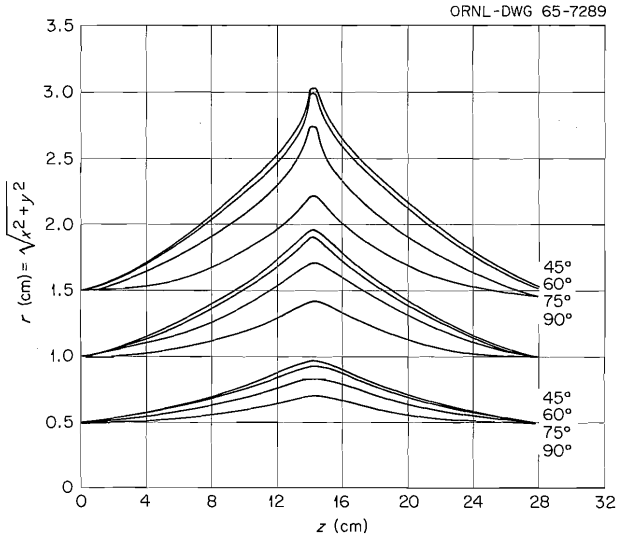

Fig. 4.35. Plot of Radial Position of Flux Lines for "Compensated" Quadrupole as a Function of Axial Distance for Initial Radial Distances of 0.5, 1, and 1.5 cm.

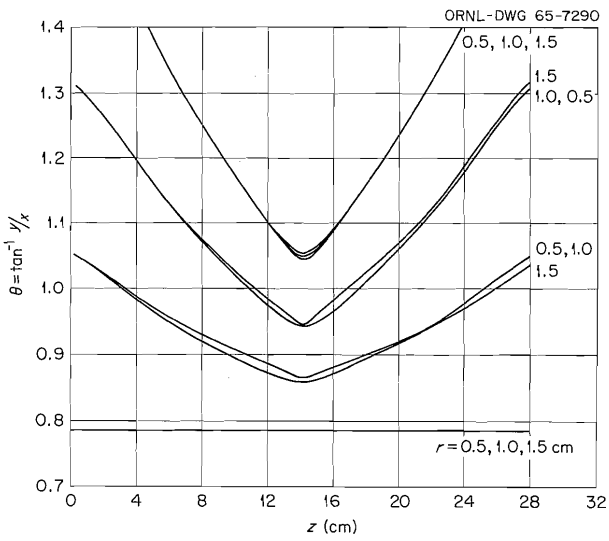

Fig. 4.36. Plot of Azimuthal Angle of Radius Vector to Flux Line for the Various Initial Radial Distances r.

4.7 THE HYDROGEN ARC IN THE LONG SOLENOID

J. E. Francis, Jr. P. R. Bell

4.7.1 Introduction

The hydrogen arc as operated in the long solenoid has three distinct regions. There is a pink central core $\frac{1}{4}$ in. in diameter corresponding to the diameter of the tip of the cathode. This core carries the major part of the current of the arc. This central core is surrounded by an intermediate region having an outside diameter of approximately 1 in. This intermediate region carries ions toward the cathode and is characterized by a paler pink color than the core. The visible part of the third region is approximately 4 in. in diameter and is a pale blue color. This outer region carries ions and gas in both directions toward the ends of the tank. Under certain conditions a net flow in either direction can be obtained.

4.7.2 Geometry

Most of the measurements have been made on an arc 245 in. long with the arrangement shown in Fig. 4.37. The cathode is mounted inside a water-cooled copper tube having an inside diameter of $1\frac{1}{4}$ in. This cathode shield is allowed to float electrically.

The anode is a water-cooled copper tube having an inside diameter of $1\frac{1}{2}$ in. A unique feature of this anode is that it extends through the tank wall and has an opening in which there can be mounted a view port or probes.

Water-cooled extensions for the cathode shield and anode, consisting of 4-in.-diam by 17-in.-long copper tubing, can be mounted on the electrodes. These have tentatively been named "bazooka" extensions.

Water-cooled baffles consisting of 4-in.-diam copper tubing with a flange to fit the main diameter of the tank were used to obtain differential pumping in various sections. These baffles were insulated from the tank so that ion saturation currents could be obtained.

Two additional insulated baffles separated by 1 in. were mounted in the center of the solenoid. These baffles were copper washers with a 5-in. inside diameter and a $7\frac{1}{2}$-in. outside diameter.

The coils on the solenoid have been reconnected so that it can be operated with a mirror field. The coils shown with a cross hatch in Fig. 4.37 are connected to one generator. The coils without cross hatch have been connected to a second generator. With this arrangement, various mirror ratios can be obtained.

ORNL-DWG 65-7291

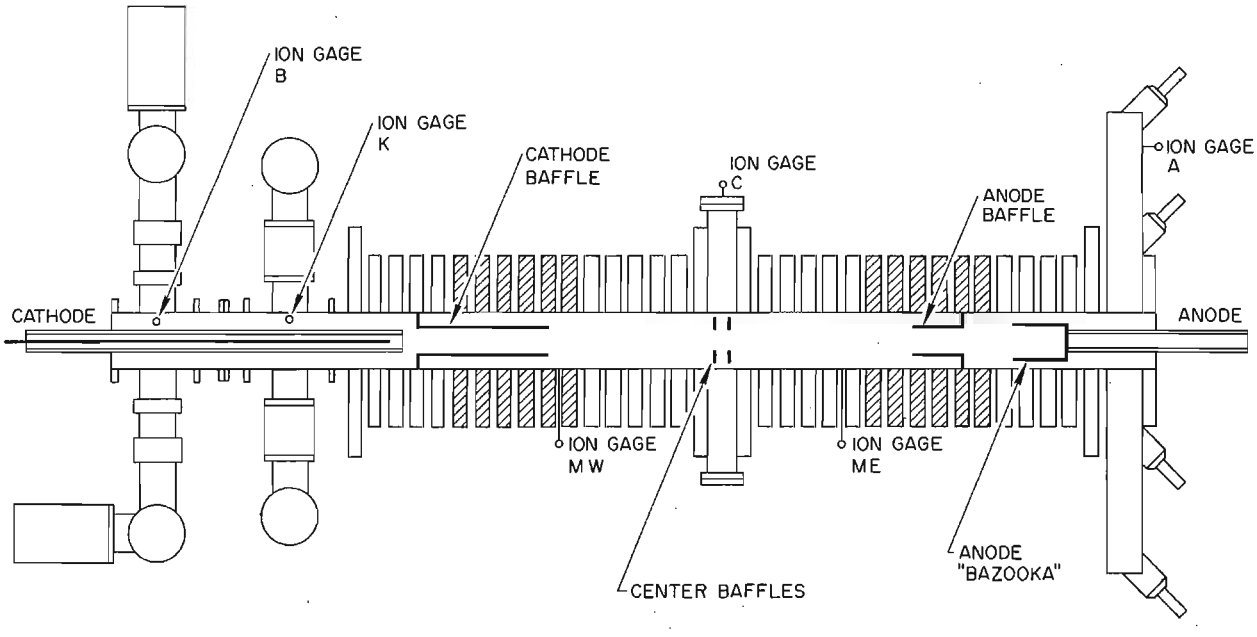

Fig. 4.37. Top-View Schematic – Long Solenoid.

4.7.3 Baffle Saturation Currents

The ion saturation currents to the baffles shown in Fig. 4.37 were measured as a function of the mirror field and baffle position while maintaining the main field constant at 8250 gauss. The results are shown in Figs. 4.38 and 4.39. It is noted in Fig. 4.38 that the saturation current to the anode decreases with increasing mirror field faster than $1/H^2$, while the saturation current to the cathode baffle decreases much more slowly. This is due to the fact that only a portion of the baffle is in the mirror field. Figure 4.39 shows the saturation currents obtained when the cathode baffle is moved 16 in. closer to the center of the solenoid. In this position it is centered in the mirror section of the field and gives almost the same variation of saturation current with mirror field as the anode baffles. The baffles mounted in the center of the tank show a slight rise with increasing mirror field, and this is attributed to trapping of the ions in the mirror. (Gage pressures for various sections of the solenoid are indicated against the right-hand ordinates for the positions shown in Fig. 4.37.) If the cathode baffle is placed in a position between the two positions used in Figs. 4.38 and 4.39, the cathode saturation-current curve falls in between the two curves shown. The change in slope of the saturation current to the center baffles when the cathode baffle is moved in indicates that the saturation current is a measure of the ions in a particular region, but does not tell where they originate. In fact, the gage pressure in the center of the tank is changed when voltage is applied to the baffles to measure saturation current. The fact that these ions are trapped by the magnetic field and tend to flow toward the end of the machine is confirmed by placing a bazooka

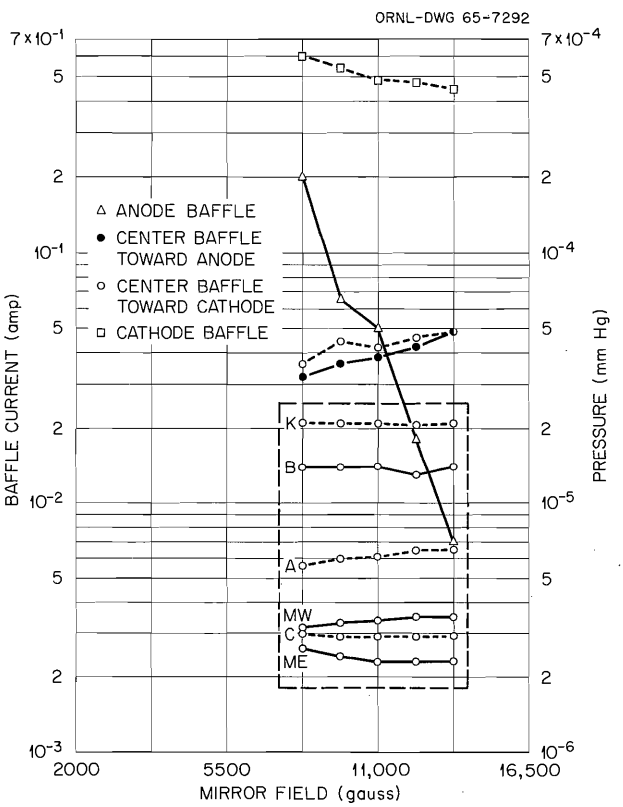

Fig. 4.38. Baffle Saturation Current vs Mirror Field for an 80-amp, 212-v, 245-in.-long Hydrogen Arc Using a Main Field of 8250 Gauss and a Gas Feed of 0.5 Atmospheric cm^3/sec. Inside the dashed lines pressure readings are given against the ordinate scale at the right; the locations of the various ion gages *A*, *B*, *C*, *K*, *MW*, and *ME* are given in Fig. 4.37.

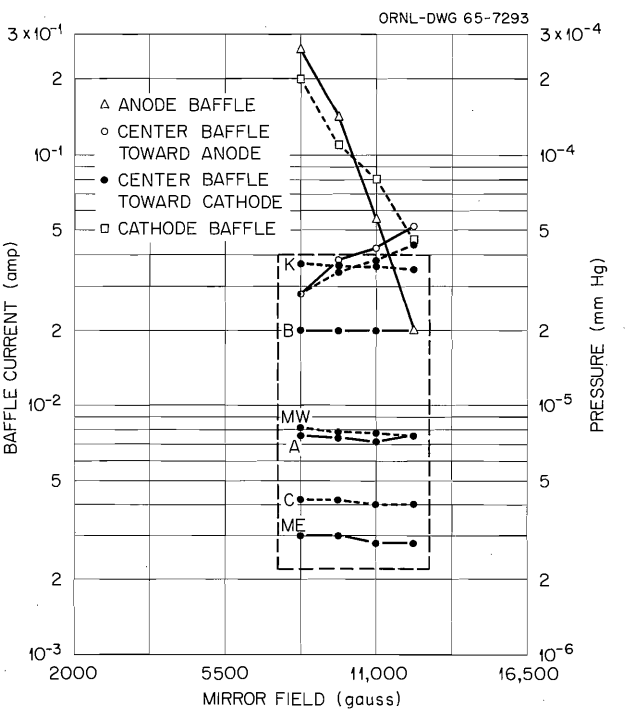

Fig. 4.39. Baffle Saturation Current vs Mirror Field for an 80-amp, 230-v, 245-in.-long Hydrogen Arc Using a Main Field of 8250 Gauss and a Gas Feed of 0.7 Atmospheric cm^3/sec (Cathode Baffle 16 in. Closer to Center of Solenoid). Pressure readings are as in Fig. 4.38.

extension on both the anode and cathode. With this arrangement it has been possible to maintain an arc of 80 amp and 240 v with a gas feed of 0.2 cm^3/sec. Without the bazooka extensions, the gas flow required is more than 0.4 cm^3/sec for the same geometry.

4.7.4 Anode Measurements

The availability of an optical viewpoint in the back of the anode has been of considerable interest and help. When the arc is struck using a high gas flow, a fireball can be seen within and near the front of the anode. As the gas flow is reduced, this fireball is drawn deeper into the anode and under optimum operating conditions fills the inside of the anode. The pressure between this fireball and the back of the anode has been measured with a thermocouple gage and found to exceed 1000 μ for the $1\frac{1}{2}$-in.-ID anode. This high pressure is not due to the pressure drop of gas flow along the anode, because with the arc not struck, the pressure is approximately 100 μ. The pressure can be lowered to less than 1000 μ by increasing the gas flow.

In order to try to determine the nature of the fireball, an insulated probe consisting of a 20-mil tungsten wire was mounted on the end of a $\frac{3}{8}$-in.-diam copper tube and supported by a boron nitride insulator. This probe was then inserted in the back of the anode, and the floating potential of this wire was measured as a function of distance from the front tip of the anode. The results are shown in Fig. 4.40. Note that the floating potential is almost one-half of the cathode potential. The position of the solenoid coils is also indicated, showing that this voltage extends beyond the coils into a region of very low magnetic field. Measurements could not be obtained closer because of disturbance to the arc. The wire was then removed and the measurements repeated for a $\frac{3}{8}$-in. diam water-cooled tube. The results are shown in Fig. 4.41. In this measurement, the probe was also shorted to the anode, and the probe current was measured for several points, as shown. These measurements indicated that the core of the arc has a high negative potential extending down into the anode.

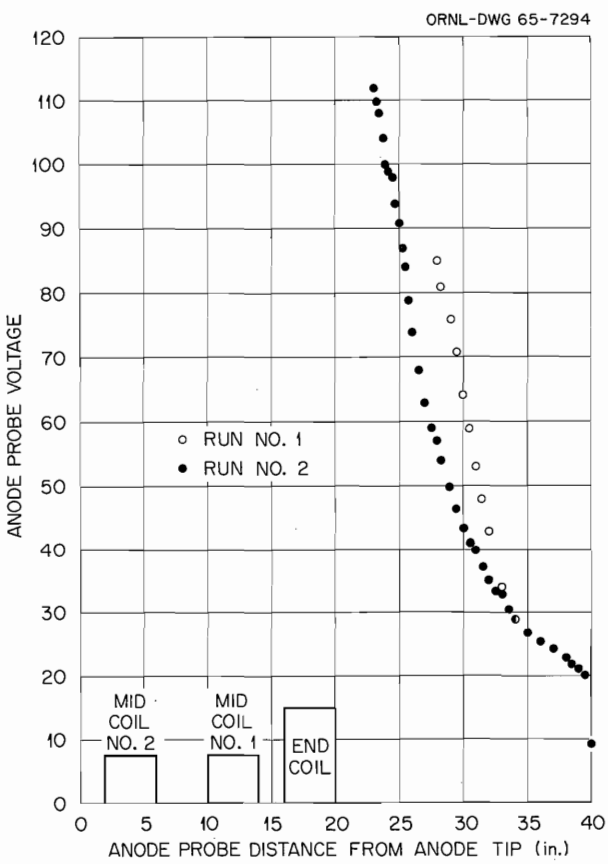

Fig. 4.40. Floating Voltage of Tungsten-Wire Probe Inside Anode vs Distance from Tip of Anode for an 80-amp, 250-v, 245-in.-long Hydrogen Arc in an 8250-gauss Field. Voltage is negative relative to anode potential.

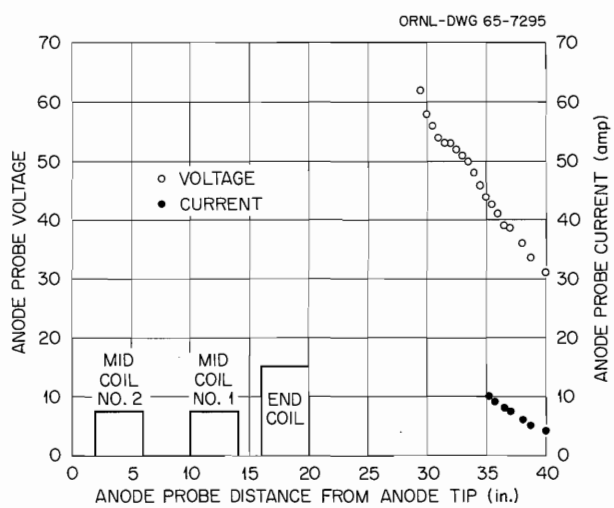

Fig. 4.41. Floating Voltage and Current to Ground of $\frac{3}{8}$-in.-diam Copper Probe Inside Anode vs Distance from Anode Tip for 70-amp, 265-v, 245-in.-long Hydrogen Arc. Voltage is negative relative to anode potential.

4.7.5 Power Distribution

The power distribution to the electrodes was obtained by measuring the inlet and outlet water temperature and measuring the flow. The results are shown in Table 4.2.

These measurements show that approximately 45% of the arc power is lost in the anode and over 15% is lost at the cathode, leaving less than 40% to be dissipated by radiation.

Table 4.2. Distribution in the Hydrogen Arc

Arc Current (amp)	Arc Voltage (v)	Arc Power (w)	Anode Power (w)	Cathode Power (w)
60	243	14,580	6260	1750
77	230	17,710	8630	2620
82	236	18,910	8630	2620
72	254	18,288	8759	4200
82	238	19,500	8800	5140

4.8 EXCITATION HEATING OF IONS BY ELECTRONS

J. Rand McNally, Jr. M. R. Skidmore
J. E. Francis, Jr.

4.8.1 Introduction

Most low-pressure discharges exhibit electron temperatures which are significantly higher than the atom (or ion) temperatures. However, in some low-pressure, magnetically confined, arc-like plasmas it is observed that the ions are hotter than the electrons. Apparently, the reduction of atom-cooling effects of the walls and the presence of strong internal radial electric fields in such discharges permit the generation of a nonthermodynamic condition in which the reverse situation arises, namely $T_+ > T_-$. Radiative excitations by the electrons also contribute to holding down the electron-excitation temperature.

We have been studying various dc arcs (H, Li, C, N, etc.) confined by magnetic fields and operated at low pressures. Surprisingly, the carbon arcs (and gas-fed carbon arcs) exhibit a *grossly* nonthermodynamic state[17] in which $T_+ \gg T_-$. It is only recently that we have formulated some novel concepts to explain the development of these unusual temperature conditions. We offer the following ideas as a preliminary hypothesis, noting full well their very qualitative nature and that even our specification of temperature for individual species is fraught with difficulties.

In essence, we have suggested that, under appropriate conditions, electrons can heat ions much more rapidly than ordinary elastic collisions permit.[18] The process involves inelastic collisions between ions and electrons that provide a large concentration of stored energy in metastable ionic states. Electron rearrangement collisions between pairs of such metastable ions can depopulate the metastable levels, in accordance with the Wigner spin-conservation rule, and the stored energy is then reflected in an increased kinetic energy of the separating ions.[18] Cyclic or chainlike processes of this nature permit the ions to "run away" in energy to some new equilibrium condition. We call the overall process by the name *excitation heating* (after a suggestion of E. D. Shipley).

4.8.2 Cooling Rate for Ions

The conventional cooling rate for ions of charge Z and of velocity v_+ colliding with slower electrons of density Δn_- is of the form[19]

$$\frac{dW}{dt} = -\frac{4\pi(\Delta n_-)Z^2e^4}{m_- v_+} \ln \frac{b_{max}}{b_{min}},$$

where the maximum impact parameter, b_{max}, is usually taken as the Debye length, λ_D, and b_{min} is usually taken as $Ze^2/3kT_-$, although Ze^2/mv_+^2 is probably more accurate.[20] This conventional

[17] J. R. McNally, Jr., and M. R. Skidmore, *Appl. Opt.* **2**, 699 (1963).

[18] *Thermonuclear Div. Semiann. Progr. Rept. Apr. 30, 1964*, ORNL-3652, p. 74.

[19] See T. K. Fowler and M. Rankin, *J. Nucl. Energy* **C4**, 311 (1962).

[20] L. Spitzer, *Physics of Fully Ionized Gases*, p. 127, Interscience, New York, 1962.

cooling rate (−90 ev/μsec for C^{2+}) is, however, in error in the electron-ion case, inasmuch as it does not take into account the reduced collision time of close impacts due to the Coulomb acceleration. The use of a reduced collision time,

$$\tau \sim \frac{2b}{v_+ + \sqrt{2Ze^2/bm}},$$

in the impulse approximation is an especially important correction for sluggish ions such as carbon, even at 500 ev. The corrected expression for the rate of cooling of the average ion is approximately

$$\frac{dW}{dt} = -\frac{4\pi(\Delta n_-)Z^2e^4}{m_- v_+}\left\{\ln(1+x)^2 - \frac{2x}{1+x}\right\},$$

where $x^2 = b_{max}mv_+^2/2Ze^2$. If we take as parameters for the carbon arc: $Z \cong 2$, $v_+ \sim 10^7$ cm/sec, $n_- = 10^{14}$ cm^{-3}, $\Delta n_- = 5 \times 10^{10}$ cm^{-3} (for a Maxwellian distribution at $T_- = 42{,}000°$K), the cooling rate is only about −12 ev/μsec for $b_{max} = \lambda_D \cong 1.4 \times 10^{-4}$ cm, but only −6 ev/μsec for $b_{max} = \lambda_D/4$. A Druyvesteyn distribution of electron energies would reduce dW/dt still further (to about −4 ev/μsec). The actual energy transfer rate is thus an extremely sensitive parameter in these carbon arcs. (The energy distribution of electrons in high-density, high-Z plasmas may also tend slightly toward a Fermi-like energy distribution, such as is exhibited by free electrons in metals, because of the strong interparticle fields; that is, the free electrons are continuously in the presence of powerful Coulomb fields which deplete the number density of very cold electrons.)

It seemed to us initially[18] that, as a result of a heating rate of 90×10^6 ev/sec, the cold group of electrons had to be significantly depleted with respect to a Maxwellian distribution at 5 ev mean energy in order to permit such high ion temperatures. Although the distribution for the electrons may be somewhat perturbed from a Maxwellian by an energy transfer rate even as large as $\sim 6 \times 10^6$ ev/sec, our present views do not require any gross depletion of the distribution function for the very cold electrons.

There is some large uncertainty in the choice of $T_- = 42{,}000°$K, since C^{2+} spectra indicate an excitation temperature of about 28,000°K whereas C^{3+} spectra give about 56,000°K.[21,22] It is quite possible that the C^{2+} λ = 4647–51 A triplet is selectively enhanced in intensity (by about a factor of 100) compared to C^{2+} λ = 5696 A; laser oscillation has also been observed for the blue triplet group.[23,24] The actual energy transfer rate is proportional to Δn_-, which for a Maxwellian distribution varies as $T_-^{-3/2}$; thus, if T_- = 56,000°K, the ion cooling rate drops by 35%.

4.8.3 Estimate of Cross Section for Heating Step

Choosing dW/dt as −6 ev/μsec as a reasonable estimate, we then require that the rate of collisional heating of a metastable ion via the exothermic inelastic collision:[18]

$$C^{2+*}(2s2p\ ^3P^0) + C^{2+*}(2s2p\ ^3P^0) \longrightarrow C^{2+}(2s^2\ ^1S) + C^{2+}(2s^2\ ^1S) + 13.0 \text{ ev} \quad (1)$$

be:

$$\frac{\Delta E_{coll}}{\tau_{coll}} = n^*\overline{\sigma_{coll}v_+}(6.5) > 6 \times 10^6,$$

or

$$\overline{\sigma_{coll}v_+} > 3 \times 10^{-8} \text{ cm}^3/\text{sec}$$

for

$$n^* \sim 3 \times 10^{13} \text{ cm}^{-3}.$$

---

[21] W. B. Ard, Jr., on the basis of microwave noise radiation at 7.4 kMc, gives T_e = 4 ev for a stable carbon arc to 8 ev for a relatively unstable arc, both operated at 200 amp, *Thermonuclear Div. Semiann. Progr. Rept. Jan. 31, 1960*, ORNL-2926, p. 43.

[22] J. R. McNally, Jr., in *Optical Spectrometric Measurements of High Temperatures*, ed. by P. J. Dickerman, Univ. of Chicago Press, 1961.

[23] R. A. McFarlane, *Appl. Phys. Letters* **5**, 91 (1964).

[24] The upper levels of the λ = 4647–61 A triplet decay only via these blue radiative transitions ($A_{ij} = 8 \times 10^7$ sec^{-1}), whereas the upper level of λ = 5696 A decays by λ = 5696 A radiation ($A_{lm} = 5 \times 10^7$ sec^{-1}) or much more rapidly via λ = 574 A, for which the Einstein transition probability is 6×10^9 sec^{-1}. The fact that the lower level of λ = 4647 A is very rapidly depopulated via λ = 538 A ($A_{jk} = 2 \times 10^9$ sec^{-1}) may contribute to the observed lasing properties of λ = 4647 A.

Thus, for $\bar{v}_{+\mathrm{coll}} \sim 1.5 \times 10^7$ cm/sec, $\bar{\sigma}_{\mathrm{coll}} > 2 \times 10^{-15}$ cm^2, a fairly reasonable figure for 500-ev ions.[25,26] The heating of all ions in the arc will increase the required collision cross section by about $\Sigma n_i/n^*$.

4.8.4 Estimate of the Excitation Cross Section

In addition, we require that the rate of excitation of an ion to a metastable state by the process (as well as all other cascade transitions into this state):

$$C^{2+}(2s^2\ {}^1S) + e \longrightarrow C^{2+*}(2s2p\ {}^3P^0) + e - 6.5 \text{ ev}$$

be:

$$\frac{\Delta E_{\mathrm{exc}}}{\tau_{\mathrm{exc}}} = f n_- \overline{\sigma_{\mathrm{exc}} v_-}(6.5) > 6 \times 10^6 ,$$

or

$$\overline{\sigma_{\mathrm{exc}} v_-} > 3 \times 10^{-8} \text{ cm}^3/\text{sec} ,$$

where f is the fraction of electrons above 6.5 ev ($f \sim 0.3$). Again, this estimate depends strongly on the energy distribution characteristic of the electrons.

4.8.5 Conclusions

The mean lifetime of ions in a 16-ft-long arc is estimated to be about 0.5 msec based on both mean Doppler drift of ions ($\sim 10^6$ cm/sec) and particle conservation – this suggests a *net* heating rate for the 500-ev ions of about 1 ev/μsec. The heating of ions by elastic collisions with faster electrons is about +0.5 ev/μsec. The *inelastic*-collisional heating rate of ions by electrons ($\sim$6 ev/μsec) thus appears to be at least a factor of 10 larger than that of elastic collisions with fast electrons.

Although accurate evaluations of the individual processes are not possible at this time, the quite reasonable requirements on the pertinent physical parameters suggest strongly the feasibility of this new mode of heating ions by multiple inelastic collision processes. It should be noted that the magnetically confined lithium arc does not exhibit such energetic ions, in agreement with expectations of the model. The fact that we have also not been able to observe high-energy nitrogen ions, except in the presence of hot carbon ions, may be related to the increased Coulomb barrier for onset of the heating mode for N^{3+} in a nitrogen plasma.

---

[25] The reaction (1) can be construed as a double-charge-exchange reaction, although the electrons lose their specificity in the collision. Hasted and Smith [*Proc. Roy. Soc.* (London) **A235**, 354 (1956)] report a cross section of about 2×10^{-15} cm^2 for the single-charge-exchange reaction $C^{2+} + Ar^0 \rightarrow C^+ + Ar^+ + 8.6$ ev for C^{2+} ions of about 1 kev.

[26] A. R. Tynes (thesis, Oregon State University, Corvallis, Oregon, 1964) gives a σv of 5×10^{-8} cm^3/sec for the helium afterglow process, $He^* + He^* \rightarrow He_2^{**} \rightarrow He_2^+ + e + \Delta E$.

5. Atomic and Molecular Cross Sections

C. F. Barnett J. A. Ray

5.1 HIGHLY EXCITED STATES OF H_2

The population and existence of highly excited states of H_2 formed from electron-capture collisions of H_2^+ in hydrogen gas have been determined quantitatively. Ions were produced and accelerated to 50 kev in a conventional ion accelerator and then magnetically analyzed. The H_2^+ beam was collimated and passed through a differentially pumped hydrogen gas cell, where electron-capture collisions produced energetic H_2 molecules. Competitive processes of dissociative ionization and also electron capture into repulsive molecular potential levels produced also an H^0 beam of one-half the initial H_2^+ energy. The intensities of these two neutral beams, H^0 and H_2^0, were determined from pulse-height analysis using a thin-window proportional counter. Charged particles were removed from the beam at the gas-cell exit by means of a transverse electrostatic field.

Two electrodes with parallel surfaces separated by 0.75 mm formed the electric field ionizer. The beam was further collimated to 0.125 mm prior to passing through the 0.25-mm apertures in the electrodes. The H^+ and H_2^+ ions formed by the electric field ionization of H^0 and H_2^0 were energy analyzed and deflected by a second electrostatic analyzer, and also detected by the proportional counter. Ionized particles produced by collisions with residual gas molecules and edges of collimating apertures were subtracted as background signal. For any neutral molecule to be observed as existing in a highly excited state the lifetime for radiative transitions would have to be greater than 2.5×10^{-7} sec, which was the transit time between collision cell and field ionizer.

Figure 5.1 shows the fraction of the H_2 particles that were ionized at different electric field strengths, and which were accordingly in high electronic quantum states (H_2^*). For a 50-kev H_2 particle, the fraction increases monotonically from 3.5×10^{-4} at an electric field of 6.8×10^3 v/cm to 6.0×10^{-4} at 4×10^4 v/cm. Also plotted on the same figure are the results obtained from electron-capture collisions of protons of equivalent velocity (25 kev) in hydrogen gas. The fraction H^{0*}/H^0 was greater than the fraction H_2^*/H_2 for all field strengths. At a field strength of 2.7×10^4 v/cm, H^{0*}/H^0 was 1×10^{-3}, corresponding to ionization of all states with principal quantum number $n > 12$.

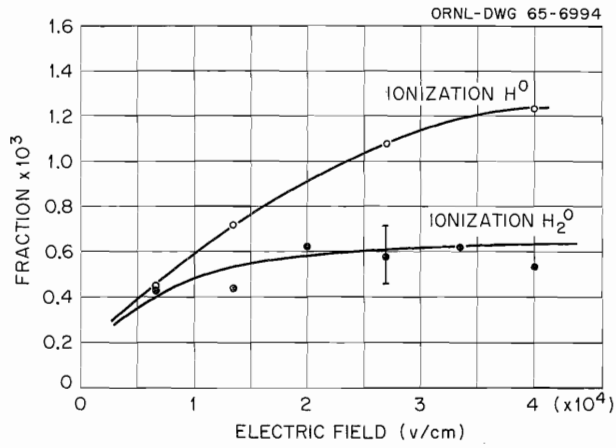

Fig. 5.1. Fraction of H^0 and H_2 in Highly Excited States as a Function of Ionizing Electric Field.

Other measurements indicate that the sum of the electron-capture cross sections into all quantum states is equal for both H^+ and H_2^+ in hydrogen gas for velocities greater than 4.4×10^8 cm/sec (100-kev H^+). For lower energies the electron-capture cross section for H_2^+ becomes increasingly larger due to the resonant characteristic of the reaction. In this series of measurements the observed H_2 molecules are those which have undergone a capture transition to a stable electronic level. The ratio of total electron capture into stable electronic levels of H_2 to the electron capture into all *n* levels of H^+ in hydrogen gas is 3.62. Obviously from the curves of Fig. 5.1 there is no correlation between total electron capture for protons and molecular ions. Also, the ratio of H^+/H_2^+ increases as the electric field increases, indicating a difference in relative population of high quantum levels in H^0 and H_2. Decreasing the H_2^+ energy to 40 kev resulted in a fraction, H_2^*/H_2, of 2.5×10^{-4}, which was essentially constant over the entire range of applied electric fields.

The observed signal of mass 2 and full energy could result from contamination of the H_2 beam by D^0 atoms. To eliminate this possibility the gas density in the collision cell was increased, and the results are shown in Fig. 5.2. For low densities the fraction formed in highly excited states was constant as the pressure increased, corresponding to single collisions. At higher pressure the fraction decreased, indicating collisional deactivation or dissociation of the uppermost levels. At much higher pressure the mass 2 signal at the detector was zero, signifying the absence of D^0 in the neutral component of the beam.

In all low-energy measurements using the electric field spectrometer there are indications of beam defocusing at large electric fields. To gain some insight into the problem the 0.125-mm collimating aperture was removed from the ionizer so that the 0.25-mm aperture of the field electrodes provided the collimation. The absolute magnitude of the H_2^0 fraction in highly excited states was the same for no collimation as it was for the 0.125-mm collimator. Exact assessment of defocusing and slit ionization is incomplete at present, although no major error contributions to the observed fractions seem to be induced by these effects. The estimated probable error is ±25%, which is shown by the single-point error bar in Fig. 5.1.

Tentatively, the excited state of H_2 has been described as a single, high-quantum orbital electron plus an H_2^+ core, with the orbital electron existing in states similar to the high quantum states of hydrogen atoms.

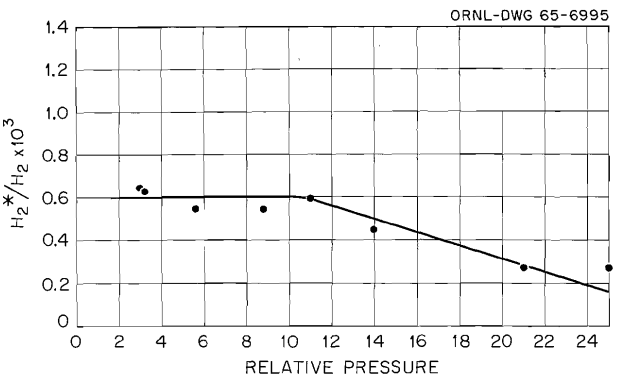

Fig. 5.2. Fraction of H_2 in Highly Excited States as a Function of Collision-Cell Pressure.

5.2 LOW-ENERGY PROTON AND HYDROGEN ATOM DETECTORS

Two methods have been used to determine the response of silicon semiconductor detectors to low-energy protons or neutral hydrogen atoms. Direct-current measuring techniques[1] have been applied by biasing out the leakage current across the barrier and determining the dc current flow as protons strike the front surface. A schematic diagram of the crystal and circuit arrangement is shown in Fig. 5.3. The particle flux striking the front surface of the cup was measured by a vibrating-reed electrometer. The gain of the silicon detector has been defined as the ratio of the output current to the input current. Figure 5.4 shows the gain as a function of the input proton current through four orders of magnitude. For proton currents greater than 10^{-11} amp the detector leakage current fluctuates violently, which indicates crystal damage. The detector gain as a

[1]This work was performed in cooperation with the Electron Cyclotron Group headed by R. A. Dandl.

ORNL-DWG 65-4023

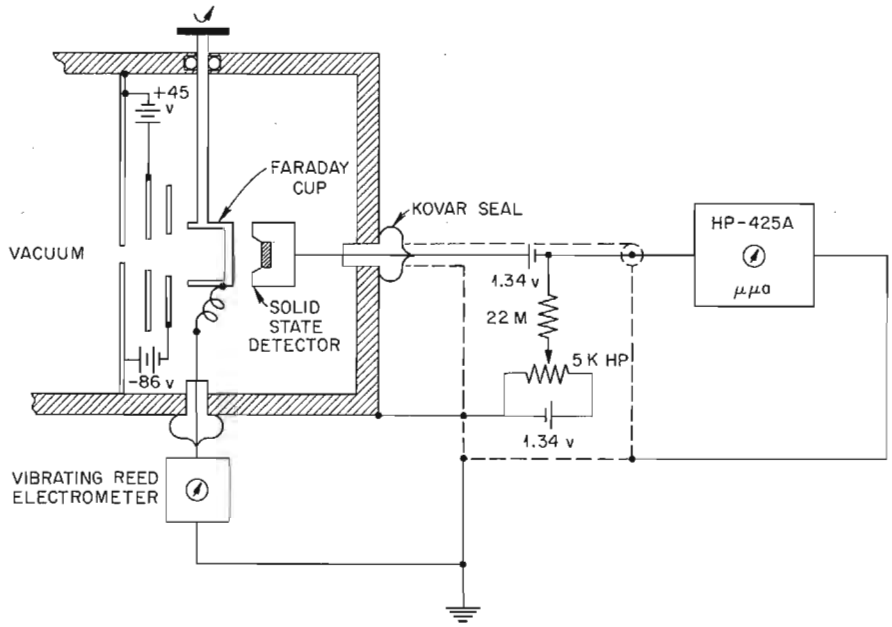

Fig. 5.3. Schematic Diagram of Experimental Arrangement Used in Detecting Low-Energy Particles.

function of H^+, H_2^+, and H_3^+ energy is shown in Fig. 5.5. The gain increased monotonically as the particle energy increased. From a linear plot of gain vs energy a constant slope determining the average expended energy per electron collected is obtained. The present values of 4.1 and 3.8 ev/electron for protons and H_3^+, respectively, can be compared with 3.53 ev/electron (ref. 2) for high-energy alpha particles and 50- to 400-kev H^+ ions and with 3.79 ev/electron (ref. 3) for electrons. All these results are within the experimental accuracy of the present series of measurements.

The other method used in the detection of low-energy protons with silicon semiconductor detectors was the conventional use of pulse-height analysis. A schematic diagram of the experimental arrangement is shown in Fig. 5.6. The silicon crystal was mounted in a copper housing through which liquid nitrogen flowed. The detector was then placed within a vacuum chamber attached to an ion accelerator capable of supplying 1- to 50-kev protons. The proton beam was collimated by 0.010-in. apertures, and the beam current was adjusted to provide ion currents less than 10^3 ions/sec. Output signals from the detector were brought out through the vacuum wall by means of a hand-picked low-leakage Kovar seal and attached directly to the input network of the preamplifier, thereby eliminating cable and coaxial connector capacitances.

For pulse amplification an ORTEC 103XL-203 amplifier system was used, which consisted of an extra-low-noise preamplifier, main amplifier, post-amplifier, and detector bias supply. The measured noise of the electronic system was 1.98 kev as determined by a precision mercury pulser and with the preamplifier input terminated by a 1-pf capacitor. The semiconductor detector was a nominal 5000-ohm-cm silicon crystal with a measured noise width at half maximum amplitude of 11.9 kev at room temperature and an optimum bias voltage of 200 v. Shown in Fig. 5.7 is the pulse spectrum for protons of energies 15 to 35 kev. The 15-kev curve has the background subtracted, while the other curves are presented as obtained directly from the pulse-height analyzer. The full width at half maximum amplitude (FWHM) increased as the proton energy decreased, indicating

[2] R. I. Ewing, *Bull. Am. Phys. Soc.* **8**, 296 (1963).

[3] C. Bussolati *et al.*, *Phys. Rev.* **136**, A1756 (1964).

energy straggling in the dead layer; however, further measurements, described below, indicate this effect to be negligible. The detector response was linear throughout this energy range, and extrapolation to zero energy indicated again a negligible dead layer in the gold film.

To extend the lower energy range of the silicon-barrier detectors, use has been made of a field-effect transistor preamplifier (FET).[4] The purpose was twofold: (1) to physically locate the preamplifier in the vacuum chamber adjacent to the crystal to minimize input capacity; and (2) to get the FET preamplifier to operate in a magnetic field. The experimental model consisted of four field-effect transistors arranged in the shape of a toroid with the silicon detector in the center. Both the entire preamplifier and detector were cooled with liquid nitrogen. The noise width was 2.86 kev as determined by the precision mercury pulser, where this width includes the effects of the entire system – preamplifier and detector. Induced microphonics caused by external vibrations were the limiting factor in the minimum measured noise width. Flow of liquid nitrogen through the cooling circuit increased the microphonics to such an extent that it was necessary to obtain data by interrupting the flow of liquid nitrogen. Shown in Fig. 5.8 are two pulse-height spectra obtained from 7.2- and 9.0-kev protons. The FWHM's determined by background subtraction from typical curves were 3.35 and 3.15 kev respectively. The optimum resolution (FWHM) was 3.0 kev, obtained with protons whose energies were between 20 and 50 kev. Also, the optimum resolution was a function of the crystal and preamplifier temperature and was obtained several minutes after interrupting the flow of liquid nitrogen.

Magnetic field effects in the preamplifier performance were determined by placing the assembly in the field of DCX-1. In placing the detector in the region of high magnetic field, the support structure was redesigned, and this increased the microphonics. Using the mercury pulser the resolution of the detector was 8.0 kev with or without the magnetic field. Experiments are continuing in the direction of microphonic elimination by resupporting and devising a cooling system free of oscillations.

[4]The preamplifier was designed and supplied by ORTEC.

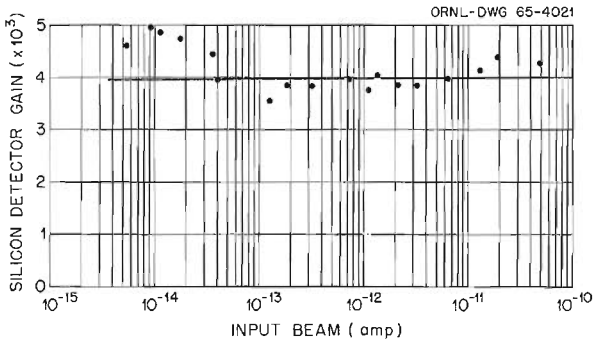

Fig. 5.4. Silicon-Detector Gain as a Function of 20-kev H^+ Current.

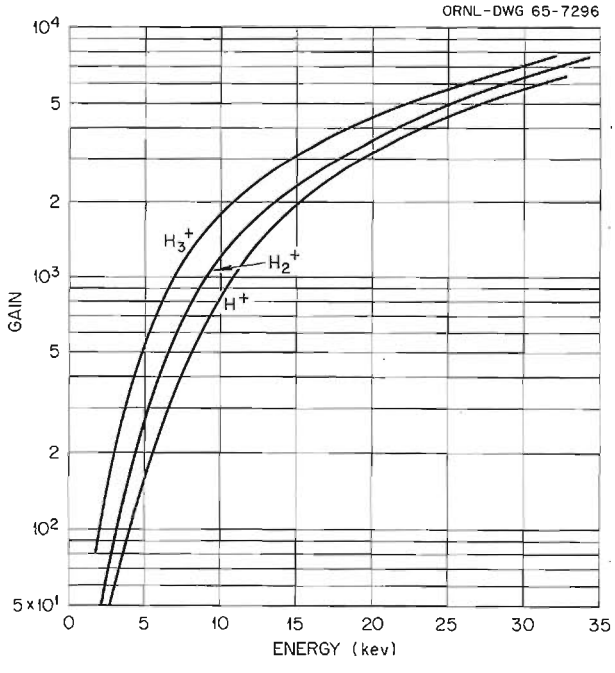

Fig. 5.5. Silicon-Detector Gain as a Function of Particle Energy.

ORNL-DWG 65-4017

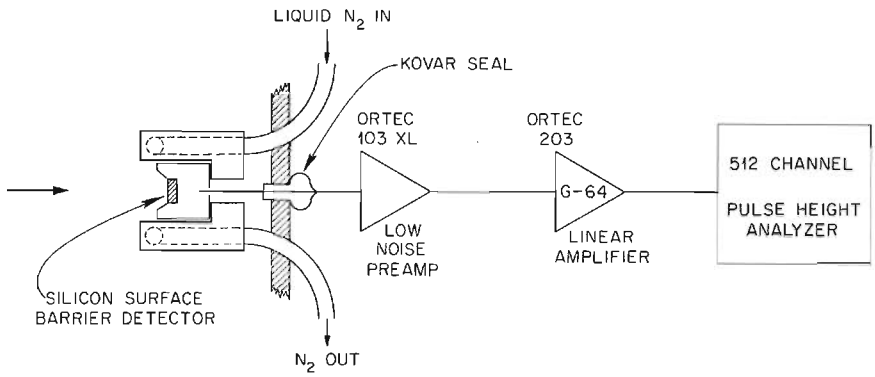

Fig. 5.6. Schematic Diagram of Liquid-Nitrogen-Cooled Silicon Detector.

ORNL-DWG 65-4020

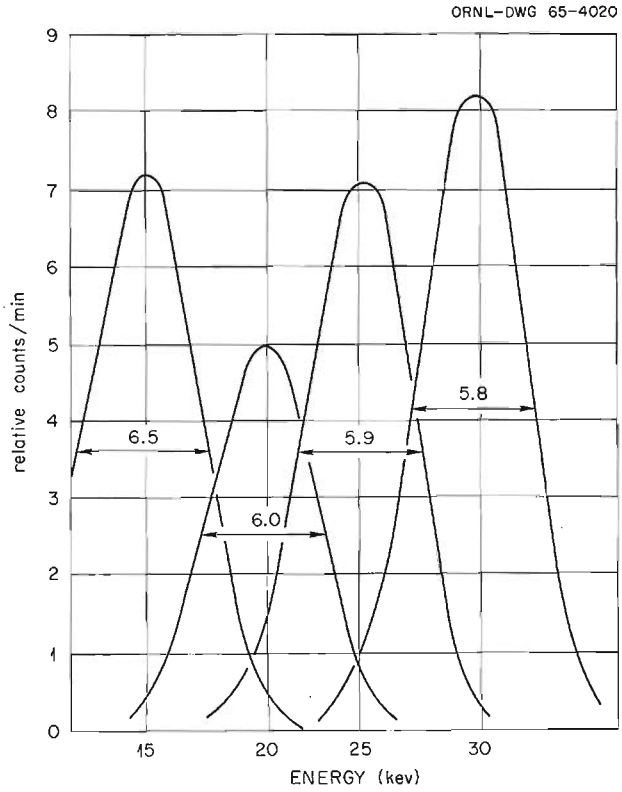

Fig. 5.7. Energy Spectrum of Low-Energy Protons.

ORNL-DWG 65-7297

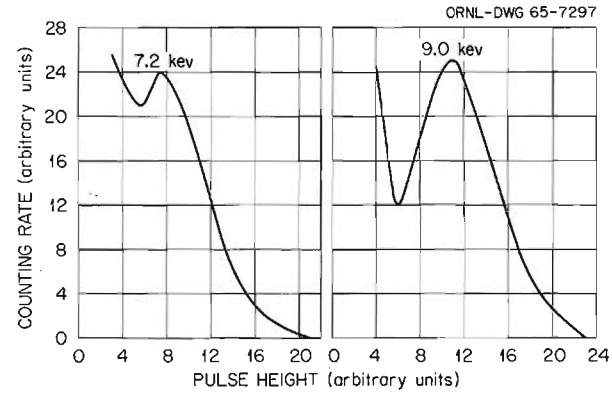

Fig. 5.8. Energy Spectrum of 7.2- and 9.0-kev Protons Using a Silicon-Barrier Detector with an FET Preamp.

5.3 THERMAL DETECTORS

Preliminary measurements have been completed using a barium titanate crystal as a thermal detector for neutral beams. Cooper[5] has reported the use of these crystals in measuring the time history of the energy radiated from a pulsed discharge. Barium titanate is in the class of pyroelectric materials which undergoes a spontaneous polarization when radiation or heat is absorbed on

[5]J. Cooper, *J. Sci. Instr.* 39, 467 (1962).

one face of the crystal. This change of polarization due to heating of the crystal gives rise to a pyroelectric current whose magnitude depends on the incident radiation. Barium titanate is spontaneously polarized at room temperature, and the rate of change of polarization with temperature is approximately linear up to the Curie point of 110°C. Calculations by Cooper have also shown that minimum detectable power is 10^{-11} w with time constants of the order of microseconds.

In the experiment a BaTi disk-shaped crystal was obtained with a silver film on the front and back surfaces. The front, or target, surface was thermally isolated and then grounded by soldering a small wire to the film. An electrical lead was taken from the rear surface and fed into a dc electrometer whose ultimate sensitivity was 10^{-13} amp. A 10-kev proton beam of 1.3×10^{-8} amp was directed on the crystal. The minimum detectable power corresponding to polarization currents of 10^{-12} amp was approximately 10^{-4} w/cm^2, which is several orders of magnitude greater than expected. For incident fluxes of 10^{-4} w/cm^2 the time constant was determined by the electrometer and not by the crystal response. Experiments are continuing to increase the sensitivity and to measure the time constant directly.

5.4 ENERGY LOSS IN FOILS

The technique of using the silicon surface-barrier detector as a dc detector has been extended to provide a novel means of measuring the energy loss of protons passing through foils. The dc gain of the detector remains constant over long periods of time. Energy losses were determined by measuring the detector gain and then placing a metal foil in front of the detector and again measuring the gain. The shift in the gain curve as a function of energy is the integral energy loss suffered by the proton in passing through the foil.

In Fig. 5.9 is shown the gain of a typical detector with and without a thin aluminum foil.[6] The thickness of the 600-A foil was determined from known evaporation rates of aluminum onto a substratum. Shown in Fig. 5.10 is the integral energy loss as a function of the proton energy. These results are compared to some recent results[7] where an energy-analyzing technique was used in determining energy loss. As is seen there is a discrepancy of a factor of 2 to 3, which seems to be outside of our experimental errors. The method of determining the film thickness is probably accurate to only 20%. Another source of error may arise from large-angle scattering events in the foil, giving rise to a class of hydrogen atoms and ions of sufficient angular spread to miss the detector. Further measurements are necessary to resolve these discrepancies.

[6]Foil provided by W. B. Ard of Electron-Cyclotron Heating Group.

[7]J. H. Ormrod *et al.*, *Can. J. Phys.* **43**, 275 (1965).

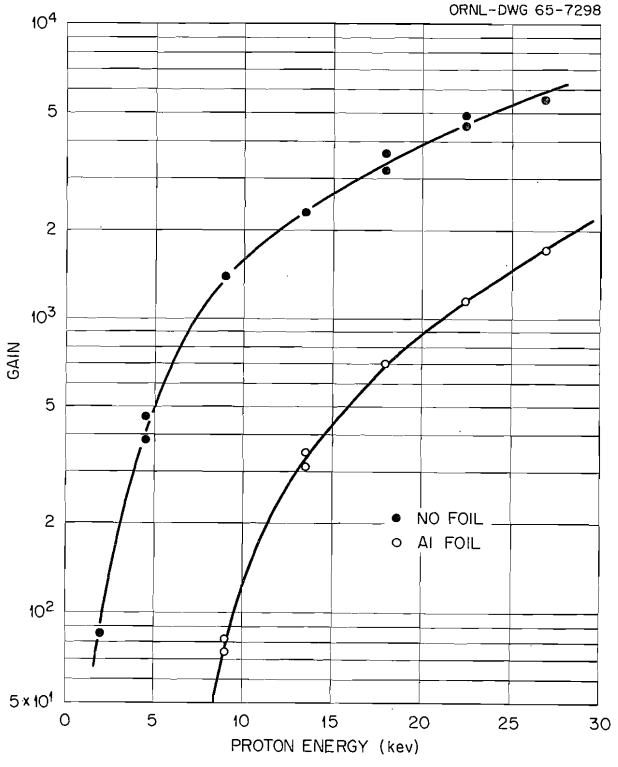

Fig. 5.9. Silicon-Barrier-Detector Gain as a Function of Proton Energy With and Without an Aluminum Foil in Front of the Detector.

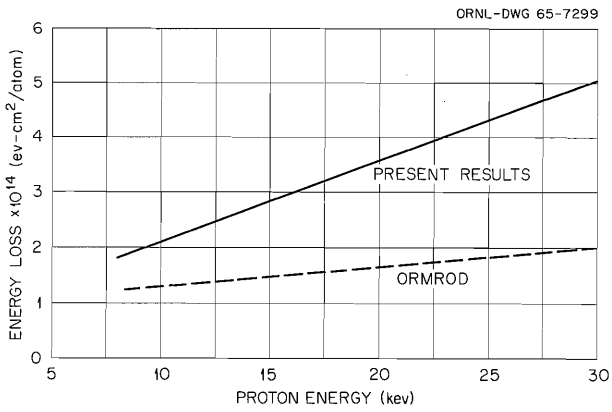

Fig. 5.10. Energy Loss of Protons Passing Through Aluminum Foil.

5.5 ATOMIC AND MOLECULAR PROCESSES INFORMATION CENTER

C. F. Barnett J. C. Thompson

The establishment of the Atomic and Molecular Processes Information Center (AMPIC) was an outgrowth of a compilation concerning atomic and molecular collisions of interest in thermonuclear research. This compilation, designated as ORNL-3113R, comprised a collection of curves, tables, and bibliographical information. The present activities broaden the scope to cover other fields of research such as astrophysics, space physics, communications, etc.

The total field of atomic and molecular collisions is enormous, and the program is being started by restricting our aims so that a thorough and critical job can be done in a useful region. Thus, we are concentrating upon the field of our major experience and region of our current experimental program. The following categories are listed as our main concern: (1) Heavy-Particle–Heavy-Particle Interactions, (2) Interactions of Particles with Electric and Magnetic Fields, and (3) Particle Penetration into Macroscopic Matter. In addition to these fields we are extending our thermonuclear compilation by adding a section concerned with particle interactions with surfaces.

The activities of the information center are based on the belief that the data must be collected and evaluated by competent technical people working in atomic and molecular physics or chemistry. Thus, this phase of the work will be executed by our research staff spending 25% of their time working on collection and evaluation problems. This effort is being augmented by consultant contracts with four members of the Physics Department staff of the Georgia Institute of Technology.

The present activities are concerned chiefly with literature search of 55 journals and 5 abstract journals. Current literature since 1963 has been searched and the relevant articles indexed. Several thousand references found in a partial literature scan since 1950 are now being processed and indexed. Machine translation of the table of contents of Russian journals prior to date of universal translation has proved successful as a means of literature search both from the standpoint of completeness and economy. At the present time studies are being made to develop a data storage and retrieval system using computer techniques.

6. High-Current Ion-Beam Production and Injection

R. C. Davis
R. R. Hall
G. G. Kelley
O. B. Morgan
R. F. Stratton

Studies have continued on the 100-kv test stand for the production of intense hydrogen ion beams in the energy range of 20 to 100 kev. Total hydrogen ion beams of 900 ma can be produced at energies of 70 kev. Well-collimated H^+ beams up to 450 ma can be produced at energies of 60 kev. Attempts to produce intense H_2^+ beams have been limited to only 150 ma from a total hydrogen beam of 300 ma.

Previously, H^+ beams of 100 ma at 60 kev had been obtained through a 1-in. aperture located 12 in. below the magnetic lens.[1] It was found that, when the beam drift space was changed to that shown in Fig. 6.1 (4 ft from lens to main target), only about 30 ma of beam at 60 kev was obtained at the main target. Figure 6.1 also shows an auxiliary coil directly under the source, which had not been added at the time of these initial experiments. Reversing the polarity of the ion source coil so that its field was bucking the stray field of the solenoid lens and then increasing the ampere-turns in this coil by a factor of 2 resulted in H^+ currents up to 90 ma on the main target at 60 kev. Increasing the the arc current in the ion source from a previous maximum of 10 to 12 amp up to 25 amp increased the H^+ beam available on the main target at 60 kev to 200 ma. Adding the 72-turn auxiliary coil around the 2-in.-ID source anode "cup" (Fig. 6.1) increased the H^+ beam to 300 ma at 60 kev, with a total hydrogen ion beam of 500 ma. This 500-ma beam required a 25-amp arc in the source, which was the maximum capacity of the arc supply being used. The arc efficiency was increased by introducing the hydrogen gas into the intermediate-electrode–anode region of the source instead of the filament "compartment." With the above leak position change, total hydrogen ion beams up to 600 ma can be obtained with only 15-amp arc current. There is no significant change in the source operation except a decrease in the gas efficiency. Although 600 ma of beam can be obtained at 60 kv, only 300 ma of this beam is obtained through the limiting apertures to the main target.

By removing the accel-decel neutralizer (Fig. 6.1) and therefore moving the source closer to the magnetic lens (Fig. 6.2), the beam quality was improved, but the system was very unstable because of PIG discharges. "Electron dumps" (radial fins located at 60° intervals) (Fig. 6.2) were incorporated into the system, and, although a small discharge was still visible, it did not affect the stability of the system. Some attempts have been made to improve and simplify these dumps, but without success. A current of 385 ma of H^+ at 60 kev can be obtained on the main target from a total beam of 700 ma using this geometry. Total hydrogen beams up to 900 ma can be obtained, but the main target is still limited to ~450 ma of H^+ at 70 kev.

During the operation of the system shown in Fig. 6.2, the following consistent results are always evident. The source magnet coil never contributes significantly to the operation. The best beam quality and the maximum attainable beam can always be obtained by adjusting the ampere-turns in the auxiliary coil. Under some conditions it is possible to readjust the ampere-turns in the auxiliary coil with the source coil energized so that the beam

[1] R. C. Davis *et al.*, *Thermonuclear Div. Semiann. Progr. Rept. Oct. 31, 1964*, ORNL-3760, pp. 64–68.

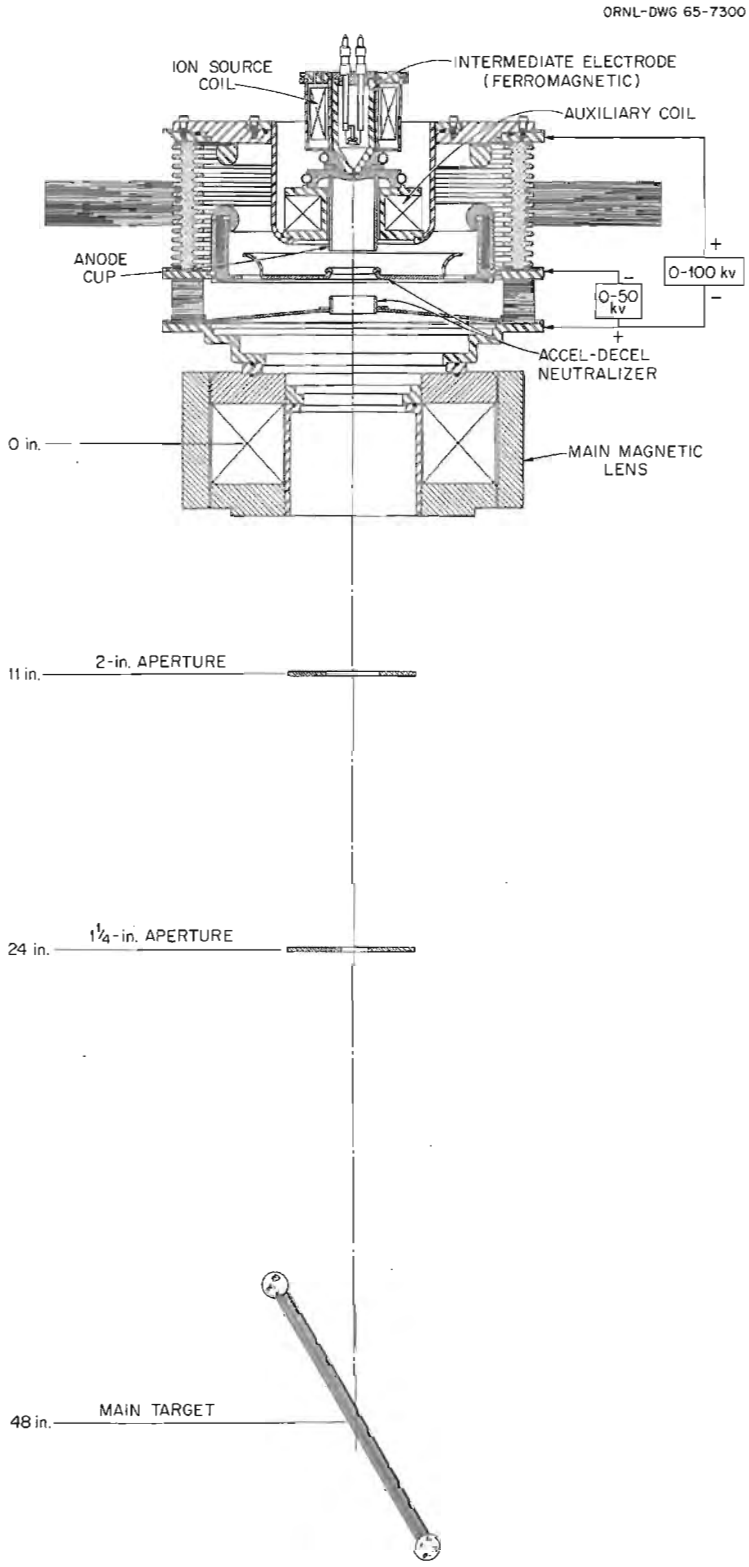

Fig. 6.1. 100-kv Ion-Beam Assembly with Limiting Apertures and Main Target.

ORNL-DWG 65-7301

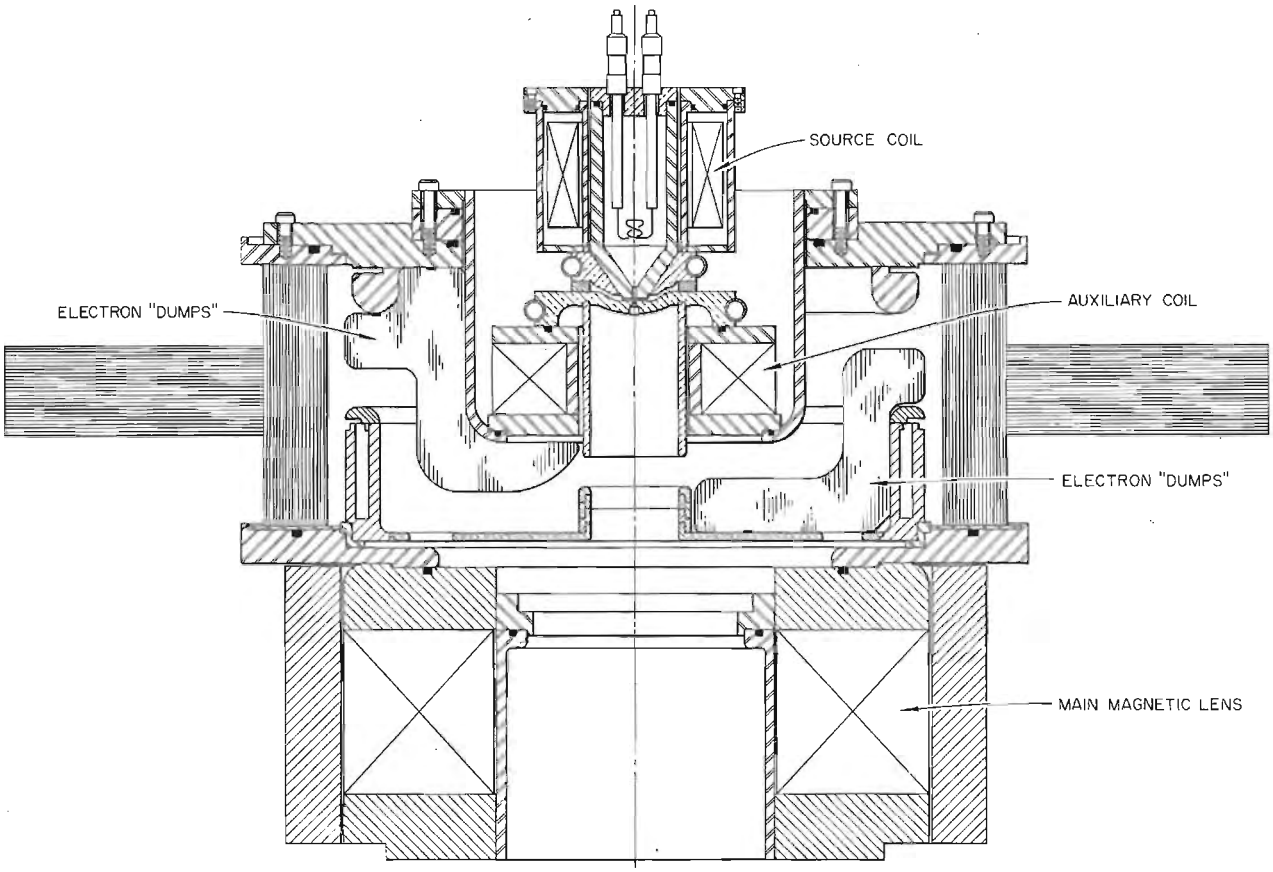

Fig. 6.2. 0–100-kv Ion-Beam Assembly with Electron Dumps Incorporated.

is almost as good as with no current in the source coil. With smaller anode "cups," the optimum ampere-turns in the auxiliary coil are very high. Under these conditions the source coil does not significantly affect the beam over a fairly large range (60 kv, 300 ma, $1\frac{1}{4}$-in. "cup," upper curve, Fig. 6.3). However, under no conditions are the beam quality and magnitude increased by utilizing the source coil in conjunction with the auxiliary coil. Without using the auxiliary coil, no source coil condition can achieve as desirable a beam.

For each source extraction configuration there is an optimum number of ampere-turns in the auxiliary coil at any beam energy, and, therefore, lens strength, to produce a beam with a minimum divergence. Figure 6.4 indicates the variation in the beam on the main target as a function of the current in the auxiliary coil, and indicates auxiliary coil currents at which axial magnetic field scans were made for Fig. 6.5. The best beam is always found with the auxiliary coil bucking the lens coil, and the magnetic scans indicate that in each case the optimum condition is with the axial magnetic field intensity essentially zero in the region of the plasma surface. These two plots also indicate that there is a larger percentage of the beam available as a useful H^+ beam at 60 kv and 300 ma when the anode "cup" is reduced from 2 to $1\frac{1}{4}$ in. In Fig. 6.6, a summary of the H^+ beam found calorimetrically on the main target at 60 kv is shown as a function of the total extracted current for several extraction geometries. The anode "cup" size was varied from 2 down to $\frac{5}{8}$ in. Figure 6.6 is incomplete in that it only indicates the beam available on the main target and does not evaluate the detailed variations in the beam quality. The initial results in the studies

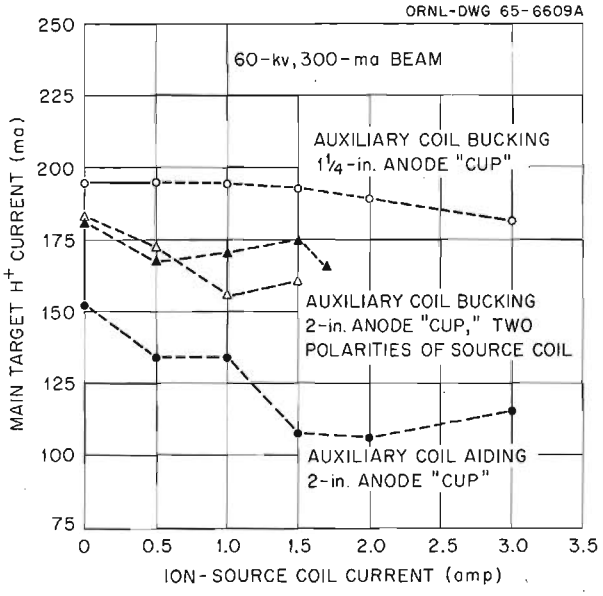

Fig. 6.3. H^+ Beam to Main Target as a Function of Current in Ion Source Coil.

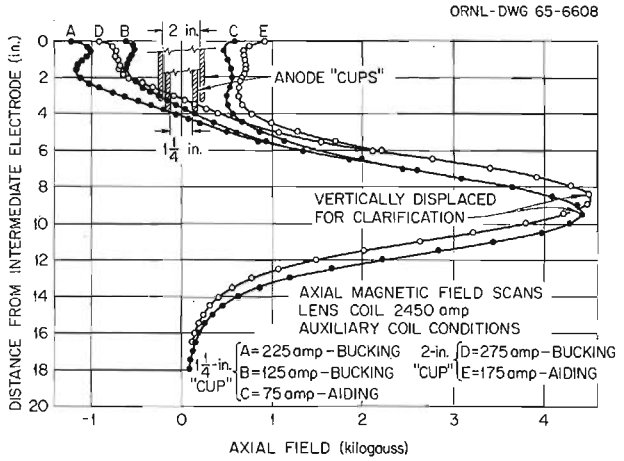

Fig. 6.5. Axial-Magnetic-Field Scans Through the Beam Extraction Region for the Conditions Indicated in Fig. 6.4.

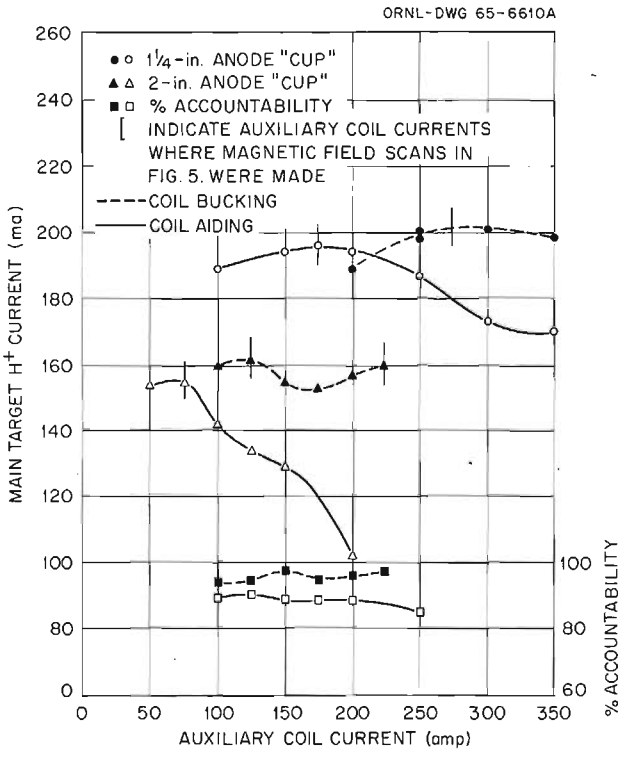

Fig. 6.4. H^+ Beam to Main Target as a Function of Current in Auxiliary Coil for Two Sizes of Anode "Cups."

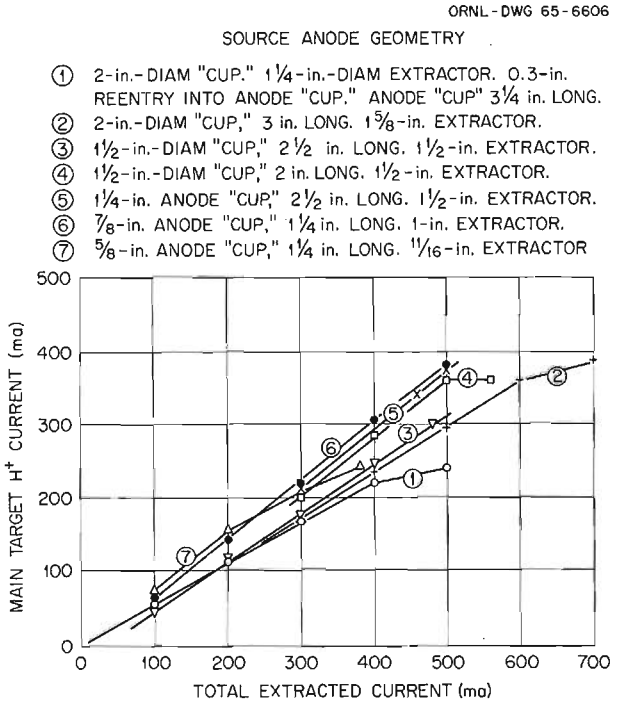

Fig. 6.6. H^+ Current to Main Target as a Function of Total Extracted Hydrogen-Ion Current for Various Source Extraction Geometries.

have indicated that for a total hydrogen ion beam of ~500 to 600 ma at 60 kev the optimum source extraction geometry is that shown in Fig. 6.7. This anode "cup" is $1\frac{3}{4}$ in. long and $\frac{7}{8}$ in. in inside diameter, and is located with the "cup's" lower surface only $\sim\frac{1}{8}$ in. below the lower surface of the auxiliary coil and 6 in. above the center of the magnetic lens. Anode-to-extractor-electrode spacings of ~0.3 in. are typically used for 60-kv extraction. This geometry is almost certainly not ideal and will probably be improved by future study. As is evident from Fig. 6.7, there are many interrelated variables involved when one tries to determine the best extraction geometry. For example, for every size of anode "cup" there is a corresponding optimum length that allows the plasma from the source to fill the cup but prevents large plasma losses to the "cup" walls. For large variations in the "cup" size, it is necessary to vary the inside diameter and thickness of the auxiliary coil.

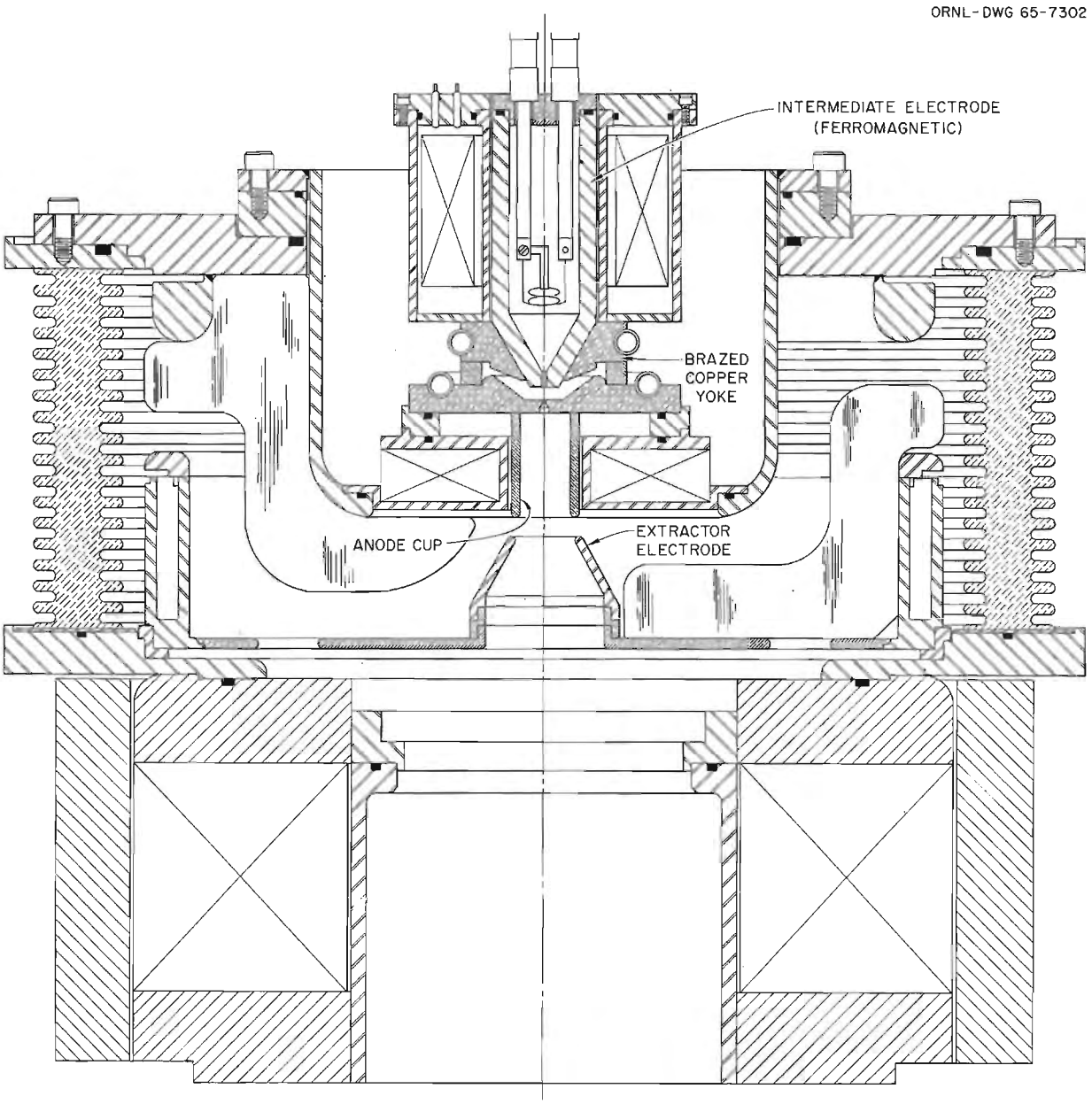

Fig. 6.7. 0–100-kv Ion-Beam Assembly with One of the Better Extraction Geometries.

As described above, the ion source coil, which is a basic part of the duoplasmatron ion source, did not improve the magnitude or quality of the beam with the systems shown in Figs. 6.2 and 6.7. An even more basic part of the duoplasmatron, the ferromagnetic intermediate electrode, was found to offer no evident advantages but certainly some potential disadvantages for these beam systems. It was found that, when this electrode is made from copper, the source performs satisfactorily for the large beams under consideration. Since one desirable operating condition for this beam system is a large dc proton beam with high gas efficiency, it is desirable to utilize a very dense arc in the ion source. For the production of a total hydrogen ion beam of ~1 amp with the above system, source arc currents of 30 to 50 amp are required for high gas efficiency, and the proper cooling of the iron intermediate electrode requires the difficult-to-fabricate brazed copper yoke shown in Fig. 6.7. By incorporating the copper intermediate electrode, it has been possible to build a very simple, flexible source for operating with these intense hydrogen ion beams (Fig. 6.8).

ORNL-DWG 65-7303

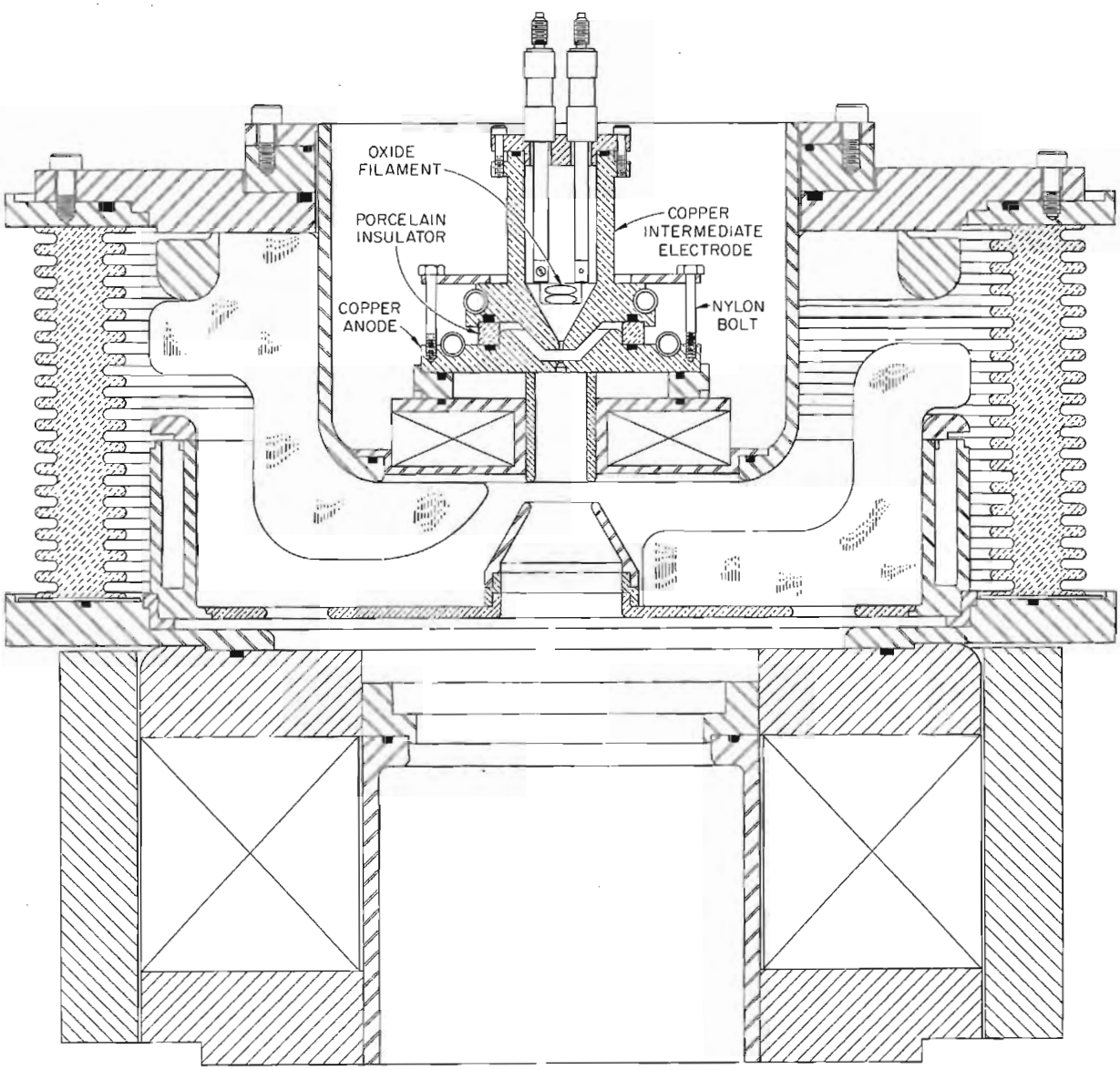

Fig. 6.8. 0–100-kv Ion-Beam Assembly with a New, Simple Ion Source.

The H^+ beam from this source is determined calorimetrically on the main target (Fig. 6.1) and is shown in Fig. 6.9. More total beam can be extracted (~1 amp), but the H^+ target current increases only slightly (~450 ma).

The sources described above are very efficient in producing H^+ beams (70 to 85%) but are very limited in the production of the intense H_2^+ beams important for molecular ion injection in thermonuclear experiments. With the 600-kv test stand,[2] H_2^+ beams of 90 to 95 ma have been obtained. Numerous attempts to increase the magnitude of this beam with the 100-kv test stand have been made with no great success. The source parameters found desirable for H_2^+ production previously[2] have been tried with large total hydrogen beams (0 to 900 ma). In order to make the H_2^+ beam be a significant fraction (50% or greater) of the total beam with currents of 200 ma or greater, it has been necessary to drastically modify the source anode. By enlarging the anode aperture of the source shown in Fig. 6.8 from 0.070 to 0.750 in., a 135-ma 600-kv H_2^+ beam can be produced with a total extracted beam of 270 ma. The gas leak is into the intermediate electrode, which has a 0.1-in. aperture. As would be expected, the gas efficiency of this source is poorer than the proton sources described above. Some of the sources that have appeared encouraging for H_2^+ production operate stably only over a very small range of variation in source operating parameters and are very difficult to evaluate fully. Since this problem is essential to future molecular injectors, it will continue to be pursued.

Modification of the 100-kv test stand that will allow a beam drift distance of 8 to 10 ft instead of the 4 ft available at present is planned within the next few weeks. This facility will provide space for a more detailed evaluation of the beam quality, beam analysis, and neutral forming devices. This facility will also have an increased pumping speed.

[2]G. G. Kelley, N. H. Lazar, and O. B. Morgan, *Nucl. Instr. Methods* 10, 263–71 (1961).

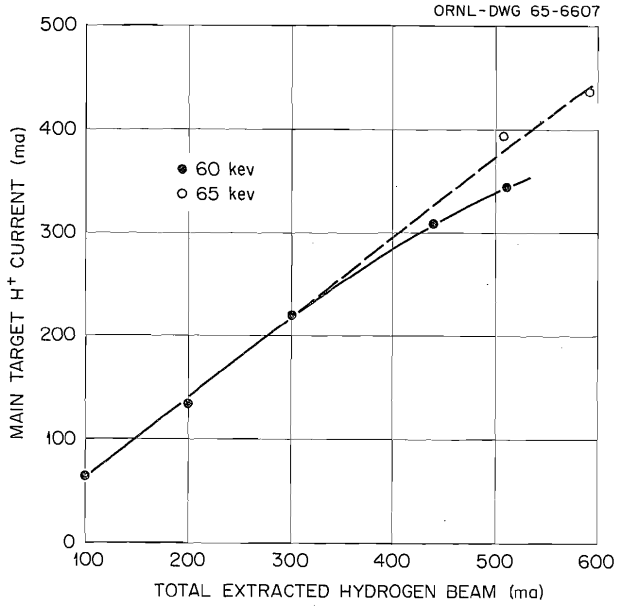

Fig. 6.9. H^+ Current to Main Target as a Function of Total Extracted Hydrogen Current for Ion Source Shown in Fig. 6.8.

7. Plasma Theory and Computation

7.1. PROSPECTS FOR MIRROR CONFINEMENT

T. K. Fowler

With this report, the Oak Ridge theory group has completed several investigations of the feasibility of stable confinement of thermonuclear plasmas by magnetic mirrors. The following set of parameters would avoid the known instabilities at reactor densities and typifies our findings. We suppose a magnetic well with well depth ΔB perpendicular to the field, and a central field value B. Then, for stability,

$$\text{mirror ratio} \parallel B = 3.3 ,$$
$$\Delta B/B = 0.3 ,$$
$$\beta = 0.3 ,$$
$$R = L = 100\ \rho_i ,$$
$$T_e/T_i \leqq 0.3 .$$

Here, ρ_i is the ion Larmor radius, R is the plasma radius, L is the plasma length, and $T_{e,i}$ are the average electron and ion energies. These parameters are chosen to avoid the known instabilities, as follows:

1. Interchange – in a magnetic well, the critical β is $1 - B^2/(B + \Delta B)^2 = 0.4$.[1] We took $\beta = 0.3$, safety factor $4/3$. Stability holds also taking into account the ambipolar potential.[2]
2. Mirror, Alfven instability – avoided with chosen β and mirror ratio.[3]
3. Universal instabilities – according to Sect. 7.2, all types of universal modes are prevented by a magnetic well of depth $\Delta B/B > (T_e/T_i)$, hence our upper limit on T_e/T_i.
4. Harris instability – avoided by $(T_\perp/T_\parallel)_i < 2$ consistent with the mirror ratio.[4]
5. Loss cone instability, ion-ion interaction – avoided if ion energy spread > 30% of the mean,[5] as would be expected at reactor densities: see Sect. 7.4.
6. Loss-cone–drift-flute instability – according to Sect. 7.3, avoided if $R/\rho_i > (\omega_{pi}/\omega_{ci})^{4/3}$. For mirror confinement, we find the typical value to be $\omega_{pi}/\omega_{ci} = 30$, hence the choice $R = 100\ \rho_i$. For example, $\omega_{pi}/\omega_{ci} = 30$ for deuterons if $n = 10^{14}$/cc and $B = 60$ kilogauss.
7. Loss cone instability propagating along B – according to ref. 6, avoided if $L < 300\ \rho_i$ with $\omega_{pi}/\omega_{ci} = 30$ as above; according to ref. 7, avoided if $L < 100\ \rho_i$. We took the shorter length.

For lower β and lower T_e/T_i, the well depth ΔB can be reduced if necessary.

Of these conditions, the length criterion, item (7) above, is probably most subject to further review. This concerns loss cone instability waves propagating along the magnetic field. Rosenbluth and Post[6] find that these waves are convective, and with no reflection at the ends, they would be damped if the machine is short but a practical length, as above. On the other hand, with end reflection, standing waves would develop. Thus

[1] J. B. Taylor and R. J. Hastie, *Phys. Fluids* **8**, 323 (1965).

[2] T. K. Fowler, *Phys. Fluids* **8**, 544 (1965).

[3] R. F. Post, *Nucl. Fusion*, Suppl. 1, 99 (1962).

[4] For example, Y. Shima, *Thermonuclear Div. Semiann. Progr. Rept. Oct. 31, 1964*, ORNL-3760, p. 72.

[5] R. A. Dory, G. E. Guest, and E. G. Harris, *Phys. Rev. Letters* **5**, 131 (1965).

[6] M. N. Rosenbluth and R. F. Post, *Phys. Fluids* **8**, 547 (1965).

the amount of reflection is crucial. Recent calculations[7] of reflection assuming a diffuse edge give a critical length somewhat shorter than ref. 6, though still not impractical, and this is the length we chose above. However, probably we have not heard the last of this subject. Fortunately, this principal point of weakness in the argument in favor of stability with mirror confinement is subject to experimental study at densities far below that required for reactors. For example, the present generation of high-energy injection experiments should shed light on this question.

7.2. ANOMALOUS PLASMA DIFFUSION IN MAGNETIC WELLS[8]

T. K. Fowler G. E. Guest

We have treated radial plasma transport in magnetic wells (magnetic gradient $dB/dr > 0$) with particular attention to low-frequency instabilities *not* stabilized by the positive gradient ($\omega < \omega_{ci}$, $k\rho_i < 1$). We take β small. The unperturbed plasma departs from thermal equilibrium only in the azimuthal current and radial pressure profile inherent in confinement. It is found that, if $dB/dr > 0$ and $\Delta B \equiv R(dB/dr) > B(T_e/T_i)$, the $E \times B$ "diffusion" coefficient is

$$D_\perp < (cT_i/eB)(\rho_i/R)(T_e/T_i + m_e/m_i)^{1/2}\,, \quad (1)$$

where ρ_i is the ion gyroradius and R is the plasma radius. If dB/dr is only positive on the average, there is an additional requirement that $L/R < (T_i/T_e)^{1/2}$, where L is the length along B over which dB/dr is negative. Applications to various thermonuclear magnetic confinement geometries are discussed. Results in some cases are encouraging and complement our previous conclusion that stochastic diffusion is also tolerable for fusion. Open questions are the β limit and the nonlinear behavior of certain velocity-space instabilities at $\omega \gtrsim \omega_{ci}$, the ion gyrofrequency.

In deriving Eq. (1), we take $D_\perp = \lambda(cE_\perp/B)$, where λ is a radial "mixing length." We estimate $E_\perp$ from the available free energy composed of two terms, $\delta W = \delta W_0 + \delta W_1$. The first term, δW_0, is the usual stabilizing term in a magnetic well, or an "average" well, if the magnetic moment μ and the longitudinal invariant J are conserved,

$$\delta W_0 = \left(\lambda \frac{dn}{dr}\right)\left(\lambda\mu \frac{dB}{dr}\right). \quad (2)$$

The term δW_1 accounts for violations of adiabatic invariance. There can be a large positive contribution to δW_1 from the release of thermal energy in a manner analogous to expansion cooling of a gas, which accounts for anomalous diffusion in several experiments where $dB/dr < 0$. We estimate this energy from nonlinear thermodynamics,[9]

$$\delta W_1 \lesssim \frac{\lambda^2}{R^2}\frac{T_e}{T_i}\,. \quad (3)$$

For sufficiently positive dB/dr, δW_0 is negative and overcomes δW_1, a condition equivalent to $\Delta B/B > T_e/T_i$ above. Essentially this stability condition is also obtained in calculations of the stabilization of universal modes by a magnetic well simulated by gravity.[10] Since δW_0 is incorrect if λ is smaller than the gyroradius, in Eq. (1) we allowed for the possibility of weak diffusion by instabilities with $\lambda \lesssim \rho_i$. Actually, in a short mirror machine such as was discussed in Sect. 7.1, such modes probably will not grow.

7.3. FLUTE INSTABILITIES AT ION GYROFREQUENCY

Y. Shima T. K. Fowler

We have examined electrostatic instabilities in a plasma cylinder in a uniform magnetic field. Because of their special importance to anomalous diffusion, we have looked for "flute modes," that is, electric field perpendicular to $\vec{B}$, at the ion gyrofrequency and its harmonics. In particular, we look for modes driven by the radial density gradient rather than ion-ion interactions, studied by Dory, Guest, and Harris (Sect. 7.4).[11] These flute modes are not damped in short plasmas, as

[7] R. E. Aamodt and D. L. Book, a preliminary report at the Annual Sherwood Theory Meeting, Princeton University, April 22–23, 1965.

[8] Abstract of paper submitted for presentation at the *Second International Conference on Plasma Physics and Controlled Nuclear Fusion Research*, Culham, England, Sept. 6–10, 1965.

[9] T. K. Fowler, *Phys. Fluids* **8**, 459 (1965).

[10] J. D. Jukes, *Phys. Fluids* **7**, 1468 (1964); F. F. Chen, *Princeton Plasma Phys. Lab. Rept.* MATT-311 (November 1964).

[11] R. A. Dory, G. E. Guest, and E. G. Harris, *Phys. Rev. Letters* **5**, 131 (1965).

are the propagating modes discussed by Rosenbluth and Post (see discussion, Sect. 7.1). Fortunately, however, the threshold density proves to be high for large plasmas.

We treat several cases, all derived from the problem studied by Mikhailovsky and Timofeev.[12] Our example of their problem is a Maxwellian distribution in rigid-body rotation, having the form for ions and electrons,

$$f_0 \propto \exp\left[-(\epsilon + \alpha p_\theta)/T\right] \qquad \text{Maxwellian}, \qquad (1)$$

where $\epsilon = \frac{1}{2}\, mv^2$ is the energy and p_θ is the canonical angular momentum for the appropriate species. The magnetic field is uniform. This distribution describes an infinitely long cylinder in rigid-body rotation at angular velocity α with a radial density profile $\propto \exp(-r^2/R^2)$. Neutrality is achieved by proper relation of α_i and α_e. We obtain the dispersion relation in cylindrical geometry without resorting to the "local" approximation, as follows. Because of the symmetry, solutions for the potential take the form $\phi = \phi(r) \exp i(l\theta - \omega t)$. Combining the linearized Vlasov equation and Poisson's equation yields an equation for $\phi(r)$ of the form,

$$-\frac{1}{r}\frac{\partial}{\partial r}\left(r\frac{\partial\phi}{\partial r}\right) + \frac{l^2}{r^2}\phi(r) = \int r'\, dr'\, K(r,r')\, \phi(r')\,. \qquad (2)$$

Because of the singular term on the left, $\phi \propto r^l$ at $r \to 0$, and the right side, proportional to f_0, vanishes at large r, which requires $\phi \to r^{-l}$ as $r \to \infty$. Together, these conditions require

$$kR \gtrsim l\,, \qquad (3)$$

where k^{-1} is a characteristic length for $\phi(r)$ at $r \lesssim R$. Further, assuming (3), the kernel K is approximately diagonalized by Bessel solutions, $\phi(r) \propto J_l(kr)$. Thus, this diagonal approximation of the integral term in (2) is sufficient for solutions satisfying the proper boundary conditions. Essentially the dispersion relation of Mikhailovsky and Timofeev follows immediately, if one also retains just one resonance term, at $n \sim \omega/\omega_{ci}$, and takes their condition

$$k\rho_i \gtrsim n\,. \qquad (4)$$

[12] A. B. Mikhailovsky and A. V. Timofeev, *Soviet Phys. JETP (English Transl.)* **17**, 626 (1963).

Here, ρ_i and ω_{ci} are the ion gyroradius and gyrofrequency.

Two other important models are derived from the Maxwellian distributions, $f_{0i,e}$ in Eq. (1), by differentiation by parameters, as in ref. 11. These are the loss cone model, for ions, with distribution

$$f_{0i} \to \frac{\partial}{\partial T_i}(T_i f_{0i})\bigg|_R \sim \epsilon_i\, f_{0i}\,, \qquad \text{loss cone}, \qquad (5)$$

and the shell,

$$f_{0j} \to -\frac{1}{R^2}\frac{\partial f_{0j}}{\partial\left(\frac{1}{R^2}\right)}\bigg|_T \sim P_{\theta j}, f_{0j}\,, \quad j = i, e, \quad \text{shell}.$$

The density profile for the loss cone is $\propto \exp(-r^2/R^2)$, and for the shell, $\propto r^2 \exp(-r^2/R^2)$. Since $K(r,r')$ is linear in f_0, the dispersion relations are obtained from the Maxwellian case simply by applying the indicated differentiations to the dispersion relation itself.

The dispersion relation for all cases can be put in the simple form

$$1 = -\alpha\left(\frac{1}{x} - \frac{\beta}{x-n}\right), \qquad x = \omega/\omega_{ci}\,, \qquad (6)$$

$$\alpha = \frac{C\,\dfrac{2l}{k^2R^2}\,\dfrac{\omega_{pi}^2}{\omega_{ci}^2}}{1 + \dfrac{\omega_{pi}^2}{\omega_{ci}^2\,\lambda_i}\,A}\,, \qquad \lambda_i = \tfrac{1}{2}\,k^2\rho_i^2\,,$$

$$\beta = \frac{1}{\sqrt{2\pi\lambda_i}}\left(1 + B\frac{k^2R^2n}{2l\,\lambda_i}\right).$$

Instability occurs if $\beta > 0$ and $\alpha \sim -n$, with constraints (3) and (4), with growth constant $\gamma \sim \beta^{1/2}$. Here, $B = 1$ for the Maxwellian, -1 for the loss cone, and 0 for the shell; $C = 1$ for the Maxwellian and loss cone, thereby dictating $l < 0$ and waves propagating azimuthally in the direction of ion diamagnetic current, while $C = -1$ for the shell, dictating unstable waves propagating in the direction of the ion diamagnetic current on the inner, steeper surface of the shell.

The quantity A, a stabilizing term coming from nonresonant particles, is shown in Table 7.1 with the results. In columns 1–3 we give the three

Table 7.1. Various Parameters for Loss Cone Instability Flute Modes

Parameter	1 Maxwell	2 Loss Cone	3 Shell	4 Loss Cone with Electron Term
A	1	$(2\sqrt{2\pi\lambda_i})^{-1}$	0	A_e
ω_{pi}/ω_{ci} at threshold	R/ρ_i	$(R/\rho_i)^{3/4}$	$(R/\rho_i)^{1/2}$	$(R/\rho_i)(\sqrt{A_e}/C_{0e})$
$k\rho_i$	R/ρ_i	$(R/\rho_i)^{1/2}$	1	$(R/\rho_i)\, A_e/C_{0e}$
$D_\perp \equiv \gamma/k^2$	$(\rho_i/R)^{5/2} D_B$	$(\rho_i/R) D_B$	D_B	$(\rho_i/R)^{5/2}(C_{0e}/A_e)^3 D_B$

cases omitting the electron contributions to A in order to show the effect of changes in the ion distribution. Then, in the last column, we repeat the loss cone case retaining only the electron contribution to A, being appropriate when A_e exceeds A in column 2. For this case $C = C_{oe}$ in (6). Here,

$$A_e = T_i/T_e\,(1 - C_{oe})\,, \tag{7}$$

$$C_{oe} = e^{-\lambda_e} I_0\,(\lambda_e)\,,$$

$$\lambda_e = \tfrac{1}{2}\, k^2\, \rho_e^2\,.$$

Note that, at $T_e \to 0$,

$$\left.\begin{aligned} A_e &\to 2\lambda_i \frac{m_e}{m_i} \\ C_{oe} &\to 1 \end{aligned}\right\} \; T_e \to 0\,. \tag{8}$$

Since the threshold density turns out to be lowest for the ion gyrofrequency in all cases, we tabulate only the case $n = 1$. For comparison, we also list as a rough estimate of anomalous radial diffusion $D_\perp \sim \gamma/k^2$ measured in units of $D_B = \rho_i^2\, \omega_{ci} \equiv cT_i/eB$.

Note the progressive weakening of nonresonant ion stabilization from the Maxwellian case to the shell, and the corresponding decrease in the resonant wavelength, k^{-1}.

We draw two conclusions. First, with the loss cone model representing mirror confinement, the threshold density is very high in large plasmas. Specifically, for parameters given in Sect. 7.1 ($\omega_{pi}/\omega_{ci} = 30$) the plasma is stable if $R \gtrsim 100\, \rho_i$, which accounts for the choice of R in Sect. 7.1.

Our second conclusion is that one must be careful to arrange injection so that the plasma density is greatest at the center. Otherwise, as in the shell model investigated, with parameters given in Sect. 7.1 instability may occur at much lower densities $\sim 10^{13}$/cc.

7.4. UNSTABLE ELECTROSTATIC PLASMA WAVES PROPAGATING PERPENDICULAR TO A MAGNETIC FIELD

R. A. Dory G. E. Guest
E. G. Harris[13]

In assaying the potential hazards of electrostatic microinstabilities it is important to distinguish between those growing waves which do or do not give rise to electric fields along the confining magnetic field lines. Thus, if $k_{||} \neq 0$ ($k_{||}$ is the component of propagation vector parallel to the external magnetic field) the waves may be damped through their interaction with an electron population of very modest temperature. But if $k_{||} = 0$, damping by electrons is negligible for electron temperatures of interest in present thermonuclear devices.

[13]Consultant from the University of Tennessee.

A search for growing electrostatic waves with $k_{\parallel} = 0$ has been made using the usual Harris dispersion relation[14] and the set of unperturbed ion distribution functions given by

$$g_0(v_\perp^2) = \int dv_{\parallel}\, f_0(v_\perp^2, v_{\parallel}^2)$$

$$= \frac{1}{\pi \alpha_\perp^2 j!}\left(\frac{v_\perp}{\alpha_\perp}\right)^{2j} \exp\left(-\frac{v_\perp^2}{\alpha_\perp^2}\right), \qquad (1)$$

with $j = 1, 2, 3, \ldots$.

These distributions are peaked in perpendicular speed with peak widths which decrease with increasing j. In fact, as $j \to \infty$, the functions approach the Dirac delta distribution. Since $g_0(0) = 0$, these distributions simulate some of the important properties of the "loss cone" inherent in magnetic mirror confinement.

If $k_{\parallel} = 0$, the dispersion relation has the form

$$\frac{k^2}{\omega_p^2} = \sum_{n=-\infty}^{\infty} \frac{n\omega_c}{\omega + n\omega_c}\, \hat{D}_n(k)\,,$$

where

$$\hat{D}_n(k) = 2\pi \int v_\perp\, dv_\perp\, J_n^2\left(\frac{k_\perp v_\perp}{\omega_c}\right) \frac{1}{v_\perp} \frac{d}{dv_\perp}\, g_0(v_\perp^2)$$

and ω_c is the ion gyrofrequency. Unless the perpendicular electron temperature is large compared to the ion temperature, the electron contribution can be neglected in considering low-frequency disturbances, $\omega \sim \omega_c$.

One finds that growing waves may occur at frequencies

$$n < \omega/\omega_c < n + 1$$

if

$$\hat{D}_n < 0\,, \qquad \hat{D}_{n+1} > 0$$

and if the plasma density exceeds a threshold value of order $\omega_p/\omega_c \gtrsim 3$. The dependence of the threshold density on the width (in $v_\perp$) of the distribution function is shown in Fig. 7.1 for a "flutelike" mode having real $(\omega) = 0$. Notice that this mode is unstable only if $j \geqq 3$, which means that the half-width is ~30% of the peak speed. Crudely speaking, the instability requirement that $\hat{D}_0 < 0$ when $\hat{D}_1 > 0$ (for the unstable zero-frequency mode) restricts the perpendicular wavelength to be roughly one gyrodiameter. The growth rate of the unstable zero-frequency mode is typically $\sim 0.1\ \omega_c$, depending on the density excess above the threshold. This growth rate is approximated by

$$\mathrm{Im}\,\omega \sim \omega_c \left[\frac{1}{2}\left(\frac{|\hat{D}_0| - k^2/\omega_p^2}{\hat{D}_1}\right)\right]^{1/2}.$$

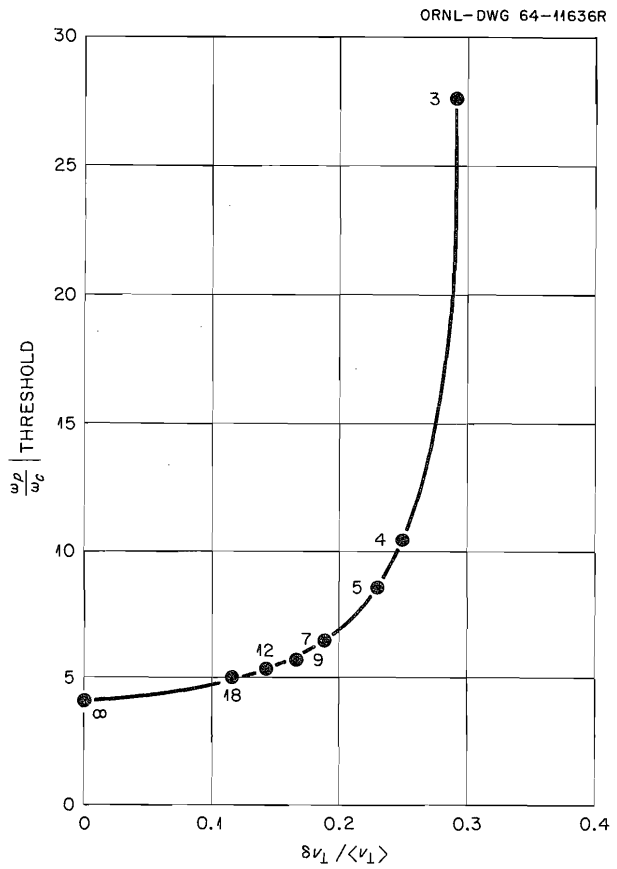

Fig. 7.1. Threshold Value of ω_p/ω_c vs the Relative Half-Width of the Distribution Function $\delta v_\perp/\langle v_\perp\rangle$, for the Zero-Frequency Mode. Point labels are j values for the distributions given by Eq. (1).

[14] E. G. Harris, *J. Nucl. Energy: Pt. C* **2**, 138 (1961).

7.5. RELATIVISTIC CORRECTIONS TO THE $k_{\parallel} = 0$ MASER INSTABILITIES

R. Dory

As described in Sect. 7.4, a uniform plasma in a magnetic field **B** is susceptible to the so-called maser instability of waves propagating perpendicular to the field if the distribution function is not monotonically decreasing in $v_{\perp}^2$ ($v_{\perp}$ is the particle velocity component normal to **B**).[15] At the suggestion of S. Buchsbaum[16] that relativistic effects could be very important to such instabilities, the calculation has been carried out again from a relativistic Vlasov equation.[17] The customary approximation of the electric field by the negative gradient of a scalar Φ is made under the assumption that β (particle pressure over total pressure) is much less than unity, a procedure justified by Drummond and Rosenbluth.[18]

The procedure is as follows: the single particle distribution function is regarded as a function of **x** and t, space and time coordinates, and of $\mathbf{u} = \mathbf{v}\gamma$, where **v** is the particle velocity and $\gamma \equiv (1 - \mathbf{v} \cdot \mathbf{v}/c^2)^{-1/2} = (1 + \mathbf{u} \cdot \mathbf{u}/c^2)^{+1/2}$. The relativistic Vlasov equation takes the form

$$\frac{\partial F}{\partial t} + \mathbf{v} \cdot \frac{\partial F}{\partial \mathbf{x}} + \frac{e}{m}(\mathbf{E} + \mathbf{v} \times \mathbf{B}) \cdot \frac{\partial F}{\partial \mathbf{u}} = 0 . \quad (1)$$

The usual procedure of linearization about an unperturbed uniform stationary state $F = F_0(\mathbf{u})$ and $\mathbf{E} = 0$ and solution by integration along unperturbed orbits yields[19] for the distribution function perturbation f evaluated at an arbitrary point and time, such as $\mathbf{x} = 0$ and $t = 0$:

$$f(\mathbf{u}) = \frac{e}{m} k_{\perp} \Phi_0 \frac{\partial F^0}{\partial u_{\perp}} e^{-ib \sin\phi} \times \sum_{-\infty}^{\infty} \frac{n}{b} J_n(b)\, e^{in\phi}/(n\omega_0/\gamma - \omega) , \quad (2)$$

where cylindrical coordinates in **u** space are $u_{\perp}$, $u_{\parallel}$, and ϕ; the potential has been assumed to have the form $\Phi_0 \exp(i\mathbf{k} \cdot \mathbf{x} - i\omega t)$ with $\mathbf{k} \cdot \mathbf{B} = 0$ and $|\mathbf{k}| = k_{\perp}$. We denote by b the quantity $k_{\perp}u_{\perp}/\omega_0$; J_n is Bessel's function; ω_0 is the gyrofrequency $e|\mathbf{B}|/m$, where m is the particle rest mass. The sum resulted from expansion of $\exp(-ib \sin\phi)$ using Jacobi's formula for generating Bessel functions. Application of Poisson's equation at $\mathbf{x} = 0$ and $t = 0$ and assumption that $\Phi_0 \neq 0$ yields the dispersion relation

$$1 = \frac{\omega_p^2}{k_{\perp}^2} \sum_{-\infty}^{\infty} \int_0^{\infty} du_{\perp} \int_{-\infty}^{\infty} du_{\parallel} \frac{\partial F^0}{\partial u_{\perp}} \gamma \frac{2\pi n\, J_n^2(b)}{n - \omega\gamma/\omega_0} . \quad (3)$$

We have set $4\pi n_0 e^2/m = \omega_p^2$, where n_0 is the particle density in the unperturbed state and $\int d^3u\, F_0 = 1$. The usual nonrelativistic analog of (3) results on setting $\gamma = 1$ and $\mathbf{u} = \mathbf{v}$.

To see the effects of relativistic velocities, we first consider the flutelike $\omega = 0$ modes. We drop the $n = 0$ term of the sum, take the limit $\omega \to 0$, and regard values of $k_{\perp}$ or b where the right side of (3) is positive as unstable for sufficiently high density.

If the distribution is $F_0 = 1/2\pi\, \delta(u_{\parallel})\, \delta(u_{\perp} - U_{\perp})$ we find for the dispersion relation

$$1 = \frac{\omega_p^2}{\omega_0^2} \gamma \frac{1}{b} \frac{d}{db} J_0^2(b) , \quad (4)$$

where b is $k_{\perp}U_{\perp}/\omega_0$ and $\gamma = (1 + U_{\perp}^2/c^2)^{+1/2}$. This agrees with the analogous nonrelativistic dispersion relation if the mass is replaced by the relativistic mass, $m\gamma$. For this case then the instability is only quantitatively affected: the threshold value of ω_p/ω_0 is decreased by a factor $\gamma^{1/2}$, and the corresponding unstable values of $k_{\perp}v_{\perp}/\omega_0$ are decreased by a factor γ.

If the distribution is $F_0 = 1/2\pi\, \delta(u_{\parallel})\, G_0(u_{\perp})$ we find for a dispersion relation

$$1 = -\frac{\omega_p^2}{k_{\perp}^2} \int_0^{\infty} du_{\perp}\, G_0(u_{\perp}) \frac{\gamma}{u_{\perp}} \times \left\{ 2b\, J_0(b)\, J_1(b) + \frac{v_{\perp}^2}{c^2}[1 - J_0^2(b)] \right\} . \quad (5)$$

---

[15] R. A. Dory, G. E. Guest, and E. G. Harris, *Phys. Rev. Letters* **14**, 131 (1965).

[16] Private communication (1965).

[17] See, for example, B. Kursunoğlu, *Nucl. Fusion* **1**, 213 (1961).

[18] W. E. Drummond and M. N. Rosenbluth, *Phys. Fluids* **5**, 1507 (1962).

[19] We apply the Landau condition that ω have a small positive imaginary part so that the $t = -\infty$ values are not present in the following equations.

The accompanying graph (Fig. 7.2) of $2b\ J_0(b)\ J_1(b)$ and of $1 - J_0^2(b)$ allows us to conclude that if $G_0(u_\perp)$ is appreciable only for velocities much smaller than c, then the stabilizing second term in the brace will be important only for waves of very long wavelength. The interesting instabilities with $1/k_\perp$ near the mean gyroradius will be only slightly affected.

For situations in which there are a considerable number of relativistic particles (as is more likely in hot-electron devices) the unstable $k_\perp$ bands are substantially reduced. Detailed calculations may show that the unstable bands can disappear completely as suggested by Buchsbaum.

The relativistic changes in the higher-frequency modes[15] include another effect besides the previously noted destabilizing overall factor γ and the stabilizing term arising from $d\gamma/du_\perp$. The third effect is the detuning of the resonance denominators caused by the relativistic reduction of the gyrofrequency to $\omega_g = \omega_0/\gamma \leqq \omega_0$. This detuning is generally stabilizing because it tends to smooth the right side of (3), but this can be important only when there are a large number of relativistic particles.

In both the flutelike and higher-frequency modes these relativistic effects are seen to be unimportant in the stabilization of a mirror-contained hot-ion thermonuclear plasma against the important instability of electrostatic waves propagating exactly perpendicular to **B** with wavelengths comparable to the mean gyroradius.

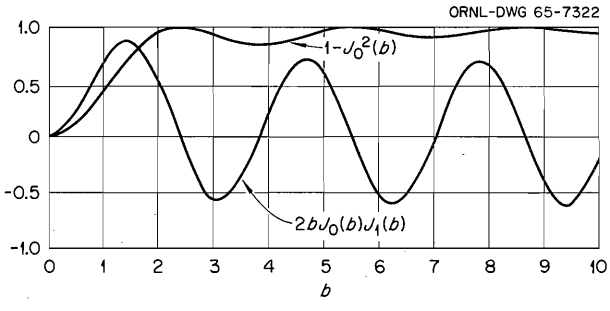

Fig. 7.2. Dependence of Nonrelativistic and Relativistic Coefficients in Eq. (5).

7.6. ELECTRON STREAMS AND ARCS IN FINITE PLASMAS

C. O. Beasley, Jr.

A dispersion relation for a previously described plasma[20] has been obtained, and a physical description of phenomena which occur in such has been attempted using the results of that dispersion relation. The plasma described is shown in Fig. 7.3. By starting with the zeroth and first moment equations for the cold background ions and the cold streaming electrons, we may obtain a second-order, homogeneous, linear differential equation in the Laplace-transformed (in time), Fourier-transformed (in the x and y directions) perturbation charge density

$$\rho_{\omega,k_\perp}(z) = e\left[n_{i_{\omega,k_\perp}}(z) - n_{e_{\omega,k_\perp}}(z)\right].$$

The solution to this differential equation is given by

$$\rho_{\omega,k_\perp}(z) = Ae^{i\Gamma_+ z} + Be^{i\Gamma_- z},$$

where

$$\Gamma_\pm = \frac{\omega}{V_e}\left(1 \pm \frac{\omega_{p_e}}{\sqrt{\omega^2 - \omega_{p_i}^2}}\right)$$

and

$$\omega_{p_{i,e}}^2 = \frac{4\pi N_{i,e} e^2}{m_{i,e}}.$$

[20] *Thermonuclear Div. Semiann. Progr. Rept. Apr. 30, 1964*, ORNL-3652, p. 104.

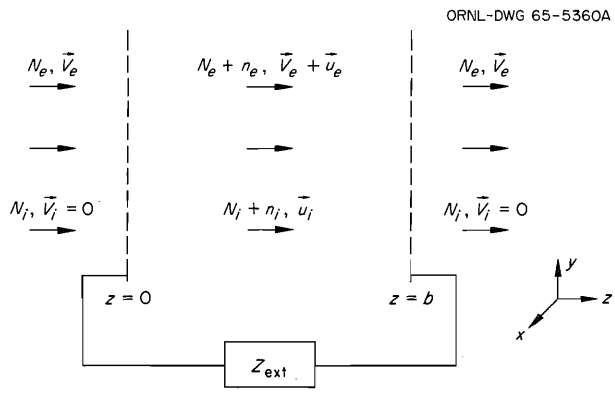

Fig. 7.3. Plasma Model.

Also we have assumed only electrostatic perturbations so that Poisson's equation holds, and the perturbation electric field $\vec{E}$ is simply related to the perturbation charge density:

$$\nabla \cdot \vec{E} = 4\pi\rho = -\nabla^2\Phi .$$

We may easily solve for the Laplace-Fourier-transformed electric field in terms of this charge density. These solutions contain three constants of integration, A, B, and $E^z(0)$.

The physically interesting case to be examined is that one in which $k_\perp = 0$. Also this case is the one which allows a potential drop across the plasma.

That the solution $\rho_\omega(z)$ without some feedback mechanism connecting the two boundaries leads to no nonconvective, nonzero-frequency modes can easily be seen by applying a delta function pulse at both boundaries at time $t = 0$. Such a boundary condition is written in the Laplace-transformed space as

$$A + B = C_1 ,$$
$$A e^{i\Gamma_+ b} + B e^{i\Gamma_- b} = C_2 ,$$

where the boundaries of the plasma are taken to be at 0 and b. However, if we allow for external feedback by some unspecified means, we may obtain nonconvective instabilities.

We allow our external feedback circuit to possess both phase shift and damping. This is represented by the statement that

$$\rho_\omega(b) = e^{iC}\, \rho_\omega(0) ,$$

where C is a complex constant representing the external circuit and where $k_\perp$ has been taken to be 0. This leads to the dispersion relation

$$\frac{1}{Z^2} + \frac{\gamma}{(Z - W)^2} = 1 ,$$

where

$$\gamma = \frac{m_i}{m_e},\ Z = \frac{\omega}{\omega_{pi}},\ W = \frac{V_e}{b\omega_{pi}}\,(C + 2l\pi) .$$

A check on the consistency of this result obtains by letting $C \to 0$. Then the dispersion relation should describe this plasma in the case in which there is a weak magnetic field in the x direction, thus imposing periodicity in the z direction. In this limit we are led to the dispersion relation

$$\frac{\omega_{pe}^2}{(\omega - \omega_{ce})^2} + \frac{\omega_{pi}^2}{\omega^2} = 1 ,$$

where

$$\omega_{ce} = \frac{2\pi V_e}{b} .$$

A plot of the roots of this dispersion relation is seen in Fig. 7.4. The solid lines in the figure represent a given W_r, and the dashed lines a given external damping. Specifying these two quantities completely determines the frequency ω_r and its growth rate ω_i. One finds unstable frequencies ranging from $0 < \omega_r \lesssim 3.6\omega_{pi}$. These observed modes are divided into two regions as far as their spatial dependence is concerned. For the region $0 < \omega < \omega_{pi}$, we find a single wave which grows convectively as well as temporally. For the region $\omega_{pi} < \omega \lesssim 3.6\omega_{pi}$, we find two purely spatially propagating waves, with almost identical, but oppositely directed velocities. Unlike the infinite two-stream plasma, the unstable modes do appear at a value of W_r greater than the limit

$$W_r = \gamma^{1/2}(1 + \gamma^{-1/3})^{3/2} .$$

Although these higher W_r modes do appear, they do so with drastically reduced growth rates. For $W_r \gtrsim 48$, increasing the external damping from zero damping at first leads to an increasing growth rate for a given unstable mode. Eventually, however, the increased damping decreases the growth rate. Also as damping is increased, the frequencies which appear begin to bunch more and more about the ion plasma frequency.

Although we do not know the relation of the phase shift and the damping parameters to their physical circuit counterparts, if we are given the two lowest observed frequencies, we may easily determine these parameters from Fig. 7.4, as well as determine what other frequencies might appear.

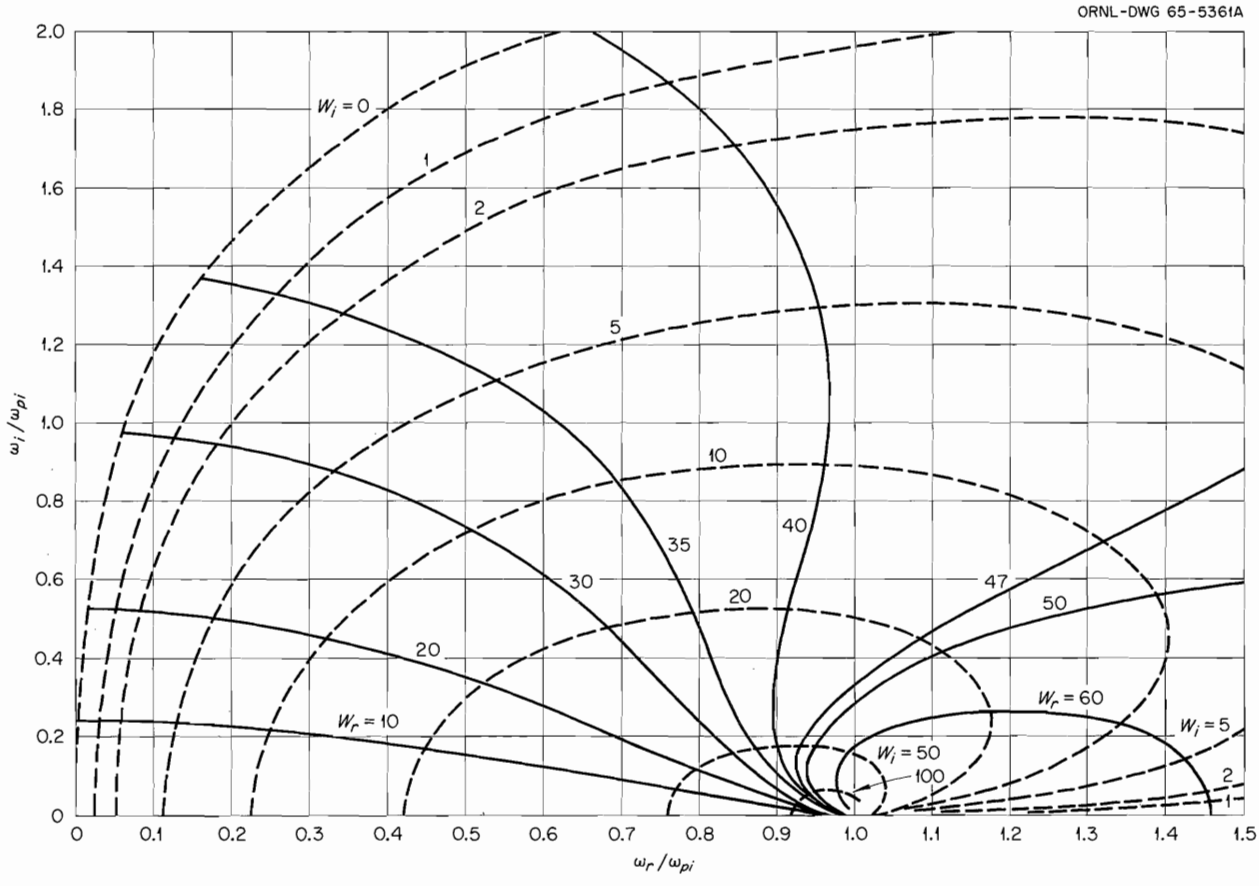

Fig. 7.4. Roots of the Dispersion Relation.

8. Magnetics and Superconductivity

8.1 REPORT ON A SEMINAR CONCERNING THE RELATIONS BETWEEN GAS AND SOLID-STATE PLASMAS (OAK RIDGE, MARCH 29–30, 1965)

T. K. Fowler W. F. Gauster

8.1.1 Introduction

As is well known, much work has been done recently on the so-called B_{min} geometry ($\int dl/B \rightarrow$ maximum for closed systems) applied to the magnetohydrodynamic stability of gas plasmas which are of interest for thermonuclear research. Experiments of this kind are often difficult to interpret, are time consuming, and are expensive. It seems to be tempting to make small-scale model experiments with corresponding magnetic field geometries performed with solid-state plasmas. This makes sense, of course, only if the following question can be satisfactorily answered: To what extent can an electron-hole, solid-state plasma be considered as analogous to a gaseous plasma?

Table 8.1 (ref. 1) compares typical characteristics of laboratory gas plasmas and plasmas in semiconductors.

[1]Compare R. Bowers and M. C. Steele, *IEEE Proc.*, pp. 1105–12 (October 1964).

Table 8.1. Typical Plasma Characteristics

	Laboratory Gas Plasma	Plasma in Semiconductor
Mobile negative charge	Electron	Electron
Mobile positive charge	Ionized atom	Hole
Densities	10^7–10^{16}/cm^3	10^{16}/cm^3
Magnetic fields encountered, gauss	10^2–10^5	10,000
Cyclotron frequency, $f_e = \frac{\omega_c}{2\pi} = \frac{eB}{2\pi m}$		
Negative charge	10 kMc	300 kMc
Positive charge	10 Mc	300 kMc
Plasma frequency, $f_p = \frac{\omega_p}{2\pi} = \frac{1}{2\pi}\sqrt{\frac{ne^2}{\epsilon_0 m}}$	10^{11} cps	10^{12} cps
Collision time, τ	10^{-5}–10^{-10} sec	10^{-10}–10^{-13} sec

An excellent review paper on plasma effects in solids was presented by J. Bok (Ecole Normale Supérieure, Paris) at a general session of the German Physical Society at the Düsseldorf Meeting (October 1964).[2]

At this laboratory, after internal discussions on the subject of solid-plasma models, it was decided to arrange an informal seminar at the Thermonuclear Division in order to learn somewhat more in detail about the relevant work of experts in this field.

Besides the interested scientific staff members of ORNL, the following persons participated in the seminar: Betsy Ancker-Johnson (Boeing Research Laboratories), J. C. Ashley (George C. Marshall Space Flight Center, NASA), S. J. Buchsbaum (Bell Laboratories), J. E. Drummond (Boeing Research Laboratories), E. G. Harris (Consultant, University of Tennessee), W. M. Hooke (Princeton Plasma Physics Laboratory), J. O. Kessler (RCA, Princeton), J. Merrill (Cornell University), J. M. Reynolds (Consultant, Louisiana State University), H. E. Rorschach (Consultant, Rice University), M. C. Steele (RCA, Princeton), and P. A. Wolff (Bell Laboratories).

Professor Reynolds' effort in arranging this seminar is highly appreciated.

8.1.2 Presentations and Discussions

The following listing of abstracts of seminar contributions is by no means complete. Likewise, only a very incomplete list of references has been given here. An extensive report on this seminar would by far surpass the space available here.

1. *T. K. Fowler* reported on the status of fusion research. The following is an abstract of his presentation:

   Stability problems facing fusion research provide a guide as to which solid-state analog experiments might be useful. In review, plasma losses by two categories of instabilities have been observed at low β (thermal pressure $\ll B^2/8\pi$), the regime suitable for analogs. These are microinstabilities at frequencies $\gtrsim$ the ion gyrofrequency ω_{ci},[3] and gross instabilities at frequencies $< \omega_{ci}$, including interchange (flute) instabilities and universal instabilities perhaps responsible for "pumpout" in stellarators.[4] As of now, the main problem for magnetic mirror confinement appears to be microinstabilities, and for magnetic tori, gross instabilities. According to a thermodynamic analysis,[5] magnetic mirrors shaped like wells, already shown to prevent flutes,[6] should also stabilize other gross instabilities.[7] The same analysis indicates that, because a toroidally confined plasma is very near stable thermal equilibrium, diffusion by microinstabilities should be tolerable in tori of about 1 m minor radius. On the other hand, while toroidal magnetic wells in an average sense are possible and have been proposed as cures for gross instability in tori,[8] the effective well depth is small, and the idea awaits test. And, enhancement of end losses from magnetic mirrors by microinstabilities remains to be assessed. No scheme has yet emerged for stabilizing the fast-growing continuum spectrum of microinstabilities predicted to occur with mirror confinement when the ion plasma frequency much exceeds ω_{ci},[9] corresponding typically to densities $10^{10-11}/\mathrm{cm}^3$, far below thermonuclear requirements.

---

[2] J. Bok, pp. 365–91 in *Plenarvorträge der Physikertagung, Düsseldorf, 1964*, ed. by K. Hecht, Deutsche Physikalische Gesellschaft e.V.

[3] G. R. Haste, J. L. Dunlap, and L. H. Reber, *Bull. Am. Phys. Soc.* **10**, 234 (1965); also, paper to be published.

[4] W. L. Harris *et al.*, *Phys. Fluids* **7**, 151 (1964); F. F. Chen, *Princeton Physics Laboratory Report* MATT-311 (1964).

[5] T. K. Fowler, *Phys. Fluids* **8**, 459 (1965).

[6] Yu. B. Gott, M. S. Ioffe, and V. G. Telkovsky, *Nucl. Fusion, 1962 Suppl.*, Part 3, 1045 (1962); C. C. Damm *et al.*, *Phys. Rev. Letters* **13**, 464 (1964).

[7] Stabilization results for gross instabilities of radial wavelength $\lambda >$ ion gyroradius if the net energy gained by particles climbing a magnetic hill, just $(\lambda^2/R^2)\mu\,\Delta B$ per ion, exceeds the maximum energy they can transfer to electric fields, $\lesssim T_e(\lambda^2/R^2)$ per ion at low β, according to Eq. (35) of ref. 3. Here ΔB is the magnetic well depth and R is the plasma radius. Thus the stability condition is $\Delta B/B > T_e/T_i$, practicable in magnetic wells, where $T_e < T_i$.

[8] H. P. Furth and M. N. Rosenbluth, *Phys. Fluids* **7**, 764 (1964); also, more recent proposals by J. B. Taylor, unpublished.

[9] M. N. Rosenbluth and R. F. Post, *Phys. Fluids* **8**, 547 (1965).

2. *E. G. Harris* presented a short lecture on collisional and anomalous diffusion in gas plasmas.
3. *Betsy Ancker-Johnson and J. E. Drummond* discussed experimental and theoretical work done at the Plasma Physics Laboratory of the Boeing Scientific Research Laboratories.[10] Betsy Ancker-Johnson showed a film which demonstrates very nicely her experimental studies on hot-electron energy transfer in *n*-InSb. The following two abstracts cover partly the essential parts of Ancker-Johnson's and Drummond's seminar contributions:

Experimental Studies on Hot-Electron Energy Transfer in *n*-InSb. – A 1-nsec-risetime pulser with automatically varying amplitude is applied to a single-crystal parallelepiped of *n*-InSb at 77°K. The sweep function of a dual-trace sampling oscilloscope is programmed to make the oscilloscope detect the field strength in the specimen and the current carried by it at given times spaced by 0.01 nsec from the beginning of the pulse. The resulting series of conductivity curves is displayed on a 21-in. oscilloscope and photographed in sequence on 16-mm film. Such a film strip showing the conductivity of *n*-InSb during the first few nanoseconds after the power is turned on was shown. Information gained from the first half dozen such films is as follows: The first indication of breakdown, as observed by the beginning of current greater than the ohmic magnitude, occurs between 0.4 and 0.9 nsec after onset of the pulse at field strengths much greater (between 750 and 1325 v/cm) than the usually stated breakdown-by-impact-ionization magnitude of 200–300 v/cm. As the current rises, the field strength at the break between the generally ohmic and the decidely superohmic current parts of the conductivity curve drops back to the usually stated value in less than 5 nsec. The slope of the conductivity curve in the superohmic region increases with time and becomes vertical in 2.6 ± 0.8 nsec. The rate of current increase during the first nanosecond after the onset of superohmic current is between 3 and 8 amp/nsec. Thereafter the rate is much smaller, probably because of self-pinching of the current.

[10]See, for instance, B. Ancker-Johnson, *Progr. Rev. Plasma Phys. Lab.*, last six months 1963, pp. 112–17; B. Ancker-Johnson and M. F. Berg, *Proc. Intern. Conf. Phys. Semiconductors, Paris, 1964*, 514–17 (July 1964); M. F. Berg and B. Ancker-Johnson, paper presented at the Sixth Annual Meeting of the Division of Plasma Physics of the American Physical Society held in New York, Nov. 4–7, 1964.

Tests of Confinement Configurations Using Electron-Hole Plasmas. – Confinement schemes, including linear *z* pinches, mirror machines with and without Ioffe bars (energized by pulsed dc or 84-Mc rf current), the stellarator, the Furth-Rosenbluth closed helix, and the Taylor toroid have been tested with electron-hole plasmas. The linear *z* pinch in electron-hole plasmas (densities up to 10^{18} cm^{-3}) becomes unstable at a plasma power level four times that required for the onset of self-constriction. Several modes of large-amplitude oscillations are observed in the power range up to approximately 20 times the onset magnitude. At still higher power levels an absolute instability occurs, thermal pinching, which has no analog in electron-ion plasmas. Uniform axial magnetic fields applied to current-carrying plasmas produce oscillations in low-β plasmas which are stabilized at approximately twice the threshold magnetic field for the onset of the oscillations. The addition of end mirrors affects in a complicated fashion both the stabilizing and confining capabilities of linear systems. Quadrupolar Ioffe bars can suppress oscillations, lower the average electric field strength sustained by the plasma, and enhance by at least 65% the plasma density remaining after the elapse of one-half the usual e-folding time. The first model of the Furth-Rosenbluth configuration has not produced a prolonged lifetime of the plasma, although the enormous plasma loss produced by either the toroidal or helical field alone can be completely restored by a suitable combination of these fields. Results obtained with an $\ell = 3$ Taylor system were reported. The low conductivity limit of the Furth-Rosenbluth theory yields a maximum growth rate ω of a flute instability in a toroidal plasma $\omega = \Omega(1 + \epsilon)$, where Ω is the usual unstabilized value and

$$\epsilon \approx -\left(\frac{3}{\nu}\right)^{1/2}\left(\Sigma + \frac{\pi}{L}\frac{\gamma^{1/2}}{2^{1/2}}\right)\left(\frac{kTaR_c}{M}\right)^{1/4},$$

provided $\epsilon^2 \ll 1$. The symbols are the same as the Furth-Rosenbluth ones, with the addition of ν, the effective momentum-transfer collision frequency of the carriers. Thus the effects of both shear and maximum $\int dl/B$ stabilization can be seen in low-conductivity electron-hole plasmas by measuring reductions in growth rates of the order of 10%. The current in a single coil controls Σ in the Furth-Rosenbluth configuration and $\int dl/B$ in the Taylor configuration. In both machines, temperature controls ϵ (especially through ν).

4. *S. J. Buchsbaum* gave a review of experimental work at Bell Telephone Laboratories on wave

propagation in solid-state plasmas. Particular attention was given to the experiment on microwave emission from indium antimonide.[11] The theory of a novel surface-wave instability which can occur in composite structures supporting helicon waves was summarized.[12]

5. *J. O. Kessler* presented a summary of work[13] done together with A. R. Moore at RCA, in which a hole-electron plasma was injected by light, and in which the plasma magnetic moment was measured for varying geometries, surface and volume recombination rates, and for two directions of illumination (giving rise to positive as well as negative magnetic moments). The experiments also showed that, under otherwise constant conditions, variations of $\omega\tau$ and surface recombination coefficients provided a means of obtaining the whole range of effects ranging from transverse thermodynamic equilibrium (dominated by volume recombination) to outward diffusion with pure magnetic confinement. The experiment described also demonstrated that the force in the direction $-\nabla B$ is substantially the same in the semiconductor case as it is in a toroidal plasma[14] (stellarator without external rotational transform). Although those experiments did not involve geometries of current interest to the fusion program, they were said to provide groundwork for further efforts in understanding plasma confinement.

   Concerning material presented by other authors, Kessler commented as follows:

Although the results obtained seem to be most encouraging, before any definite inferences can be drawn, more work is required regarding the relative roles of surface and volume current-carrier pair recombination. In particular, a study should be made of: possible variations of surface recombination coefficients with magnetic fields, of possible geometrical magnetic field-induced carrier concentrations near the surface, and, in a more general sense, of recombination, using *one* fixed magnetic field geometry with a systematic variation of the surface-to-volume ratio in the semiconductor slab. It might be still doubtful whether or not the same mirror confinement and Ioffe-bar stabilization conditions prevail in the InSb and fully ionized gas plasma case. This because of the small ratio of momentum-randomizing times to transit times prevalent in InSb, as well as the somewhat marginal values of $\omega_{\text{cyclotron}} \times \tau_{\text{lattice collisions}}$.

6. *H. E. Rorschach* gave a brief discussion of plasma resonances in solids from the point of view of a set of phenomenological equations, similar to the Bloch equations for magnetic resonance. Solutions were found for the "u" and "v" modes for the "slow passage" case corresponding to the propagation of helicon waves. Two other questions were briefly discussed: (1) the contribution of the helicon modes to the heat capacity, and (2) the possibility of a heavy-ion plasma in a solid.

7. *M. C. Steele* presented a summary of the instabilities that have been studied in solid-state plasmas. He pointed out that such studies could be of value for thermonuclear plasmas because of the similarity of densities. Clearly, the analogies have to be taken with a grain of salt since many of the other plasma properties are very different (temperature, scattering, etc.). In particular, two-stream instabilities in the presence of magnetostatic fields were discussed. Such effects have recently shown microwave generation in solids such as InSb.

   Steele also discussed the use of microwave propagation in solids as a diagnostic tool for studying confinement, pinch instabilities, and other parameters that characterize the plasma.

8. *P. A. Wolff* discussed the possibility of obtaining cyclotron-resonance amplification in InSb. He published recently a detailed report on this subject[15] with the following abstract:

A scheme for amplifying cyclotron resonance radiation in InSb is outlined. To obtain amplification two requirements must be satisfied. The first is that the electron velocity distribution be monoenergetic. Such distributions can be produced by photoexciting electrons in cold *p*-type InSb. Detailed calculations show that, with a reasonable electron density, the distribution remains monoenergetic throughout the electron lifetime. The second requirement for amplification is that stimulated absorption of cyclotron radiation be inhibited as compared to stimulated emission. This criterion is met by producing the photoelectrons at an energy just

[11] S. J. Buchsbaum, A. G. Chynoweth, and W. Feldman, *Appl. Phys. Letters* **6**, 67 (1965).

[12] G. A. Baraff and S. J. Buchsbaum, *Appl. Phys. Letters*, to be published.

[13] A. Moore and J. O. Kessler, *Phys. Rev.* **132**, 1494 (1963).

[14] S. Yoshikawa *et al.*, *Phys. Fluids* **6**, 932 (1963).

[15] P. A. Wolff, *Physics* **1**, 147–57 (1964).

below that of the optical phonon in InSb. As a consequence, the stimulated absorption line is broad compared to that for emission, so the latter predominates. Numerical estimates indicate that there is a reasonable chance of producing a far infrared amplifier based upon this technique.

8.1.3 Conclusion

For any laboratory doing thermonuclear research it will be of interest to be informed about progress in the understanding of the properties of plasma in solids. Certainly the interesting attempt by B. Ancker-Johnson to study containment geometries using solid-state plasmas typifies the advantages possible. On the other hand, as J. O. Kessler warns above, a clean interpretation of solid-state experiments requires much more understanding of surface effects and other differences between solid-state plasmas and gas plasmas. J. E. Drummond gave a most stimulating summary at the closing of the seminar. Perhaps the consensus at the symposium is expressed by the following statement which he made at another occasion: "So the value of plasmas in solids is just this: a possible warning and an occasional clue. In science and in politics, we should never place ourselves beyond the reach of contradiction."

8.2 A NOTE ON THE *G-v* OPTIMUM RELATIONS FOR MAGNET COILS

W. F. Gauster

8.2.1 Introduction

The meaning of "*G-v*" optimization is to find the parameters of coils with known volume factors v which have maximum Fabry factors G. In his first classical paper,[16] Fabry presented a table of correlated v-G_{max} values for coils with rectangular cross sections and uniform current densities; however, he did not indicate how he determined these figures. Recently, D. B. Montgomery[17] presented an equation for finding, in a simple way, approximate values of these parameters. He too did not show a derivation of his equation.

Since the *G-v* optimum relation is of importance for conventional and superconducting[18] magnet coils, an exact reevaluation of this problem seemed to be desirable. This is the subject of the following note. Furthermore, new types of graphs will be shown which are convenient for coil design work.

8.2.2 The Optimization Equation

Using standard designation (Fig. 8.1), the Fabry factor is

$$G = \frac{1}{5}\sqrt{\frac{2\pi\beta}{\alpha^2 - 1}}\ \ln\frac{\alpha + \sqrt{\alpha^2 + \beta^2}}{1 + \sqrt{1 + \beta^2}}. \qquad (1)$$

The volume factor is determined by

$$v = \frac{\text{total coil volume}}{(\text{coil inside radius})^3} = 2\pi(\alpha^2 - 1)\beta. \qquad (2)$$

[16]Ch. Fabry, *L'Éclairage Électrique* 17(43), 133–41 (1898).

[17]D. B. Montgomery, *Spectrum* 1(2), 103–13 (1964).

[18]See for instance R. W. Boom and R. S. Livingston, *Proc. I.R.E.* 50, 274 (1962).

ORNL-DWG 65-7304

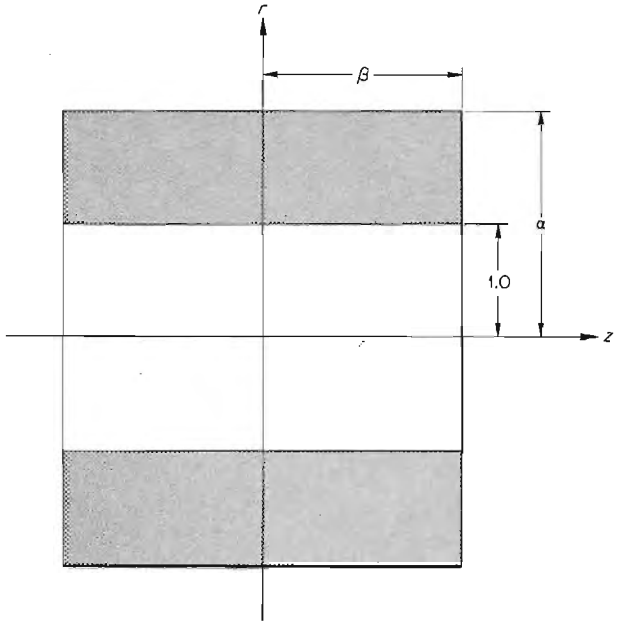

Fig. 8.1. Normalized Magnet Coil with Rectangular Cross Section.

It is rather involved to perform the desired optimization with the usual mathematical methods. The following way, which is based on the physical meaning of some of the quantities concerned, is much simpler.

As is well known,[16] Fabry's equation,

$$H_0 = G\sqrt{\frac{P\lambda}{\rho a_1}}\,, \tag{3}$$

expresses the field strength H_0 (in gauss; it is usually assumed that H_0 is measured at the coil center) by the ohmic power P (in watts), the packing factor

λ = conductor net cross section ÷ total conductor cross section (including insulation, etc.) , (4)

the specific conductor resistivity ρ (in ohm-centimeters), and the inside coil radius a_1 (in centimeters).

For a coil with a uniform current density j (in amperes per square centimeter) in the conductor,

$$P = \rho j^2 \lambda V = \rho j^2 \lambda v a_1^{\,3}\,. \tag{5}$$

Therefore

$$H_0 = \lambda j a_1 G\sqrt{v}\,. \tag{6}$$

Using the designation

$$G\sqrt{v} = F = \frac{2\pi}{5}\beta \ln\frac{\alpha + \sqrt{\alpha^2+\beta^2}}{1+\sqrt{1+\beta^2}}\,, \tag{7}$$

Eq. (6) becomes

$$H_0 = \lambda j a_1 F\,. \tag{8}$$

This equation does not contain the ohmic power P and, therefore, can be applied to superconducting coils.[19]

From Eq. (2) follows

$$\left.\frac{d\alpha}{d\beta}\right|_{v=\text{const}} = -\frac{\alpha^2-1}{2\alpha\beta}\,. \tag{9}$$

Therefore, if G is a maximum, considering v = constant:

$$(\alpha^2-1)\frac{\partial G}{\partial \alpha} = 2\alpha\beta\frac{\partial G}{\partial \beta}\,. \tag{10}$$

Because of Eq. (7), a similar equation holds for the function F:

$$(\alpha^2-1)\frac{\partial F}{\partial \alpha} = 2\alpha\beta\frac{\partial F}{\partial \beta}\,. \tag{11}$$

From Eq. (8) follows that $\partial F/\partial\alpha$ can be determined from the field produced by a cylinder with the inside radius α, the radial thickness $d\alpha$, and the length β:

$$\frac{\partial F}{\partial \alpha} = \frac{2\pi}{5}\frac{\beta}{\sqrt{\alpha^2+\beta^2}}\,. \tag{12}$$

The value of $\partial F/\partial\beta$ can be found from the field generated by a pair of disk coils with inner radii 1.0, outside radii α, and axial thickness $d\beta$, located at $z = +\beta$ and $-\beta$, respectively:

$$\frac{\partial F}{\partial \beta} = \frac{2\pi}{5}\left(\frac{1}{\sqrt{1+\beta^2}} - \frac{\alpha}{\sqrt{\alpha^2+\beta^2}} + \ln\frac{\alpha+\sqrt{\alpha^2+\beta^2}}{1+\sqrt{1+\beta^2}}\right)\,. \tag{13}$$

Finally, substitution of Eqs. (12) and (13) in Eq. (11) yields:

$$\ln\frac{\alpha+\sqrt{\alpha^2+\beta^2}}{1+\sqrt{1+\beta^2}} = \frac{3\alpha^2-1}{2\alpha\sqrt{\alpha^2+\beta^2}} - \frac{1}{\sqrt{1+\beta^2}}\,. \tag{14}$$

This is the desired relation between α and β which characterizes the G-v optimum relation.

8.2.3 Numerical Values

Table 8.2 contains the newly calculated values (β_1), Fabry's figures (β_2), and β_3 calculated from Montgomery's equation:[17]

$$5\beta_3 = 3\alpha + 1 - \frac{4}{\alpha^2}\,. \tag{15}$$

This table shows also the values of the volume factors v_1, v_2, and v_3 and of the Fabry factors G_1, G_2, G_3 which were calculated by means of the corresponding β values.[20]

[19] Graphs of $F(\alpha,\beta)$ and other graphs for magnetic coil design were made in the Thermonuclear Division. They have been reproduced by several authors. It is intended to publish a new, revised edition.

[20] I appreciate very much the cooperation of G. J. Atta and A. R. Jenkins of the Mathematics Division, who were in charge of the numerical calculations.

Table 8.2. *G-v* Optimum Relation for Magnet Coils with Rectangular Cross Sections and Uniform Current Densities

α	β_1	β_2	β_3	v_1	v_2	v_3	G_1	G_2	G_3
1.200	0.4614	0.36	0.3644	1.2755	1.0	1.0075	0.0862	0.08	0.0789
1.470	0.7344	0.55	0.7118	5.3568	4.0	5.1919	0.1311	0.12	0.1302
1.670	0.8998	0.89	0.9151	10.114	10.0	10.286	0.1491	0.15	0.1495
2.400	1.4168		1.5011	42.375		44.8952	0.1751		0.1756
3.090	1.8586	1.88	1.9702	99.822	100	105.82	0.1792	0.179	0.1791
3.095	1.8618		1.9735	100.35		106.38	0.1792		0.1791
4.200	2.5394		2.6746	265.50		279.64	0.1749		0.1744
6.600	3.9783	3.65	4.1416	1063.8	1000	1107.5	0.1580	0.16	0.1574
8.700	5.2297		5.4094	2454.3		2538.6	0.1449		0.1443
10.800	6.4804	6.9	6.6731	4708.6	5000	4848.6	0.1341	0.13	0.1336
13.900	8.3271	8.3	8.5359	10056.6	10000	10308.7	0.1216	0.12	0.1212
30.00	17.9298	17.7	18.1991	101278	100000	102799	0.0872	0.09	0.0870

These numerical results have been used to draw a graph (Fig. 8.2) which shows α and β_1 as functions of the volume factor v_1. Figure 8.3 represents G_1 in its dependence on v. The maximum of $G(v)$ is very flat. It can be shown that α and β for this point can be exactly determined by means of Eq. (14) and a simultaneous equation

$$\beta = \frac{\sqrt{3\alpha^4 - 2\alpha^2 - 1}}{\alpha^2 - 1} . \qquad (16)$$

In this way the values $\alpha = 3.095$, $\beta = 1.8618$, $v = 100.35$, and $G = 0.1792$, as shown in Table 8.2, have been obtained.

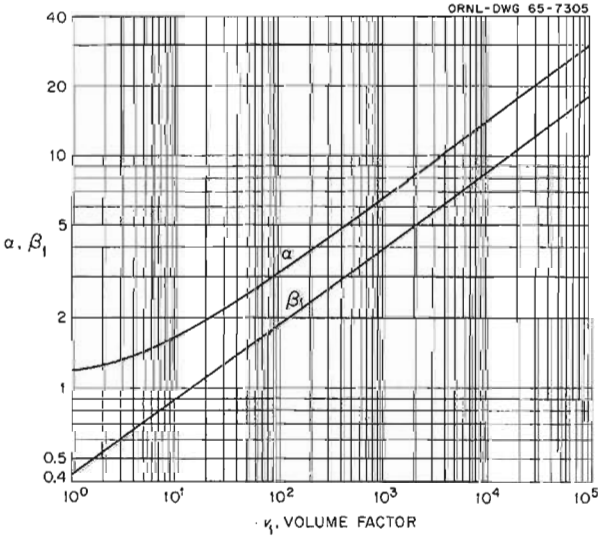

Fig. 8.2. α and β_1 Values from Table 8.2.

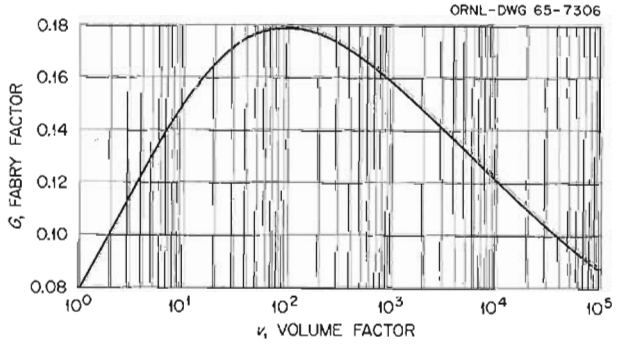

Fig. 8.3. G_1 Values from Table 8.1.

8.2.4 Conclusion

A new method has been used for an exact recalculation of Fabry's *G-v* optimum relation for magnet coils with rectangular cross section and uniform current-density distribution. It shows that appreciable deviations occur for small α and β values. For medium and large α and β values, Fabry's figures are sufficient for practical use. D. B. Montgomery's simple formula yields, in general, better results.

8.3 INVESTIGATIONS ON THE POSSIBILITY OF USING INDIUM ARSENIDE FILMS FOR CRYOGENIC MICRO HALL PROBES[21]

J. E. Simpkins

8.3.1 Introduction

The development of micro Hall probes consisting of thin bismuth films has been described in a previous report.[22] These probes were used to measure the "proximity effect" of soft superconductors.[23]

There are certain inherent disadvantages with bismuth which restrict its use as a cryogenic magnetic probe. Among these is the fact that its Hall coefficient is very temperature dependent. Also, cracks may occur in this material at liquid-helium temperatures causing abrupt changes in its conductivity during an experiment. Therefore, the results are not always reproducible.

Certain III-V semiconducting compounds exhibit a very large Hall effect. Outstanding among these are indium antimonide and indium arsenide. In its bulk form, indium antimonide may have the higher Hall coefficient; but because of the relatively high temperature dependence of its revelant properties, it was decided to investigate the properties of indium arsenide films instead. The Hall coefficient of this material may be nearly constant over a wide temperature range.

[21] A more complete report will be issued as ORNL-3808.

[22] J. E. Simpkins, *Thermonuclear Div. Semiann. Progr. Rept. Apr. 30, 1964*, ORNL-3652, pp. 129–31.

[23] W. F. Gauster *et al.*, *Thermonuclear Div. Semiann. Progr. Rept. Apr. 30, 1963*, ORNL-3472, p. 88.

8.3.2 Preparation of InAs Films

The electrical characteristics of a compound semiconducting film depend upon the following considerations:

1. Any impurity may yield an increase in carrier concentration, and cause a lower mobility. This requirement demands that the materials used for the evaporation be of very high purity and that they not be contaminated by other components within the evaporator. Indium and arsenic of $99.9997^{+}\%$ purity were used in quartz containers heated by tungsten filaments.

2. A high vacuum is required if films of high purity are desired. At a pressure of 10^{-6} torr, one monoatomic layer per second of impurity from the background gas would be deposited on the substrate if the sticking coefficient were 1.[24] If the substrate is maintained at an elevated temperature, some of this impurity is reevaporated. Since the sticking coefficient is less than 1, with an evaporation rate of 10 A/sec and a substrate temperature of about 400°C, the ratio of indium arsenide to impurity is much greater than 10.

A pressure of 5×10^{-8} torr was achieved in the evaporator. During deposition of the films, the pressure ranged from 5×10^{-7} to 2×10^{-6} torr, depending on the deposition rate.

3. The presence of boundaries between the crystallites influences the electrical characteristics of the film.[25] Günther found that films composed of larger crystallites exhibited a larger Hall coefficient, and he concluded that scattering at crystallite boundaries limits electron mobility.[26]

The size of the crystallites is influenced by the temperature of the substrate. A higher temperature favors the growth of larger crystallites, since the impinging atoms have higher surface mobility at the higher temperature.

4. The substrate itself may influence the structure of the film if chemical combination or alloying occurs. Epitaxial films of several materials have been grown on crystalline substrates, but this has not been observed with indium arsenide.

[24] K. H. Behrndt, "Preparation of Thin Films," p. 28 in *Thin Films*, American Society for Metals, Metals Park, Ohio, 1964.

[25] R. L. Petritz, *Phys. Rev.* **104**, 1508 (1956).

[26] K. G. Günther, "Vaporization and Reaction of the Elements," pp. 313–25 in *Compound Semiconductors*, vol. 1, ed. by R. K. Willardson, Reinhold, New York, 1962.

The substrate must be able to withstand the temperatures involved in cryogenic experiments. Also, the expansion characteristics of substrate and film must be compatible so that undue stresses are not incurred at low temperatures. Both glass and mica seem to meet these requirements.

Figure 8.4 shows a schematic diagram of the arrangement for depositing indium arsenide films, incorporating Günther's "three-temperature method."[26] A temperature for the less-volatile component, T_A, is chosen so that sufficient vapor pressure is obtained from this component to carry out the evaporation at the desired rate. A temperature for the more-volatile component, T_B, is chosen so that there is an excess of this material in its vapor phase ($2n_A \leqq n_B \leqq 10n_A$). The substrate is heated to a temperature, T_C, ($T_B < T_C < T_A$), so that the excess of component B is re-evaporated. Typical deposition temperatures for indium and arsenic were 840 and 257°C respectively.

The quartz crystal and the associated electronics, similar to that used by Behrndt[27] and indicated in the figure, were used to monitor film thickness during deposition. It was calibrated by making use of Tolansky's interferometric method.[28]

All the substrates consisted of either glass or mica. The glass substrates were cleaned in detergent and vapor degreased in alcohol. A clean surface of mica was prepared by cleaving. All substrates were subjected to ion bombardment in situ before depositing.

Electrical contacts able to withstand temperatures to 1.2°K were made to the film by depositing gold over a section of the indium arsenide and soldering wires to the gold film with indium solder.[29]

[27]K. H. Behrndt and R. W. Love, *Vacuum* **12**, 1 (1962).

[28]S. Tolansky, *Multiple-Beam Interferometry of Surfaces and Films*, chap. II, Clarendon Press, Oxford, England, 1948.

[29]R. B. Belser, *Rev. Sci. Instr.* **25**, 180 (1954).

ORNL-DWG 65-7307

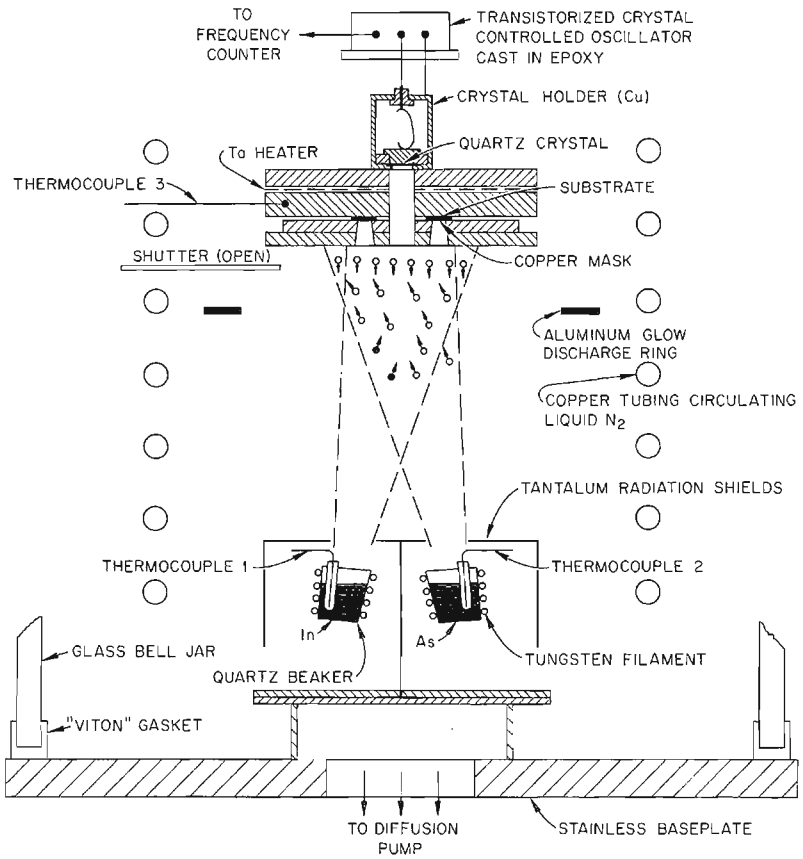

Fig. 8.4. Schematic Showing the Arrangement Inside the Evaporator for Depositing Indium Arsenide Films.

8.3.3 Experimental Results

The Hall coefficient, R_H, is defined by

$$E = R_H jB \quad , \tag{1}$$

where E, j, and B are mutually perpendicular. Since the current density, j_x, is

$$j_x = nev_x \quad , \tag{2}$$

then

$$E_y = -B_z j_x \frac{1}{ne} \, . \tag{3}$$

Therefore

$$R_H = -\frac{1}{ne} \tag{4}$$

and

$$n = -\frac{r}{R_H e}, \tag{5}$$

where n is the charge carrier density and r is the ratio of Hall mobility to drift mobility, usually assumed to be unity for most III-V compounds.[30] The Hall mobility, μ_H, is determined from the relation

$$\mu_H = |R_H \sigma| \, . \tag{6}$$

The measured Hall voltage is

$$V_H = \int_0^b E_y \, dy \quad , \tag{7}$$

and from the definition of the Hall coefficient, (1),

$$V_H = \frac{R_H I_x B_z \times 10^{-8}}{d} \quad , \tag{8}$$

where R_H is in cubic centimeters per coulomb, I_x is in amperes, B is in gauss, and V_H is in volts. Equation (8) assumes that R_H is independent of applied magnetic field.

The temperature dependence of the Hall coefficient of films containing various concentrations of donor impurities is shown in Fig. 8.5. The temperature dependence of the conductivity of these same samples is shown in Fig. 8.6.

Conductivity continued to decrease slowly below 70°K, while the Hall coefficient remained constant (with the exception of sample 90G). This behavior indicates an increase in electron mobility with increasing temperature instead of an increase in carrier concentration, since the Hall coefficient remained constant. Above 77°K the Hall coefficient becomes smaller while the conductivity increases, indicating a change in carrier concentration. These observations agree qualitatively with those of Sladek for the bulk material.[31] An increase in the Hall coefficient at temperatures below 3.5°K was observed in sample 90G, indicating a decrease in electron concentration at these low temperatures. The values of impurity concentration indicated in the figures refer to 4.2°K.[32]

Dependence of the Hall coefficient upon magnetic field intensity at 300 and 4.2°K is shown in Fig. 8.7. Sample 90G, with higher impurity content, exhibits an increase in its Hall coefficient between 25 and 30 kilogauss. Sample P8, with a probe geometry similar to that used for the bismuth probes, has a length-to-width ratio of only 2.2 and voltage contacts which are wide compared to probe length. This arrangement results in a lower Hall coefficient.[33] Sample HT600, which contains the lowest impurity density, has a high length-to-width ratio (10^3), a low voltage-contact-width-to-probe-length ratio, and the highest Hall coefficient. This geometry is the best of all those considered here. The sign of the Hall coefficient of sample HT500 reverses at 17 kilogauss, indicating a reversal from p- to n-type behavior. All other samples contained an excess of donor impurity.

Figure 8.8 shows the output voltage of 3 microprobes with a current density of 1.5×10^3 amp/cm^2 at room temperature and at 4.2°K. The probes were linear from 0 to 50 kilogauss. Changes in sensitivity as a result of thermal cycling for sample 90G and for an SBV552 (a commercial Hall generator utilizing phosphorus-doped indium arsenide in bulk form) are shown in Fig. 8.9.

Magnetoresistivity as a function of transverse magnetic field at room temperature and at 4.2°K is shown in Fig. 8.10.

---

[30] D. J. Reid, "Electrical Analysis of III-V Compound Semiconductors," p. 161 in *Compound Semiconductors*, vol. 1, ed. by R. K. Willardson, Reinhold, New York, 1962.

[31] R. J. Sladek, *Phys. Rev.* **105**, 460 (1957).

[32] The corresponding values of impurity concentrations of very pure bulk samples are lower by an order of magnitude. Compare T. C. Harman, H. L. Goering, and A. C. Beer, *Phys. Rev.* **104**, 1562 (1956).

[33] I. Isenburg, B. R. Russell, and R. F. Greene, *Rev. Sci. Instr.* **19**, 685 (1948).

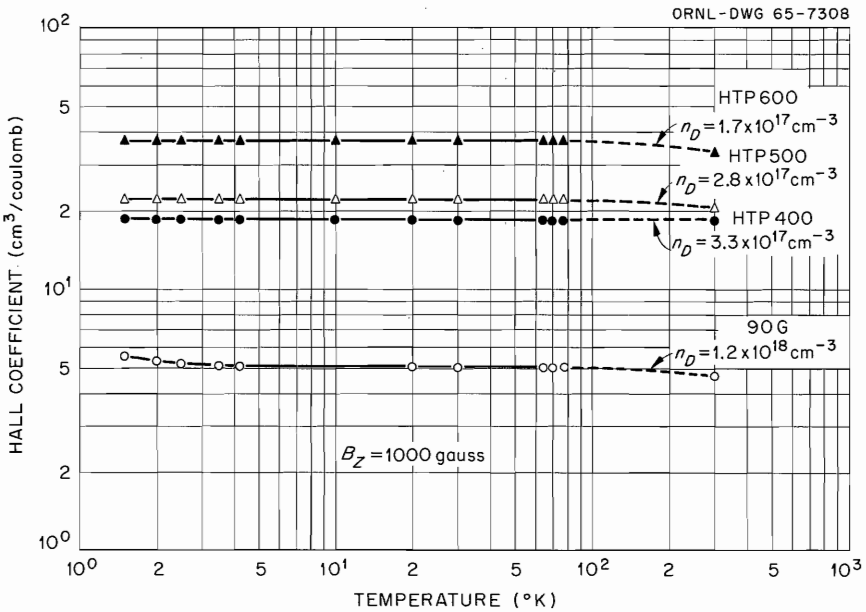

Fig. 8.5. Hall Coefficient as a Function of Temperature.

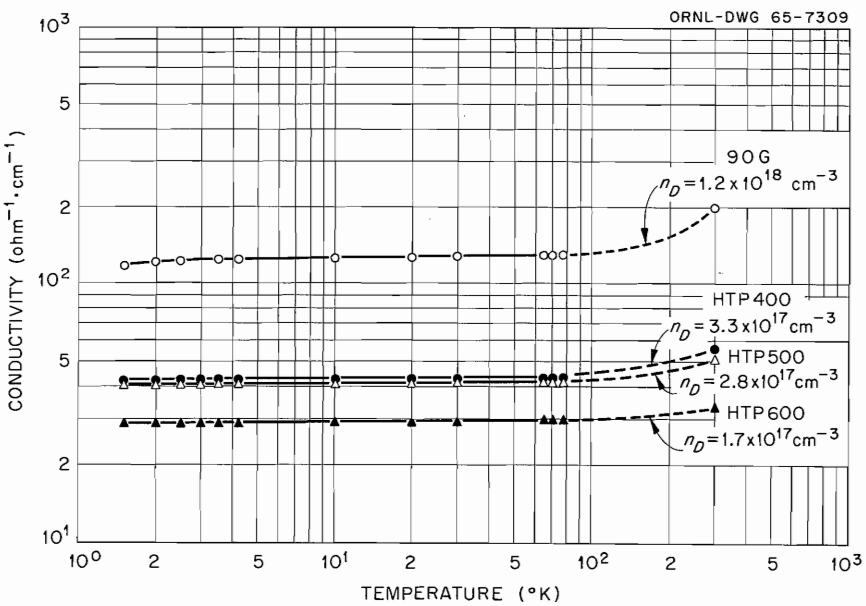

Fig. 8.6. Conductivity as a Function of Temperature.

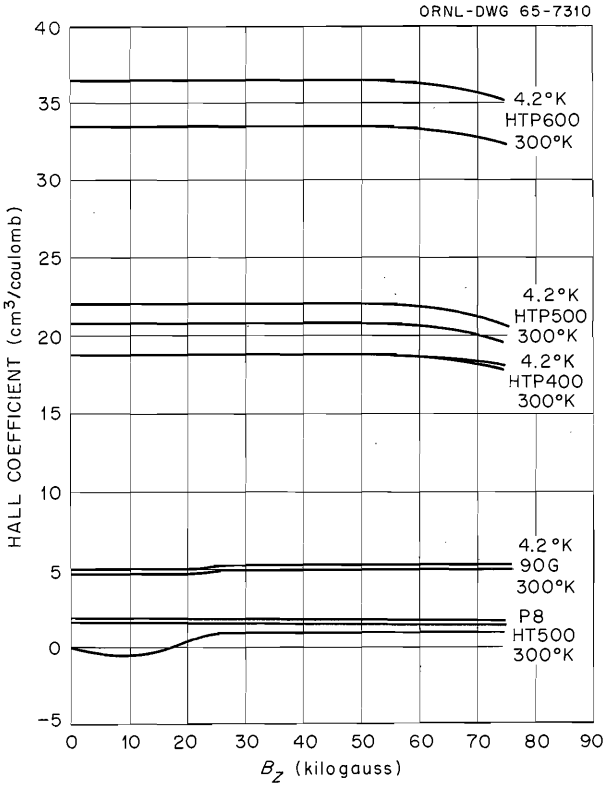

Fig. 8.7. Hall Coefficient as a Function of Magnetic Field Intensity.

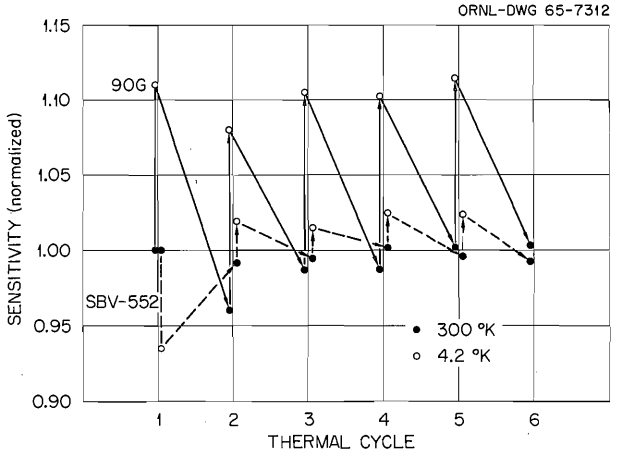

Fig. 8.9. Change in Sensitivity upon Thermal Cycling from 300 to 4.2°K.

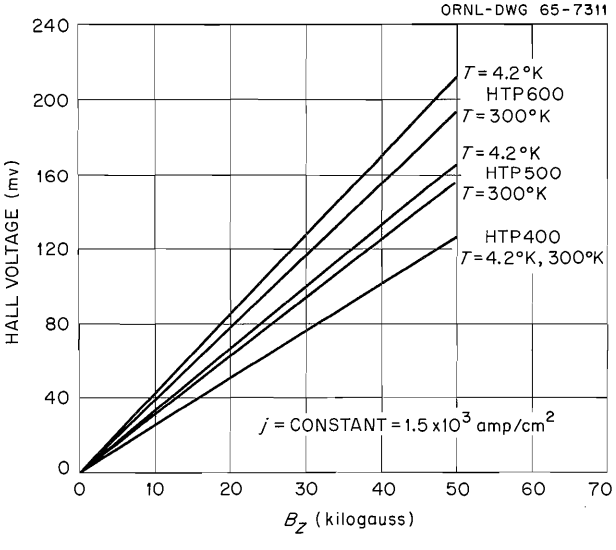

Fig. 8.8. Hall Voltage as a Function of Magnetic Field with Constant Current Density for Three Indium Arsenide Microprobes.

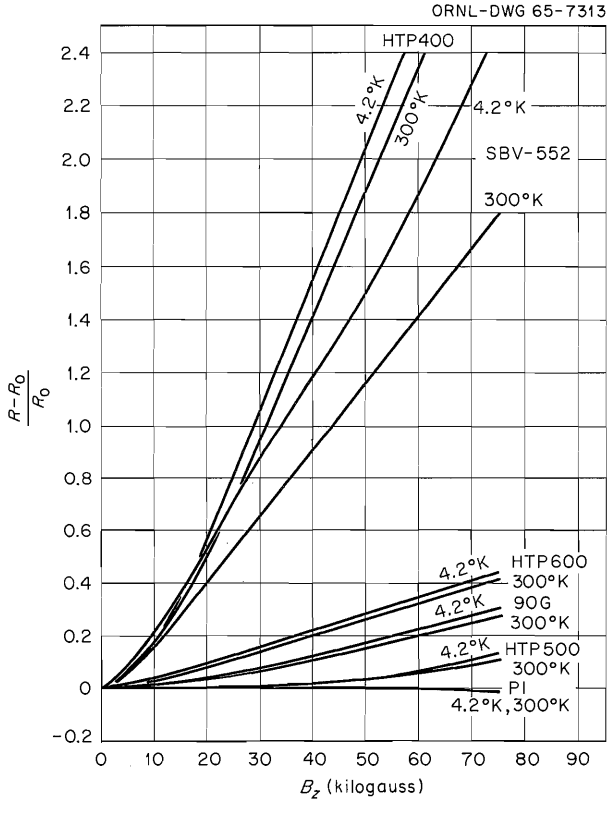

Fig. 8.10. Magnetoresistivity at 300 and 4.2°K as a Function of Magnetic Field.

8.3.4 Conclusions

These preliminary investigations indicate that it is possible by means of vacuum deposition to obtain indium arsenide films which exhibit electrical behavior similar to the bulk material. These films may be used satisfactorily as Hall generators at 4.2°K and below. Their sensitivity is sufficiently high that they may be employed to measure magnetic fields of less than 1 gauss intensity at these low temperatures, and their response is approximately linear from 0 to 50 kilogauss. Their temperature dependence is very slight between 300 and 4.2°K, and their change in sensitivity upon thermal cycling is relatively small.

Provided a good Hall geometry is used, their size is limited only by the dimensions of the masks used in their deposition. A length-to-width ratio of at least 3 is desirable for maximum sensitivity. It is necessary that the ratio of width of the voltage arms to length of the Hall plate is small.

The impurity concentrations were as low as 2×10^{17} cm^{-3}, which is an order of magnitude above those of very pure specimens of bulk material. It would be extremely difficult to achieve fully this level; however, some improvement of the above-mentioned film purity, and thereby of the Hall coefficient, should be possible. If it were feasible to grow epitaxial indium arsenide films, they would exhibit an even larger Hall coefficient and thus greatest sensitivity.

8.4 A SIMPLE SYSTEM FOR INTRODUCING 200 AMP INTO LIQUID-HELIUM ENVIRONMENTS

K. R. Efferson

It is intended to construct a 50-kilogauss superconducting solenoid with an Nb–25% Zr seven-strand cable. Such a solenoid will require approximately 200 amp input current at the highest field values. Since nonsuperconducting power leads must carry current to the solenoid, which is immersed in liquid helium, the leads can account for considerable liquid-helium loss due to Joule heating and thermal conduction.

Liquid-nitrogen cooling of the high-temperature ends of the leads reduces the losses due to thermal conduction, and using stranded input leads can make some use of the heat capacity of evaporating helium. A system of this type has already been reported.[34] In order to make maximum use of the heat capacity of the helium vapors, it is desirable to have the leads built in the form of a more efficient heat exchanger. Mathematical procedures for optimizing such a system have been worked out by Williams,[35] who constructed heat-exchanger leads of helical copper fins such as are used in some commercial heat exchangers, for the special case of 10 amp input current.

A much simpler design has been used here to construct a set of test leads optimized to carry 200 amp without liquid-nitrogen cooling. The leads are made from appropriate lengths of copper tubing, where the evaporating helium is forced to pass through the tubing to the atmosphere (Fig. 8.11). Styrofoam surrounds the leads and fills the upper portion of the Dewar, thus preventing helium vapors from making contact with warmer parts of the system.

Optimization for 200 amp per lead by means of Williams's method yielded $l/2a \approx 420$ cm^{-1}, where l is the length and a is the conducting cross section of one of the leads. Thus, 37 in. of $^3/_{16}$-in.-OD copper tubing was required for each lead. A set of leads constructed in this manner worked quite well for currents up to 150 amp; however, at 200 amp the helium gas emerging from the leads was much hotter than room temperature. Furthermore, the pressure in the Dewar increased so considerably that the full current strength of 200 amp was not considered permissible for this special lead design. It was felt that viscous drag in the leads was preventing the helium vapors from emerging from the leads fast enough to avoid dangerous overpressure. This problem could readily be solved by using $^1/_4$-in.-OD copper tubing, which has a larger ratio of inside-hole area to conducting area; however, since some data were already available on the $^3/_{16}$-in. tubing, it was decided to shorten the existing leads and see how critical the length was regarding helium losses.

[34] R. L. Brown, D. L. Coffey, and W. F. Gauster, *Thermonuclear Div. Semiann. Progr. Rept. Oct. 31, 1962*, ORNL-3392, p. 77.

[35] J. E. C. Williams, *Cryogenics* 3, 234 (1963).

On reducing the length by 24% (to 28 in.), it was found that the helium vapors emerged only slightly warmer than room temperature when the leads were carrying 200 amp and that only about a 10% increase in helium consumption occurred (Fig. 8.12). Even with the 10% increase in helium losses, it is felt that the results are quite reasonable. For example, at 100 amp the 0.1 cm/min loss represents only 46% of the losses obtained with the more elaborate liquid-nitrogen-cooled system previously tested.[34]

The evaporation rates obtained in this test indicate that this 50-kilogauss system can easily be designed to give 2 hr working time with the field at its peak value. Since most work will not involve continuous operation at high field values, the time between helium transfers should be much greater than 2 hr.

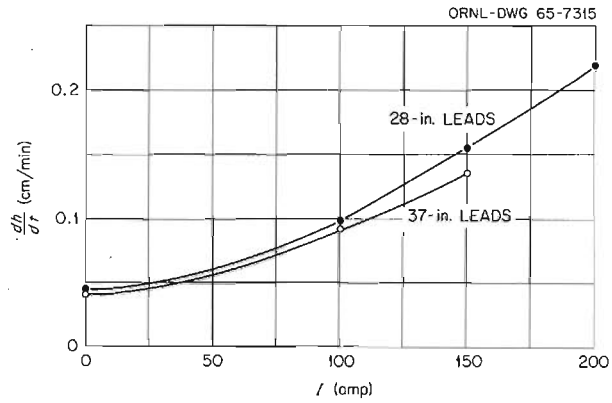

Fig. 8.12. Rate of Change of Helium Level vs Current for 37- and 28-in. Leads. Rates are for $4\frac{1}{2}$-in.-ID Dewar.

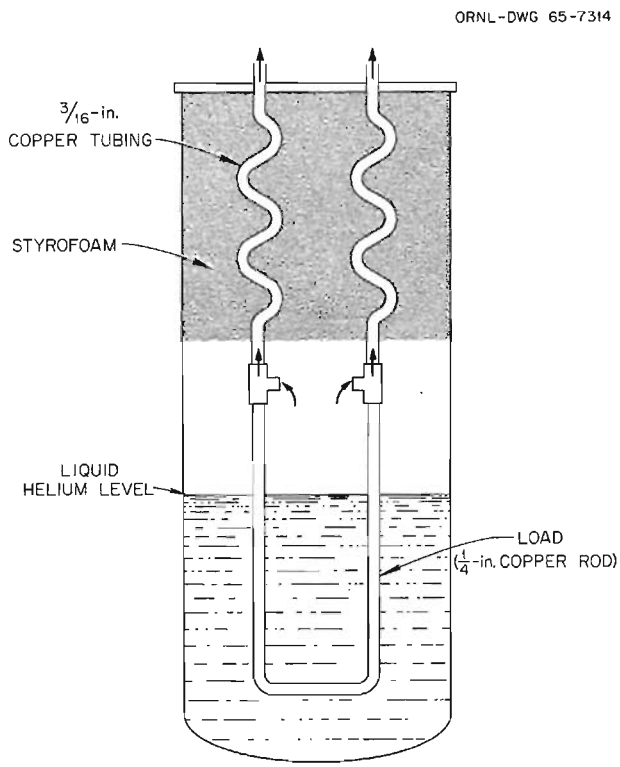

Fig. 8.11. Schematic of Helium-Vapor-Cooled Lead Test System.

8.5 INVESTIGATIONS OF FLUX JUMPS IN NIOBIUM-ZIRCONIUM

H. A. Ullmaier

8.5.1 Introduction

Investigations of superconducting niobium-zirconium magnet coils show the close relationship between the so-called "degradation effect" and the "flux jump" phenomenon. Basic experiments were made by Y. B. Kim[36] and co-workers; P. W. Anderson[37] attempted, successfully, to elucidate the physical background. Recently this working group and many others continued this kind of research and produced a wealth of interesting results.

The flux jump phenomenon can be studied most easily by using hollow or solid cylinders in longitudinal external fields. Wipf and Lubell studied the flux jumping in Nb–25% Zr under nearly adiabatic conditions.[38] They measured the external field strength H_{fj} at which the first flux jump occurs as a function of the rate of field rise, dH_{ext}/dt. They developed a simplified theory for the one-dimensional case.

[36] Y. B. Kim, C. F. Hempstead, and A. R. Strnad, *Phys. Rev.* **129**, 528 (1962).

[37] P. W. Anderson, *Phys. Rev. Letters* **9**, 309 (1962).

[38] S. L. Wipf and M. S. Lubell, *Westinghouse Scientific Paper* 65-L JO-Lotem-P3 (Mar. 5, 1965).

Similar work is being done here; however, we try to consider more in detail the influence of the sample radii and of the "history" of the external field application.

The phenomena connected with flux jumps in superconducting magnet coils are much more involved. Whereas the flux jump in cylinders initiates regularly at the cylinder surface, the first flux jump in coils may or may not occur at the "critical position" on the inner coil surface. Besides the external field, the transport current must be considered. Furthermore, the transient phenomena are determined by the complicated electrical, magnetic, and thermal conditions along the turns and across the winding layers. Finally, the electromagnetic performance of the entire electric circuit (including current source) must be considered.

8.5.2 Experiments with Hollow and Solid Cold-Worked Nb–25% Zr Cylinders

Figure 8.13 shows the experimental arrangement. The rate of the field sweep of the superconducting coil M, which produces the increasing external field, was $dH_0/dt = 400$ oersteds/sec. The sudden change of the flux in the sample S during a flux jump was detected by means of a pickup coil wound around the sample. The resulting signal was recorded either by an X-Y recorder or an oscilloscope. A typical diagram obtained by the X-Y recorder is shown in Fig. 8.14.

One group of experiments was performed in the following way: The temperature of a sample was changed from room temperature to 4.2°K by immersing into liquid helium. In this way, each sweep was applied to a "virgin" sample (these types of experiments are marked in Fig. 8.14 by horizontal arrows). Another group of experiments employed samples with a "magnetic history" (marked by crosses). In these cases the field was raised until the first flux jump occurred and then lowered with a very slow rate in order to avoid a flux jump caused by the decreasing field. At $H_0 = 0$, the sample contained trapped flux. After waiting until the sample achieved thermal equilibrium, the field was raised until the first flux jump occurred. The results of these experiments, represented in Fig. 8.14, are as follows: A solid cylinder with a 3.2-mm outer diameter and a tube with the same outer diameter and a 1.6-mm inner diameter produced approximately the same results.

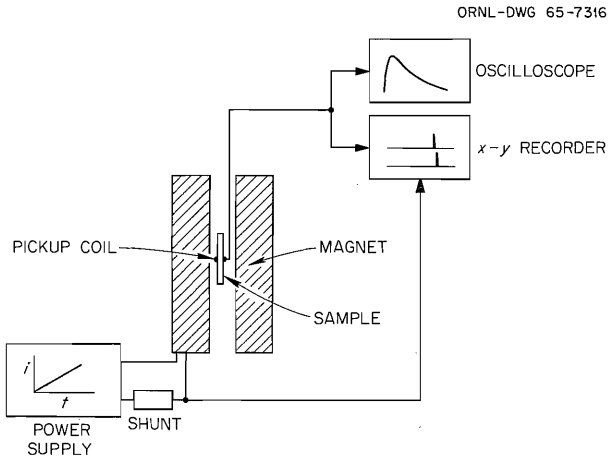

Fig. 8.13. Experimental Arrangement for Investigation of Flux Jumps in Superconducting Cylinders. The magnet is itself a superconducting coil, and the sample is a Nb-Zr cylinder about 3 mm in outside diameter.

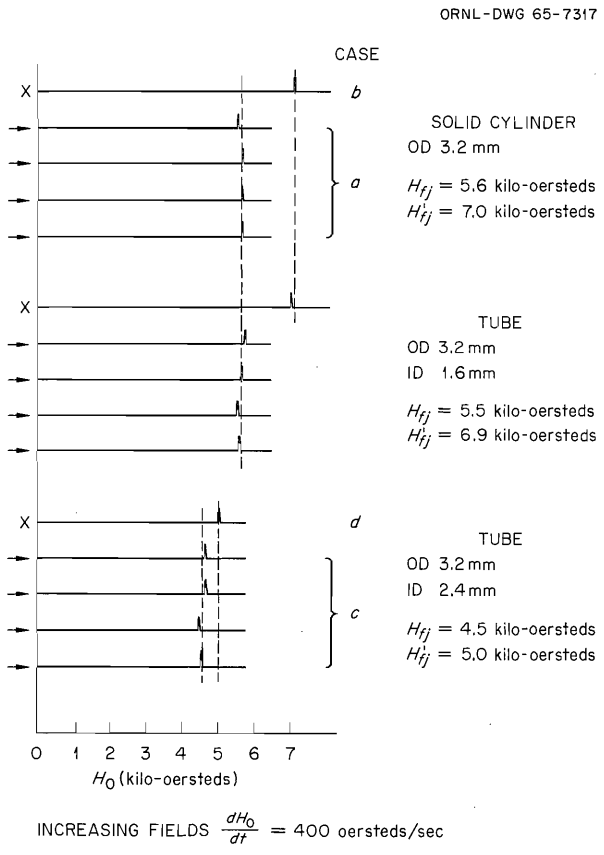

Fig. 8.14. Critical Fields for Nearly Adiabatic Flux Jumps.

With "virgin" samples the critical field strength, H_{fj}, was about 5.5 kilo-oersteds. In samples with "magnetic history," H_{fj} increased to around 7 kilo-oersteds. Although the external conditions were the same, a tube with a 3.2-mm outer diameter and a hole of 2.4 mm showed a critical field strength of 4.5 kilo-oersteds ("virgin" sample) and 5 kilo-oersteds (sample with "magnetic history") respectively.

8.5.3 Discussion of the Experimental Results by Means of Simple Models of Hard Superconductors

These results can be qualitatively explained by applying Bean's model[39] of hard superconductors. In a first approximation the influence of the temperature on the current density has been neglected. A more realistic presentation will be made at another time.

Figure 8.15 shows the field and current distributions inside a cylinder in a longitudinal field.

[39] Bean's very simple model does not consider the dependence of I_c on B. It is used here as a first approximation (compare *Thermonuclear Div. Semiann. Progr. Rept. Oct. 31, 1963*, ORNL-3564, pp. 107–21).

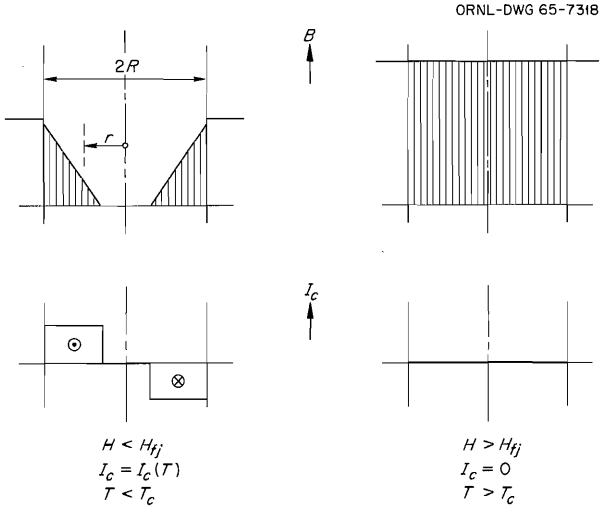

Fig. 8.15. Fields and Shielding Currents in Superconducting Cylinders.

When the external field H_0 is increased with a rate of change dH_0/dt, flux enters the sample. This change of flux will induce an electric field strength around a concentric circle which has its maximum value E on the surface of the cylinder:

$$2\pi RE = -\frac{d\Phi}{dt} . \tag{1}$$

Because E has the same direction as the shielding current density I_c, an energy per unit volume of

$$dW = EI_c\, dt = \frac{I_c}{2\pi R}\, d\Phi \tag{2}$$

is dissipated. This leads to a temperature rise dT. Under adiabatic conditions,

$$\frac{I_c}{2\pi R}\, d\Phi = c\, dT . \tag{3}$$

In general, I_c, Φ, c, and T are correlated in a rather complicated manner, and, as mentioned previously, solutions which consider this fact will be published later. For the assumptions made, and for $R \to \infty$, Eq. (3) leads to a simple expression for H_{fj}. In this case, Φ is given by

$$\Phi = 2\pi R\, \frac{B_0}{\mu_0 I_c} \cdot \frac{B_0}{2} \quad (B_0 = \mu_0 H_0) ,$$

$$\frac{d\Phi}{dt} = \frac{\pi R}{\mu_0 I_c}\, 2B_0\, \frac{dB_0}{dt} = 2\pi RE , \tag{3a}$$

$$dW = EI_c\, dt = \frac{B_0}{\mu_0}\, dB_0 = c\, dT .$$

Integrating gives

$$\frac{B_0^{\,2}}{2\mu_0} = \int_{T_0}^{T_c} c(T)\, dT . \tag{4}$$

It will be shown at another place that this equation holds under more general conditions. If the upper limit of the integral is T_c, the critical temperature at the field B_0, H_{fj} is determined by $\mu_0 H_{fj} = B_0$. Equation (4) is identical with an equation derived by Wipf and Lubell[38] in a different way. In the cases considered here (Fig. 8.14), the simple equation (4) cannot be applied because the condition of large radii (compared with the field penetration depth) is not satisfied. However, it is

possible to obtain a qualitative explanation of the experimental results if the flux distributions inside the samples are considered.[40]

Figure 8.16 shows the field distribution under the previously introduced simplifications at a certain external field strength $H_0 = B_0/\mu_0 < H_{fj}$ for the four cases shown in Fig. 8.14. Equation (3) suggests that the power dissipation increases with the magnitude of the flux that is finally achieved inside the sample. As shown in Fig. 8.16*a* and *c* ("virgin" samples), in the case of a hollow cylinder the critical value Φ will be achieved at a lower external field than in the case of a solid sample. Figures 8.16*b* and *d* indicate that in the case of trapped flux at $H_0 = 0$ a higher external field H_0 is necessary in order to achieve the critical flux change. There is no difference in H_{fj} for the solid sample and the cylinder with 1.6-mm hole, because the field does not penetrate far enough to reach the hole.

8.5.4 Velocity of the Longitudinal Propagation of Flux Jumps in Nb–25% Zr Cylinders

Figure 8.17 shows the experimental arrangement. The sample is a solid Nb–25% Zr cylinder with a 3.2-mm diameter and a 50-mm length. Around the sample, two pickup coils C_1 and C_2 and a heater H are arranged. The resistance of the manganin wire used for the heater was 3 ohms, and it was energized by discharging a capacitor of 500 μf. The initial voltage was 40 v, and the time constant of the circuit was $\tau = RC = 1.5$ msec. Flux jumps were caused either by using heat pulses at various constant external fields H_0 or by sweeping the field with a constant dH_0/dt without heat pulses. Because of the finite longitudinal propagation velocity of the superconducting-normal boundary, the flux change occurs earlier in C_1 than in C_2. The distance between the coils divided by the time difference Δt gives the propagation velocity v.

Figure 8.18 shows a typical oscillogram. Since the coils C_1 and C_2 were wound in opposite senses, the peaks of the two voltage pulses have opposite directions. By determining the areas under the voltage-time curves (which were equal within the accuracy of measurement), the flux change $\Delta\Phi$ corresponding to flux jumps could be calculated. For the example shown in Fig. 8.18, $\Delta\Phi$ was 2.3×10^{-6} v-sec. Using this value and assuming a Kim field distribution, it is possible to get an estimate of the critical current density I_c. This calculation yields for 20 kilogauss a current density of 4×10^8 amp/m^2, which is in fairly good agreement with values obtained from magnetization measurement.[41] Figure 8.19 shows plots of Δt and v, respectively, vs external field strength. The points obtained by heating the sample are almost identical with the results of the field-sweep experiments. The curves show a break at 10 kilo-oersteds. In order to find an explanation for this performance, additional experiments with other sample dimensions are being planned.

[40]In a later report some solutions of Eq. (3) will be discussed, and the results will be compared with extended measurements on samples with various dimensions.

[41]The results of these magnetization measurements were kindly provided by R. H. Kernohan.

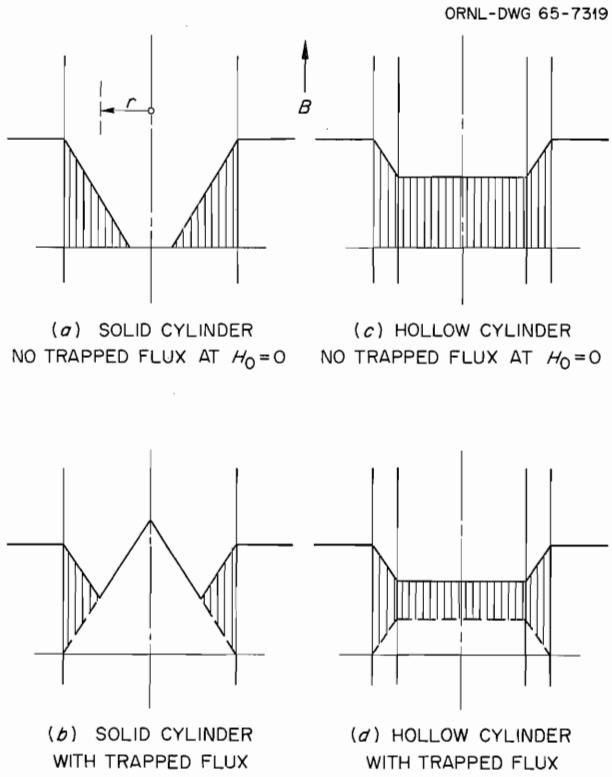

Fig. 8.16. Solid and Hollow Cylinder With and Without Trapped Flux.

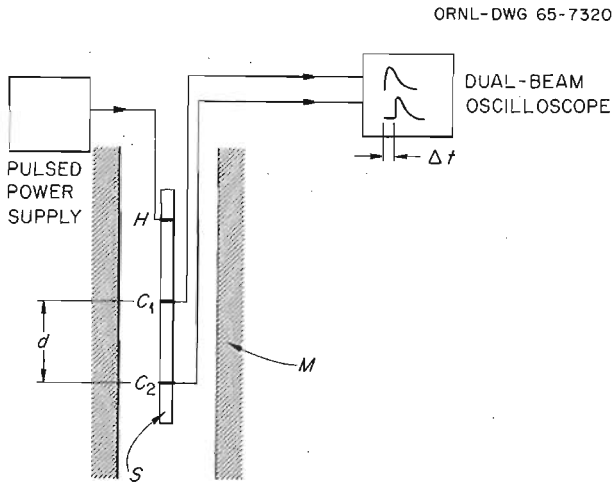

Fig. 8.17. Propagation-Velocity Measurement of Flux Jumps.

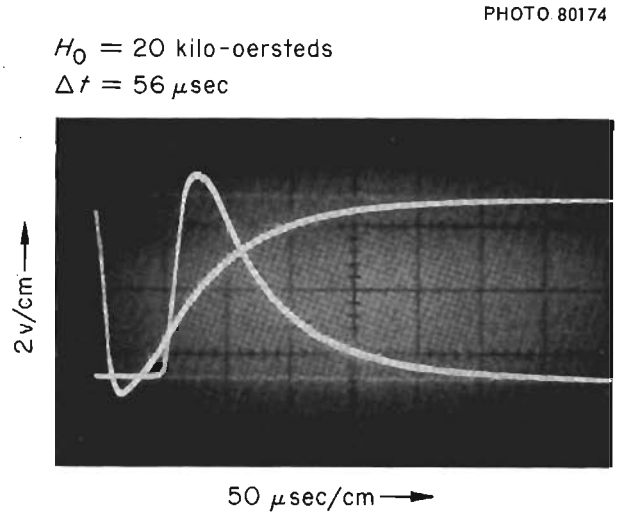

Fig. 8.18. Oscillograms of Flux Jumps.

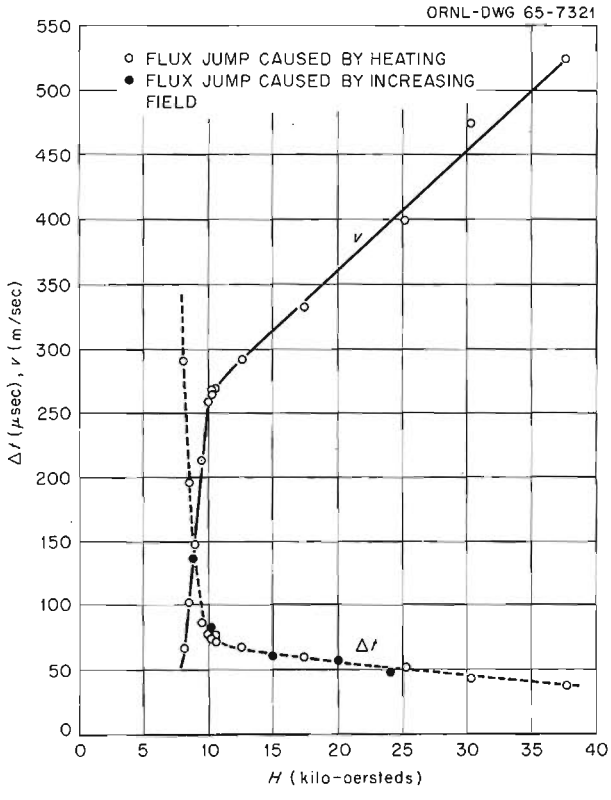

Fig. 8.19. Dependence of Propagation Velocity v and Propagation Times Δt on the External Field.

8.5.5 Flux Jumps in an Nb–25% Zr Test Coil

The coil used had a 23-mm outer diameter, a 9.2-mm inner diameter, and a 25-mm length; 1700 turns of unplated, nylon-insulated 10-mil Nb-Zr wire were wound on a Micarta spool. The coil was exposed to an increasing or decreasing magnetic field produced by a superconducting magnet coil. The flux jump observations were made with the sample coil self-field opposing the external field. Figure 8.20 shows X-Y recorder diagrams with different preset currents through the test coil. The flux jumps are indicated by the voltage change across a series resistance of 1 ohm in the sample circuit.

With increasing sample currents, the flux jumps start at higher external fields and extend over wider ranges. For currents up to 15 amp, quenching did not occur. Flux-jump traces with decreasing external fields are represented in Fig. 8.21. The direction of the flux jumps is now reversed. The starting field strength of the flux-jump zones is higher with larger currents.

An analysis of the magnitude of the resulting fields inside of the coil volume shows that flux jumps at field strengths smaller than 5 kilogauss

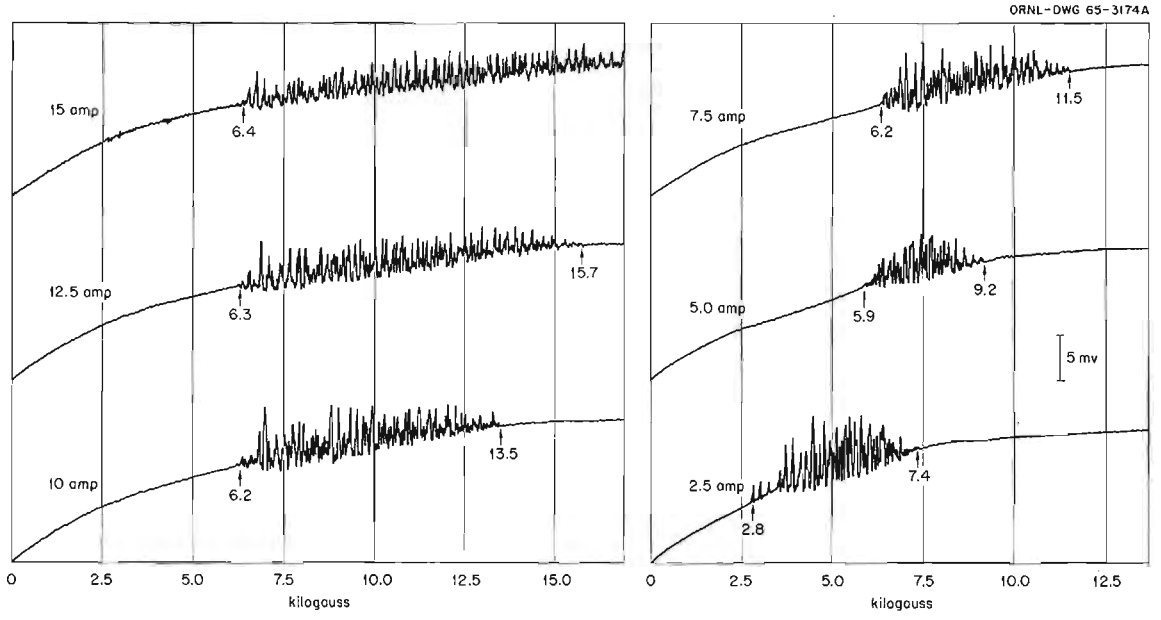

Fig. 8.20. Flux Jumps in Bare Nb–25% Zr Wire Coils (Increasing Field).

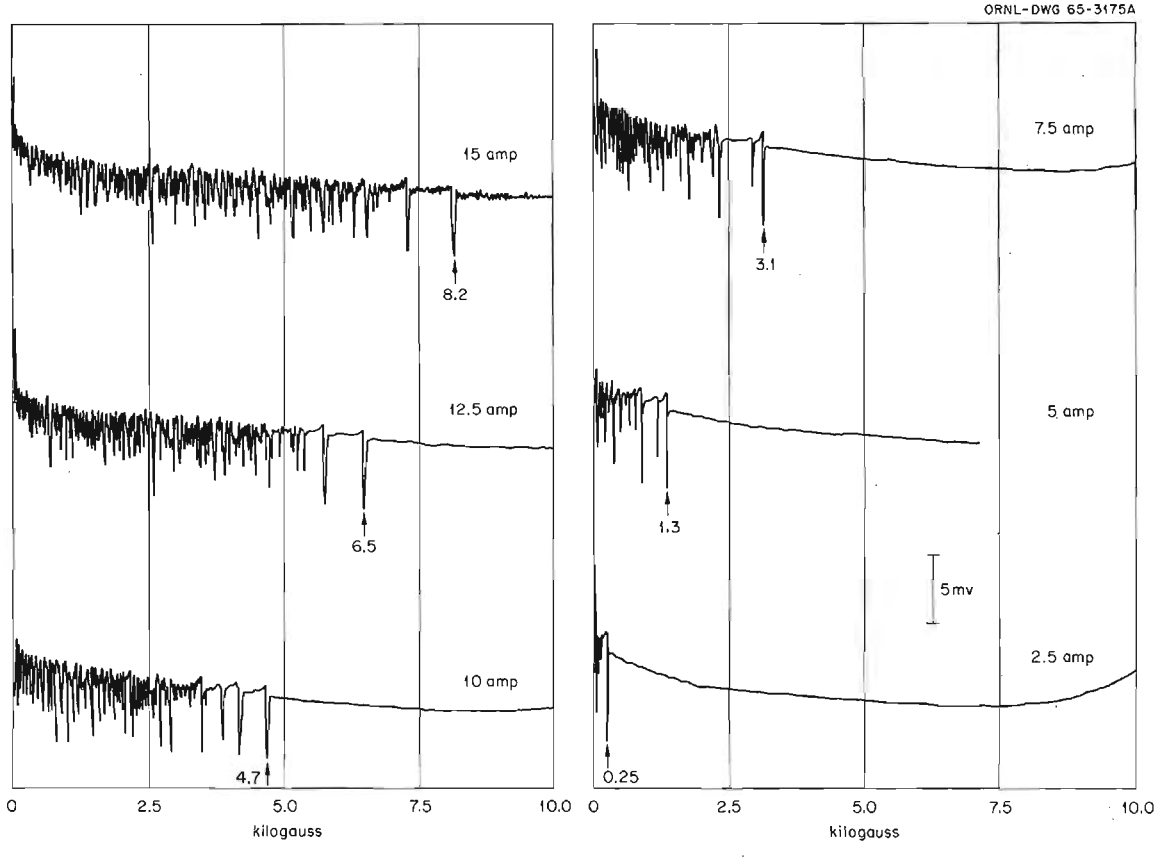

Fig. 8.21. Flux Jumps in Bare Nb–25% Zr Wire Coils (Decreasing Field).

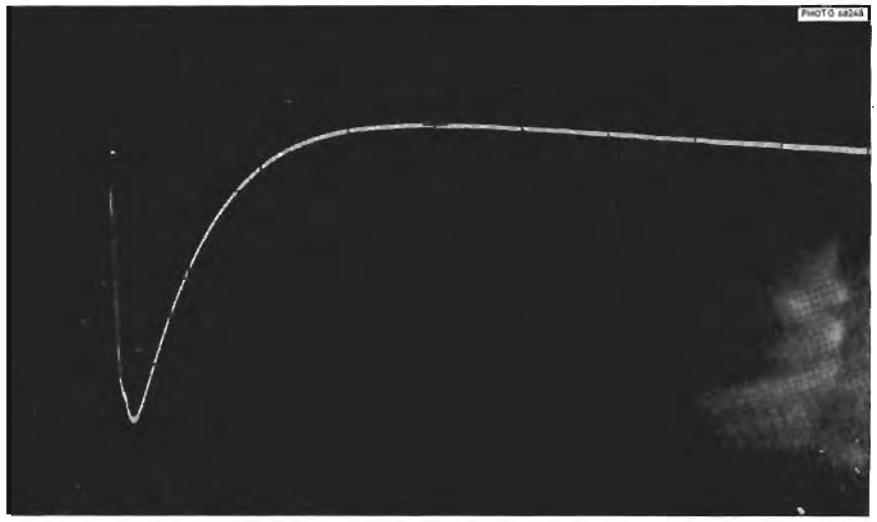

Fig. 8.22. Oscillogram of a Flux Jump in a Test Coil, Decreasing Field (20 msec/cm, 10 mv/cm).

are dangerous.[42,43] This agrees with magnetization measurements in external fields with varying transport currents. The flux jumps were also observed by means of an oscilloscope. A typical trace is shown in Fig. 8.22. However, it is difficult to analyze the voltage-time performance because it is determined not only by the flux-jump conditions in the hard superconductor but also by the inductance, capacitance, and resistance of the entire circuit.

8.6 EXPERIMENTAL SIMULATION OF LARGE HIGH-FIELD SUPERCONDUCTING MAGNET OPERATION[44]

W. F. Gauster D. L. Coffey

Sample coils of large diameter but with small cross-sectional areas have been tested in applied external fields up to 75 kilogauss (generated by a conventional 7-Mw water-cooled magnet with a $6\frac{1}{2}$-in. working diameter). By an appropriate choice of sample cross sections, it can be assumed that the "large-diameter, small-cross-section sample coils" will approximately reproduce the electrical, magnetic, and thermal conditions in a corresponding partial volume within the windings of a large superconducting coil. It is hoped that the evaluation of the test results with these sample coils will produce meaningful data which can be applied to the design of large superconducting magnet coils.

With sample coils of copper-clad, nylon-insulated Nb–25% Zr wire (core diameter, 0.010 in.), I_c-H_c curves (Fig. 8.23) were obtained which had minima for external fields of about +3 and about −12 kilogauss and maxima at around +15 and −30 kilogauss. With zero external field, the quenching currents scattered between 26 and 46 amp. Contours for $|\overline{B}|$ = constant (Fig. 8.24) show large volumes with $|\overline{B}| \leqq 5$ kilogauss for the two mentioned minimum points of the quenching characteristic and for zero external field. At these relatively low flux densities, the magnetic moment reaches maximum values and the energy release by flux jumps becomes large. This is in qualitative agreement with preliminary flux-jump measurements.

[42]Compare "Experimental Simulation of Large High Field Superconducting Magnet Operation," this report, sect. 8.6.

[43]M. R. Beasley *et al.*, *Phys. Rev.* 137, A1205 (1965).

[44]Abstract of the summary report covering the period from July 1, 1964, to February 28, 1965, of the activity of the ORNL Thermonuclear Division under Government Order No. H-7184 for the George C. Marshall Space Flight Center, National Aeronautics and Space Administration (D. L. Coffey, Project Engineer; W. F. Gauster, Project Supervisor) (ORNL-TM-1083).

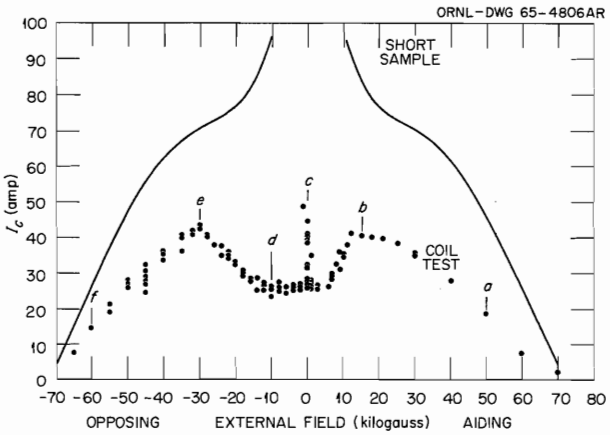

Fig. 8.23. 2250-turn-coil Reexamination.

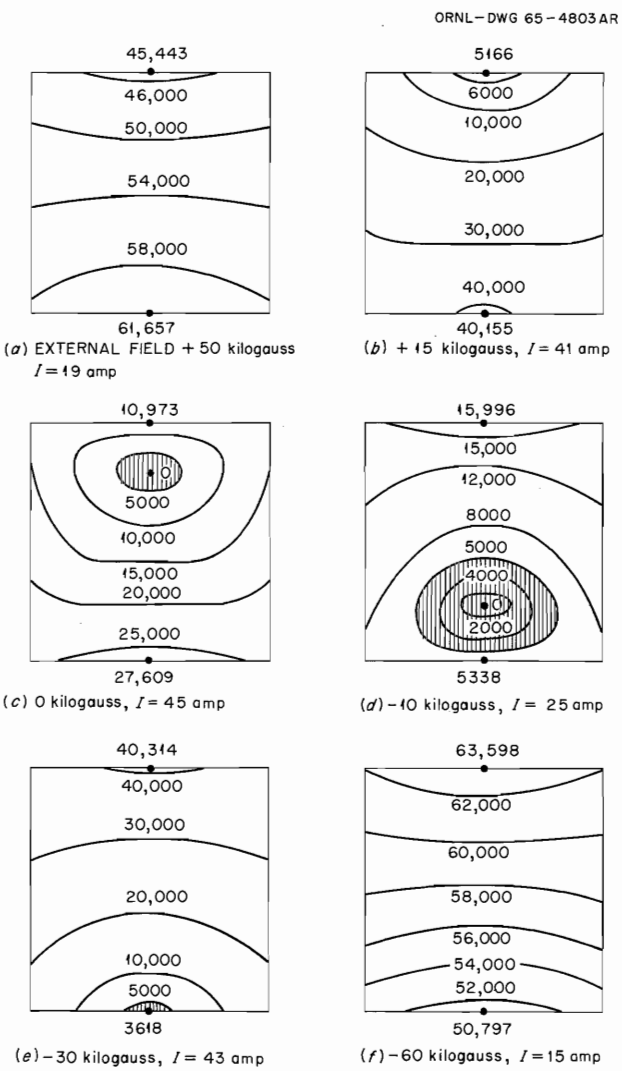

Fig. 8.24. Approximate Field Profiles Inside 2250-turn Coil.

9. Chemistry of Tritium in Controlled Fusion Devices[1]

R. A. Strehlow D. M. Richardson[2]

If tritium is used in controlled fusion devices, efficient recovery will be essential. The chemistry of tritium must be carefully examined to determine if such recovery will be possible. An initial survey of factors affecting the chemical behavior of tritium in a conceptual power reactor was made. A breeder reactor was chosen for consideration because this concept appeared to present the most promising route to the control of fusion energy.[3,4] Chemical aspects of the fuel cycle may be surmised using published information for hydrogen. Although many problems in estimating tritium inventories exist, a careful consideration of the possibilities discussed here has led to initial experiments to determine whether the phenomena discussed in this section do exist and to assess their significance to the controlled thermonuclear reaction program.

A generalized tritium flow path for a thermonuclear reactor includes tritium flow to and from three functional regions (source, plasma, and blanket), as shown in Fig. 9.1. In the assumed reactor, tritium is injected into a plasma, where a portion burns. Part of the unburned portion may flow to the vacuum processing region, the balance into the blanket. Tritium in the inventory will be lost by decay, permeation, and processing inefficiencies. Since the atom density (per cubic centimeter) of tritium will probably be about 10^{15} in the source, 10^{10} in the vacuum system, and possibly 10^{19} in the blanket region, separate processing methods for these regions appear to be desirable. To provide a basis of cost estimation, one of the reactor concepts of Homeyer[5] has been examined. Table 9.1 shows some of the operational parameters which he derived. Table 9.2 shows the estimated approximate volumes of various blanket-assembly materials required for such a reactor.

If the net breeding ratio is assumed to be 1.1 tritium atoms produced and recovered per tritium atom burned, the maximum tolerable inventory is that which yields a decay rate equal to the breeding gain rate. For the assumed reactor concept this maximum inventory is about 7×10^7 atm cm^3 of tritium.

[1]This section is a revision of material published in *Reactor Chem. Div. Ann. Progr. Rept., Jan. 31, 1965*, ORNL-3789, p. 336-40.

[2]Reactor Chemistry Division.

[3]D. J. Rose and M. Clark, *Plasma and Controlled Fusion*, p. 294, MIT Press, Cambridge, and Wiley, New York, 1961.

[4]W. R. Allis (ed.), *Nuclear Fusion*, p. 20, Van Nostrand, Princeton, 1960.

[5]W. G. Homeyer, Ph.D. Thesis, MIT, December 1962.

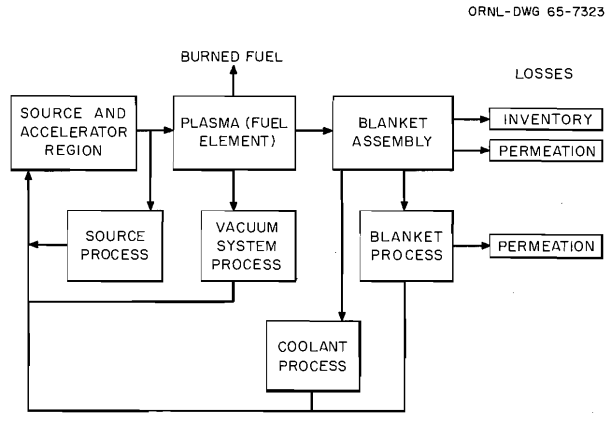

Fig. 9.1. Tritium Fuel Cycle for a Generalized Thermonuclear Reactor.

Table 9.1. Assumed Parameters for a Mirror-Field Reactor with Ion-Injection Feed

Thermal power	1000 Mw
Fuel burnup rate	8×10^5 atm cm^3/day
Fractional burnup	0.1 of the injected tritium
Injected current per source	5 amp
Number of sources	~200
Length of reactor	130 m
Diameter (wall to wall)	2 m

Table 9.2. Volume of Materials in Blanket

Material	Volume (cm^3)
Mo (first wall)	2×10^7
Coolant (Li_2BeF_4)	10^9
Graphite	2×10^8
Pb	3×10^8
INOR-8 (Hastelloy N)	6×10^7

9.1 SOURCE PROCESSING

Un-ionized tritium effuses from the ionizing region of an ion source to the vacuum volume of the source accelerating region, where it must be removed rapidly to maintain low pressure. This gas could be immediately recycled by recompression to a higher partial pressure. This may be accomplished by mechanical molecular pumping or diffusion pumping.

The inventory of tritium in a source structure may be estimated for an assumed 50-lb mass of steel per source. Inasmuch as atomic or ionic hydrogen fluxes on metals result in the formation of surcharged hydrogen alloys containing many times the equilibrium amounts of hydrogen,[6] precise estimation of the hydrogen content is difficult. Literature data for nickel exposed to high-pressure gaseous hydrogen indicate that Sieverts' relation (solubility is proportional to the square root of the pressure) begins to fail at about 120 atm; the solubility approaches a value of 200 atm which is not a function of pressure.[7] This corresponds to a solubility of about 10 atm cm^3/cm^3 for nickel at room temperature (atom ratio of 2×10^{-3}). With electrochemically discharged fluxes of hydrogen ions on iron up to 2.4×10^{17} sec^{-1} cm^{-2}, no solubility limit has been observed to concentrations of 0.5 atm cm^3/cm^3 (ref. 8) (much higher than the equilibrium value at 1 atm and room temperature of 0.05 atm cm^3/cm^3). Estimates 10^5 times the equilibrium solubility have been made for the extent of occlusion of electrochemically discharged hydrogen in copper, based on the relation derived by Tafel[9] [$\log P_{atm} = 34(0.8 + 0.1 \log I_c$ amp/cm^2)]. Since electrochemically derived estimates include electrophoretic effects and involve a liquid-solid interface, the appropriateness of the direct application of the Tafel relation to the plasma-wall hydrogen flux is questionable. However, the data for nickel[7] suggest that a factor of 10 to 15 in excess of the equilibrium value at 1 atm (1 atom per 10^3 metal atoms) may be used to give a possible hydrogen content. Consequently, a single 50-lb source assembly might contain 10^5 atm cm^3; for the assumed reactor design with 200 such sources, between 10^7 and 10^8 atm cm^3 seems a reasonable lower boundary to the inventory. Since this is within the estimated range of the maximum tolerable inventory estimate, sources designed to operate at elevated temperatures or with a minimum quantity of metal in the ionizing region may be needed.

If the desired injected species is DT^+, the other ions (of masses 3 to 9) which contain tritium will need to be deposited in the accelerator region in a way which allows simple removal.

[6]See, for example, D. P. Smith, *Hydrogen in Metals*, pp. 145–55, 276–79, Univ. of Chicago Press, Chicago, 1948.

[7]See A. Sieverts, *Z. Metallk.* **21**, 37–44 (1929) for a review.

[8]G. Borelius and S. Lindblom, *Ann. Physik* **82**, 201 (1927).

[9]J. Tafel, *Z. Physik. Chem.* **50**, 641 (1905); **34**, 187 (1900).

9.2 VACUUM SYSTEM PROCESSING

The nature of the vacuum system processing will be dictated primarily by the fuel-element characteristics: volume, fractional burnup, feed rate, and the fraction of tritium which enters the blanket assembly. A minimum tritium atom flux to the wall of 10^{12} cm^{-2} sec^{-1} (0.1% of the injected tritium) is expected. For any of the injected tritium which strikes the walls as ions or atoms, the fraction released from the surface will depend on the kinetics of transport through the wall (and ultimate removal) relative to that of desorption. In this section we will arbitrarily assume that equal amounts are desorbed and otherwise removed and that any desorbed tritium reaching the plasma region does not yield an additional atom or ion impact with the wall (e.g., desorbed tritium which is ionized by electrons can escape the plasma region in a flow along a magnetic line of force). In this case, half of the unburned fraction must be reprocessed. For a fractional burnup of 0.1, and using the standard source of Homeyer for comparison (Table 9.1), the vacuum system processing rate would have to be 3×10^6 atm cm^3/day. At a lower fractional burnup of 0.02, perhaps 1.5×10^7 atm cm^3/day would have to be processed. The processing rates given for tritium must be multiplied by the atomic ratio (D + T + H)/T, a factor equal here to at least 2. The inefficiency of the source processing should increase this load by no more than a factor of 2 (estimating effusive flow at 200 liters/sec from each source at a pressure of 10^{-5} torr). Mercury diffusion pumps or turbomolecular mechanical compressors (with appropriate lubricants) might be used in possible recovery processes for the vacuum system; palladium membranes might serve to separate the tritium from helium.

Thermal cycling of exothermic absorbers would require the dissociation energy plus a specific heat energy for the absorber and could be accomplished with the expenditure of about 10^6 cal/g-mole. At 10^3 moles/day, about 2 Mwhr/day would be the resulting power cost for this process.

Cryogenic trapping offers one possibility of separating the various hydrogen isotopes from each other as well as from helium. An estimate[10] for the helium cost of 3 kwhr/liter, with a hydrogen adsorption energy of 3 kcal/mole and ΔH_v of helium = 5×10^3 j/liter, leads to the need for 10 kwhr per mole of T_2. This [multiplied by the atom ratio (D + T + H)/T] is about 10 Mwhr/day for the hypothetical reactor. The power required for temperature cycles to 8°K would require perhaps an equal amount of energy for the specific heat of the adsorber material. The total cryogenic trapping process would use some 1 to 2% of the total electrical power output. A liquid-helium plant of about 200 to 400 liters/hr (0.5 Mw installed power for liquefaction) would be needed for this process.

A more serious consideration in the vacuum process design, however, is the possibility that intermittent dumping of the entire fuel volume might be required in order to purge the plasma of accumulated helium. If we follow Rose and Clark[3] and assume that introduction of nonadiabatic regions will allow continuous purging, we, of course, have assumed nonexistence of the problem. We will, nonetheless, consider this possible process requirement, and, if it is necessary to dump after 0.05 of the tritium is burned, then our fractional burnup is decreased by a factor of 20; if we assume that dumping is required on an hourly schedule, an additional 10^5 atm cm^3/hr would have to be processed, presumably at a much higher than steady-state rate, in order to reprepare the plasma region for another startup. A diffusion pump compression process mentioned above appears to offer the simplest means for accomplishing the needed task. Some ten or so 50,000-liter/sec pumps and a foreline surge volume of probably less than 10^2 m^3 should be adequate for this method. Restarting in a system having an elevated wall temperature might present several more serious problems because of the high neutral flux from the wall as compared with that at first startup. Coupled with the power cost, problems such as these would add heavily to process costs.

Since unburned fuel leaving the plasma will be ionized, the surcharging effect might be utilized to allow isotope separation and recovery of the hydrogen isotopes. Processes similar to those described below for blanket processing may be applied to vacuum processing.

[10] R. B. Scott, *Cryogenic Engineering*, p. 68, McGraw-Hill, New York, 1959.

9.3 BLANKET ASSEMBLY PROCESSING

To this point no serious impediments have appeared regarding fuel cycle costs or feasibility based upon existing technology. However, with the expected flux of tritium atoms to the blanket wall of 10^{12} cm^{-2} sec^{-1} (0.1% of the fuel feed), crude application of the Tafel relation mentioned above leads to a possible equivalent pressure of some 10^5 atm. Therefore, in the absence of effective sinks for the tritium contained in the metal wall and blanket assembly, the blanket inventory may fall in the range of 1 to 10 atm cm^3/cm^3. This corresponds to a steady-state inventory of from 5×10^7 to 5×10^8 atm cm^3 total (10^2 to 10^3 days supply) in the wall. Moreover, this inventory would be located in close proximity to the plasma and consequently would be important in stability considerations for any tritium-burning fusion device.

A different method of estimating the inventory may be described which, nevertheless, leads to a similar result. For the endothermic hydrides (Mo, W, Fe, Ni, etc.), collision statistics on the surface facing the vacuum will determine the emission rate. A tritium-metal atom ratio of perhaps 5×10^{-5} (0.2 atm cm^3/cm^3) with a tritium jump frequency of 10^{-7} sec (based on a 20,000-cal/mole activation energy and a 10^{-13} sec frequency factor) yields an expected emitted molecular flux of about 10^{12} sec^{-1} cm^{-2} (equal to the loading flux). With this estimate one would expect the total inventory for the blanket assembly to be more than 10^7 atm cm^3.

To the extent that these estimates are valid, a process is needed in which tritium is removed efficiently from a wall containing only low concentrations at the surface. Three possible methods for accomplishing this removal are:

1. those which increase the frequency of T-T collisions at the solid-vacuum interface leading to T_2 desorption;
2. those which form a sink for tritium in the blanket by solid-state reactions; and
3. those which permit removal of individual atoms of tritium rather than molecules.

Thermal cycling of the blanket assembly or inclusion of a palladium region in the blanket assembly, for example, would be of the first type, but because of thermal stress, nuclear, and design problems, they do not seem presently attractive.

Inclusion of masses of zirconium, an example of the second type listed above, would pose numerous problems because of the need for periodic disassembly. Mechanical separation and thermal processing might be advantageous to the neutron economy of the reactor and might not prove too costly if the accumulation periods were of the order of six months or more. Vapor deposition of titanium, cerium, zirconium, or yttrium in a region of the vacuum system on a surface contiguous with the blanket assembly volume would allow the recovery of the tritium by a vacuum system process. All these approaches require extensive study to establish their technological feasibility.

The greatest decrease of the inventory, however, appears to be afforded by processes of the third class listed above. This type includes oxidation and reduction of contained tritium atoms, removal as individual atoms or ions to a vacuum, isotopic dilution with hydrogen or deuterium, or removal as a covalent compound (e.g., as tritomethane or tritoethane, from carbon-containing titanium which has been freshly sputtered in the absence of water).[11] Inasmuch as the molybdenum will probably have a large carbon content, either due to the presence of graphite or as an initial impurity, it is possible that similar processes will occur at the plasma-wall interface. We have not yet observed this reaction except with titanium.

A chemical reduction of occluded tritium to tritide ion presumably would be accomplished if liquid lithium were used as coolant.

Oxidative processes for the removal of tritium atoms from the surcharged metal appear to be possible for $LiF\text{-}BeF_2$, previously discussed as a breeder coolant.[12]

One of the additional complications regarding the blanket inventory and other losses is that, if removal of tritium atoms is not possible, permeation of hydrogen to voids in the blanket assembly will result in hydrogen pressures of perhaps hundreds of atmospheres or more. The structural integrity of the blanket assembly under surcharging conditions must be examined. The flux of tritium through the entire assembly can also result in a total leak of perhaps several percent per day to the gaseous region surrounding the reactor. Even in the best

[11] *Thermonuclear Div. Semiann. Progr. Rept. Oct. 31, 1964*, ORNL-3760.

[12] C. J. Barton and R. A. Strehlow, *Blankets for Thermonuclear Reactors*, ORNL-3258 (June 27, 1962).

case, with an efficient sink for tritium in the blanket assembly, a total leakage to the ambient gas of perhaps 10^4 atm cm^3/day may exist.

To summarize the blanket processing outlook, since intolerable steady-state inventories may occur, fuel-cycle studies regarding hydrogen transport in and removal from blanket materials are required; surcharging processes must specifically be investigated. These considerations are based on a rather extensive and tenuous analogy to electrochemical phenomena, which themselves are not well understood. Accordingly, an apparatus was assembled using existing equipment to allow a study to be made in order to begin to determine:

1. if the postulated phenomenon of surcharging of metals in the presence of bombardment or glow discharge actually occurs;
2. how temperature, current density, material, and dimension affect the occluded quantity;
3. whether diffusive flow in the metal is a critical parameter in processing considerations; and
4. how the isotope effects alter the inventory and processing outlook.

Initial results indicated that at a pressure of 0.5 torr as much as 2 atm cm^3 of H_2 per cubic centimeter of molybdenum wire could be occluded at temperatures near ordinary room temperature as a result of glow discharge bombardment (at about 1 kev). This value is about 10^3 times the equilibrium solubility of hydrogen in molybdenum expected at this pressure. It appears, therefore, that the postulated phenomenon does exist, and it remains to be determined how significant it is to the tritium fuel cycle.

9.4 COOLANT PROCESSING

The simplest assumption regarding the coolant is that the tritium is contained as lithium tritide or as tritium fluoride (for the two coolants considered here). In this case the estimates of Homeyer will hold approximately, and no particular problem should be expected. If there is an appreciable quantity of tritium gas in the coolant salt, however, from whatever source, tritium leakage to the heat exchangers, piping, etc., could require processing of the gas surrounding this allied equipment. This possibility would presumably not increase the total inventory by more than perhaps 10^4 or so atm cm^3.

9.5 TRITIUM INVENTORY

The estimated amounts of tritium in the various parts of the proposed reactor are listed in Table 9.3. The large ranges indicate the uncertainties due to the expected unique chemical environments.

Table 9.3. Estimated Inventory of Tritium (10^7 atm cm^3)

		Comments
Sources	0.5–10.0	Must be designed for minimum inventory
Accelerators	0.2–20.0	Even at low inventory levels, the processing may require large throughputs
Blanket, structure	0.2–20.0	
Blanket and coolant	0.5–3.0	Assuming processing
Storage	0.5	One week supply
Total	1.9–53	Probable maximum tolerable inventory 5–10

9.6 STARTUP PROCESSING

An additional problem regarding the nature of reactor startup should be considered here. If we assume an initial protium content in the blanket components equal to an atom ratio of 10^{-4}, there will be in the reactor perhaps 10^{10} atm cm^3. Isotope separation would probably be required to remove this protium, although operation of the device with deuterium might simplify the processing. Cryogenic separation techniques, considered above, might be used. The isotope effect (especially pronounced for temperatures less than 400°C, where ^1H tunneling dominates) during a surcharging process to load the metal could lead to a promising recovery and isotope separation scheme. Gas chromatographic separation offers a third processing possibility.

10. Fusion Chain Reactions

J. R. McNally, Jr.

10.1 INTRODUCTION

During this report period, we have studied further the concept of charged-particle fusion chain reactions outlined previously.[1] There, a qualitative discussion was presented on the concept of fusion chain reactions in which protons (and deuterons, tritons, ^{3}He, or energetic alphas as chain centers) may catalyze the burning of ^{6}Li or other nuclear fuels, quite analogous to chemical chain reactions except for the energy scale of the events. The following sections summarize some of our present thoughts on the subject.

10.2 REVISED NUCLEAR CROSS SECTIONS

Figure 10.1 is a revised set of graphs of nuclear cross section data, expressed in terms of σv, the reaction rate parameter, vs the energy of the projectile. We have taken certain liberties with published literature data in order to obtain σv, the most common assumption being to assume spherical symmetry of differential cross sections. The results tabulated in Fig. 10.1 are quite qualitative; however, they suggest strongly the potentiality of a very-high-temperature D · ^{6}Li fusion system which can breed t and ^{3}He in situ somewhat better than a D · D system at the same temperature.

[1] *Thermonuclear Div. Semiann. Progr. Rept. Oct. 31, 1964*, ORNL-3760, sect. 10, pp. 98–99.

10.3 THEORETICAL MULTIPLICATION CONSTANT

Figure 10.2 illustrates one of the reaction sequences for energetic alpha particles in

ORNL-DWG 65-2697A

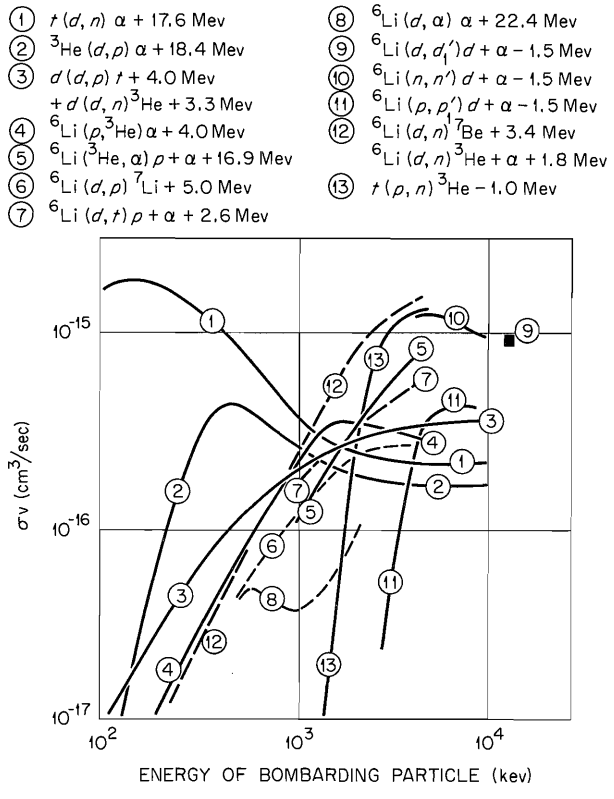

Fig. 10.1. Reaction Rate Parameter, σv, vs Energy of Particle (Data Only Approximate in Numerous Cases). Note many reaction channels available for the D·^{6}Li case.

catalyzing the burning of ^{6}Li (in this case down to alpha particles). The threshold for the endothermic reaction producing ^{6}Li* is 3.6 Mev (Q = −2.18 Mev); however, the threshold for direct three-body breakup is only 2.5 Mev (Q = −1.47 Mev). The cross section for the endothermic reaction is quite high at high energies ($\sigma v > 10^{-15}$ cm^3/sec at 31 Mev) and, by analogy with other disintegration reactions, is expected to be comparable to the (p,p') reaction or the (n,n') reaction near the threshold. Since the first two alpha products will have low energy in general, they are probably inactive centers, and the theoretical multiplication constant is then about 2 in two generations, or $\bar{k}_2$ = 1.41 per generation, via this particular reaction sequence. A more detailed analysis of the generation of chain centers by 1-Mev-proton- and 1-Mev-deuteron-initiated reactions in a lossless ^{6}Li plasma gave $\bar{k} \cong 1.46$ and 1.43 respectively (some guessing of branching ratios was necessary since the cross sections are not adequately known). Chain-breaking processes whereby active chain centers become inactive can occur by a variety of circumstances such as particle escape, slowing down, (p,n) reactions, etc.

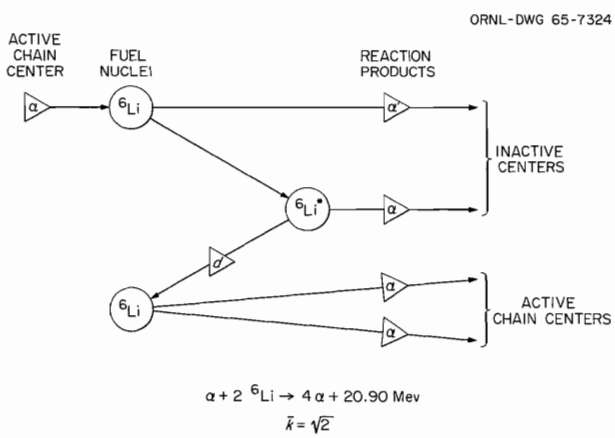

Fig. 10.2. Fusion Chain-Reaction Sequence Initiated by Energetic Alpha Particle (E_α > 3.6 Mev for First Reaction Shown; but, if Three-Body Breakup, E_α > 2.5 Mev). Other reaction channels compete with this selected sequence of reactions and should be included to evaluate a theoretical multiplication constant, $\bar{k}$.

10.4 THERMALLY INDUCED CHAIN-CENTER GENERATION

Thermal (or thermonuclear) reactions become increasingly important at very high energies in fuel such as ^{6}Li·D because of their chain-branching property via the thermal generation of new chain centers. Thus, D·D reactions (curve 3) and D·^{6}Li reactions (curves 6, 7, 8, and 12) produce p, t, ^{3}He, and energetic alpha particles as additional chain centers. In this way the theoretical multiplication constant of about 1.4 to 1.5 for ^{6}Li alone is enhanced so that additional losses of chain centers may be permitted in a reacting system. The total reaction rate parameter, σv, for the several charged-particle-producing reactions between two ^{6}Li nuclei (^{10}B + d, ^{11}B + p, α + ^{8}Be) is about 1.3×10^{-17} cm^3/sec at 2.1 Mev but is rising very rapidly;[2] hence, if $T_+ \gtrsim 0.5$ Mev, one can expect a few ^{6}Li·^{6}Li thermal reactions, which will enhance the multiplication factor further. Note that for deuteron energies above about 400 kev the *total* σv for all D·^{6}Li reactions is greater than that for D·D reactions.

10.5 CHAIN-BREAKING REACTIONS

An important process for converting tritons to ^{3}He by (p,n) reactions above 1 Mev is shown in curve 13 of Fig. 10.1; the resulting ^{3}He can react more fruitfully in a magnetically confined plasma since the reaction products are more likely to be charged, and also a larger fraction of the available Q will show up in these charged particles. A disadvantage is the chain-breaking nature of the reaction, that is, two chain centers ($t + p$) generate one chain center (^{3}He) and an escape neutron — chain-breaking processes of this type (at very high energy) usually introduce an energy sink as well as a reduction of the theoretical multiplication constant of a fusioning plasma (in a thick plasma, where the neutron may be capable of further reaction, no chain breaking occurs in this step). The ^{6}Li$(p,n)^6$Be reaction is very endothermic (−5.2 Mev), so that very little chain breaking is to be expected from this reaction if $T_+ \sim 0.5$ Mev.

[2]See M. N. Huberman, M. Kamegai, and G. C. Morrison, *Phys. Rev.* **129**, 791 (1963).

The endothermic nature of the $d(x,x')p + n$ reactions[3] ($Q = -2.2$ Mev), plus the reduced activity of the proton compared to the deuteron chain center, makes this an important chain-breaking reaction for very energetic particles ($x = p$ requires > 3.3-Mev proton on cold deuteron).

10.6 THE GRAD-BURKHARDT EFFECT

The D·T, D·^{3}He, D·D, and D·^{6}Li magnetically confined, fusioning plasmas operating at high electron temperatures ($T_e > 60$ kev) require external power feed to compensate for the strong electron-cyclotron radiation, especially if the plasma β is low. Such reacting plasmas would be subcritical, that is, external power feed would have to be supplied to sustain the reaction. Grad proposed that, provided the plasma were stable, a high-β plasma in a minimum-B geometry would reduce the magnetic radiation from a volume to a quasi-surface effect. Burkhardt developed Grad's concept and showed that for an idealized magnetic confining wall there is a modest critical plasma size above which magnetic radiation is less than ordinary bremsstrahlung radiation.[4] In an actual plasma, such an ideal can be approached by minimum-B, high-β plasmas; thus, if the average (rms) magnetic field inside the plasma is 10% of the "wall" field, the overall effect of magnetic radiation can be reduced at least 100 fold. Optimistically, one should therefore consider, at our present stage of controlled fusion research, any type fusion fuel for which ordinary bremsstrahlung radiation and the appropriate energy transfer rates define a practical ignition temperature.

10.7 SELF-STABILIZING REACTION MODES

Endothermic reactions, chain-breaking reactions, and $\overline{\sigma v}$-falloff at high temperatures all give rise to a virtual negative reactivity which, like the negative temperature coefficient of the fission chain reaction, introduces a self-stabilizing influence on the reactivity level. The D·T reaction has a negative temperature coefficient above $T_+ \cong 60$ kev since above this temperature $\overline{\sigma v}$ decreases with increasing plasma temperature. The Grad-Burkhardt effect (or thick absorbing plasma) is an essential requirement of such a high-temperature D·T plasma if one is to ensure both self-sustainment and reaction stability.

---

[3] R. N. Henkel, J. E. Perry, Jr., and R. K. Smith, *Phys. Rev.* **99**, 1050 (1955).

[4] H. Burkhardt, *Nucl. Fusion* **2**, 1 (1962); see also H. Grad, *Plasma Physics and Thermonuclear Research*, vol. 2, p. 189, Pergamon, New York, 1963.

11. Design and Engineering: Notes

11.1 ENCAPSULATION OF ELECTROMAGNETS

J. F. Potts W. K. Russell
W. Halchin H. L. Watts

The technology of air-core electromagnets at the Thermonuclear Division has not heretofore included a full development of techniques for complete encapsulation or potting of coils. Two principal reasons are offered for this: (1) The employment of such techniques usually implies the use of rather precisely built molds or resorting to machining operations after impregnation. Economics and schedules do not often favor this method, particularly in large one-of-a-kind systems, where the space factor must be a maximum and dc current density is high. (2) The matrix material must stand up under severe stresses magnetically produced, while withstanding considerable electrical and thermomechanical stresses, and retain its high degree of dimensional stability. A lack of sufficient understanding of the necessary materials and methods has frequently resulted in coils fabricated by "open" techniques. The need for such understanding is highlighted by some early failures of encapsulating coils and emphasized by the near impossibility of economically repairing these coils.

We have been awaiting an opportunity to develop a sufficiently detailed understanding of the problems of encapsulation so that a choice of it as a fabrication method may be objectively considered, rather than being ruled out only because of ignorance concerning its proper application.

The recent conception of a small vacuum-arc facility, called the "J-Arc Facility," is affording us such an opportunity. When a magnetic field is produced for a small plasma system, gas conductance and diagnostic access are bad if the vacuum wall is inside the confining field coils. The obvious solution is to make canned coils and place them inside a larger vacuum system. This seems to be an expensive alternative compared to organic encapsulated coils. The aforementioned problems would have to be solved by formulating a matrix material which had a low specific outgassing rate and with which dependable vacuum seals could be made to coil conductors and cooling lines. The J-Arc Facility provides two other fortuitous circumstances for encapsulated coil development: (1) There is not a tight completion schedule, which affords time for technique development. (2) Its magnet system is to be made up of a number of small modular coils, which affords the opportunity of distributing mold costs over a number of units, and, most important, the cost of a modular unit is small enough that the concern over failure of techniques during development is not too great.

Neither the encapsulation project nor the J-Arc Facility is completed, but sufficient progress has been made to warrant an interim report.

11.2 EPOXY ENCAPSULATION FOR ELECTRICAL COILS

W. Halchin

As of this writing, six coils for the J-Arc Facility have been encapsulated in epoxy. The coils are made of $\frac{1}{4}$-in. square hollow conductor, epoxy coated (Fig. 11.1). They are wound two-in-hand, two pancakes thick, with adjacent pancakes wound in the opposite sense. Dacron sheet is inserted

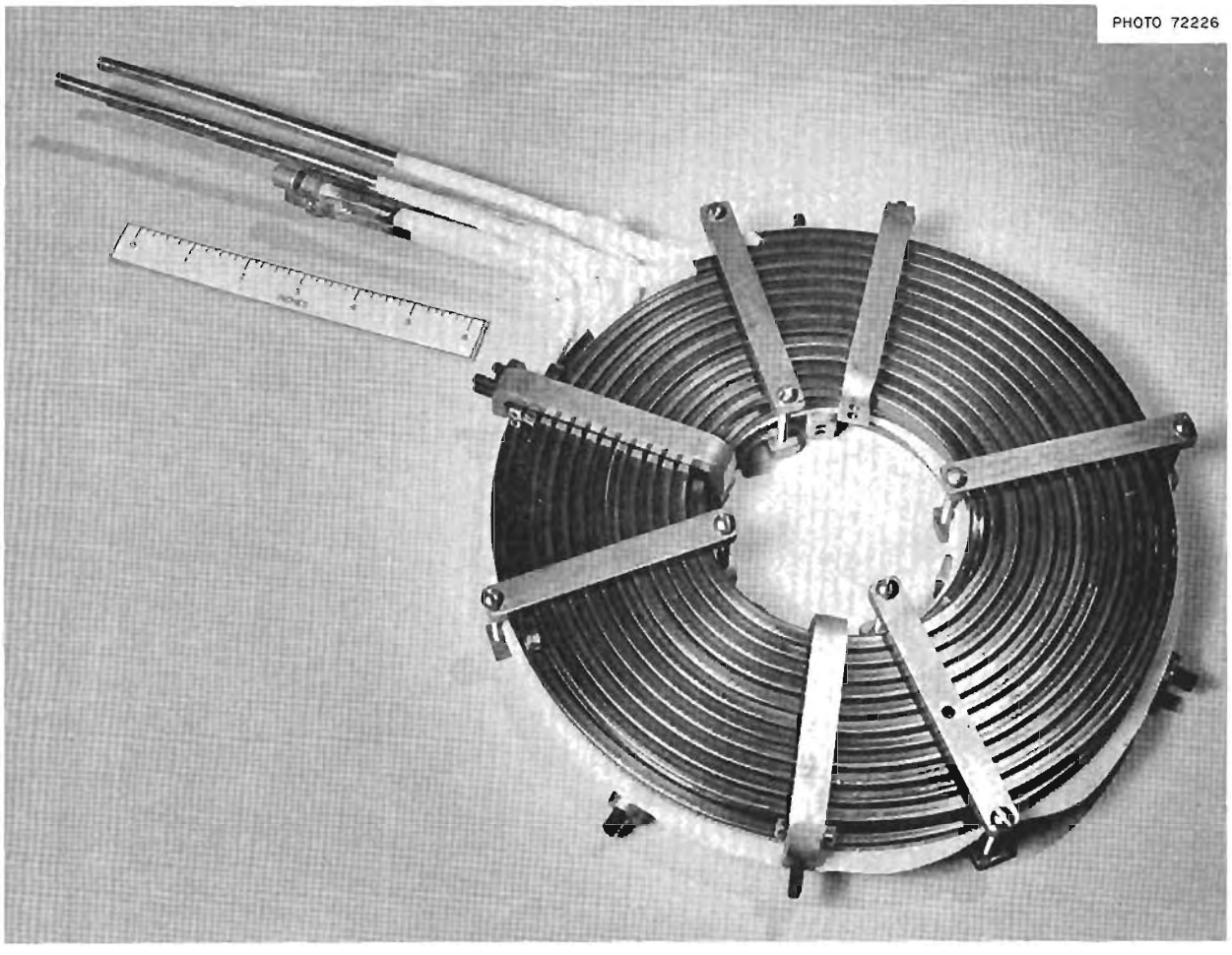

Fig. 11.1. J-Arc Coil After Winding but Before Ground Wrap.

between pancakes. The coil modules are approximately 10 in. in outside diameter, 4 in. in inside diameter, and 1 in. thick, with leads and cooling lines to extend outside the vacuum system through an integrally encapsulated stainless steel nozzle. The first coil was encapsulated by using a Micarta mold lined with Mylar. The epoxy was homogeneous, and the coil was well impregnated. Because of a short, this coil could not be fully tested, but, by sectioning it, valuable information on the problem of bonding of epoxy to copper was obtained. The succeeding coils were encapsulated by using an aluminum mold (Fig. 11.2), which held the outside surface of the epoxy to close tolerance, with a minimum of epoxy over the windings. The second coil was subjected to tests to determine outgassing rate (see Sect. 11.4) and the ability to withstand thermal changes and magnetic forces. During testing the epoxy cracked at several places as a result of thermal changes. As of this writing, four additional coils have been fabricated without the adverse effect of stresses.

It was recommended by the Y-12 Development Laboratory that Jones-Dabney 5101 Epoxy with Z hardener be used. Their previous work had shown that this epoxy system exhibits minimum outgassing, and it has the further advantage of a relatively low curing temperature. A further recommendation was to add Shell Epon 871 to increase elasticity.

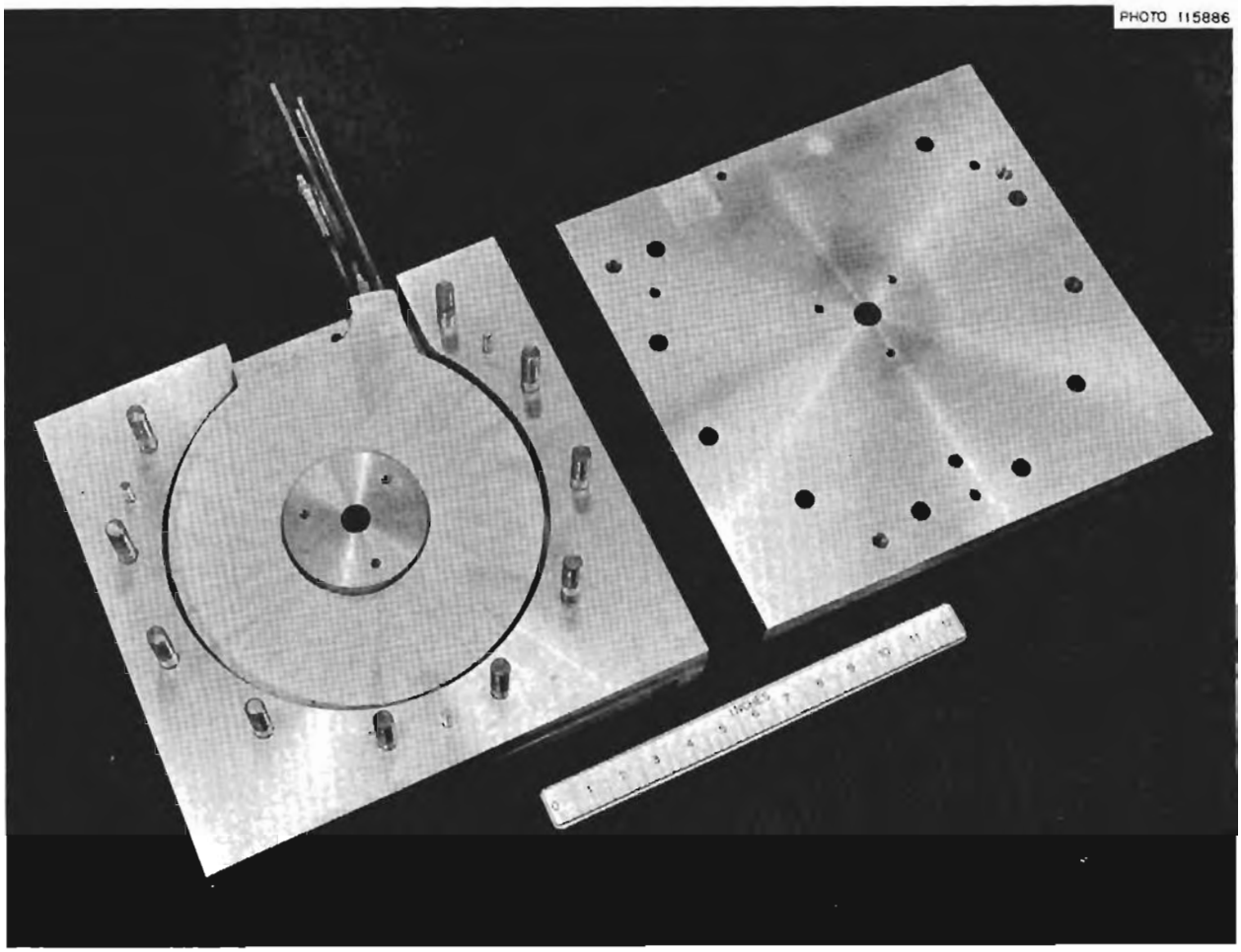

Fig. 11.2. J-Arc Coil with Encapsulating Mold.

The first and second coils were encapsulated with Jones-Dabney 5101 (100 parts) and Z hardener (19 parts), which gives 10,000 psi tensile strength and 3% elongation. As a result of the epoxy cracking on the second coil, the third coil was encapsulated with Jones-Dabney 5101 (35 parts), Shell Epon 871 (65 parts), and Z hardener (14.5 parts), which gives 3400 psi tensile strength and 24% elongation.

Since the second coil cracked, small test samples simulating coils (3 in. in diameter and $^3/_{16}$ in. thick) were encapsulated in a $3^1/_2$-in.-diam. by $^1/_4$-in.-thick mold. These test coils contained various percentages of Shell Epon 871, which acts as a flexibilizer. When subjected to thermal shock, the test samples showed that it was necessary to use about 65 parts of Shell Epon 871 as flexibilizer to allow enough elasticity for prevention of the cracking.

11.3 ENCAPSULATING TECHNIQUE

W. Halchin

A coil is covered with Dacron cloth and wrapped with Dacron tape to reinforce the epoxy. Meticulous care in cleaning and handling all components is necessary to assure complete bonding of the constituents. The Dacron-covered coil is placed into

and centered in the cavity of the enclosed aluminum mold (Fig. 11.2). The coil is suspended and held in position by clamping the coil leads to a bracket on top of the mold. The mold with coil then is preheated to 150°F. This is to help keep the viscosity of the epoxy low during filling and impregnating. After heating, the mold with coil is placed in a vacuum chamber which is evacuated to pressure of less than 50 μ.

The epoxy (about $1\frac{1}{4}$ qt for a J-Arc coil), while still in an open-top container, is put through a preliminary degassing cycle by subjecting it to a 230°F preheat and then evacuating to 20 μ. After cooling, the constituents are mixed at ambient pressure and temperature. The mixture is heated to 130°F, where the viscosity is much lower. This heated epoxy is then slowly fed into a degassing chamber which is held at a pressure of less than 50 μ.

To expose the maximum epoxy surface for degassing within this chamber, the epoxy flows over a series of five 8-in.-long baffles. The baffles are placed on a 30° angle from horizontal. At the bottom, below the baffles, is a container where the degassed epoxy is collected. After all the epoxy is in the degassing chamber, the chamber is raised to atmospheric pressure. The degassed epoxy is then released to fill the mold, which was preheated to 170°F and is in a vacuum. After the mold is filled, it is placed in a furnace at 140°F for 2 hr, and then cured overnight at 150°F at atmospheric pressure.

Currently, coils are being manufactured of acceptable quality (Fig. 11.3). However, work is continuing to improve the process and to explore other epoxy systems and possible advantages of certain fillers. Some shrinkage in the present receipt is one reason for continuing the development. Futhermore, coil systems other than that of the J-Arc Facility will require further exploration of encapsulation systems to complete the original objective.

11.4 EPOXY OUTGASSING

W. K. Russell

With the J-Arc coils (27,000 cm^2 of epoxy area) exposed to the high-vacuum region, the question of surface outgassing required serious investigation. To answer this question, the outgassing rates of various epoxy samples were observed. The system used to determine the flow rates consisted of a test chamber in which the epoxy samples were placed and heated, a tube with a conductance of 35 liters/sec, ionization gages to read the pressure at each end of the tube, and a pumping system.

To shorten the time required to reach gas flow equilibrium in the test chamber, the epoxy samples were preconditioned under rough vacuum and at 90°C for several days before being removed and placed in the test chamber, where they were kept at 90°C and under high vacuum until the gas flow had stabilized. At this time the sample heaters were turned off and pressure readings recorded as the sample temperature decreased.

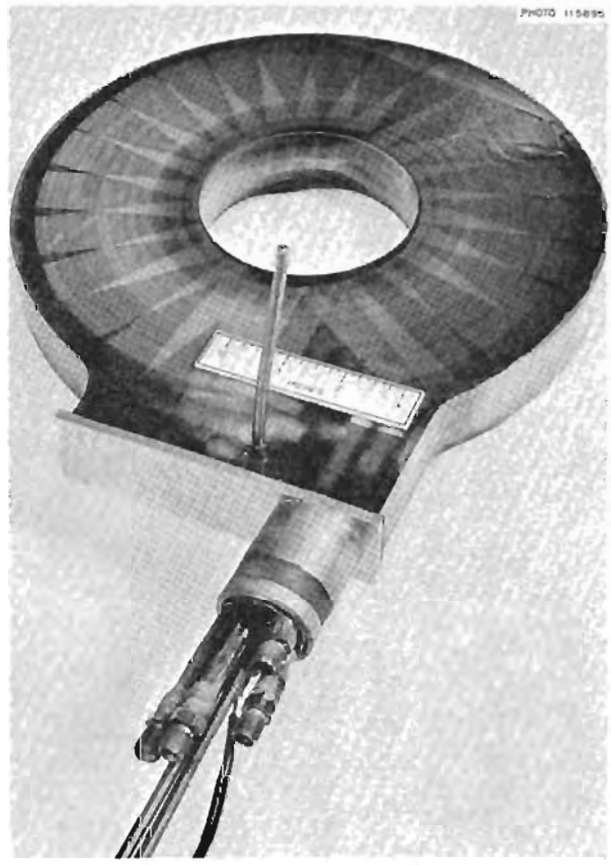

Fig. 11.3. Completed J-Arc Coil.

The various epoxy samples tested produced little difference in their final gas flow. The major difference observed was that initially some samples gave off a tremendous amount of gas while others did not. After a period of time, the amount of gas given off by all samples decreased until finally their gas flow rates were very nearly equal. Figure 11.4 is an epoxy outgassing flow-rate curve that is fairly typical for the samples tested.

The gas flow rate of one J-Arc coil was determined. The coil was placed in the test chamber and heated to 90°C with circulating hot water. After the gas flow rate from the coil had stabilized, the circulating hot water was valved off, and pressure readings were taken in the same manner as before. Figure 11.5 is the gas flow rate curve for this coil.

A comparison of the gas flow rates between the epoxy samples and the coil shows that they differ approximately by a factor of 10. This difference may be due to the sample heaters and heater leads being within the test chamber; therefore the coil outgassing rate should be more correct.

The gas flow from the J-Arc coils will depend on the length of time the coils are postbaked under vacuum, the postbake temperature, and, after cooling, their normal operating temperature. But, from the data now available, it appears that the J-Arc Facility can be operated in the mid-10^{-7}-torr pressure range, with 16 coils in place.

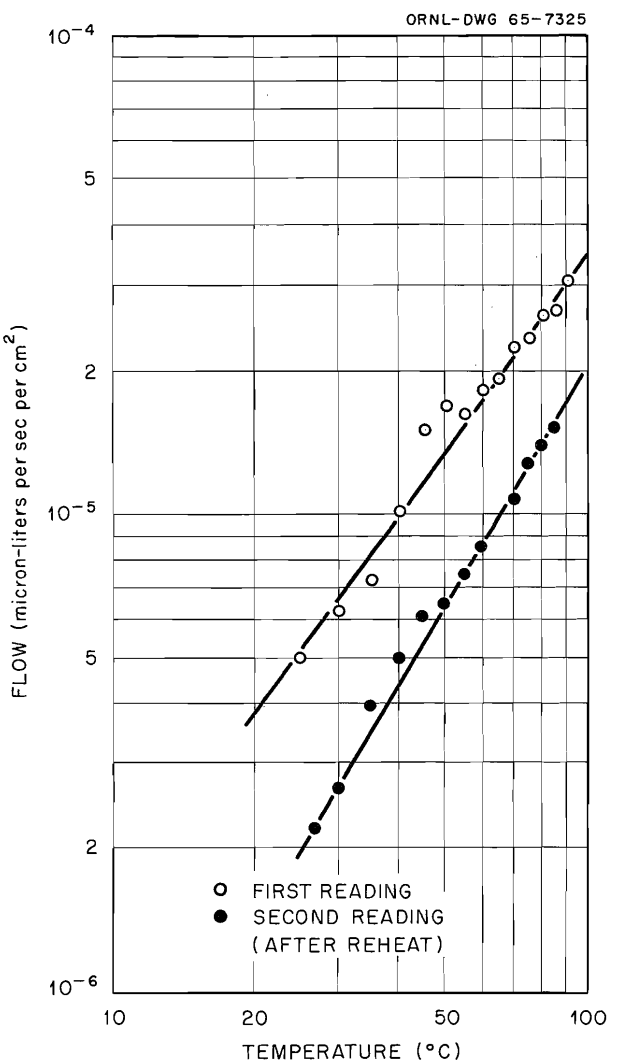

Fig. 11.4. Outgassing of Epoxy Sample.

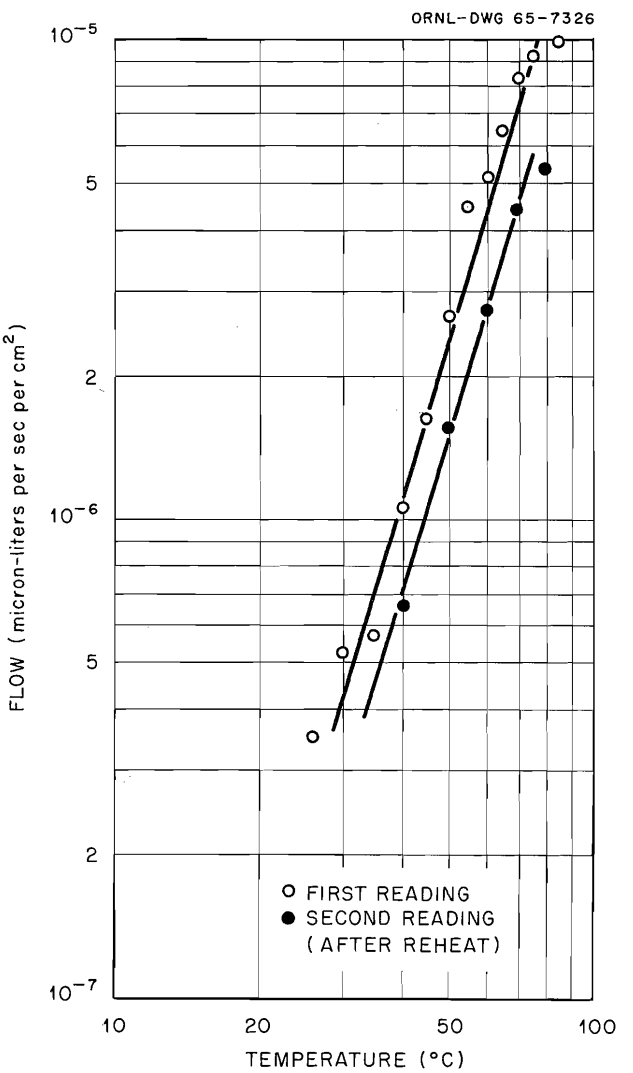

Fig. 11.5. Outgassing of No. 1 J-Arc Coil.

These pragmatic tests were chosen in preference to attacking the complicated matter of quantitatively evaluating the residual gas in the system. This method is giving repeatable comparative results, even though the interpretation of ionization gage readings in the presence of organics is ignored. The aforementioned prebake in a rough vacuum system reduces the contamination of gages, particularly a problem with some silicones. Work is continuing to evaluate the effective area of epoxy produced by various molding techniques and the possible relative water-loading rates of various epoxies when subsequently exposed to air.

11.5 COILS FOR NONVACUUM SERVICE

H. L. Watts

A new epoxy resin, recently developed by Marblette Corporation, is a room-temperature-cure heat-resistant material. It is now being evaluated by us. We have subjected it to thermal shock without failure by encapsulating a hollow-core copper conductor coil and heating with 210°F steam through the coil, then cycling to 78°F by passing water through the coil, repeating the cycle numerous times. Further tests will be conducted to determine other performance aspects. The sample has also withstood severe mechanical shock. Some properties that are specified in the manufacturer's product bulletin are: operating temperature, 170°C; cure, room temperature for 24 hr; dielectric strength, 400–450 v/mil; hardness, Shore D – 86. The ambient-temperature cure is a very attractive aspect to simplify processing where vacuum service is not a requirement.

11.6 ALUMINUM CORONA SHIELD FABRICATION

R. L. Hill

The fabrication and use of aluminum electrostatic shields to control electric fields in the vicinity of high-voltage circuits to minimize corona production have long been a part of high-voltage technology and consequently a part of controlled thermonuclear reactions technology. However, the unusual requirements of dimensions, material thickness, and fit-up to be met in the construction of the accelerator-target shield of the Project HENRE warrants a description of the fabrication techniques developed by E. C. Alexander, of the Y-12 Plant Metal Preparation Division, in cooperation with the author.

Press forming and mechanical spinning were the fabrication techniques considered. The former

ORNL-DWG 65-7329

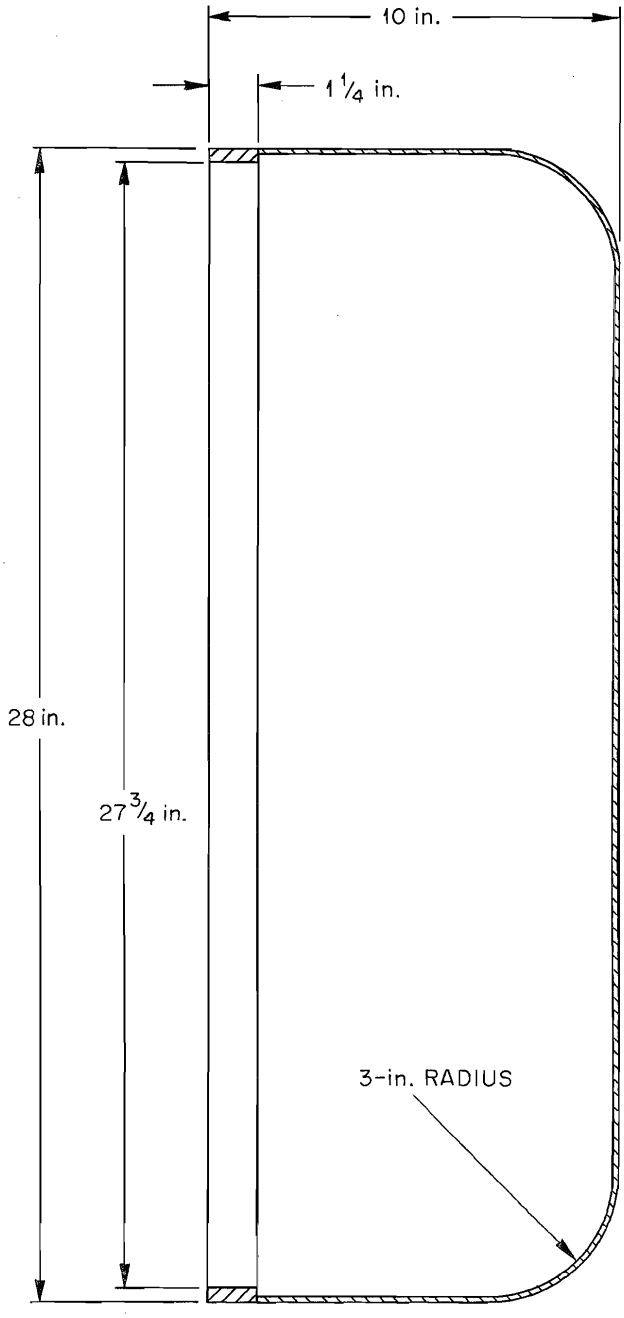

Fig. 11.6. HENRE Corona Shield – Female Part.

was ruled out by the time and expense which would be required to make special metal forming dies – a method usually justified by quantity production. Since this shield was expected to be the only one of its kind, the latter technique was employed, and a description of this method follows.

The material initially chosen for the job was 5056 aluminum. This material repeatedly cracked on the second or third stage of reduction spins after annealing. Subsequently, 1100-series aluminum was tried in the dead-soft condition and proved very satisfactory.

A spinning block was laminated of maple wood and turned to approximately 38 in. in diameter and 15 in. long, with a 3-in.-radius corner on one end in preparation for the first spin of the female part shown in Fig. 11.6, starting with a flat sheet of aluminum. The forming roller (Fig. 11.7) was made from standard tool steel, hardened to 50–52 on the Rockwell "C" scale, then finish ground. Significant dimensions are the 4-in.-diam roller with ½-in.-radius rim.

For spinning we used a 46-in. Bullard vertical turret lathe with a maximum table speed of 150 rpm. We feel that, had it been available, a table speed of around 350 rpm would have been preferable. The contour templates used with the standard follower button were outside-diameter sections of the finished parts. Extreme care was taken not to crowd the roller into the parts upon contact at the start of spinning. At the beginning of each spin sequence, pressure was applied manually, then controlled by the template follower. Care was also taken all through the process not to scratch or dent the parts.

ORNL-DWG 65-7328

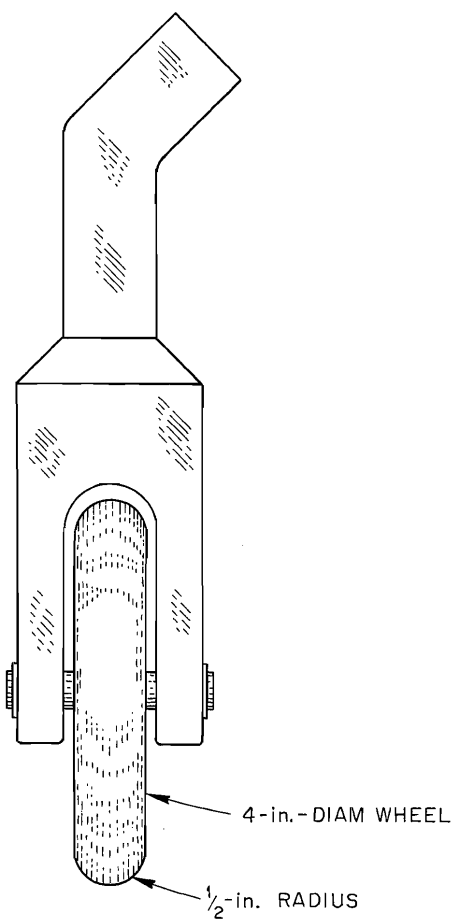

Fig. 11.7. HENRE Corona Shield – Forming Roller.

ORNL-DWG 65-7327

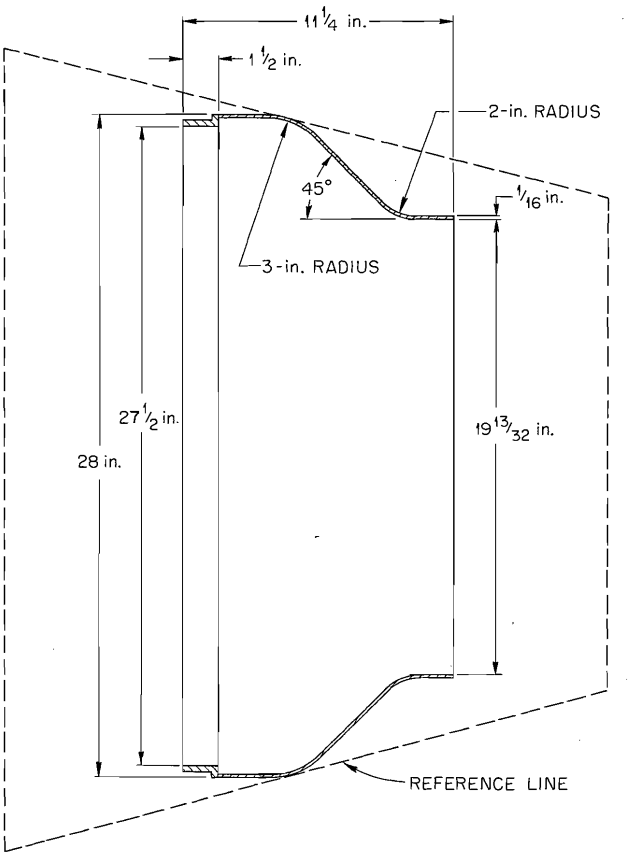

Fig. 11.8. HENRE Corona Shield – Male Part.

After the first and all subsequent spins except the last, the parts were annealed in a standard open-air furnace whose temperature was maintained at 650°F, for 1 hr. The maple block was reshaped after each spin to permit approximately 20% reduction at each of five stages of the female part.

After completion of the female part, the maple block was reshaped into the final form of the male part (Fig. 11.8). The initial preparation of the male part involved cutting and welding an aluminum sheet into the frustum of a cone (dashed line in Fig. 11.8). Three reduction spins were made on the male part, following the first two with anneals.

Trimming, welding of end rings onto the spinnings, and hand-tool polishing completed the parts. The techniques described here were felt out during fabrication, and many false starts were omitted from the description. The techniques developed would be directly applicable to a variety of similar fabrication problems.

11.7 HIGH-TEMPERATURE ELECTROSTATIC PROBES

W. J. Leonard J. F. Potts

An investigation is being undertaken to determine the possibility of constructing coaxial electrostatic probes which could be used proximate to "hot" plasmas for electric field measurements. The desired probe would consist of a central wire conductor 0.005 to 0.010 in. in diameter located in a ceramic rod of suitable high-temperature electrical resistivity. Outside the ceramic should be a coaxial refractory metal sheath 0.002 to 0.005 in. in overall thickness. The overall diameter of the probe should not exceed 0.040 in.

For service-temperature considerations, tantalum, molybdenum, and tungsten wire were considered for use as the central element. Pyrolytic boron nitride is considered the most desirable ceramic material. This ceramic in this form must be deposited on the wire by a process under development. Since hot pressing is the only other acceptable method of placing boron nitride on a wire, some preliminary attempts were made to hot press powdered boron nitride on a 0.010-in. tungsten wire, within the size limitations desired for a probe. No success was experienced in these attempts.

In another approach, aluminum oxide was chosen as the insulating material because of acceptable electrical properties and amenability to a cold-pressing and sintering fabrication process. Wires 0.005 and 0.010 in. in diameter were inserted in a die cavity filled with powdered Al_2O_3. Cold-pressed rods 0.040 and 0.050 in. in diameter and 4 in. long were produced. These rods were then sintered in a furnace at 1300–1400°C under an inert atmosphere. Some densification of the ceramic took place during sintering. The 0.040-in.-diam rods had a continuous coating only about 2 in. long between crack and spalls. The 0.050-in.-diam rods could be produced with continuous coatings of 4 in., but contained some surface cracks. The wire was not centrally located in any of the specimens. Thus, cold pressing and sintering were considered to be impractical for use with such small-diameter wire and coatings.

A slurry of Al_2O_3 wetted with alcohol or water was made. The wires were dipped in the slurry and sized to produce rods in the range of 0.030 to 0.040 in. in diameter. These were dried and similarly sintered. The ceramic "beaded" along the length of the wire as a result of the sintering process. Beads were $\frac{1}{4}$ to $\frac{1}{2}$ in. long, with bare wire showing at some of the reduced-diameter positions. The ceramic could be spalled from the wire quite easily. The buildup in diameter at beaded positions resulted in many cracks in the ceramic coating.

The slurry was again used, and wires were dipped to form a very thin ceramic coat (approximately 3–5 mils in thickness) and dried. The coated wire was heated to the temperature range required for sintering (1300–1400°C) by passing an electrical current through the wire. The work was enclosed in a large bell jar under an argon atmosphere. The sintered specimen appeared entirely satisfactory. No surface cracking was detected, and wires would undergo some bending before the ceramic would flake off, indicating a rather good bond. Samples of the ceramic-coated wire were again dipped in slurry, dried, and resintered to produce additional ceramic thickness. This process could be repeated several times to build up apparently sound rods 0.030 to 0.040 in. in diamter.

It was noted that tantalum-coated wire was brittle and could be easily fractured. By conducting bare-wire tests in the jar, it was determined that the atmosphere was of insufficient purity to

prevent embrittlement of tantalum by the reaction of the metal with oxygen and nitrogen. Tantalum will dissolve approximately 3% oxygen by weight into solution at the temperature required for sintering, which severely embrittles the metal. Molybdenum and tungsten wire form a protective oxide coating and, unlike tantalum, are prevented from absorbing any appreciable amount of oxygen during the time at temperature. A higher-purity-atmosphere enclosure is being set up for further work with this technique.

A technique for coating a tungsten wire with pyrolytic boron nitride is being tried. The wire is maintained in a heated inert-atmosphere muffle furnace, while the gas mixture of NH_3 and BCl_3 is passed into the furnace, reacting on the wire surface and forming pyrolytic boron nitride. This appears to be the most promising method yet investigated for ceramic coating small-diameter wires, but only preliminary results have been attained.

11.8 BRAZING CONNECTORS TO ELECTROMAGNET COILS

W. J. Leonard J. F. Potts
H. L. Watts

In many of the magnet coils used in Thermonuclear Division facilities, connectors must be joined at various locations. The connectors, when joined to the copper conductors, serve as electric terminals and cooling-water connectors, Since the conductors are often covered with organic insulation, care must be taken not to thermally damage the insulation during fabrication. Brazing has been found to be the only satisfactory method of joining within the imposed limitations. The oxyacetylene-torch brazing process does not consistently produce the high-quality result required. Inert-gas tungsten–arc brazing is an acceptable process for making these joints. However, the process requires a very high level of operator skill to consistently produce joints of satisfactory quality.

A program was therefore initiated to investigate the use of induction coils as the heat source for brazing. The copper conductors used were 0.345-in. square tubes with a 0.203-in.-diam channel. Rectangular copper adapter blocks with a recessed bottom slot drilled to accommodate the two terminal ends of the copper conductors were used (see Fig. 11.9). The conductors, when inserted in the connector, leave about 0.001–0.002 in. clearance.

ORNL-DWG 65-7330

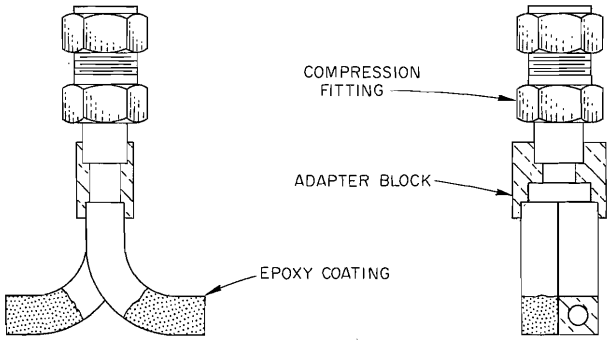

Fig. 11.9. Electromagnet-Coil Connector.

Copper tubing, $\frac{1}{4}$ by $\frac{3}{8}$ in. and having a $\frac{3}{64}$-in. wall thickness, was used to construct induction heating coils. The coils were made to several inner dimensions to study the effect of varying the inductive coupling. The resulting range of clearance between the work and coils was from $\frac{1}{16}$ to $\frac{3}{16}$ in. The coils were two-turn coils, some of which had different inner dimensions for the upper and lower turns.

The two high-frequency generators used were: (1) 30 kw, 150 to 400 kc; (2) 50 kw, 9600 cps.

The connectors with tubing inserted were placed in a vertical position and the coil slipped over the connector box. The braze filler metal (15% Ag, 5% P, bal Cu) was in the form of $\frac{1}{16}$-in. wire, which was cut to proper length and shaped to fit the outer tube surface. This filler-metal ring was preplaced inside the copper connector box. The induction coil was water cooled, while argon was circulated through the conductor tubing during brazing and subsequent cooling.

The high-frequency equipment did not produce any satisfactory brazes, as the temperature on the work surfaces reached extreme values before a necessary amount of heat could be conducted inwardly to melt the filler metal. The lower-frequency equipment did produce uniform heating, with proper heat conduction to the filler metal.

By optimizing the reactance in the primary circuit, the most efficient coupling gave an input of 50 kw into the work, producing a braze in approximately 4 sec. However, the best-quality brazes were

produced under coupling conditions of 15 kw input with a brazing time of 10 to 12 sec. The relatively short time at temperature resulted in no damage to the insulation material on the copper conductors.

All completed test brazements were subjected to a helium leak test, using a sensitivity of 10^{-6} std cm^3/sec detectable leak rate. None of the brazed connectors (10- to 12-sec brazing time) indicated a leak.

Satisfactory brazements which were sectioned showed complete flow of filler metal in the gap between the tubes and connectors, with no porosity in most cases and up to 10% porosity maximum in others. The porosity which did occur was small, isolated, and of spherical geometry.

11.9 BRAZE WELDING COPPER-NICKEL TUBING

W. J. Leonard

In the DCX-1 installations, copper tubing is used on the inner copper liner. As such, the tubing is brazed to the liner wall to secure intimate contact for heat transfer purposes. It is also necessary to make a vacuum-tight connection wherever the tubing penetrates the stainless steel outer vessel wall or wherever the tubing penetrates the inner copper vessel. This requires a tube-on-sheet joint for constructing a jacket, and a tube-to-header joint for entering a vessel. Initially, $\frac{1}{2}$-in.-diam, 0.035-in.-thick wall of OFHC copper tubing was used, but due to the corrosion problem encountered in operation, the wall thickness of the tubing has been increased to 0.062 in.; the latter condition is less desirable from a heat transfer point of view.

During the evacuation cycle of the installation, the copper tubing alternately transfers liquid nitrogen and 600°C high-pressure building steam. These service conditions have resulted in micro-fissure formation in the copper tubing, which affects the vacuum. Tubing failure has occurred within 12 hr of operation in the thin-wall tubing. Increasing the tubing wall thickness to the present value only prolongs the operation time possible, since the inherent corrosion mechanism remains.[1] Since this corrosion attack is thought to be an intergranular penetration of corrosion products through the tubing wall, due to alternate oxidation and reduction reactions induced by the combination of the high temperature (600°C) and quality of the steam, it was considered desirable to attempt replacement of the copper tubing with a material considered functional for this application, which would withstand the environment. A copper-nickel alloy (70% copper, 30% nickel) was chosen for evaluation.

An investigation was made of the weldability of copper-nickel alloy and of the problems in making copper-nickel-to-copper and copper-nickel-to-stainless-steel joints. All welding and braze welding were performed with inert-gas tungsten arc welding equipment. Welding of copper-nickel alloy to itself was performed quite successfully. Welding copper-nickel tubing either as jackets or as headers to austenitic stainless steel plates was accomplished using copper-nickel filler wire. Braze welding the latter materials was also accomplished using any one of the following filler metals: (1) 15% Ag, 5% P, bal Cu; (2) 72% Ag, bal Cu; (3) 60% Ag, 30% Cu, 10% Sn.

Copper-to-copper-nickel brazed joints were successfully made by braze welding, using any of the above braze filler metals. No welds of acceptable quality were obtained by welding copper to copper-nickel, using either copper or copper-nickel filler rod.

A length of copper-nickel tubing, $\frac{1}{2}$ in. in outside diameter, with a wall thickness of 0.047 in., is presently being operated in the DCX-1 system to evaluate the corrosion resistance of this material under service conditions.

[1] R. E. Clausing, internal memorandum 59-12.

12. Design and Engineering: Service Report

J. F. Potts, Jr.

The results of the Engineering Services Group are generally reported incidentally with those of the research groups of the Thermonuclear Division. The Group executes or coordinates engineering design, shop fabrication, building operations, and maintenance for the Division. During this interval, members of the Group have also engaged in a modest amount of technology development, reportable progress of which may be found in the "Notes" section of this report.

Design activities for this reporting period are summarized as follows:

Jobs on hand 11-1-64 on which work had not started	7
New jobs received	153
Total jobs	160
Jobs completed	142
Jobs in progress	9
Backlog of jobs 4-30-65	9
Total drawings completed for period (does not include drawings for slides, reports, etc.)	255

Shop fabrication for this reporting period is summarized as follows:

Machine Shops

Completed jobs requiring 16 man-hours or less	149
Completed jobs requiring 17 to 1200 man-hours	215
Completed jobs of miscellaneous character (in plating, carpenter, electrical, glass, lead, etc., shops)	117
Average manpower per week (machine shop)	23.7
Average manpower per week (miscellaneous)	3
Completed jobs by outside contractors	2

Electromagnet Fabrication

Completed jobs	10
Number of jobs in progress	6
Average manpower (per week)	3

Publications, Papers, and Traveling Lecture Program

PUBLICATIONS

Open Literature

Author(s)	Title of Article	Journal
Igor Alexeff and R. V. Neidigh	Some Stabilized Plasma Experiments	*Phys. Fluids* **8**, 110 (1965)
I. Alexeff, W. D. Jones, and R. V. Neidigh	A Stroboscopic Shutter for Visually Studying Plasma Oscillations	*Rev. Sci. Instr.* **36**, 44 (1965)
Igor Alexeff, R. V. Neidigh, and W. F. Peed	Beam-Plasma Interaction Experiments and Diagnostics	*Phys. Rev.* **136**, A689 (1964)
R. A. Dandl, A. C. England, W. B. Ard, H. O. Eason, M. C. Becker, and G. M. Haas	Properties of a High "β" Plasma Produced by Electron-Cyclotron Heating	*Nucl. Fusion* **4**, 344 (1964)
R. A. Dory, G. Guest, and E. G. Harris[1]	Unstable Electrostatic Plasma Waves Propagating Perpendicular to a Magnetic Field	*Phys. Rev. Letters* **14**, 131 (1965)
T. K. Fowler[2]	Bounds on Plasma Fluctuations and Anomalous Diffusion	*Phys. Fluids* **8**, 459 (1965)
T. K. Fowler[2]	Microwave Index of Refraction in a Mirror Field	*Phys. Fluids* **7**, 1873 (1964)
W. F. Gauster	High Field Superconductors and the Development of Superconducting Magnets	p. 75 in *Plenarvorträge der Physikertagung* (Proceedings of the German Physical Society, Düsseldorf, Germany, Oct. 5–9, 1964), German Physical Society, Düsseldorf, Germany, 1964
W. F. Gauster and D. C. Freeman, Jr.[3]	Superconducting Magnet Coils for Thermonuclear Research	*Nucl. Fusion* **4**, 185 (1964)
R. A. Gibbons[4] and N. H. Lazar	Deuterium Arc Flute Stabilization	*Phys. Rev. Letters* **13**, 703 (1964)
G. Guest	The Effect of Convective Instabilities on the Longitudinal RF Impedance of a One-Dimensional Beam-Plasma System	*Intern. J. Electronics* **18**, 147 (1965)
H. Postma, W. Huizenga,[5] and H. de Kluiver[5]	Experiments with an Improved Method of Ion Beam Extraction from an Ion Source	*Phys. Letters* **14**, 103 (1965)

[1]Consultant, University of Tennessee.
[2]Physics Division. (Now at General Atomic, San Diego, Calif.)
[3]Consultant, Linde Div., Union Carbide Corp.
[4]Deceased.
[5]FOM Inst. voor Plasma-Fysica, Rijnhuizen, Jutphaas, Netherlands.

ORNL Reports

Author(s)	Title	Number	Date
M. W. Garrett	An Elliptic Integral Computer Package for Magnetic Fields, Forces, and Mutual Inductances of Axisymmetric Systems, and a Versatile Line-Tracing Routine	ORNL-3575	April 1965
W. F. Gauster and D. L. Coffey	Experimental Simulation of Large, High Field, Superconducting Magnet Operation	ORNL-TM-1083	March 1965
A. H. Snell	Thermonuclear Division Semiannual Progress Report for Period Ending October 31, 1964	ORNL-3760	February 1965

PAPERS PRESENTED AT SCIENTIFIC AND TECHNICAL MEETINGS

American Physical Society, New York, Nov. 4–7, 1964

W. D. Jones and I. Alexeff, "Study of Ionic Sound Wave Pulses Using Electronic Noise Rejection."

I. Alexeff, W. D. Jones, M. Rankin, and D. Montgomery,[1] "Simple Momentum Probe for Plasma Studies."

G. R. Haste, J. L. Dunlap, and L. H. Reber,[2] "Radial Proton Losses in DCX-1."

C. E. Nielsen,[3] J. L. Dunlap, and L. H. Reber,[2] "Longitudinal Oscillations of Electrons and Fast Protons in a Mirror Field."

J. L. Dunlap, G. R. Haste, and L. H. Reber,[2] "Particle Accountability Measurements with Lorentz-Force Trapping in DCX-1."

C. F. Barnett and J. A. Ray, "Production of H^0 by Carbon Arc Dissociation of H_2^+."

R. A. Gibbons[2] and N. H. Lazar, "Deuterium Arc Flute Stabilization."

G. E. Guest and R. A. Dory, "Effect of a Loss Cone on the Electrostatic Stability of a Uniformly Magnetized Plasma."

Sixth Japan Conference on Radioisotopes, Tokyo, Japan, Nov. 16–19, 1964

D. A. Ross, C. C. Harris, M. M. Satterfield, and P. R. Bell, "Development of Instrumentation in Nuclear Medicine."

D. A. Ross, C. C. Harris, M. M. Satterfield, and P. R. Bell, "New Challenges in Clinical Counting."

D. A. Ross, C. C. Harris, M. M. Satterfield, and P. R. Bell, "Advances in Clinical Scanning Equipment."

Symposium on Recent Advances in Nuclear Medicine, Philadelphia, Mar. 19–20, 1965

C. C. Harris, M. M. Satterfield, and P. R. Bell, "Comparison of Various Methods of Rate Recording."

C. C. Harris, "A Beta-Type Dose from Non-Beta-Emitting Nuclides."

C. C. Harris, "Collimators for Low-Energy Isotopes."

---

[1]Consultant, University of Maryland.

[2]Deceased.

[3]Consultant, Ohio State University.

IEEE Particle Accelerator Conference, Washington, D.C., Mar. 10–12, 1965

O. B. Morgan, G. G. Kelley, and R. C. Davis, "Intense Hydrogen Ion Beam Production from the Duoplasmatron Ion Source."

G. G. Kelley, O. B. Morgan, and R. C. Davis, "A 600-kv Direct Current Injector."

American Physical Society, Washington, D.C., Apr. 26–29, 1965

R. V. Neidigh, I. Alexeff, and W. F. Peed, "Burnout by Beam-Plasma Interaction."

I. Alexeff and W. D. Jones, "Observation of Cut-Off of Ionic Sound Wave Propagation near the Ion Plasma Frequency."

W. D. Jones and I. Alexeff, "Properties of Ionic Sound Waves in a Collisionless Discharge Tube Plasma."

The Institute of Physics and the Physical Society, Symposium on Atomic Spectra and Radiation Processes, Oxford, England, Apr. 12–14, 1965

J. R. McNally, Jr., "On the Possibility of Excitation-Heating of Ions to High Temperature." (Taken as read.)

TRAVELING LECTURE PROGRAM

The Traveling Lecture Program is conducted in cooperation with the Oak Ridge Institute of Nuclear Studies as a part of the AEC's program of disseminating scientific and technical information to universities, particularly those in the South. Lectures delivered by ORNL personnel present unclassified information to university undergraduate and graduate students and members of the faculty. The lectures serve to stimulate interest in research in the university departments and also to assist the teaching staff in expanding the scope of instruction offered under their regular curricula. Through such personal contacts, ORNL staff members are also able to observe departmental activities at the universities. Listed below are members of the Thermonuclear Division who participated in the Traveling Lecture Program during this report period.

W. B. Ard	"Particle and Energy Balance in a Microwave Heated Plasma," University of Miami, Coral Gables, Fla., Sept. 24, 1964.
A. C. England	"Properties of a Plasma Produced by Electron-Cyclotron Heating," Michigan State University, East Lansing, Feb. 1, 1965.
C. O. Beasley, Jr.	"Thermonuclear Research at ORNL: An Analysis of Advancements and Problems (A)," Vanderbilt University, Nashville, Tenn., Nov. 13, 1964.
C. O. Beasley, Jr.	"Thermonuclear Research at ORNL: An Analysis of Advancements and Problems," Florida State University, Tallahassee, Nov. 17, 1964.
C. O. Beasley, Jr.	"Thermonuclear Research at ORNL: An Analysis of Advancements and Problems," University of Miami, Coral Gables, Fla., Nov. 19, 1964.
C. O. Beasley, Jr.	"Thermonuclear Research at ORNL: An Analysis of Advancements and Problems (G)," Howard College, Birmingham, Ala., Dec. 10, 1964.
C. O. Beasley, Jr.	"Thermonuclear Research at ORNL: An Analysis of Advancements and Problems (G)," Jersey City State College, Jersey City, N.J., Feb. 3, 1965.

C. O. Beasley, Jr. "Thermonuclear Research at ORNL: An Analysis of Advancements and Problems (A)," Louisiana State University, Baton Rouge, Mar. 24, 1965.

C. O. Beasley, Jr. "Thermonuclear Research at ORNL: An Analysis of Advancements and Problems (A)," Texas A and M University, College Station, Mar. 25, 1965.

J. R. McNally, Jr. "Spectroscopic Studies of Ultra-High Temperature Plasmas," Southern Missionary College, Collegedale, Tenn., Jan. 12, 1965.

J. R. McNally, Jr. "Spectroscopic Studies of Ultra-High Temperature Plasmas," University of Louisville, Louisville, Ky., Mar. 19, 1965.

ORNL-3836
UC-20 – Controlled Thermonuclear Processes
TID-4500 (43rd ed.)

INTERNAL DISTRIBUTION

1. I. Alexeff
2. W. B. Ard
3. C. F. Barnett
4. C. O. Beasley
5. M. C. Becker
6–11. P. R. Bell
12. D. S. Billington
13. E. P. Blizard
14. C. W. Blue
15. G. E. Boyd
16. R. L. Brown
17. E. H. Christy, Jr.
18. D. L. Coffey
19. F. L. Culler
20. J. S. Culver
21. R. A. Dandl
22. R. C. Davis
23. S. M. DeCamp
24. R. A. Dory
25. J. L. Dunlap
26. H. O. Eason, Jr.
27. R. S. Edwards
28. K. R. Efferson
29. A. C. England
30. J. C. Ezell
31. D. E. Ferguson
32. J. L. Fowler
33. J. E. Francis, Jr.
34. J. H. Frye, Jr.
35. W. F. Gauster
36. J. H. Gillette
37. D. A. Griffin
38. W. R. Grimes
39. G. E. Guest
40. E. Guth
41. G. M. Haas
42. W. Halchin
43. C. C. Harris
44. G. R. Haste
45. R. E. Hill
46. J. L. Horton
47. A. S. Householder
48. H. C. Hoy
49. R. P. Jernigan, Jr.
50. W. D. Jones
51. G. G. Kelley
52. M. T. Kelley
53. R. L. Knight
54. H. W. Koppe
55. M. O. Krause
56. J. A. Lane
57. C. E. Larson
58. N. H. Lazar
59. G. F. Leichsenring
60. W. J. Leonard
61. R. S. Livingston
62. J. N. Luton, Jr.
63. J. F. Lyon
64. H. G. MacPherson
65. J. R. McNally, Jr.
66. O. D. Matlock
67. K. Z. Morgan
68. O. B. Morgan
69. R. V. Neidigh
70. M. L. Nelson
71. J. Neufeld
72. C. E. Parker
73–74. R. B. Parker
75. W. F. Peed
76. H. Postma
77. J. F. Potts
78. M. Rankin
79. J. A. Ray
80. R. G. Reinhardt
81. D. M. Richardson
82. D. A. Ross
83. P. W. Rueff
84. W. K. Russell
85. H. E. Seagren
86. Y. Shima
87. E. D. Shipley
88. J. E. Simpkins
89. M. R. Skidmore
90. M. J. Skinner
91–111. A. H. Snell
112. W. L. Stirling
113. R. F. Stratton, Jr.
114. R. A. Strehlow
115. E. H. Taylor
116. H. A. Ullmaier
117. H. L. Watts
118. A. M. Weinberg

119. E. R. Wells
120. T. A. Welton
121. G. C. Williams
122. W. L. Wright
123. A. J. Wyrick
124. O. C. Yonts
125. Gale Young
126. Owen Eldridge (consultant)
127. J. W. Flowers (consultant)
128. D. C. Freeman, Jr. (consultant)
129. M. W. Garrett (consultant)
130. H. Grad (consultant)
131. E. G. Harris (consultant)
132. D. E. Harrison (consultant)
133. W. Heckrotte (consultant)
134. G. W. Hoffman (consultant)
135. V. W. Hughes (consultant)
136. E. W. McDaniel (consultant)
137. D. R. Montgomery (consultant)
138. C. E. Nielsen (consultant)
139. W. B. Pardo (consultant)
140. J. M. Reynolds (consultant)
141. H. S. Robertson (consultant)
142. H. G. Rorschach (consultant)
143. D. J. Rose (consultant)
144. L. P. Smith (consultant)
145. P. M. Stier (consultant)
146. J. D. Tillman (consultant)
147. Mary E. Williams (consultant)
148–168. Thermonuclear Division Library
169. Reactor Division Library
170. Biology Division Library
171–173. Central Research Library
174. Laboratory Shift Supervisor
175–248. Laboratory Records Department
249. Laboratory Records, ORNL RC
250–251. ORNL – Y-12 Technical Library Document Reference Section

EXTERNAL DISTRIBUTION

252. S. C. Brown, Massachusetts Institute of Technology
253. O. Buneman, Stanford Electronics Laboratories
254. M. B. Gottlieb, Princeton University
255. F. W. Crawford, Stanford Electronics Laboratories
256. T. K. Fowler, General Atomic, San Diego, California
257. J. L. Tuck, Los Alamos Scientific Laboratory
258. D. W. Kerst, University of Wisconsin
259. A. C. Kolb, Naval Research Laboratory
260. Morton A. Levine, Air Force Cambridge Research Laboratories
261. J. A. Phillips, Los Alamos Scientific Laboratory
262. R. F. Post, University of California, Lawrence Radiation Laboratory
263. A. Simon, General Atomic, San Diego, California
264. L. Spitzer, Princeton University
265. E. Teller, University of California, Lawrence Radiation Laboratory
266. C. M. Van Atta, University of California, Lawrence Radiation Laboratory
267–268. Research and Development Division, AEC, ORO (1 copy each to H. M. Roth and R. B. Martin)
269–272. Controlled Thermonuclear Research Branch, AEC, Washington (A. E. Ruark)
273. L. D. Smullin, Massachusetts Institute of Technology
274–284. USAEC, Division of Research, Controlled Thermonuclear Research Program (Stephen O. Dean)
285–607. Given distribution as shown in TID-4500 (43rd ed.) under Controlled Thermonuclear Processes category (75 copies – CFSTI)